UNIVERSITY OF SOUTHAMPTON

Faculty of Engineering, Science and Mathematics

School of Civil Engineering and the Environment

Vortex-Induced Vibrations of a non-linearly supported rigid cylinder

by

Sylvain Bourdier

Thesis for the degree of Doctor of Philosophy

September 2008

UNIVERSITY OF SOUTHAMPTON

Abstract

Faculty of Engineering, Science and Mathematics
School of Civil Engineering and the Environment

PhD Thesis

Vortex-Induced Vibrations of a non-linearly supported rigid cylinder

by Sylvain Bourdier

Vortex-Induced Vibrations (VIV) are a complex fluid-structure interaction problem. VIV are particularly strong for low-mass structures subject to a low damping, as encountered in the offshore industry, in which structures experiencing VIV can also be subject to strong structural non-linearities.

In this project, investigation of the VIV of a low-mass low-damping rigid cylinder subject to structural non-linearities is carried out first experimentally. Non-linearities considered are the symmetric or asymmetric limitation of the amplitude of the cylinder with soft or stiff stops placed at different offsets from the cylinder and implying a non-smooth non-linearity of the system. Experimental results show that a strong perturbation of the dynamics of the cylinder occurs when amplitude limitation is strong, and flow visualisations displaying a modification of the vortex wake suggest a change in the fluid-structure interaction affecting the vortex formation process. Attention is also given to the impact velocities in the different cases of amplitude limitation with stiff stops, as they are an important factor in the design of structures.

Two different wake oscillator models are then used to simulate the VIV of the same rigid circular cylinder in the same conditions of non-linear structural restraints. Results show that these simple models exhibit some features observed experimentally, giving in some cases a good estimation of the experimental data.

Contents

Declaration of authorship

I, **Sylvain Bourdier**, declare that this thesis entitled, "Vortex-Induced Vibrations of a non-linearly supported rigid cylinder" and the work presented in it are both my own, and have been generated by me as a result of my own original research. I confirm that:

- This work was done wholly or mainly while in candidature for a research degree at this University;
- Where any part of this thesis has previously been submitted for a degree or any other qualification at this University or any other institution, this has been clearly stated;
- Where I have consulted the published work of others, this is always clearly attributed;
- Where I have quoted from the work of others, the source is always given. With the exception of such quotations, this thesis is entirely my own work;
- I have acknowledged all main sources of help;
- Where the thesis is based on work done by myself jointly with others, I have made clear exactly what was done by others and what I have contributed myself;
- Parts of this work have been published as:
  - S. Bourdier and J.R. Chaplin. Vortex-induced vibrations of a rigid cylinder on nonlinear elastic supports. *Proceedings of the 6th international conference on FSI, AE & FIV+N, Vancouver*, 2006.

Signed: _____

Date: _____

Acknowledgements

This doctoral thesis, as all others, is the product of many years of study and research on a reasonably focused subject. I thank my supervisor, Pr. J.R. Chaplin for offering me the opportunity to conduct such a project. The guidance and help but also the freedom he gave me have been invaluable to its development. During the different stages of this project, I came across challenging problems, related to different fields of engineering. The resulting diversions that I followed, studying the vibrations of beams or discovering the beauty of non-linear dynamics, undoubtedly lengthened this project, but they have been a very enjoyable and constructive part of my education.

The design of the experimental setup used in the experiments conducted as part of this thesis was also somewhat a team effort and I want to thank the people who helped make it all come together. I am particularly thankful to to Ken Yeates for his interest and suggestions, and to all the technicians of the Lab of the department of Civil Engineering and the Environment, Mike, Dave and Earl, who have always shown concern and been very helpful. I also thank the department of Ship sciences for allowing me to use the Lamont towing tank. I am also grateful to my examiners, Pr. Steve Bishop and Dr.Mingyi Tan for their comments and suggestions that have made this thesis more clear, relevant, and interesting. I acknowledge also the support during the first 3 and a half years of this project of the Engineering and Physical Sciences Research Council.

These years in Southampton have also been an invaluable life experience to me. I enjoyed living in England thanks to all the wonderful people I met here. There has been many of them, at uni and in this lively Portswood village, but I want here to mention some special to me. I would start by Dominique for being so kind helping on my arrival at uni and for sharing with passion this common interest in fluid-structure

interaction problems. There is also Fab for his constant support notably through his help in Matlab or Latex, for our passionate arguments about sciences and these intense games of backgammon, Milie for her delightful e-mails that lightened my spirits many times during all these years, Ange for the many joyful moments, Ju and Wawan for the sessions of extreme darts, Axel for all the fun at juggling and capoeira, Nico, H and Joss for the relaxing breaks during the writing. There's also some special thanks to Natacha, just because my whole life has been so much improved by her influence, I am and will always be deeply grateful.

I want to thank my family, particularly my mum and dad who have always been so supportive and preciously present in the difficult moments. I will mention also my brothers Niak and Babe and my sister Daï, the love of their big brother and his regrets not to have been more present during that time.

Finally, I want to thank Marie, ma chérie, first for her support and patience during these most difficult last months, but mostly for being here on my side, indulging me with her smile every day.

Nomenclature

A^*	Reduced amplitude
A^*_{max}	Maximum reduced amplitude
c	Structural damping coefficient
C_a	Added mass coefficient
C_R	Compliance ratio
D	Cylinder diameter
D_F	Fractal (box-counting) dimension
e	Non-dimensional offset between cylinder's rest position and stop position
f	Oscillation frequency
f_{vs}	Vortex shedding frequency behind a fixed cylinder, $f_{vs} = S_t U/D$
f^*	Frequency ratio, $f^* = f/f_n$
k	Structural stiffness coefficient
L	Cylinder's length
L_b	Length of the horizontal beams holding the frame

m	Oscillating structural mass
m^*	Mass ratio, $m^* = m/(\rho\pi D^2/4)$
m_e	Embedding dimension
f_n	Natural frequency in still water
q	Reduced lift coefficient
R_e	Reynolds number
S_c	Scruton number
S_G	Skop-Griffin parameter
S_t	Strouhal number
U	Flow velocity
U_c	Characteristic velocity of the system $U_c = 2\pi f_n D$
$\dot{Y}_i$	Impact velocity (m/s)
$\overline{V_i}$	Average reduced impact velocity
V_i	Reduced impact velocity
y	Non-dimensional cylinder's displacement, $y = Y/D$
V_{imax}	Maximum reduced impact velocity
C_L	Lift coefficient
δ	Separation between two trajectories at time t
ϵ	Neighbourhood size
λ	Maximum Lyapunov exponent

ρ	Fluid density
τ	Time delay for attractor reconstruction
ζ	Total damping coefficient in water, $\zeta = c/(2\sqrt{(}km)$
ζ_H	Hydrodynamic damping coefficient
ζ_s	Structural damping coefficient in air

Chapter 1

Introduction

Structures are often observed vibrating in the wind; for example, electrical cables for example can vibrate and generate a sound. This phenomenon was known and used by the ancient Greeks as it is told that the God of poetry, or "original Poet", Orpheus held poetry readings accompanied by the music of Aeolian Harps. These strange

Figure 1.1: 9-strings aeolian harp, made by luthier A.Robb. *http://www.art-robb.co.uk/aeol.html*

musical instruments, made of strings stretched above a sounding box produce music when the wind blows across the strings. They were rediscovered by artisans of the Renaissance era and became a very popular household instrument at that time, but it is only with Strouhal in 1878 that the frequency of the aeolian tones produced by a wire in the wind was discovered to be depending on the wind velocity and the wire

diameter. Vibrations of these strings, observed by Lord Rayleigh to be occurring in the plane perpendicular to the flow, have been attributed to the shedding of vortices by the structure, and hence named Vortex-Induced Vibrations (VIV), with the observations of Bénard in 1908 and Von Karman in 1912.

Vortex-induced vibrations are encountered today in many different fields of engineering as they occur in a large number of configurations of different scales, in different fluids, air or water principally. Chimney stacks, buildings, aeroplane wings, and offshore structures all experience VIV. The potential destructive power of flow-induced vibrations was made clear by the collapse of the Tacoma Narrows bridge in May 1940, and extensive research has been conducted for the last sixty years on this fluid-structure interaction problem. Research has mainly been directed towards the understanding of the phenomenon, its modelling and its reduction.

The offshore oil & gas industry is particularly faced with the problem of dealing with VIV. With most of the onshore and shallow-water regions reaching a peak in terms of reserves and production growth, exploitation is moving to deeper waters. The sustainability of this approach to the energy problem that faces our civilisation is questionable since, in the most optimistic scenarios, the world's supply of oil is estimated to end around 2040. Exploitation of the last exploitable resources of these carbon-based energy conveyors is however needed to allow for a transition to a more diversified, sustainable and environmentally-friendly energy generation.

In the offshore industry the long slender flexible pipes (risers) used to convey fluids from the sea bed to the surface exhibit wave-induced, vessel-induced and vortex-induced vibrations. As these risers become longer nowadays for the exploitation of deep-water fields, they also become more flexible and can vibrate like guitar strings, producing fatigue damage and ultimately their failure. As water depths increase, wave and vessel motion-related damage remain at roughly the same level or even diminish, but as currents can act over the full length of the riser, VIV

may make the largest contribution to the overall riser fatigue damage.

In shallow waters the usual practice was to design riser arrays with sufficient spacing to avoid contact between risers by placing perforated plates along their length to hold them in place, but avoiding interaction becomes more difficult and expensive as production moves to deeper waters. Riser arrays with small spacing have become advantageous from both a practical and economical point of view, and the industry now accepts the occurrence of clashes between risers.

The state of the art concerning the VIV of rigid circular cylinders is now well advanced. Principles of the fluid-structure interaction and influence of the main parameters on the dynamics of the cylinder and of the vortex wake have been largely investigated. However most of the studies consider the cylinder subject supported by linear dash pots and linear dampers, and little is known about the influence of non-linearities of the support system of the cylinder on its vibration.

This project therefore aims at investigating the influence of strong structural non-linearities on the VIV of a low-mass low-damping rigid circular cylinder. Attention is given to cases where the cylinder is subject to non-linear mooring springs, or loosely-fitted supports, for which the physical constraints on the cylinder's oscillation can be considered as non-smooth non-linearities of the structural stiffness. Structural non-linearities considered are discontinuities in the system's stiffness, as produced by the presence of soft or stiff stops, placed symmetrically or asymmetrically at some distance from the cylinder. Similar non-linearities have been observed to induce changes in the dynamics of vibrating systems such as impact oscillators or loosely-fitted tubes in array leading in some conditions to chaotic motions, and one can expect amplitude limitation to strongly modify the dynamics of the fluid-structure interaction present in VIV.

After design, realisation and validation in the case of linear restraints of an

experimental setup, experimental investigation of the problem is first conducted for different cases of symmetric or asymmetric amplitude limitation, with different offsets. Modification of the VIV is investigated studying the changes in the dynamics of the cylinder using non-linear dynamics tools, as well as those of the vortex wake using flow visualisations.

Numerical simulation of VIV is important in the design of structures, but direct simulation of the phenomenon is limited to cases with small Reynolds number, of simple geometric configuration and at small scales, and will be so for the next decades due to computation costs. Modelling of VIV with simple phenomenological models can result in some conditions in a good estimation of the VIV of structures, and is often used in their design. This approach of the problem is also undertaken here with two wake oscillator models, in order to evaluate their ability to predict the VIV of low-mass low-damping structures subject to strong structural non-linearities.

Chapter 2

Vortex-Induced Vibrations of rigid cylinders

In 1878, Strouhal [1] carried out one of the first aeroacoustical study on the aeolian tones generated by a wire in an air flow. He noticed that the frequency f of the sound produced by the wire was proportional to the wind speed U divided by the wire diameter D: $f = 0.185\ U/D$. He also found that the sound volume greatly increased when the natural tones of the wire coincided with the aeolian tones. Lord Rayleigh showed one year later that the vibrations took place mainly in the cross-flow direction, but it was only with the flow visualisations by Bénard in 1908 [2] and the stability analysis by Von Karman in 1912 [3] that these vibrations were attributed to the shedding of vortices by the structure, hence the name Vortex-Induced Vibrations.

Vortex-induced vibrations are encountered in many fields of engineering where the presence of a structure, often a bluff body, in a fluid stream generates a separated flow over a large proportion of its surface. In appropriate conditions, the separation of the flow induces an unsteady flow generating the shedding of vortices by the structure alternately from one side and the other [4]. These vortices form a periodic

pattern of vortices known as a Von Karman vortex street. The shedding of vortices results in an oscillating flow pressure field on the structure, which causes its vibration. Studies of VIV refer to different forms of structures, such as plates, sharp-edged or square cross-section bodies, but circular cross-section bodies have received a particular attention as the cylinder is an important shape in practical applications. Surveys dealing with various bluff bodies can be found in Bearman [5], Parkinson [6], or in the book by Blevins [7].

2.1 Fluid-structure interaction

Abernathy & Kronauer [8] showed that it is the growth of two parallel shear layers which leads to the formation of a vortex street. The separation of the flow caused by the presence of a structure, such as a cylinder, in a fluid flow results in the appearance of shear layers and induces the alternative shedding of vortices behind the structure. A non-dimensional number, the Strouhal number S_t , characterizes the frequency of the vortex shedding in the vortex street of a fixed cylinder f_{vs} .

$$S_t = \frac{f_{vs}.D}{U} \tag{2.1.1}$$

The Strouhal number depends on the Reynolds number [7], but it is nearly constant in the subcritical range ($300 \leq R_e \leq 1.5.10^5$) where most of engineering problems occur, at a value of about 0.2, close to the value deduced by Strouhal.

The shedding of vortices creates an oscillating pressure field around the cylinder, which can cause it to vibrate if it is movable. In this case, the motion of the cylinder in return modifies the process of formation and shedding of vortices. Vortex-induced vibration is a strong fluid-structure interaction phenomenon, not primarily in the sense of intensity of forces, but of the simultaneity of evolution of fluid and structure [9]. Temporal synchronisation of the evolutions of fluid and structure is

dominant. When the characteristic time scales associated with the vortex shedding and the structure are of the same order, i.e. when $f_{vs} = \mathcal{O}(f_n)$, f_n being the natural frequency of the structure in still fluid, the fluid-structure interaction becomes stronger. In this condition, the reduced velocity U_r, reflecting the synchronisation of flow and structure by encompassing flow and structure parameters, takes values close to 5:

$$f_{vs} = \mathcal{O}\left(f_n\right) \Leftrightarrow \frac{U}{f_n.D} = U_r = \mathcal{O}\left(\frac{U}{f_{vs}.D}\right) = \mathcal{O}\left(\frac{1}{St}\right) \approx 5 \tag{2.1.2}$$

In this situation, the system is said to be locked-in, and the cylinder can present large amplitude oscillations. Fluid-structure interaction can drive the shedding of vortices by the structure to take place at the same frequency as the cylinder's oscillation, leading to high amplitude oscillations of the cylinder over a whole range of flow velocities.

The cylinder oscillates in both in-line and cross-flow directions, but in-line oscillations, taking place at twice the frequency of cross-flow oscillations, are always much smaller than these latter, and therefore of less importance for most engineering applications. This is why, even if some studies deal with cylinders with two degree of freedom [10–13], the majority of the research conducted on the VIV of a rigid circular cylinder considers the cylinder restrained to move only in the cross-flow direction. Jauvtis & Williamson [11] have shown that this restriction does not significantly affect the VIV of the cylinder, as long as the mass ratio m^* (defined in next section) is higher than 6.

When the transverse amplitude of oscillation of the circular cylinder is large enough, fluid-structure interaction can increase the strength of the vortices or the mean drag on the cylinder, but the motion of the cylinder can also alter the phase, sequence and pattern of vortices in the wake [7].

2.2 Lock-in phenomenon

Vortex-induced vibrations of an elastically-supported rigid circular cylinder are dependent on the flow velocity, as the oscillating pressure field around the structure created by the shedding of vortices is the excitation phenomenon driving the cylinder. Motion of the cylinder resulting from this excitation depends on its structural parameters. Amongst them, the mass of the cylinder and the stiffness and damping of its restraints are the most important.

The range of flow velocities over which high-amplitude oscillations occur, called the lock-in domain, depends on the mass of the cylinder, generally presented in its non-dimensional form m^* , defined as the ratio of the mass of the cylinder m by the displaced mass of fluid:

$$m^* = \frac{m}{\rho\pi D^2/4} \tag{2.2.1}$$

The amplitude of oscillation in the lock-in range depends also on the damping of the system, appearing in the damping ratio ζ defined as the ratio of the structural damping c by the critical damping of the system:

$$\zeta = \frac{c}{2\sqrt{km}} \tag{2.2.2}$$

Several combined mass-damping parameters, as the the Skop-Griffin parameter $S_G = 2\pi^3 m^*\zeta U_r^{-2}$, the Scruton number $S_c = \frac{\pi}{2}\frac{m^*\zeta}{\rho D^2}$ or the simple combined mass damping parameter $m^*\zeta$ have been used to compare maximum amplitudes reached by the cylinder, but also to differentiate high-$m^*\zeta$ cases from low-$m^*\zeta$ cases. Indeed, the response of the cylinder can be very different depending on the mass and damping ratios.

Figure 2.1 illustrates this influence of the mass ratio and damping ratios on the characteristic response of the cylinder. Experimental amplitude and frequency responses from Feng [14] in air with $m^* = 248$ and $m^*\zeta = 0.36$ and from Khalak &

Williamson [15] with $m^* = 2.4$ and $m^*\zeta = 0.013$ are compared. Here the maximum reduced amplitude A^*_{max}, being the maximum amplitude reached by the cylinder divided by its diameter D, as well as the frequency ratio $f^* = f/f_n$, the ratio of the oscillation frequency f to the natural frequency f_n measured in still fluid, are plotted against the reduced velocity U_r.

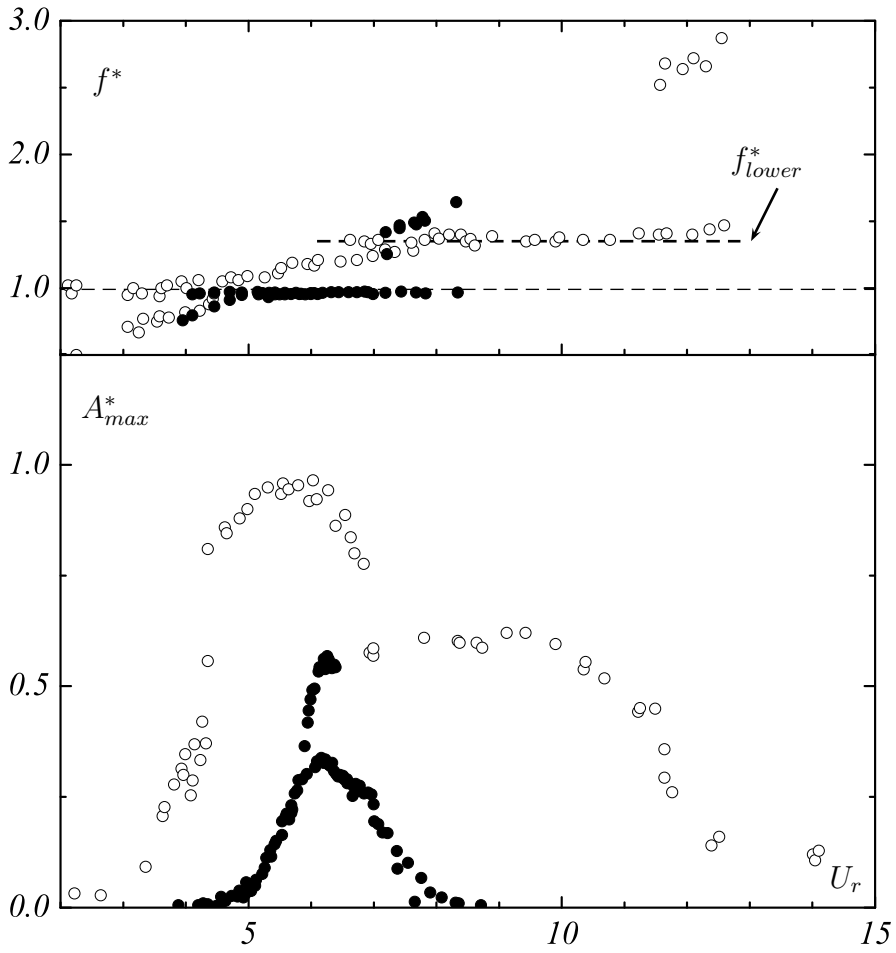

Figure 2.1: Influence of mass and damping ratios on the cylinder response. (○): Low-$m^*\zeta$ case, $m^* = 2.4$ and $m^*\zeta = 0.013$, from [15]; (●): high-$m^*\zeta$ case, $m^* = 248$ and $m^*\zeta = 0.36$, from [14].

The much larger lock-in domain and much larger amplitudes obtained in the low-$m^*\zeta$ case is clearly apparent on the amplitude plot. The pattern of the amplitude responses is also different. The high-$m^*\zeta$ case exhibits three domains, the initial

branch in the first part of the lock-in domain where the amplitude of the cylinder increases with U_r, and the lower branch where the amplitude of oscillation decreases slowly with U_r, and the desynchronisation phase where the amplitude decreases abruptly to become nil for large U_r.

In the low-$m^*\zeta$ case, after the initial branch, another branch, first identified by Khalak & Williamson [15], where the amplitude of oscillation reaches large values, therefore called the upper branch, appears. The amplitude of oscillation in the wider lower branch remains about the same, before the desynchronisation phase. The differences in the patterns of these curves reveal the existence of different modes of interaction between the cylinder and the fluid, as will be seen in section 2.3.

The frequency response of the cylinder presents also differences depending on the mass ratio, as illustrated by figure 2.1(a). In the high-$m^*\zeta$ case, the cylinder oscillation frequency is locked on its natural frequency, giving $f^* = 1$ over the whole lock-in range. Out of the lock-in range, it is equal to the Strouhal frequency. When the mass ratio is decreased, the oscillation frequency does not lock any more on the natural frequency in the lock-in domain. In the upper branch, f^* is somewhere between 1 and its Strouhal value, and increasing with U_r. In the lower branch, it stays nearly constant at a value f^*_{lower} marked on the graph by a dashed line, depending on the mass ratio. Govardhan & Williamson [16] established a relation based on experimental results between f^*_{lower} and m^*:

$$f^*_{lower} = \sqrt{\frac{m^* + C_a}{m^* - 0.54}} \tag{2.2.3}$$

where C_a is the ideal added mass coefficient. This coefficient represents the influence of the mass of fluid carried along by the cylinder because of its motion. This mass of fluid moved by the cylinder is distributed throughout the surrounding fluid and manifests its presence when the cylinder accelerates. It can only be calculated by computation in the case of an unsteady separated viscous flow produced by an oscillating cylinder. It is one of the best known but least understood fluid dynamics

characteristics. Charles Darwin, grandson of the creator of the theory of evolution, has shown in 1953 that the added mass for a body translating uniformly in an infinite expanse of ideal fluid represents a mass of fluid entrained by the cylinder during its motion. It follows that for a cylinder moving with a velocity $U(t)$ in the direction of a unit vector $\mathbf{i}$ in a reservoir of otherwise stationary inviscid fluid, the added mass force on the accelerating cylinder per unit depth can be calculated by means of the velocity potential, and equals:

$$\mathbf{F} = -\rho\frac{\pi D^2}{4}\frac{dU}{dt}\mathbf{i} \ . \tag{2.2.4}$$

The negative sign shows that the added mass force acts in opposition to the acceleration of the body, and so, for a spring-mounted damped cylinder vibrating in a reservoir of stationary ideal fluid, the equation of motion is:

$$m\ddot{y} + c\dot{y} + ky = -\rho\frac{\pi D^2}{4}\frac{dU}{dt} \ , \tag{2.2.5}$$

from which, by replacing U(t) by dy/dt, the following is obtained:

$$\left(m + \rho\frac{\pi D^2}{4}\right)\ddot{y} + c\dot{y} + ky = 0 \tag{2.2.6}$$

where the increase of the structural mass of the cylinder for its dynamic analysis by the added mass is here obvious. Usually in the equations the added mass is divided by the displaced mass of the body, to define an added mass coefficient C_a. The values of these coefficients for other cross sections in inviscid flows can be found in standard reference works. The ideal value of C_a for a cylinder is $C_a = 1$. As noted by Sarpkaya [17], Stokes showed in 1851 that viscosity also affects the added mass and "*In unsteady flows, neither is the drag equal to its steady state value nor is the added mass equal to its inviscid flow value*". Nevertheless, the ideal value of 1 for C_a is commonly used by authors.

Equation 2.2.3 also implies the existence of a critical mass ratio $m_c^* = 0.54$ below which the lower branch of excitation does not exist any more, and therefore the upper

branch expands to infinity. Indeed, with $m^* = 0.52$, Govardhan and Williamson [16] found high amplitude oscillation beyond the limits of their facility, at $U_r \approx 20$.

2.3 Switches in vortex modes

In his experiment with high-$m^*\zeta$, Feng [14] observed jumps in the phase between the transverse force on the cylinder and its motion, simultaneously with the observed amplitude jumps. These phase jumps are associated with switches in vortex shedding mode. Brika & Lanneville [18] showed with smoke visualisations that the initial and lower branches in the high mass ratio cases are associated with two different modes of vortex shedding, as shown by their photographs and sketches presented in figure 2.2.

In the initial branch, two single contra rotative vortices are created in every oscillation cycle of the cylinder, forming a wake pattern similar to a Karman vortex street. This mode presented in figure 2.2(a) has been called the 2S mode.

In the lower branch, two pairs of contra rotative vortices are shed per oscillation cycle, as illustrated by figure 2.2(b); hence this mode was named the 2P mode. The phase jump at the transition initial⇌lower found by Feng reveals changes in the timing of vortex shedding. Brika & Lanneville found the build-up time to be longer for the 2P regime than for the 2S regime, and the decay time greater in the 2S mode than in the 2P. The switching mechanism between the two modes takes place over several periods of cylinder motion and both in-phase and out-of-phase vortex shedding occur during the transition. In high-$m^*\zeta$ cases, the transition between initial and lower branches is found to be hysteretic, occurring at different flow velocity when the flow velocity is increased or decreased.

In the case of low-$m^*\zeta$, the transition between initial and upper branches in the

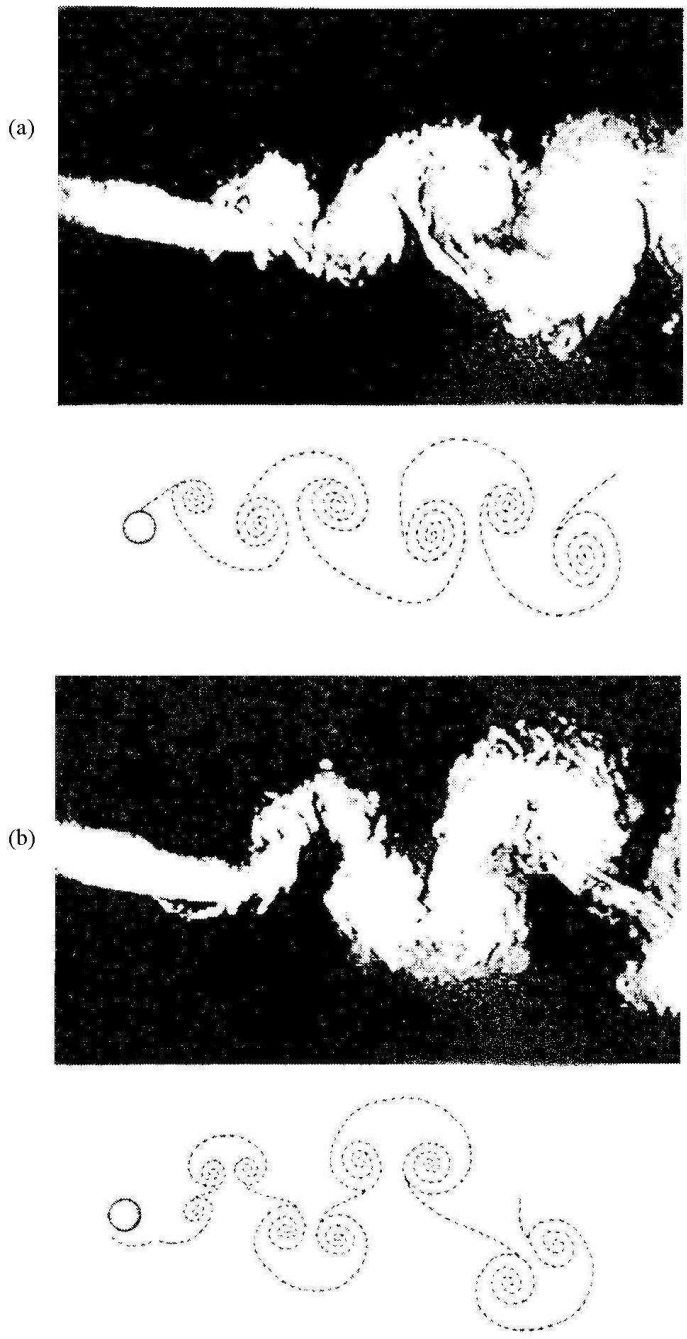

Figure 2.2: Photographs and sketches of the 2P and 2S modes. (a): 2S mode; (b): 2P mode. *From [18].*

low-$m^*\zeta$ case is also hysteretic. The wake exhibits a 2S mode in the initial branch, and switches to a 2P mode in the upper branch, but one in which the second vortex

of each pair is weaker than the first, whereas both are of equivalent strength in the 2P mode appearing in the lower branch. This transition is found to involve an intermittent switching between the two modes. In the transition range, the cylinder can remain during a number of cycles locked on the upper branch vibration mode and switches to the lower branch oscillation mode, where it remains for some periods before switching back to the upper mode. This intermittent switching occurs over a short range of reduced velocities, where the time spent in the upper branch mode decreases while approaching the lower branch.

Another mode, the P+S mode, when a pair of vortices and a single vortex shed per cycle has been observed by Williamson & Roshko in forced experiments [19] at Re numbers below 300. This mode is not normally found in free vibration experiments, however Singh & Mittal [20] reported the occurrence of this mode in their simulations of free VIV at Re$>$ 300.

Jauvtis & Williamson [11] observe that when the cylinder is free to move also in-line (X-Y motion), with the same natural frequency in both directions, the freedom to oscillate in-line affects only very slightly the transverse vibration when the mass ratio m^* is larger than 6. However, for mass ratio below 6, a dramatic change in the fluid-structure interaction occurs, and the upper branch of vibration changes into a super-upper branch in which significant in-line motion appears, leading to very high transverse oscillation, up to maximum amplitudes of 1.5 diameters. They discovered the corresponding wake pattern to be a 2T mode, in which the cylinder sheds two triplets of vortices per oscillation cycle.

Jeon & Gharib [21] extend the idea of a vortex formation time, initially developed for vortex rings, to bluff-body flows. They stipulate that the vortex formation time is intimately related to the time the vortex is attached to the cylinder. In their forced X-Y experiment they vary the formation time by varying the streamwise acceleration superimposed on the transverse motion. They show that increasing the formation

time increases the number of vortices formed per cycle. With the cylinder describing a figure-of-eight motion, accelerating in the flow direction at the extremes of the transverse motion, they obtain short vortex formation times, and the cylinder sheds only one single vortex per half-cycle. With no in-line motion, the formation time increases and the cylinder sheds two vortices per half-cycle. When it describes a figure-of-eight decelerating at the extremes of the transverse motion, the cylinder sheds three vortices per half-cycle. These observations lead them to state that "*the wake of a circular cylinder seems to be paced by a vortex formation time*". This notion of vortex formation time can be related to the shedding of triplets of vortices in the super-upper branch, as the Lissajous figures presented in [11] in this domain at high amplitude show the cylinder describing a figure-of-C, and therefore decelerating in-line when reaching its extremes of transverse amplitude. According to the theory developed by Jeon & Gharib, this motion should lead to large formation times and therefore to the shedding of several vortices, which is observed with the shedding of triplets of vortices.

Much progress has been made, both numerically and experimentally, toward the understanding of the inherently non-linear, self-regulated, multi-degree-of-freedom phenomenon that is VIV. The coupling between the motion of the structure and the instability mechanism leading to vortex shedding can result in a lock-in phenomenon responsible for large amplitude oscillations over a whole range of reduced velocities. Investigations are mainly concerned with the interaction of a rigid body, mainly a rigid circular cylinder, whose degrees-of-freedom have been reduced from six to often one or two, and subject to linear restraints. In these cases, mass and damping ratios influence the dynamics of the fluid-structure interaction, and different modes of oscillation of the cylinder, corresponding to different modes of vortex shedding, can occur. Instantaneous hydrodynamic forces on the structure however still cannot be expressed as function of the many governing parameters and much remains in the domain of descriptive knowledge.

2.4 Motivations and objectives of present work

In most applications complex structures experiencing VIV move with six degrees of freedom, and structural restraints used to maintain them in place can be non-linear, and dependent on the degree of freedom. Examples of structural non-linearities occurring in such applications can be found in the offshore industry.

2.4.1 Moorings of offshore floating platforms

Spar platforms recently developed to go in deep waters ($> 2000m$) are exposed to sea currents and experience VIV. These huge cylindrical floating platforms, schematically represented in figure 2.3, amongst the biggest in use, consist of a large vertical cylinder on top of which is fixed a typical rig platform. The cylindrical part serves to stabilize the platform and to allow for movement to absorb the force of potential hurricanes. To fix ideas, the cylinder or hull of the classic Spar platform Genesis operating in 2,600 ft (790 m) of water is 122 ft (37 m) in diameter and 705 ft (214 m) long. In figure 2.3, a photograph of the Genesis hull leaving port Aransas, Texas gives a more expressive impression of its size.

As for all floating structures, systems of cables or moorings are used to limit their displacement and maintain them above the region to be developed. The Genesis platform is for example held in place with a 14-point mooring system, each mooring line being approximately 3000 ft (914 m)-long, composed of 5 in (12.7 cm)-diameter chain and wire rope. The physical constraints exerted by moorings on floating structures involve a strong non-linearity of the system stiffness. When the structure moves, the tension in its moorings increases and they behave like non-linear hardening springs.

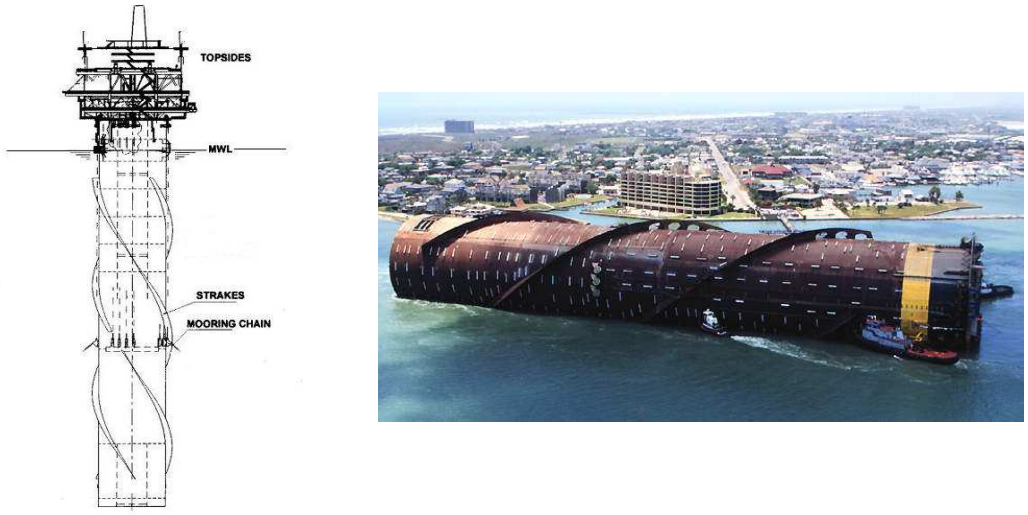

Figure 2.3: Scheme of a Spar platform, *from [22]*, and picture of the Genesis hull, *from http://www.offshore-technology.com/projects/genesis/*

VIV of a Spar platform is an important consideration in the design of Spar mooring system and risers; it is complex issue that involves a large number of parameters, including the current characteristics, the Spar hull characteristics, and the dynamic characteristics of the moored system [22]. A Spar has typically three or four groups of mooring lines which present non-linear force-displacement characteristics and can be modelled by bi- or tri-linear spring systems. Irani et al. [22] show that the non-linearity of the mooring stiffness reduces dramatically the VIV of a Spar and explain that this is a result of the increase of the transverse stiffness of the mooring system with increasing in-line offset which reduces the natural period leading to lower reduced velocities.

Stappenbelt & Thiagarajan [23], [24] mention that for many restrained floating structures, the non-linear compliance can be modelled by a third order polynomial stiffness of the form $k_1 y + k_3 y^3$ and that for example typical maximum compliance ratio $C_R = \frac{k_3 D^2}{k_1}$ for shallow-water catenary moored structures is about 0.1. In [23], they study the influence of such non-linearity of the stiffness in the equation of a

sinusoidally forced single degree of freedom mass-spring-damper system. They therefore obtained the well-known Duffing equation, whose solution shifts the maximum amplitude reached in the lock-in domain to a higher value of U_r than in the linear case. They show that an increase of the compliance ratio C_R just slightly decreases the maximum amplitude of vibration observed in the lock-in domain but that this one occurs at a reduced flow velocity increasing with C_R increasing.

The work of Hover & Triantafyllou [25] can also be mentioned here, as they studied the influence of structural non-linearity on the VIV of cylindrical structures, but at larger mass ratio. In their paper they argue that certain shallow-sag cable structures possess non-linear compliance properties which arise from the static curvature and differentiate then from taut-string systems. They consider the non-linearity made of quadratic and cubic terms leading to a stiffening spring with asymmetry. The VIV test they conduct show that the effects of the non-linearity in the lock-in region are minor, but they notice one variation due to the non-linearity, a vortex-shedding frequency in the lock-in domain located well above the value found in the purely linear system.

The non-linear smooth behaviour of the stiffness as considered in [23], [24] can be a good approximation of the compliance of moored floating structures in usual sea conditions. However it can be argued that during rough sea conditions, where the combined effect of wave-, flow- and vortex-induced vibrations can lead to violent motions of the structure, the rapid tensioning of the moorings could be approximated by a step increase of the system stiffness, and the restraints applied on the structure by the moorings could be approximated by a non-smooth discontinuity of the system stiffness.

2.4.2 Clashes of risers

Risers used also in the offshore industry to conveys fluids from the sea bed to a floating structure are also subject to strong structural non-linearities. The need for offshore industry to move to deeper waters makes these vertical pipes longer and more flexible. The unsteady forces due to vortex shedding cause them to vibrate like guitar strings, sometimes with a high number of vibrational modes. Vortex-induced vibrations produce fatigue of the risers and can cause body clashing in multiple riser systems. It can cut the lifetime of a typical riser worth about 5 million dollars down to only about one year.

Some systems for suppressing VIV have been developed, such as the strakes, a helicoidal string spiralling down the riser, also used on chimney stacks or Spar platforms and visible on the schematic presented in figure 2.3, or the fairings, air plane wing shaped cross-section encasing the riser. These systems, usually placed only on the top of the risers where sea currents are stronger, do reduce vibrations. Along the risers, constraint systems are also used to limit their vibration and to hold them in place together. Usually they consist of some sort of metal plates with holes for risers to pass through. The holes are oversized, and the vibration of the riser leads to impacts with the plate.

In these multiple riser configurations, close risers vibrating sometime clash together at some point along their length, and the repetition of impacts increases their fatigue. The usual philosophy was to design riser arrays in such a way that contact would not occur, but this is not possible in water depth of 5,000 ft (1500 m) and beyond [26]. Nygard et al. estimated with a 3D numerical model the stresses in the riser at impact through the simulation of the most extreme event, the clashing of a connector of a drilling riser with a production riser. They found the stresses in the riser to be within acceptable condition for most types of conditions, but did not estimate fatigue and

wear which occurs with repetitive impacts.

2.4.3 Fluid-riser-soil interaction at touchdown point

The bottom end of a riser conveying fluid from the sea bed to the surface also rests in some cases on the sea bed, as in the case of a Tension-Leg Platform (TLP) illustrated in figure 2.4. The point where the riser first touches the soil, called the touchdown point (TDP), is critical in the analysis and design of steel catenary risers. When the riser oscillates, due to the combined effect of wave-, flow- and vortex-induced vibrations, the TDP moves and after some cycles the riser creates a trench in the sea bed, thought to be formed through a combination of the applied vessel motions and fluid flow across the riser and the seabed [27]. The curvature of the riser can be large in the touchdown area, because of the non-linear geometric boundary at the sea bed, leading to high stresses in the riser and fatigue. Numerous efforts have recently been made towards the understanding and modelling of the very complex fluid-riser-soil interaction in the touchdown area, and many are concerned with the effect of this boundary condition on the riser. Aranha et al. proposed an analytical expression for the bending moment in which it depends non-linearly on the displacement of the TDP and the dynamic tension applied in the riser [29]. This analytical asymptotic solution shows good

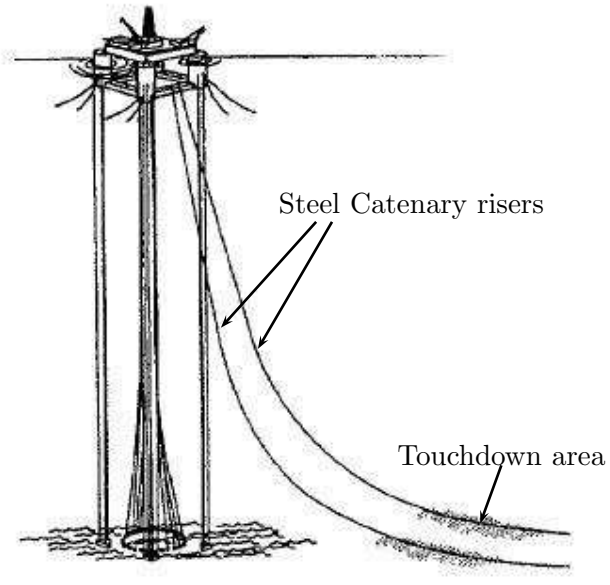

Figure 2.4: Configuration of steel catenary risers on a TLP Platform. *From [28].*

agreement with experimental results [30] but only in the absence of shock between the riser and the floor. For the numerical simulation of the riser-soil interaction, some frequency-domain and time-domain models, valid for small motions about the static TDP, cut the mooring off at the touchdown point and attach an equivalent linear spring and/or dashpot. The lift-off and grounding approach, in which the mass of the discrete nodes or elements is reduced to zero as they approach the bottom, simulates a perfectly rigid sea bed with no impact and smooth rolling and unrolling of the cable. A third approach is to model the sea bed as an elastic foundation. For this, several seabed models have been developed ([31], [32], [28]) to simulate the soil-riser interaction in SCR analysis, but require the determination of the appropriate stiffness and damping constants to associate with a given type of soil.

The assumption that there is no impact between the riser and the sea bed has been shown to be valid as long as the translational speed of the TDP does not exceed the transverse wave speed of the mooring line [33]. If it exceeds it, a shock wave is formed and impact occurs on the sea bed. Storm and current action on a deep-water production vessel can indeed pull the riser upwards from its trench and induce repetitive impacts of the riser on the sea bed. The structural implications of the shocks on the riser depend on whether the excess happens during loading (mooring moving upward) or unloading (mooring moving downward). Loading shocks occur less frequently and lead to a snap load in the tension while unloading shocks occur under less severe excitation conditions and therefore more frequently and lead to slack tension at the touchdown point [34].

In this problem of fluid-riser-soil interaction, in which the riser is subject to a non-linear one-sided (contact-type) boundary condition [35], research has mainly been conducted on the structural implications of this geometric non-linear boundary condition on the riser, and on the modelling of the soil-riser interaction. But in the catenary region close to the TDP, the riser experiencing VIV is subject to

asymmetrical structural restraints due to the boundary condition, and little is known on the effect of this structural asymmetric non-linearity on the strong fluid-structure interaction existing in vortex-induced vibrations as this phenomenon has mainly been investigated in conditions of linear structural restraints.

2.4.4 Objectives of present work

The main objective of this work is to investigate how strong structural non-linearities, such as rapid tensioning of moorings or impact with close components, can affect the VIV of a structure presenting, as in the case of offshore applications, a low mass ratio and subject to a low damping.

The VIV of a rigid circular cylinder being the basic model for such problems, the fundamental case of a low-mass low-damping rigid circular cylinder experiencing VIV is considered. The cylinder's support system, usually considered made of a system of linear springs and dash pots, will be modified in order to approximate the structural non-linearities sometimes encountered by some offshore structures experiencing VIV, and its response to VIV will be investigated for different cases of non-linear structural restraints.

The presence of non-linearities in its support system is expected to affect the VIV of the low-mass low-damping rigid cylinder, and this most importantly in conditions where vortex shedding usually drives the cylinder to describe large amplitude oscillations when subject to linear restraints. It can be argued that the large amplitude vibrations found to occur in the super-upper branch for a very low mass ratio ($m^* < 6$) rigid cylinder when it is able to move also in the in-line direction with the same natural frequency as in the cross-flow direction [11] would certainly be affected by the presence of the structural non-linearities before stabilisation. It could therefore be assumed that the VIV of such a low-mass low-damping rigid cylinder free

to describe X-Y motions would be affected by a structural non-linearity in approximately the same way as those of the same cylinder restrained to move only in the cross-flow direction. For this reason, and most importantly also, in order to limit the complexity of the project, the cylinder will be restricted move only in the cross-flow direction.

We have presented in chapter 2 the now well described main features of the VIV of a low-mass low-damping rigid cylinder subject to linear structural restraints, i.e with constant damping and stiffness coefficients, as illustrated in figure 2.5(a). As offshore structures are often subject to non-linear compliance, few studies have dealt with the effects of a smooth non-linearity of stiffness of the cylinder's support system, which can model for example the effect of moorings on SPAR platforms in usual sea conditions. In these cases, the stiffness coefficient of the system is considered smooth

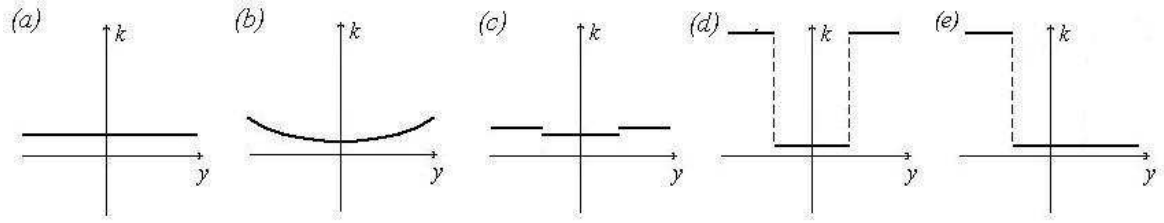

Figure 2.5: Stiffness coefficient of the cylinder's support system.(a): Constant behaviour in the linear case; (b): Smooth non-linear hardening restraints; (c): Cases with impacts on symmetrically-placed soft stops; (d): Symmetric cases with impacts on stiff stops; (e): Asymmetric cases with impacts on one stiff stop.

non-linearly dependent of the cylinder's non-dimensional displacement y, for example of the form $k_1 + k_3 y^2$ as in figure 2.5(b). In last sections, we presented some examples of strong structural non-linearities encountered by some offshore structures experiencing VIV. In order to model strong structural non-linearities similar to those seen in last sections, the stiffness of the cylinder's support system is considered here a piecewise-smooth discontinuous function of the displacement: the cylinder, supported by a system of linear springs and dash pots, experiences an instantaneous increase of

the stiffness coefficient of its supports when reaching some value of displacement. Such structural non-linearity is equivalent to the presence of a spring, or a purely elastic stop, in the system on which the structure can impact during its vibration.

Different configurations of such type of structural non-linearity can be achieved in order to model different cases of structural non-linearities encountered by structures subject to VIV. Symmetric cases with the cylinder's amplitude limited on both sides by stops placed at the same distance from its rest position can be investigated. In setting the stiffness coefficient of the stops to a relatively low value, of the order of that of the cylinder's linear restraints, as in figure 2.5(c), cases with impacts on symmetrically-placed soft stops, structural restraints approximating those exerted by moorings on floating structures during rough sea conditions conditions, can be achieved. In setting the stiffness coefficient of the stops to a very large value, as in figure 2.5(d), the restraints become similar to those of a body with imperfectly-fitting structural restraints. Asymmetric cases with only one stiff stop limiting on one side the cylinder's motion, as in figure 2.5(e), approach for example the non-linear one-sided boundary condition a riser is subject to close to the sea bed.

2.4.5 Overview of the Thesis

These extreme case of non-linear structural restraints, i.e the symmetric or asymmetric amplitude limitation of the motion involved by the presence of other components close to the vibrating structure, are also often encountered in other vibrating mechanical systems for which the driving mechanism is different. In order to later compare our results concerning the VIV of a low-mass low-damping rigid cylinder with impacts to the response of other vibrating systems subject to similar non-smooth structural non-linearities, a short review of the effect of amplitude-limiting stops on the dynamics of impact oscillators and arrays of tubes in

cross-flow will be given in the next chapter. As non-linear dynamics theory and tools have been applied to, and proved useful in the investigation of the dynamics of vibrating systems with impacts, a brief presentation of non-linear dynamics theory, now of common use in that field of mechanics, will first be given.

As, to our knowledge, no experimental or numerical investigation of the influence of such structural non-linearities on the VIV of a low-mass low-damping rigid cylinder has been done yet, an experimental investigation of the problem was first of all conducted in order to get first experimental data to investigate the problem. The experimental setup designed and used in towing tanks to carry out experimental tests of VIV of a low-mass low-damping rigid circular cylinder is first described in chapter 4. The response of the cylinder restrained to move in the cross-flow direction to the VIV reproduced with this experimental setup is also presented in the case of linear structural restraints, in order to validate its response by comparison with experimental data from similar experiments in the literature.

Chapter 5 first presents how a non-smooth non-linearity of the stiffness of the cylinder's support system was achieved by inserting stops in the system. Investigation of the effect of a symmetric non-smooth non-linearity was first of all carried out for small values of the stops stiffness, i.e. in condition of impacts on symmetrically-placed soft stops. Effect of the strength of the non-linearity on the dynamics of the rigid cylinder was investigated by varying the stiffness ratio ,defined later, and the offset. The stiffness of the stops was then greatly increased, to reach conditions close to those of symmetrically-placed rigid stops. The effects of a strong symmetric amplitude limitation of the cylinder on its VIV were then investigated by studying the changes in the dynamics of the cylinder using non-linear dynamics tools, and in the fluid-structure interaction using flow visualisations, for different offset values.

Chapter 6 presents the experimental results concerning the VIV of a low-mass low-damping rigid circular cylinder subject to asymmetric non-smooth structural

restraints, i.e in the case of impacts on one stiff stop. As for double-sided impacting cases, changes in the dynamics of the cylinder and in the fluid-structure interaction caused by asymmetric amplitude limitation were investigated for different offset values.

The experimental results obtained can then be used for comparison with numerical simulations of the same tests in order to assess the ability of the model used to predict the VIV of structures with non-linear compliance. Indeed, numerical models are used by engineers to simulate VIV of structures to help for their design. These models generally predict more or less accurately VIV of structures with linear constraints, and are often calibrated by fits with experimental results in this case. However, the structural arrangement of structures in applications often involves structural non-linearities, and one can wonder if these models can be valid in such cases.

Amongst the many models used for prediction of VIV of offshore structures, some wake oscillator models, the "Milan" wake oscillator model and a Van Der Pol wake oscillator model, introduced in the first part of chapter 7, present motivations for investigating their responses in the case of non-linear structural restraints. In order to assess the ability of simple phenomenological numerical models to predict the VIV of structures subject to strong structural non-linearities, simulations of the experimental tests undertaken in this project have also been conducted with these two different wake oscillator models. Dynamics of the cylinder predicted with the Milan oscillator in the different cases with impact on stiff stops experimentally investigated are first presented and data are compared to experimental data, before presenting those obtained in the same cases with the Van Der Pol wake oscillator.

Finally, in chapter 8, we give a brief summary of the thesis, highlight the main results obtained during this project, and also discuss possible orientations for future research.

Chapter 3

Presence of structural non-linearities in vibrating systems

Systems subject to VIV often encounter in real cases some physical constraints leading to structural non-linearities. As non-linear constraints can produce changes in the dynamics of vibrating systems leading to unwanted behaviour, it is important to know if such changes can appear in vortex-induced motions of non-linearly supported structures. A better understanding of the non-linear dynamics of such systems could be helpful in the adjustment of the constraints and improve the lifetime of structures.

Recently developed non-linear dynamics concepts have been developed and applied with success to investigate complex dynamical systems in many fields of science. Chaotic behaviour has been observed in astronomy with Poincaré studying the three-body problem, in fluid dynamics and turbulence with Kolmogorov, in weather prediction where Lorenz discovered the sensitivity to initial conditions with the famous butterfly effect, in population growth with the famous logistic equation introduced by P.Verhulst [36], in chemistry with the Belousov-Zhabotinsky oscillating reaction, and in many more other fields.

non-linear dynamics tools have also been used to investigate the effect of structural non-linearities on the dynamics of harmonically-excited systems impacting on stops. In these non-linear systems, the structural restraints considered are similar to the ones considered in this project, the excitation phenomenon though is different. Major results concerning the effect of structural non-linearities on vibrating systems will be briefly presented, in order to later compare the behaviour of these systems to that considered in this project, excited by vortex shedding. As some notions of non-linear dynamics are needed to present the work previously done in this area, concepts of non-linear dynamics including theories of stability and bifurcation are briefly introduced in next section; the reader can refer to the books of Guckenheimer & Holmes [37] or Moon [38] for more information. Particular attention is given to Lyapunov exponents and their calculation from experimental time series, as estimates of this invariant will be performed later in this work.

3.1 Non-linear dynamics concepts

3.1.1 Phase space, trajectories

To describe a mechanical system with N degrees of freedom and predict its next state, N position variables q_i and their time derivatives $\dot{q}_i$ have to be known. With these $2N$ dynamical variables, the state of the system is totally determined as N equations of motion can link accelerations $\ddot{q}_i$ to velocities $\dot{q}_i$ and positions q_i. These equations of motion are generally non-linear differential equations of second order of the form:

$$\ddot{q}_j = f_j(q_i, \dot{q}_i) \qquad (i, j = 1..N) \ , \tag{3.1.1}$$

which can generally be expressed as a dynamic system of $2N$ first order differential equations:

$$\begin{cases} \dot{x}_i = y_i \\ \dot{y}_i = g_i(x_j, y_j) \qquad\qquad (i,j = 1..N) \end{cases} \tag{3.1.2}$$

where $x_i = q_i$ and $y_i = \dot{q}_i$ are the dynamic variables of the system. Considering a state vector $Q = [x_i, y_i]^t$, the dynamic system can be expressed as:

$$\dot{Q} = F(Q) \ , \tag{3.1.3}$$

where F is a vector function tangent to the trajectory referred to as a vector field. Determination of equations of motion can, in principle, lead by integration to the knowledge of the system future states. The system evolution is described in the $\mathbb{R}^{2N}$ space $(x_i, y_i), i = 1..N$, called phase space. Cauchy [39] first showed that, for a system of differential equations with no random term, there can be only one unique solution corresponding to a set of initial conditions. From a given state of the system, described by one point in the phase space, the system can only evolve toward one future state. Its evolution with time, solution of the system of differential equations, forms a trajectory, or orbit, in the phase space. An equilibrium position would be represented in the phase space by a point, whereas a periodic solution would form a closed curve. All the solutions of the dynamical system 3.1.3 form a flow of trajectories $\Phi_t : \mathbb{R} \to \mathbb{R}^{2N}$. In order to obtain the flow Φ_t, the system of $2N$ differential equations has to be integrable, and for this, N constants of the motion are needed. In most non-linear problems however one or more of these constants are unknown and the considered system cannot be integrated. This is the case of the three-body problem, addressed by Poincaré in his pioneer memoir in 1889 [40], in which he states that "*when a system is not integrable, the study of its periodic solutions is of first importance*".

3.1.2 Fixed points, bifurcations of fixed points

The most obvious solutions are the system equilibria. When the system is in an equilibrium position, its trajectory in the phase space is a fixed point. Fixed points in the phase space are solutions of the equation $\dot{Q}_* = 0$. As $\dot{Q} = F(Q)$, their coordinates Q_* can be found by solving $F(Q) = 0$. These fixed points Q_* are the only ones in the phase space where trajectories can cross, making them the only exceptions to the uniqueness principle. Equilibria can be stable or unstable. The stability of a fixed point is studied by applying a small perturbation so that $Q_* \to Q_* + \xi$ to the system placed at the considered fixed point:

$$\dot{Q}_* + \dot{\xi} = F(Q_* + \xi) \ . \tag{3.1.4}$$

Using $F(Q_* + \xi) = F(Q_*) + J_F(Q_*)\xi + O(\xi^2)$, where $J_F(x)$ is the Jacobian matrix of F given by $J_F(x) = \left[\frac{\partial F_i}{\partial q_j}\right]$, the system evolution $\dot{\xi}$ resulting from the perturbation can be obtained by the variational equation:

$$\dot{\xi} = J_F(Q_*)\xi + O(\xi^2) \ . \tag{3.1.5}$$

Eigenvalues Γ_i of the Jacobian matrix solve $J_F(Q_*)\xi_i = \Gamma_i \xi_i$, and allow the variational equation to be rewritten:

$$\dot{\xi}_i = \Gamma_i \xi_i \ , \tag{3.1.6}$$

giving after integration,

$$\xi_i(t) = \xi_0 e^{\Gamma_i t} \ . \tag{3.1.7}$$

Depending on the sign of the real part of the eigenvalue Γ_i, the perturbation ξ_i will be amplified or damped, and the spectrum of eigenvalues of $J_F(x)$ gives the evolution of the perturbation ξ, and describes the stability of such equilibria.

Different types of singular points, presented in figure 3.1, exist, around which the trajectory will develop. *Nodes* where an infinity of trajectories can meet, *saddles*

where only two trajectories meet, *sinks* that close trajectories approach asymptotically like a logarithmic spiral and, only in conservative systems, *centres* can be found, surrounded by trajectories enveloping themselves. With the variation of a

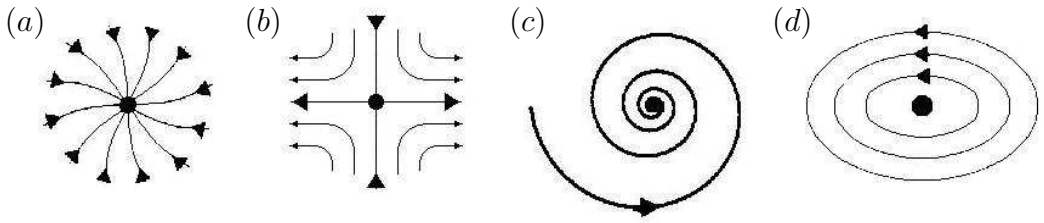

Figure 3.1: Different types of singular points.(a): node; (b): saddle; (c): sink; (d): centre.

control parameter μ, the nature of fixed points can change, involving changes in the system behaviour. This happens through a bifurcation. Bifurcations are subcritical if the number of singular points decreases, super critical if it increases, or transcritical if the number of singular points stays unchanged. Different bifurcations of singular

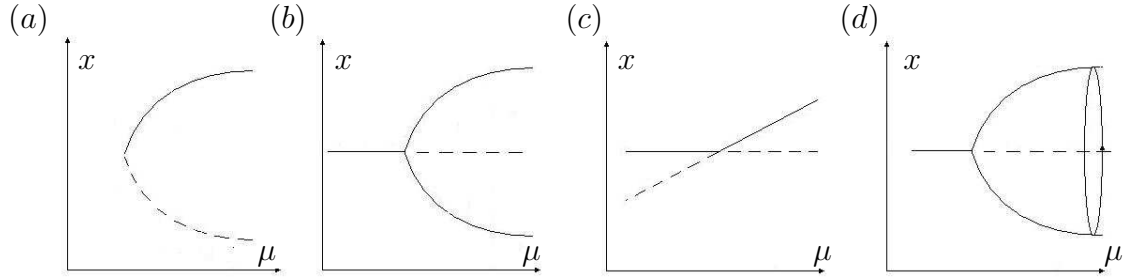

Figure 3.2: Bifurcations of singular points. (a): Saddle-node bifurcation; (b): Supercritical pitchfork bifurcation; (c): Transcritical bifurcation; (d): Supercritical Hopf bifurcation.

points have been observed, like the saddle-node, pitchfork or transcritical bifurcations. Those are illustrated with their bifurcation diagrams, presenting the stability of the fixed points as a function of the control parameter μ, in figure 3.2.In these bifurcation

diagrams, stable fixed points are presented with plain lines, and unstable ones with dashed lines. Figure 3.2(d) illustrates a Hopf bifurcation, which occurs when the destabilisation of a stable node leads to the stability of a periodic orbit.

3.1.3 Limit cycles, bifurcations of limit cycles

The transitive state in phase space ultimately filled by a single steady state trajectory is called an attractor. A sink represented by a single point in phase space is an attractor as all trajectories converge to it, and ultimately finish on it. Limit cycles, like the one appearing after a supercritical Hopf bifurcation, are also attractors. Like fixed points, limit cycles can be subject to destabilisation. Their stability can be studied through that of a periodic point using an appropriate transformation linked to the periodicity of the limit cycle. This transformation is made through the use of a Poincaré section, defined as a local cross section $\Sigma \subset \mathbb{R}^{2N}$. This cross section must be chosen so that the flow is everywhere transverse to it. Successive intersections of the flow with the cross section are plotted on a map, forming a Poincaré map:

$$x_{n+1} = G(x_n) \ . \tag{3.1.8}$$

To a periodic solution of the vector field F corresponds one periodic point x_* of the map G, defined by $x_* = x_{n+p} = x_n$ where p is the period of the limit cycle. Stability of periodic orbits can be studied by introducing perturbations ξ at the point x_* in directions perpendicular to the flow. Eigenvalues Λ_i of the Jacobian matrix of G at x_* reveal the stability of the periodic orbit. If $|Re(\Lambda_i)| < 1$, the direction associated with Λ_i is stable, whereas if $|Re(\Lambda_i)| > 1$, the direction is unstable. Bifurcations of periodic orbits occur when, with the variation of a parameter, one of the eigenvalues Λ_i of the system sees its norm equal to one. The periodic orbit becomes unstable, and the system switches to another state. Most of the bifurcations encountered with singular points can be found with periodic orbits, as it is the case with the Hopf

bifurcation as illustrated by figure 3.3. When a pair of complex conjugates

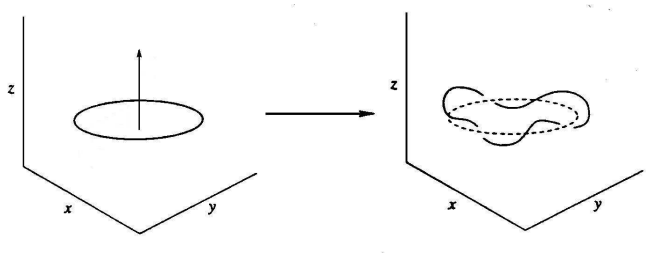

Figure 3.3: Hopf bifurcation of a limit cycle.

eigenvalues cross the unit circle on the right, the existing stable limit cycle loses its stability and undergoes a Hopf bifurcation, through which the trajectory folds itself on a tore encircling the first limit cycle. The evolution of the system is then characterised by two frequencies, one related to the rotation around the principal axis, and the other related to the rotation around the tore. Depending if the ratio of these frequencies is rational or not, the system can be periodic or semi-periodic.

Another type of bifurcation, the period doubling bifurcation, also known as flip bifurcation, can however occur only with periodic orbits. Period doubling appears

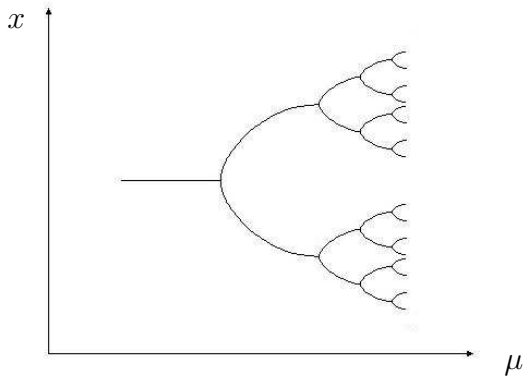

Figure 3.4: Bifurcation diagram of a period-doubling cascade.

when a periodic limit cycle loses its stability when one of the eigenvalues of the system takes the value -1. In figure 3.4, a period-1 limit cycle stable for low values of the parameter μ undergoes a period-doubling bifurcation and a period-2 cycle

appears. In this example, with further increase of the control parameter μ, the period-2 cycle undergoes another period-doubling bifurcation into a period-4 cycle, and so on. This succession of period-doubling bifurcations has been observed in many dynamical systems and is named a period-doubling cascade. All orbits created are 2^i-periodic and the higher the period, the closer successive bifurcations will be. M.J. Feigenbaum [41] showed that these period-doubling cascades follow a universal scaling law. If μ_i is the critical value at which the 2^i-periodic cycle changes into a 2^{i+1}-periodic cycle, then:

$$\delta_F = lim_{i \longrightarrow \infty} \frac{\mu_i - \mu_{i-1}}{\mu_{i+1} - \mu_i} = 4.6692016091029... \tag{3.1.9}$$

This relation involves the existence of an accumulation point μ_∞ where the period of the periodic cycle is infinite, and chaos occurs.

3.1.4 Lyapunov exponents

Jacques Hadamard [42] studying in 1898 a free particle moving without friction on a surface of constant negative curvature showed that all trajectories in this system are unstable and that every trajectory moves away from every other one with a exponential separation rate. The sensitivity to initial conditions was made more popular in 1972 by E.Lorenz with a talk entitled "*Predictability: Does the Flap of a Butterflys Wings in Brazil set off a Tornado in Texas?*" which gave birth to the name butterfly effect. This unpredictability of future states despite a deterministic time evolution is characteristic of chaotic systems. Two trajectories with close but different initial conditions can diverge after some time, but whereas in predominantly periodic systems this divergence can appear and evolve slowly, in chaotic systems, the divergence is exponential, and quantified by the Lyapunov exponent. To quantify the sensitivity to initial conditions of a system, two trajectories are chosen with infinitesimally close initial conditions. The separation δ between their positions in the

phase space at an instant t will evolve with time. If the separation is considered exponentially dependent on time, a rate of exponential divergence λ can be introduced, giving:

$$\delta(t) = e^{\lambda t}\delta_0 \ , \tag{3.1.10}$$

where δ_0 is the infinitesimal separation in the phase space between the two initial conditions.

But the system can be more sensitive to the variation of one of its parameters than of another one, therefore the rate of divergence of close trajectories λ, called the Lyapunov exponent, can be different depending on the orientation of the initial difference vector δ_0 in the phase space. In a non-linear system with N dimensions, the time evolution of δ can be described by its time evolutions in tangent spaces, and therefore N Lyapunov exponents λ_i, each corresponding to one of the N linear subspaces of $\mathbb{R}^N$, can be obtained. The set of these N Lyapunov exponents is often referred as to the Lyapunov spectrum.

If one Lyapunov exponent λ_i in the spectrum is positive, close trajectories with an initial difference vector δ_0 having a non-zero component in this direction will diverge exponentially fast. As infinitesimal perturbations can occur in any directions of the phase space, the presence of only one positive Lyapunov exponent in the Lyapunov spectrum results in an extra sensitivity of the system to disturbances, and in a loss of its predictability. The determination of the greatest Lyapunov exponent of the spectrum, generally simply referred to as the Lyapunov exponent λ, is therefore sufficient to judge the predictability of the dynamical system considered. It can be defined as follows:

$$\lambda = \lim_{t\to\infty}\left(\lim_{\delta_0\to 0} = \frac{1}{t}\ ln\frac{\delta(t)}{\delta_0}\right) \ . \tag{3.1.11}$$

This is a classical test in chaotic studies as λ is an indicator of the nature of the motion: it has the dimension of an inverse time and gives a typical time scale for the

divergence of close trajectories.
If $\lambda > 0$, the system is chaotic, and λ quantifies the 'strength' of chaos in the system, as the larger the exponent the greater the divergence.

If $\lambda = 0$, the system is in some steady state mode, two different orbits will keep on a long term their initial separation. This is for example the case of trajectories around a fixed centre point as in figure 3.1(d). Such systems are said in Lyapunov stability.

If $\lambda < 0$, trajectories are all attracted by a stable fixed point or or stable limit cycle. In a same way, the more negative the exponent, the more stable the limit cycle.

Even if the equations of motion of a non-linear system are known, the determination of the Lyapunov exponent cannot generally be achieved analytically as the system is often not integrable. It has to be noted that an analytical method to obtain asymptotic estimates for the Lyapunov exponent of vibrating systems containing one amplitude limiting stop is presented by Meijaard in [43]. The dynamics of the system close to the stop are approximated by a one-dimensional non-smooth non-invertible map from which an estimate of the Lyapunov exponent can be extracted. The method is applied to a two-degree-of-freedom dynamical system made of two coupled oscillators and analytical predictions are close to numerical values.

The experimenter however usually obtains a time series of a single measured quantity, being only a projection on a 1-dimensional space of the attractor corresponding to the underlying non-linear system, whose mathematical expression is usually unknown. The experimental determination of the Lyapunov exponent of the system then requires the use of other techniques.

3.1.5 Calculation of Lyapunov exponent from experimental time series

3.1.5.1 Attractor reconstruction

The Whitney embedding theorem [44] states that a euclidean space of dimension $2N+1$ $\mathbb{R}^{2N+1}$ is necessary to fully embed the dynamics of a N-dimensional system. That is in $\mathbb{R}^{2N+1}$ no two points from an N-dimensional system can map onto themselves and the image of a N-dimensional manifold is completely unfolded in $\mathbb{R}^{2N+1}$. This latter is called an embedding of the N-dimensional system. The evolution of the system is totally described by time series of $2N+1$ measurements.

The ergodic theorem [45] often used in chaos theory states that the average of a measurement over space can be equal to its average over time. Studying the system from a great number of trajectories of a finite time length or from one trajectory of long time length of the attractor is then equivalent. The Takens embedding theorem [46] shows that instead of $2N+1$ measured signals, $2N+1$ time-delayed measurements from a single noise free signal $Y_i = [y_i, y_{i-\tau}, y_{i-2\tau}..., y_{i-2N\tau}]$ suffice to embed a N-dimensional manifold. Requirements are that the measurement function is $\mathbb{C}^2$ and couples all degrees of freedom of the system. The pseudo attractor reconstructed from the time-delayed vectors Y_i in $\mathbb{R}^{2N+1}$ has then the same properties as the original attractor. This method of delays allows the experimenter to reconstruct a pseudo attractor from a measured time series of a single variable of the system. However, in practice the experimenter is faced with some problems.

Indeed even if in theory any time delay can be used to reconstruct the attractor, in practice the limited amount of data and the presence of noise ensures that efficiency of the method depends on the choice of the time delay τ. If τ is too small, successive delay vectors will be correlated too much, if it is too large they will be independent

and not representative any more of the dynamics of the system. Different values for the optimal time lag for attractor reconstruction have been presented, and methods concentrate on the measures of autocorrelation [47] or mutual information [48]. The time where the autocorrelation function decays to $1/e$ is often accepted as relevant though. Moreover the experimenter has, if any, a limited idea of the number of dimensions N of the system studied and another difficulty encountered is the choice of the embedding dimension $m_e = 2N + 1$. It has to be large enough to fully embed the underlying system, but not too large as it would add redundancy to the data and affect performances of algorithms later using the data. In Takens's original theorem, N is the dimension of the phase space containing the attractor, that of its support. But Sauer et al. [49] have shown that using the box-counting or fractal dimension D_F of the attractor, which represents the actual active phase space and is smaller than N, can be sufficient. In some cases, an attractor may even be reconstructed in spaces of dimension between D_F and $2D_F$.

3.1.5.2 Wolf Algorithm

The first algorithm to calculate the main Lyapunov exponent from experimental time series was developed by Wolf et al. [50] in 1984. The first step of this algorithm is the attractor reconstruction in a m_e-dimensional phase space by the method of delays, involving the choice of m and τ. From this reconstructed pseudo-attractor, the algorithm starts at the beginning of the record with the first state vector and looks for its first neighbour. The first neighbour chosen is the first state vector whose vector

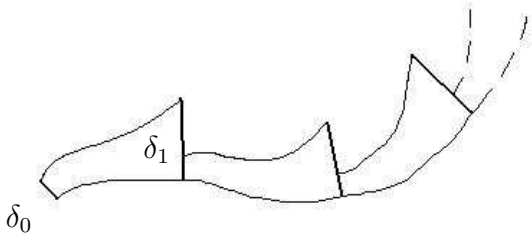

Figure 3.5: Principle of distance separation measurement while following the fiducial trajectory.

separation δ_0 from the considered vector is smaller than a neighbourhood size ϵ set by the user. As illustrated by the schematic representation in figure 3.5, the algorithm then measures the distance δ_1 between the images of these points after an evolution time Δt, also set by the user. Estimation of the Lyapunov exponent is made by taking the logarithm of the ratio δ_1/δ_0. The image of the first chosen point is then considered as another reference point, and a replacing neighbour conserving the orientation of the separation vector δ_1 is chosen.

Averaging of the logarithm of the ratio $|\delta_1/\delta_0|$ from the successive images of the initial point until the end of the record, i.e. on the fiducial trajectory, gives an estimation of the exponential growing rate of separation of close trajectories, i.e. the Lyapunov exponent. Characteristic evolution of the Lyapunov exponent computed with this algorithm on a chaotic time series is shown in figure 3.6. This figure was obtained during the validation of this algorithm made using a classic chaotic system, the Henon system presented later in section 3.1.5.4 page 41. This calculation carried out on a time series numerically obtained from the Henon system shows the progressive stabilisation of the Lyapunov exponent value while the algorithm advances along the time series. This algorithm has been widely used, but it has some weaknesses. Rosenstein et al. [51] argue that the following of the fiducial trajectory fails to take advantage of all data, and that the conservation of the phase space orientation when finding a new neighbour is unnecessary when calculating only the largest Lyapunov exponent. Kantz et al. [47] argue that it does not present the possibility of testing for exponential growth of the separation of trajectories, but just

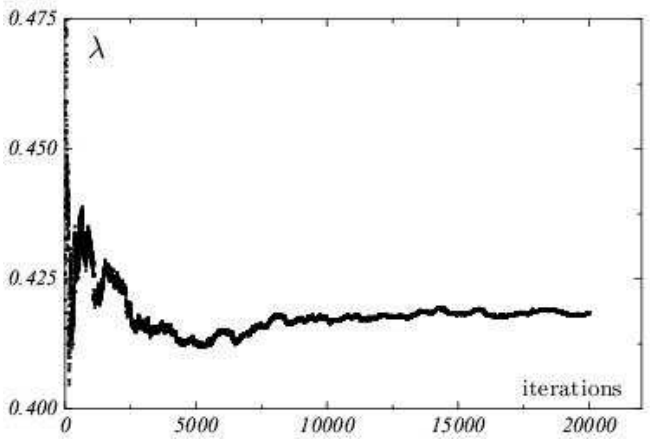

Figure 3.6: Characteristic evolution of the calculated Lyapunov exponent along the record with Wolf's algorithm.

assumes it, resulting in finite Lyapunov exponent for stochastic data.

3.1.5.3 Kantz's algorithm

The algorithm presented in [47] tests for exponential divergence of the separation and helps to decide whether or not the considered time series is chaotic.
For every point of the pseudo m_e-dimensional reconstructed phase space, its computes the average evolution of the separation between it and all of its neighbours, found using an efficient box-assisted method, with time. It then averages it over all the points of the phase space and the average evolution of separation of close trajectories $\delta(t)$ over the whole data is obtained. A characteristic plot of this average evolution $\delta(t)$ obtained with this algorithm from a chaotic time series, obtained from the Henon system, is given in figure 3.7. The average divergence of close trajectories is for this system exponential. In this semi logarithmic representation the curve starts with a straight line, whose slope corresponds to the main Lyapunov exponent measured from the time series. It can be noted that after this increase, the plot tends toward the standard deviation of the data.

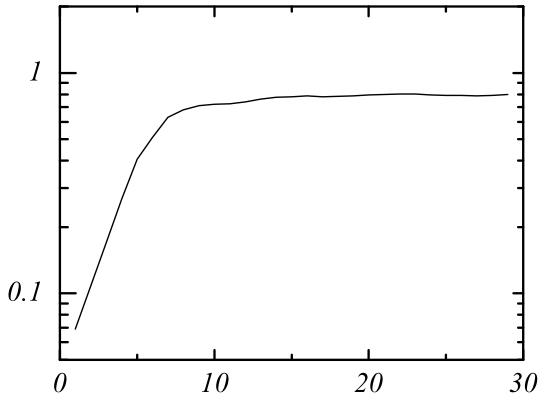

Figure 3.7: Characteristic evolution of the average growth of the separation.

Apart from the embedding dimension m_e and the time lag τ for the reconstruction, the user also has to set the neighbourhood size ϵ, the minimum number of reference points for the averaging, distant from a minimum distance, having a minimum number of neighbours. The time length on which the average evolution of the

separation is computed has also to be set.

3.1.5.4 Validation of the algorithms

In order to validate the implementation of these two algorithms for the determination of the main Lyapunov exponent from an experimental time series, and to acquire some experience in judging of the influence of the different parameters involved, validations of Wolf's and Kantz's algorithms were undertaken. Using the mathematical formulations of two classical chaotic systems whose Lyapunov exponent are known, chaotic time series were created, and the two algorithms were then applied to these time series to determine their Lyapunov exponent. Comparison of the estimates obtained with the analytical value gives the relative error.

Equations for the Henon system and parameters used are presented in table 3.1, as well as the corresponding analytical Lyapunov exponent. The two algorithms for

Henon system			
Equations	Parameters	Init. cond.	Theorical λ [ref.]
$x_{i+1} = 1 - ax_i^2 + y_i$	$a = 1.4$	x(0)=0.1	0.418 [52]
$y_{i+1} = bx_i$	$b = 0.3$	y(0)=0.0	

Table 3.1: Chaotic system used for the validation of the algorithms for Lyapunov exponent determination.

Lyapunov exponent determination were applied to the time series of x issued from this system. As illustrated by table 3.2, the results obtained are for both algorithms extremely sensitive to some parameters used in the algorithms. The time lag τ for the reconstruction was fixed to 1 so that reconstructed vectors were made of successive x_i. The neighbourhood size ϵ has to be small so as not to encompass false neighbours, but not too small to still have a reasonable average number of neighbours. While

increasing the amount of data, ϵ could be reduced to obtain as many neighbours as with fewer data but larger ϵ, but of better quality as their initial separation is smaller. With experimental time series though, the amount of data is imposed by the length of the record and ϵ has to be chosen carefully.

Here the dimension of the system is known, $N = 2$ for the Henon system; reconstruction of the attractor should then be optimal for $m_e = 5$. However for every value of ϵ chosen, the error can be smaller with m_e lower than five. Examples of calculation and results presented up to here were carried out on time series issued from a mathematical formulation, i.e. noise-free, with a known dimension, and with an analytically known Lyapunov exponent. Errors obtained with different parameters show that ϵ can be adjusted with the amount of data, and that m_e could be lower than $2N + 1$ in some cases to obtain good result. The algorithm presented by Wolf et al. shows a better stability to variations of parameters than the one presented by Kantz et al., and its use is simpler as fewer parameters have to be set. Indeed, for the second, the number of reference points, the distance between them and their minimum number of neighbours have to be set and influence the result obtained. The experimenter has to be very careful when using this algorithm. Nevertheless, results obtained from the two algorithms are close to analytical values, their errors depending on many parameters. The algorithms are then validated, and will be used on experimental time series obtained in this project.

When using either of the algorithms, the experimenter has to judge the influence of different parameters before assigning a value to the Lyapunov exponent of an experimental time series. Several tests with different parameters like m_e, τ and ϵ have to be made. The presence of noise in the data also influences the performance of these algorithms and use of noise reduction algorithms is advised in [47] for optimisation of results.

These briefly presented concepts of non-linear dynamics have been developed and

		n = 10000				n = 20000			
		λ		relative error		λ		relative error	
eps	m	wolf	kantz	wolf	kantz	wolf	kantz	wolf	kantz
0.1	2	0.4239	0.3760	1.42%	10.05%	0.4220	0.3765	0.97%	9.93%
0.1	3	0.4191	0.3712	0.26%	11.21%	0.4209	0.3721	0.69%	10.98%
0.1	4	0.4162	0.3714	0.42%	11.15%	0.4169	0.3729	0.26%	10.79%
0.1	5	0.4153	0.3742	0.64%	10.48%	0.4194	0.3765	0.33%	9.93%
0.1	6	0.4191	0.3829	0.27%	8.41%	0.4201	0.3846	0.51%	8.00%
0.1	7	0.4185	0.3912	0.12%	6.40%	0.4200	0.3926	0.47%	6.07%
0.1	8	0.4157	0.3944	0.55%	5.63%	0.4195	0.3991	0.37%	4.53%
0.1	9	0.4162	0.3923	0.42%	6.14%	0.4176	0.4069	0.10%	2.65%
0.1	10	0.4144	0.3740	0.86%	10.53%	0.4176	0.4189	0.11%	0.22%
0.05	2	0.4213	0.4147	0.79%	0.80%	0.4200	0.4160	0.48%	0.48%
0.05	3	0.4201	0.4111	0.51%	1.64%	0.4212	0.4141	0.78%	0.93%
0.05	4	0.4183	0.4181	0.07%	0.03%	0.4211	0.3860	0.75%	7.66%
0.05	5	0.4192	0.4167	0.28%	0.30%	0.4208	0.3886	0.67%	7.04%
0.05	6	0.4175	0.4183	0.11%	0.06%	0.4204	0.3976	0.57%	4.89%
0.05	7	0.4184	0.4252	0.10%	1.72%	0.4200	0.3951	0.47%	5.49%
0.05	8	0.4178	0.3683	0.05%	11.89%	0.4191	0.3872	0.26%	7.37%
0.05	9	0.4171	0.3554	0.21%	14.97%	0.4185	0.4293	0.12%	2.71%
0.05	10	0.4147	0.3396	0.78%	18.77%	0.4161	0.3782	0.47%	9.52%
0.02	2	0.4186	0.4063	0.14%	2.81%	0.4212	0.4124	0.77%	1.35%
0.02	3	0.4178	0.4066	0.05%	2.73%	0.4206	0.4164	0.62%	0.38%
0.02	4	0.4185	0.3970	0.11%	5.03%	0.4203	0.4196	0.55%	0.37%
0.02	5	0.4175	0.4178	0.13%	0.04%	0.4195	0.4254	0.36%	1.77%
0.02	6	0.4166	0.3730	0.33%	10.76%	0.4202	0.4230	0.52%	1.18%
0.02	7	0.4157	0.3353	0.54%	19.80%	0.4194	0.3963	0.33%	5.19%
0.02	8	0.4119	0.3639	1.46%	12.94%	0.4189	0.3624	0.22%	13.30%
0.02	9	0.4057	0.3633	2.94%	13.09%	0.4162	0.3440	0.44%	17.70%
0.02	10	0.3917	0.4126	6.29%	1.29%	0.4110	0.3898	1.67%	6.76%
0.01	2	0.4203	0.4275	0.56%	2.28%	0.4200	0.4302	0.48%	2.92%
0.01	3	0.4197	0.4337	0.40%	3.75%	0.4204	0.4304	0.58%	2.97%
0.01	4	0.4179	0.4338	0.03%	3.79%	0.4198	0.4287	0.42%	2.56%
0.01	5	0.4168	0.3761	0.28%	10.02%	0.4192	0.4325	0.28%	3.48%
0.01	6	0.4154	0.3920	0.62%	6.22%	0.4184	0.3927	0.10%	6.06%
0.01	7	0.4089	0.4137	2.17%	1.02%	0.4173	0.3532	0.16%	15.51%
0.01	8	0.3959	0.4232	5.29%	1.23%	0.4137	0.3981	1.04%	4.76%
0.01	9	0.3827	0.4366	8.44%	4.46%	0.4052	0.3798	3.06%	9.14%
0.01	10	0.3637	0.4509	13.00%	7.86%	0.3923	0.3998	6.15%	4.35%

Table 3.2: Lyapunov exponents and relative errors obtained with Wolf's and Kantz's algorithms on time series issued from the Henon system.

used to investigate the dynamics of non-linear systems in many fields of science. They proved very useful in investigating the behaviour of vibrating systems with structural non-linearities, as for the widely used sinusoidally-excited mechanical systems with impacts or for the fluid-induced vibrations of cylinders in arrays. Better understanding of the dynamics of such systems and of the influence of their different system parameters has been reached, for different conditions of structural non-linearities. In order to compare the dynamics of the present system, in which the forcing is of a different nature, to similar non-linear systems, a short review of the research carried out on vibrating systems with impacts is next given.

3.2 Influence of structural non-linearities in vibrating systems

In sinusoidally-excited mechanical systems, such as those encountered in industry, some of the components experience repetitive contacts with each other. When considering one of these components, the parts it impacts on may be considered as stops limiting its amplitude of vibration. In these sinusoidally-driven systems, the presence of stops can lead to changes in the system dynamics, and result in loss of performance or improper functioning in some conditions. A large number of configurations of mechanical systems with impacts have been investigated and reported in [53]. Extensive literature exists on the dynamical behaviour of such systems. One and two degree of freedom systems with impact occurring on one or two sides have received most attention, as they exhibit most of the characteristic non-linear phenomena encountered in these systems, and because of the apparent simplicity of the nature of the non-linearity involved. But the presence of stops results in a strong non-linearity of such systems. The induced jumps in stiffness or damping, or both, induce a piecewise-linearity of these systems, which therefore are

non-smooth. Piecewise-smooth systems are able of exhibiting most of the bifurcations also exhibited by smooth dynamical systems, as saddle-node, Hopf or period-doubling bifurcations, but they can also exhibit bifurcations characteristic of piecewise-smooth systems, due to the discontinuity or discontinuity-induced bifurcations [54].

3.2.1 Impact oscillators

Considerable effort has been devoted to the analysis of the single-degree-of-freedom impact oscillator with rigid impacts, as schematically represented in figure 3.8(a). In this model, impacts are described with the Newton impact theory involving a condition of impenetrability and a coefficient of restitution. This system is a deterministic system, but combination of instability and impenetrability conditions of impact motion can result in unpredictable states of the system, i.e. in chaotic motions [55]. The chaotic behaviour of these impact oscillators, caused by the strong non-linearity of the impact and corresponding instabilities of periodic motions, is referred to as deterministic chaos. Successive zones of stability of single-impact

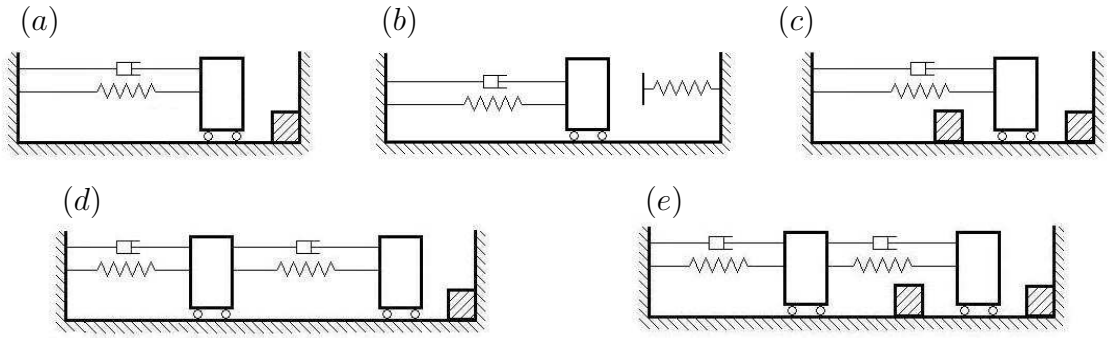

Figure 3.8: Different configurations of impact oscillators.

harmonic and sub-harmonic motions have been identified when varying some parameter of the system such as the forcing amplitude [56], the forcing frequency [57], [58], [59] or the stop position [60], [61]. Periodic motions of such a

vibro-impact system can be characterized by the symbol $z = p/n$, where p is the number of impacts which take place in n forcing cycles. The parameter z, originated by Peterka, is of important significance in analysing the periodic-impact motions and bifurcation characteristics. It takes rational values for periodic motions. Between windows of stability of periodic orbits, chaotic windows, in which z takes irrational values, are also observed. Phenomena are observed in impact oscillators related to the discontinuity which have no counterpart in smooth dynamical systems.

Grazing bifurcations are one of the most common discontinuity-induced bifurcation. They occur when a stable periodic orbit with zero or more impacts is destabilised by a parameter change in such a way that a new impact occurs. This latter then takes place with zero impact velocity, and is called a grazing impact. Grazing bifurcations are associated with rich and complex dynamical behaviour, such as the sudden loss of stability or existence of the orbit, the creation of a large number of periodic orbits, and the possibility of localized attracting chaotic motion [62].

Intermittent chaotic behaviour has been observed to arise in a one-degree-of-freedom single-sided impacting system though grazing bifurcation [60], [55]. Chaotic behaviour in such a simple system can also appear through cascade of period-doubling bifurcations of periodic cycles [57]. Four routes from periodic to chaotic motions, via grazing bifurcation, saddle-node bifurcation and intermittency characteristics have been identified in the apparently simple one-degree-of-freedom single-sided impacting system [63].

Chatter, when infinitely many impacts occur in a finite time, resulting in the mass apparently staying against the stop for some time is observed for some values of parameters. Illustration of the occurrence of chatter given in [61] with the time series of displacement is presented here in figure 3.9.

In the case of a finite spring stiffness of the stop, the time of contact cannot be

neglected, and the oscillator is said to impact on soft stops. Several mathematical models of soft impacts exist, based on different behaviours of the contact force with the deformation of the soft stop.

The influence of stiffness hardening on a one-degree-of-freedom mechanical system with soft impacts on a single stop as depicted in figure 3.8(b) has been investigated [64], [65]. Major results are that regions of subharmonic and chaotic impact motions develop from grazing boundary and become wider with increase of the stop stiffness, and that the structure of fundamental and subharmonic impact motions does not depend considerably on the model of soft impact.

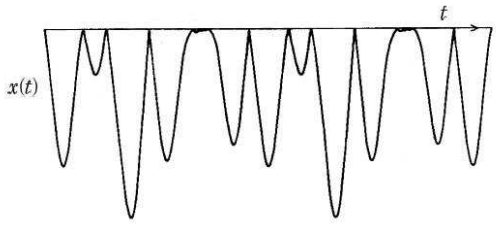

Figure 3.9: Example of $\infty/6$ chattering cycle. *From [61].*

Period-doubling cascades and grazing bifurcations are also observed for a two-degree-of-freedom system impacting on a single stop as presented in figure 3.8(d). Characteristic bifurcation diagrams of impact velocities obtained by Luo et al. [66] with variation of the forcing frequency for such a system are presented here in figure 3.10. The complete bifurcation diagram in figure 3.10(a) shows successive windows of stability of $z = 1/n$ cycles. Between successive windows of stability of $1/n$ motion, windows of chaotic motions are observed. The bifurcation diagram in figure 3.10(b) allows a closer inspection of one of these chaotic windows. At $\omega \approx 2.35$, the 1/1 cycle loses its stability through Feigenbaum period-doubling cascade and the system falls into chaos with ω increasing. An inverse period-doubling cascade follows that leads to the stabilisation of the 1/2 cycle. This one, contrary to the first one, is discontinuous because of a grazing bifurcation of the 2/4 cycle leading to a 3/4 cycle occurring when ω crosses the value of 2.869628 decreasing. In the route to chaos via adverse period-doubling bifurcation of z = 1/2 impact motion, there exist grazing bifurcations, which cause singularities so that the period-doubling cascade of z = 1/2

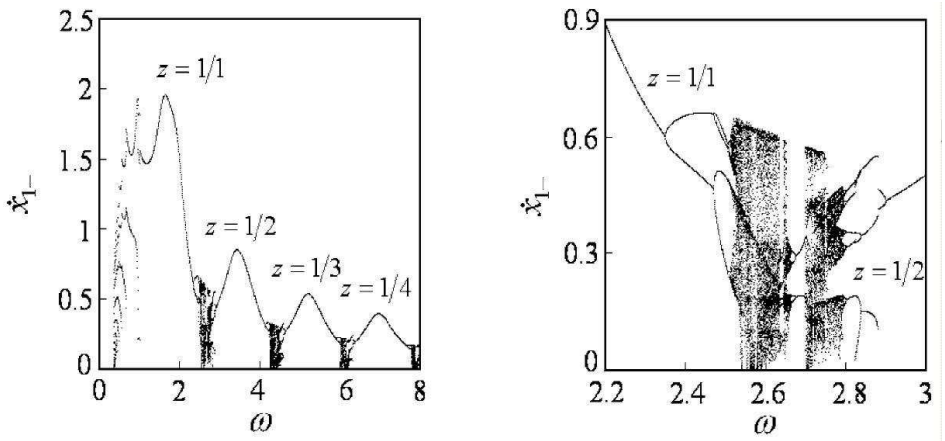

Figure 3.10: Bifurcation diagrams of impact velocities for the two-degree-of-freedom impact oscillator with asymmetric amplitude constraints. *From [66].*

impact motion is discontinuous [66]. Other routes from periodic-impact motions to chaos, via period-doubling, Hopf bifurcations and tori doubling, are found to exist in the vibro-impact system [67].

In this configuration stable single impact period-1 orbits can undergo a supercritical flip bifurcation under variations of the ratio of the forcing frequency to the natural frequency leading to stable single impact period-2 orbit. The coexistence of stable single impact period-3 and period-1 motions for some parameter values suggest the existence of a saddle-node bifurcation through which appears the period-3 orbit.

Harmonically excited system with symmetric amplitude limitation as the forced single-degree-of-freedom vibratory system with motion limiting stops symmetrically placed on each side presented on figure 3.8(c), have also been thoroughly investigated as of interest also in many applications.

Nguyen et al. [68] found for systems having symmetrical gaps periodic responses where the frequency of impact on both sides are usually equal, among which chatter responses where the mass bounces successively on the same stop with a high frequency during an oscillation cycle. They also found responses with different

frequencies of contact on each side: that is impact occurring only on one side, chatter occurring at one stop only or at different frequencies on both stops. Erratic responses exhibiting random-like dynamic behaviour with non-periodic contacts of varying magnitude also are found. Their parametric study shows that every system parameter, amplitude and frequency of the driving force, system stiffness and damping, stops stiffness and damping, mass of the oscillator or gap clearance, influences forces and frequencies of contacts, as well as the nature of the dynamics.

The case of a two degree of freedom impact oscillator with symmetrically placed limiting stops on both sides, as represented in figure 3.8(d), is of interest also in many applications. Luo & Xie [66] characterize the periodic motions in this system by the symbol $n-p-q$, where p and q represent the number of times the oscillator impacts respectively on the left-hand side or right-hand side stop, during n forcing cycles.

They observed in numerical tests different routes of 1-1-1 symmetrical motion to chaos while varying the forcing frequency ω. At high values of ω, 1-1-1 symmetrical motion are stable. When decreasing the forcing frequency, two 1-1-1 antisymmetrical motions appear through a pitchfork bifurcation, one stable and one unstable, their stability being determined by the initial conditions. When ω further decreases, the stable 1-1-1 antisymmetrical motion loses its stability through a succession of period doubling bifurcations, which eventually result in apparently non-periodic, or chaotic motions. The period doubling cascade is observed to be discontinuous due to grazing bifurcations. Moreover, they show that Hopf bifurcations of 1-1-1 symmetrical and antisymmetric motions occur in two degree of freedom vibro-impact systems with symmetrical rigid stops when it does occur in a single degree of freedom system. A common feature of single degree of freedom and two degree of freedom systems with symmetrically placed stops is that a large gap values will lead to narrow windows of chaotic motions and high impact velocities, whereas smaller gap sizes lead to large chaotic windows and small impact velocities.

Another example of vibrating systems involving structural non-linearities can be found in arrays of tubes in cross-flow.

3.2.2 Support-influenced dynamics in arrays of non-linearly supported tubes in cross-flow

In heat exchangers used for example in nuclear power plants, a turbulent fluid flow passes through arrays of tubes. These tubes are subject to flow-induced vibrations causing tube wear and fatigue and ultimately leading to tube failure. Anti-vibration systems are usually used to limit the amplitude of vibration at some point along their length. The tubes are threaded through oversized holes in baffle plates allowing for easy threading and thermal expansion. Some of the tubes vibrating can impact with the baffle plate, leading to structural non-linear restraint. If this problem involves fluid-induced vibrations of non-linearly supported tubes, it is different from the one addressed here as the fluid-structure interaction phenomenon is different in tube arrays. They are subject to fluid elastic instability, generally accepted to be caused by two mechanisms, a velocity-controlled, negative damping mechanism, and a stiffness-controlled one [69]. These result in a Hopf bifurcation at a critical flow velocity, above which oscillation occurs. Fluid elastic instability occurs only in the case of tubes in arrays, and no analogy can be made with a single cylinder experiencing vortex-induced vibrations [70]. However, research concerned with such systems is of interest here as investigating the effect of non-linearities introduced by loose supports on the dynamics of flow-induced vibrations of cylinders.

Investigating the dynamics of heat-exchanger tubes impacting on loose supports with the use of non-linear dynamics tools, Païdoussis & Li [69] have first shown with their single degree of freedom numerical model that chaotic vibrations can be observed in certain parameter regions. The use of bifurcation diagrams and Lyapunov exponents

made clear that chaotic oscillations are possible for sufficiently high reduced velocities. Cai & Chen [71], [72] confirmed this result using phase portraits, power spectral density, Lyapunov exponents and correlation dimensions of numerical simulations of a loosely supported tube vibrating in cross-flow, as well as bifurcation diagrams.

Mureithi et al. [70, 73, 74] investigated both numerically and experimentally the influence of impact on loose support on the response of a tube placed in row 3 of a tube array allowed to move in cross-flow as well as in-flow directions. No other bifurcation than the Hopf bifurcation leading to fluidelastic instability is observed with linear constraints and only stable limit motions ensue. For amplitude-limited motions, chaotic motions are observed at the onset of impacting, and a sequence of bifurcations, including period-doubling, flip and pitchfork bifurcations, follows when the flow velocity is increased which can lead to chaotic motions. They show that chaotic motion is more likely to occur for small gap sizes [73], and identified two mechanisms leading to chaos: a switching mechanism at the onset of impacting and a type I intermittency route to chaos [75] at large flow velocities [74].

Chapter 4

Validation of the experimental setup with linear structural restraints

To investigate the VIV of a cylinder subject non-linear structural restraints such as discontinuities in the system stiffness, a low-mass low-damping experimental setup was designed. It was first tested in the case of linear restraints, and validated by comparison of its response to previous data from the literature. The design of the apparatus allowing to vary the strength of the non-linearity introduced, cases with relatively small symmetric jumps in the system stiffness are carried out first. The strength of the non-linearity is then increased, and cases with very high jumps in the system stiffness, as if limited by a stop, are investigated. The effect of asymmetric amplitude limitation on the cylinder's dynamics and on the vortex shedding process is investigated.

4.1 Validation of the experimental setup in the linear case

4.1.1 Experimental setup

To obtain a uniform flow with very low turbulence, experiments were firstly carried out in a 30m-long 1.5m-deep 2m-wide towing tank. The 30 mm diameter cylinder, with length to diameter ratio $L/D = 10$, was placed horizontally, in order to avoid free surface effects, at a depth of $5.5D$ beneath the surface. To limit free ends effects, the cylinder was equipped with $2.5D$ diameter circular ends plates. Both the cylinder and the end plates were made of Perspex. The cylinder was restrained to allow it to move only in the vertical i.e. cross-flow direction, by a system based on three aluminium beams. As shown in the picture 4.1, the cylinder is held at both ends below an aluminium frame, to which are clamped the ends of three beams.

These beams, whose other ends are clamped on a frame attached to the carriage, are horizontal when the cylinder is in its mean position. Extension springs supporting the frame to compensate for the weight of the system have been chosen to obtain a natural frequency of the cylinder in water at about 1 Hz, providing a reduced velocity range of 4 - 15 with a velocity varying from 0.12 to 0.45 m/s. The three beams maintain the cylinder in the vertical plane defined by their three moving ends. When the cylinder vibrates vertically, the beams bend in a clamped-clamped first mode of vibration. Their length being much greater than the cylinder oscillation, the position of the plane of oscillation of the cylinder is not significantly affected by the bending of the beams. Their dimensions, 15 mm $\times$ 1.5 mm $\times$ 920 mm, have been designed with structural vibration software to obtain their first vibrational mode, in experimental conditions, i.e. clamped-clamped with moving mass supported by a spring at one end, at around 1Hz. A low mass ratio of $m^* = 2.08$ was obtained with

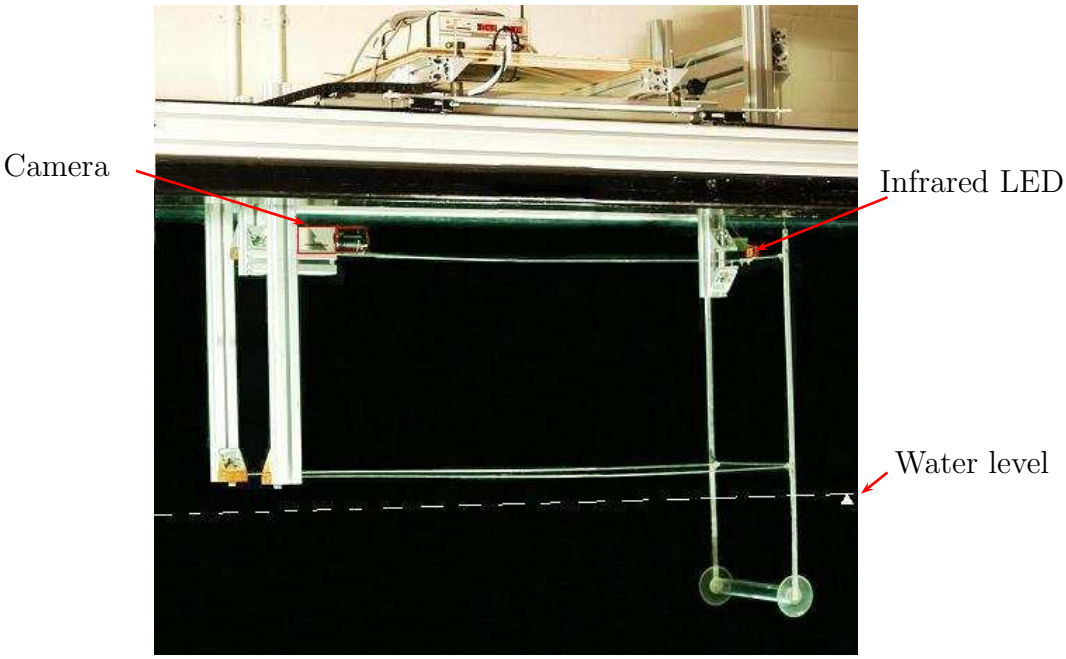

Figure 4.1: Photograph of the experimental setup.

the use of a hollow cylinder and lightweight components.

The design of our experimental apparatus resulted in a low structural damping ζ_s , due to the dissipation of energy in the springs and in the horizontal beams, and measured to be about 0.2 % in air. However, due to the design of the experiment, the hydrodynamic damping ζ_H produced by the oscillation in water of the end plates and the immersed length of the beams holding the cylinder is to add to the structural damping in air to obtain the total damping in still water $\zeta = \zeta_s + \zeta_H$. Indeed, as mentioned in [76], end plates attached to the cylinder can give rise to significant oscillating forces. In the present experiment, when the cylinder is immersed in water and vibrating under VIV, hydrodynamic damping is created by shear stress on the end plates and the immersed length of the arms holding the cylinder.

If the flow around these immersed parts is considered parallel when the experimental apparatus is carried along the towing tank, then the hydrodynamic damping produced in the cross-flow direction can be approximated by that existing on a plate

of same surface oscillating in its own plane at an angular frequency ω in an unbounded and at rest fluid of kinematic viscosity ν. According to Stokes [77], in the case of an infinite plate, the component of shear stress in phase with the velocity is equal to $\rho V\sqrt{\omega\nu/2}$. Integrating it over the surface of the immersed parts oscillating at a characteristic frequency of 1 Hz gives an estimation of the hydrodynamic damping $\zeta_H = 0.59$ % . Hydrodynamic damping is in this system about three times bigger than the structural damping because of the small oscillating mass, and increases the overall system damping to $\zeta = 0.79$ %.

The position of the cylinder is measured by a non-contacting Hamamatsu C2399 optical displacement system composed of a light weight LED placed on the frame holding the cylinder, whose infrared emission is detected with high accuracy by a camera placed on the frame. The output signal from the camera, relative to the vertical displacement of the LED, is recorded by a PC through a 12-bit acquisition board, at a sampling frequency of 800 Hz. This high value of sampling frequency has been chosen to capture accurately moments where the cylinder impacts on a stiff stop.

When subject to linear restraints, this experimental setup presents characteristics of low-$m^*\zeta$ experiments. Its response exhibits the initial, upper and lower branches of excitation, and is similar to experimental data from the literature. However, the old and heavy carriage towing the cylinder in this tank could sometimes present some important variations of its velocity at some instants during some tests. No instantaneous feedback on the carriage velocity was available in this facility and these variations of velocity could not be accurately measured, but just observed by visual inspection and made clear also from the noise produced by the carriage. These variations of velocity seem to have affected the quality of the results obtained. The long waiting time between tests, of about an hour, did not allow the carrying of many tests, and tests with different structural conditions could only be carried out only at few flow velocities. Anyway, these first results, presented at the 6th international

conference on FSI, AE & FIV+N at Vancouver [78], show modifications of the dynamics of the cylinder when it is subject to strong structural non-linearities leading in some cases to chaotic motions. They motivated a deeper analysis of these modifications, and particularly the investigation of a likely modification of the wake. Fluid-structure interaction may indeed be modified by the insertion of a non-linearity in the structural restraints of the cylinder.

In order to get information on the vortex wake, flow visualisations were needed. For this purpose, the 42cm-wide 1m-high and 13m-long glass-walled wave tank of the hydraulics department was equipped with a system for towing a carriage over the water on most of its length. The experimental apparatus described earlier was attached onto the carriage and the cylinder could then be towed on an effective distance of 10m.

A second set of tests was carried out in this tank, before the realisation of flow visualisations at some chosen reduced velocities with different structural restraints. The presence of a wave dissipation beach at the end of the tank decreased the waiting time between tests to about 15 minutes, which made it possible to carry out many more tests, and to obtain data on a more refined scale over the useful reduced velocity range. The brand new towing system used for the second set of experiments in the glass-walled tank proved to be very efficient since its velocity was controlled by a servo system and was very stable after the acceleration phase. In this second series of tests, the mass ratio was slightly reduced, to $m^* = 1.74$. The structural damping in air was measured through free decay tests to be at about the same value at 0.2%, keeping constant the effective damping in water at $\zeta = 0.79$ %. Natural frequency in water was measured to be $f_n = 0.9765$ Hz.

In this glass-walled tank, flow visualisations were carried out by injecting some dye in the water in front of the cylinder. The dye was injected using a thin tubing system, in the direction of the flow, at different points along the middle plane of the cylinder

in front of it while this latter was towed in the tank. The dye helps in marking streamlines in the flow and in visualizing the vortices shed by the cylinder. Different types of dye have been used, as well as different video recording systems, but the best results were obtained using a high speed camera recording 125 frames per second, in black and white tones, and a white sheet as background, with some red food colouring for dye. The camera could however not be mounted on the carriage, and had to be fixed, recording the motion of the cylinder on a window of only about 40 cm wide.

Doing flow visualisations revealed itself to be experimentally challenging as many parameters had some effect on the quality of the visualisation. For example the viscosity of the dye, changed by adding glycerine to it, seemed to have some effect on its diffusion in water, rendering it slower. The flow rate of the dye was also a very important parameter, and had to be approximatively adjusted depending on the velocity of the cylinder. The focus of the camera had to be done in the plane where the dye was injected, but the dye itself diffuses in three dimensions and does not stay in only one plane. The flow visualisations are therefore not of the best quality, but vortex formation can be observed on the recorded videos, from which pictures of typical vortex wakes were extracted, to be presented later. These flow visualisations could have been improved for example by using a laser sheet to illuminate the plane in the middle of the cylinder. The dye could also have been injected from the cylinder, but this would have implied experimental difficulties in having a tubing system for the dye inside the cylinder. Other flow visualisation techniques as particle image velocimetry could also have resulted in better flow visualisations.

4.1.2 Validation of the experimental setup

During a typical test of VIV with linear restraints, the cylinder is started from rest in the towing tank filled with still water, and accelerated up to the chosen velocity, set

in cm/s, at which it travels over the remaining length of the tank. The displacement of the cylinder was recorded from about five seconds before its start, to capture at the beginning of each record the exact cylinder's rest position, and recording continued for some time after it had travelled the tank and stopped. The algorithm developed for post-processing first measures the rest position of the cylinder before the start of oscillations, detected using a condition on the dispersion of data. With this measure and the regression coefficient in V/m obtained from the calibration of the PSD, data are then converted in non-dimensional displacement. This is illustrated by the raw time series of displacement recorded at $U = 0.14m/s$, corresponding to $U_r = 4.78$, and shown in figure 4.2(a). Data considered for the tests

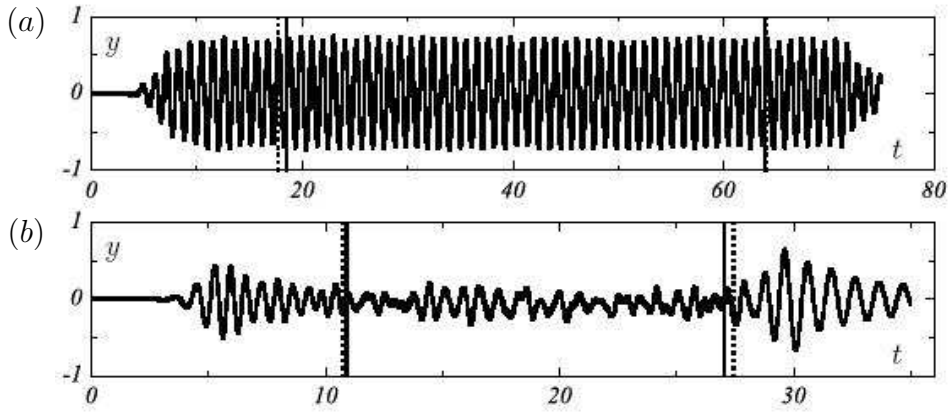

Figure 4.2: Raw time series of displacement recorded in the case with linear restraints with $m^* = 1.74$ and $m^*\zeta = 0.0137$, at $U_r = 4.78.(a)$ and $U_r = 13.31$ (b).

are taken some time after the start of oscillations, to remove those corresponding to the acceleration period, during a time corresponding to the travel of the carriage over some length in the the test tank, before the carriage slowed down and stopped, before that the cylinder marks these oscillations of decreasing amplitude at the end of the record while decaying in moving water. These times are marked on the time series presented in figure 4.2 with vertical lines. Data between the two internal vertical lines, corresponding to zero-crossings with positive velocity, are those considered in the results later presented.

As illustrated by the raw time series of displacement recorded for $U_r = 13.31$ presented in figure 4.2(b), the history of the cylinder during the acceleration period is particularly clear during tests at high flow velocities, and the start of the consideration of data had to be carefully set, individually for each time series. As the velocity for the test is increased, the useful timespan over which the cylinder is towed at the chosen speed, set individually, decreases and is varied between 7.5m and 6m.

The equation of motion for a cylinder oscillating in the cross-flow direction under vortex-induced excitation can be written as:

$$m\ddot{Y} + c\dot{Y} + kY = F(t) \tag{4.1.1}$$

where Y is the position of the cylinder, $\dot{Y}$ and $\ddot{Y}$ its velocity and acceleration at time t, m is the mass of the cylinder, c and k the structural damping and stiffness coefficients of the system. $F(t)$ is the instantaneous force on the cylinder resulting of the non-uniformly distributed pressure field around the cylinder.

With linear restraints, the system is continuous, therefore the displacement $Y(t)$ is a smooth function of time, i.e. of class C^∞. It is in this case rather easy to use any type of filter on the raw data of displacement to remove most of the noise, which is primarily of electrical nature, from it, and eliminate the high frequency components sometimes appearing in the signal at high flow velocities. In the case of linear structural restraints, reconstruction of the signal of displacement $Y(t)$ from its samples is done using the Shannon-Whittaker interpolation formula. This is equivalent to applying a brick-wall low-pass filter on the data, so that the obtained reconstructed signal of displacement does not contain any frequency component over a cut-off frequency, which was set here for each time series at five times the vortex shedding frequency for a fixed cylinder $f_{vs} = 0.2U/D$. Such processing of the data gave Signal-to-Noise Ratios (SNR) between 60 to 100 dB. Numerical derivation of the filtered displacement with five-point centred-difference schemes results in nearly noiseless time series of velocity and acceleration.

For each of these filtered time series of displacement, the maximum amplitude of oscillation of the cylinder is recorded from its envelope, and FFT of the signal is conducted to obtain frequency distributions. Amplitude and frequency responses of the cylinder subject to linear restraints obtained during the two sets of experiments conducted are presented in figure 4.3 with data from [79] obtained with $m^* = 2.4$ and $m^*\zeta = 0.014$ added for comparison. The general trend of the cylinder's response for

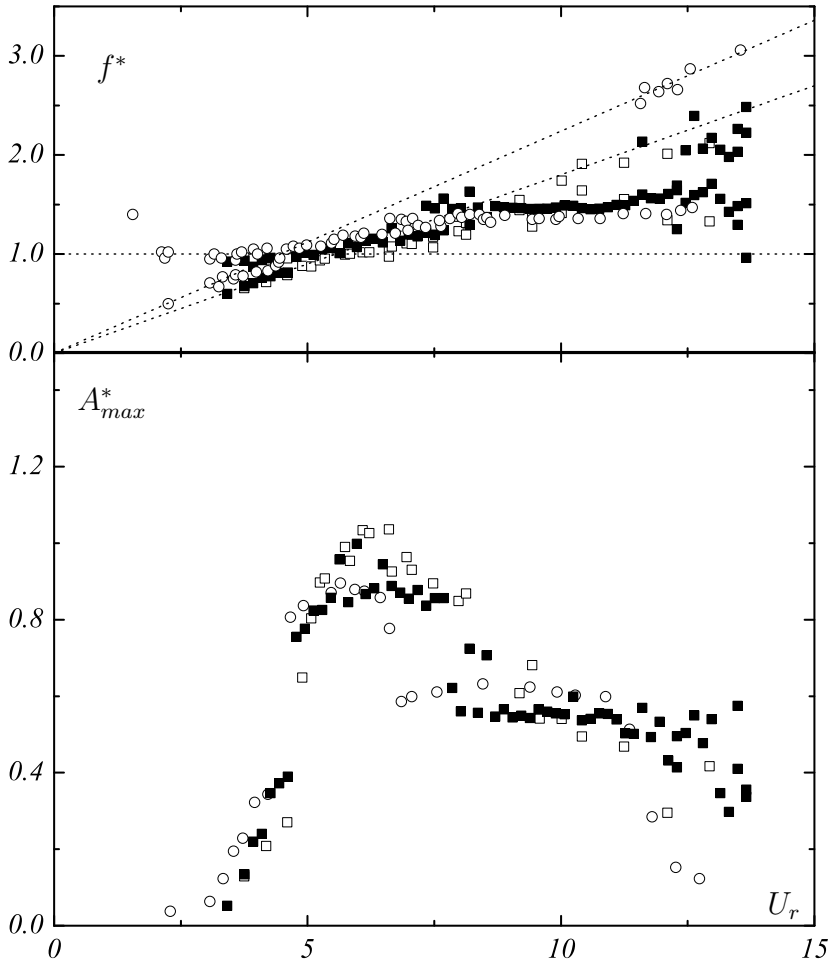

Figure 4.3: Amplitude responses and dominant frequencies of present work, (□): $m^* = 2.08$ and $m^*\zeta = 0.0164$, (■): $m^* = 1.74$ and $m^*\zeta = 0.0137$, and comparison with data from [80], (○): $m^* = 2.4$ and $m^*\zeta = 0.014$.

both of the conducted series of experiments is in agreement with data from the

literature. The amplitude response exhibits a lock-in range displaying the three different branches of response, i.e. initial, upper and lower branches as expected for such a low mass ratio and low damping experimental setup, and as presented for the low-$m^*\zeta$ case in figure 2.1 page 9. Data used here for comparison were chosen as obtained with an experimental setup with close structural parameters. The mass ratio is, in both the present two sets of experiments undertaken, slightly lower than that of the data used for comparison. For both sets the lock-in range, as well as the upper branch range, are wider than for $m^* = 2.4$, which is in agreement with experimental results from [80].

For the case of $m^* = 1.74$ and $m^*\zeta = 0.0137$, amplitudes reached in the different branches agree well with values from [79]. The maximum amplitude reached in the upper branch shown to be depending on $m^*\zeta$, which are almost the same here, is at about the same value.

Large amplitudes of about $1.1D$ are reached in the upper branch with the experiment carried out in the first towing tank, with $m^* = 2.08$ and $m^*\zeta = 0.0164$. These are rather high for such values of m^* and ζ. This difference can be due to variations in the velocity of the relatively old and heavy carriage used for these tests. These, even if only over one or two metres, involve some deceleration and acceleration phases of the flow around the cylinder, which can affect the fluid structure interaction. Variations of velocity of the carriage must have modified at some moments the fluid-structure interaction, leading to large maximum amplitudes in the upper branch or, as will be seen, to the presence of peaks at f_{vs} early in the lower branch, at $U_r = 10.41$.

The difference in maximum amplitude in the two sets of experiments conducted can also be due to a difference in damping possibly caused by a small difference in the depth at which the cylinder was placed, the immersed part of the system contributing a lot to the overall damping. From the larger amplitudes reached in the upper branch during the first series of tests, it could be suggested that the damping in this case was

slightly lower than wished for because the cylinder could have been placed slightly closer to the surface. This would have decreased the immersed length of the rods holding the cylinder, and the hydrodynamics damping produced on them.

Frequency responses of both sets of experiments also present a low-$m^*\zeta$ response type, with the discrepancy of the frequency ratio from 1 in the lock-in domain as expected with such a low-mass ratio low-damping system. Frequency distributions present, in the initial branch and in the desynchronisation regime, a peak at the vortex shedding frequency f_{vs}, corresponding to the frequency of vortex shedding behind a fixed cylinder $f_{vs} = S_t U/D$. However the value of S_t fitting the different data differ. From the data from Khalak & Williamson [79], the fit gives $S_t \approx 0.224$, while for both our sets of experiment, the fit gives $S_t \approx 0.18$. These differences could be due to a difference in the Reynolds number, as the vortex shedding frequency depends on it. In the present experiment the Reynolds number is not constant and takes values from about 3000 to about 12000.

Spectra after desynchronisation are also very complex in both our sets of experiments. The cylinder is excited by a non-periodic vortex shedding, as no distinguishable wake pattern is observed after desynchronisation, and can here reach some unusually high amplitude in some cases. At large flow velocities, the high frequency of excitation made some higher modes of vibration appear in the horizontal beams of the cylinder support system. These high modes of vibration certainly induced some high frequency component in the vibration of the cylinder, that are not due to vortex shedding. Small peaks at about 18, 20, 36 and 40 Hz are sometimes present in the frequency distributions of the non-filtered time series of displacement. One should remember that the original signal corresponds to the displacement of the LED placed on the cylinder support. Part of these measured high frequency components must have been dissipated by the support itself or damped by the hydrodynamic damping of the flow around the cylinder, but another part of them

must have been transferred to the cylinder, slightly modifying the VIV of the cylinder at high flow velocities. These high frequency components are nevertheless considered as negligible, and not taken into account in the presented results and are removed by the post-processing conducted on the data.

The behaviour of the present experimental setup with linear restraints is generally in agreement with the literature. In both sets of experiments carried out, amplitude and frequency responses clearly present low-$m^*\zeta$ characteristics. Results obtained in the first experiments present perturbations of the dynamics cylinder, revealed by slightly high amplitudes of vibration in the upper branch and noisy frequency distributions. These also lead to the appearance of oscillation components at f_{vs} early in the lower branch. The second series of tests with $m^* = 1.74$ and $m^*\zeta = 0.0137$ is much more reliable. The larger number of tests conducted, about 70 for the linear case over the lock-in domain, also allows us to observe with more details that the dynamics of the cylinder agrees with the literature.

4.1.3 Dynamics of the cylinder with linear restraints

Different tools can be used to analyse the nature of the motion when the cylinder is subject to VIV. The computation of the instantaneous frequency made possible with the Hilbert transform involving the computation of the imaginary part of the signal is for example particularly useful to observe, as in [79], intermittent switching between modes as in the transition between upper and lower modes. This section is however just aimed at confirming that the VIV reproduced with this experimental setup are similar to those observed in other similar experimental investigations. For this, closer observation of the amplitude and frequency responses, and of some selected time series of displacement are sufficient to confirm the nature of the dynamics of the cylinder when subject to linear restraints. Observation of flow visualisations is also

important to show that the wake behind the cylinder exhibits the different modes found to occur in such low-$m^*\zeta$ cases.

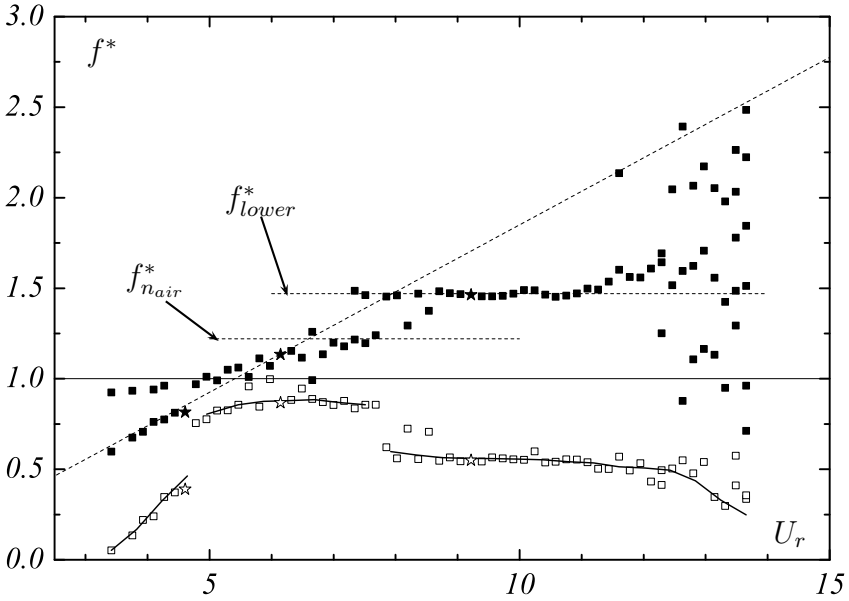

Figure 4.4: Main peaks in frequency ratio distributions (■) and maximum amplitudes reached (□), marked with their tendency curve (——), for $m^* = 1.74$ and $m^*\zeta = 0.0137$, with linear constraints.

Figure 4.4 presents just the amplitude and frequency responses of the cylinder from the second set of experiments. Maximum amplitudes and peak frequencies are presented in the same graph and with the same scale to ease identification of the different branches of excitation and their transitions. Data plotted with stars correspond to the tests where flow visualisations have been conducted.

In a first part of the initial branch, for U_r between 3.75 and 4.44, the frequency distributions display two peaks with one corresponding to the Strouhal frequency of vortex shedding behind a fixed cylinder $f_{vs} = 0.18U/D$ and the other to the natural frequency of the system f_n in water. This, appearing in the frequency distribution for $U_r = 4.10$ presented in figure 5.15, has been shown to reveal the quasi-periodic nature of the motion in this branch [15], which is clearly illustrated by the time series for $U_r = 4.44$ presented in figure 4.5(a).

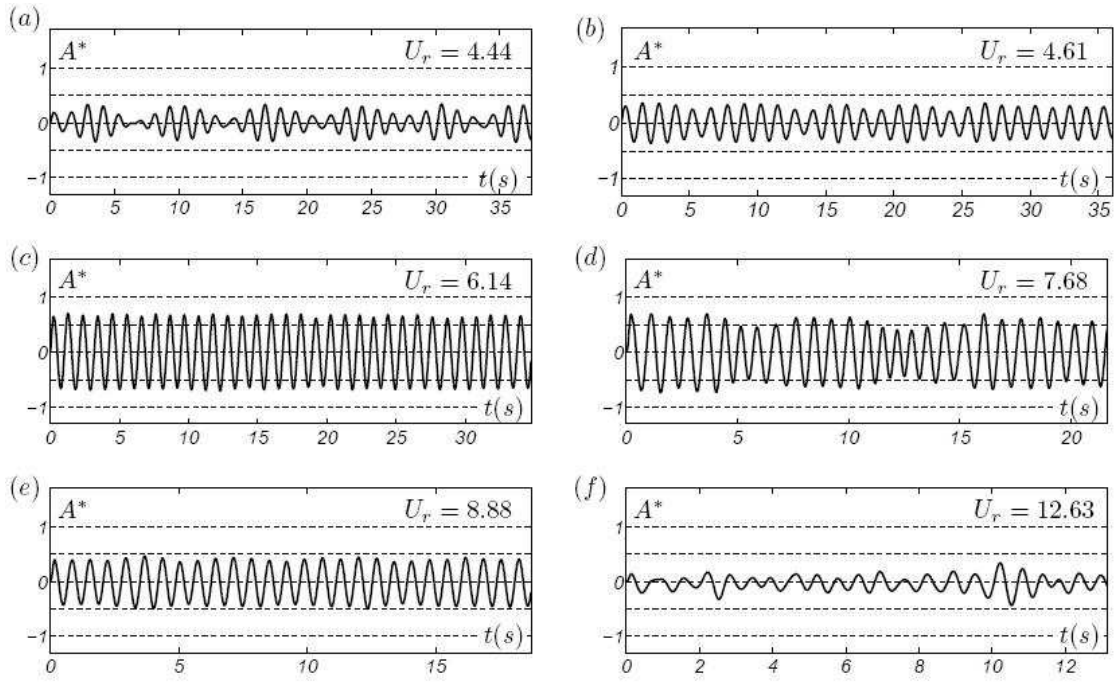

Figure 4.5: Time series of displacement for the linearly-restrained cylinder.

In a second part of the initial branch, for $U_r = 4.61$ here in figure 4.5(b), the motion is periodic, as only one peak appears in the frequency distributions at about f_{vs}. The amplitude of oscillation is still relatively small, with $A^*_{max} = 0.39$. Flow visualisations conducted at this reduced velocity, and presented in figure 4.6(a), reveal the 2S mode of vortex formation expected at this reduced velocity.

At $U_r = 4.78$, the cylinder switches to the upper branch of oscillation. The amplitude jumps to about $0.8D$ and the frequency to f_n. This has been shown to be caused by a jump in the phase angle between the fluid force and the cylinder's displacement due to a switch in vortex shedding mode. Indeed, while in the lower branch the vortex shedding was in 2S mode, in the upper branch it changes to a 2P mode, with the second vortex weaker than the first one. This mode was observed, as shown by the three pictures presented in figure 4.7 extracted from a video recorded at $U_r = 6.14$. In the first picture of this figure, the cylinder has just shed two contra rotative vortices.

The first of these vortices being stronger than the second one, it affects it and weakens it, making it disappear very quickly. The motion of the cylinder, presented for this reduced velocity in figure 4.5(c), is periodic with very low amplitude modulation. It stays so in the upper branch, with a frequency slightly increasing with U_r up to a value close to $f_{n_{air}}$, until some intermittent switches between the upper branch mode and the lower branch mode of oscillation appear from $U_r = 7.51$. The time series of displacement for $U_r = 7.68$ in figure 4.5(d) illustrates this intermittent nature of the motion as the amplitude of the motion can be observed to switch readily between the high amplitude mode existing in the upper branch and the lower amplitude mode existing in the lower branch. As both modes of oscillation have a different frequency, frequency distributions present two main peaks.

In [79], it is found that the transition between upper and lower branch finishes when $f/f_{n_{air}} \approx 1$, the reduced frequency f^* jumping to f^*_{lower}. This is verified here as $f \approx f^*_{n_{air}}$ for $U_r = 7.68$ and the frequency of the motion jumps to a value of about 1.48 at $U_r = 7.85$, as well as its amplitude to 0.6 D. Two time series at $U_r = 8.19$ and $U_r = 8.53$ exhibit however upper branch modes of vibration with a larger amplitude and a frequency larger than $f^*_{n_{air}}$ but consistent with the increase of f^* in the upper branch. Over all the lower branch of excitation the motion is periodic, with an amplitude and frequency remarkably constant at respectively about $0.55D$ and $f^* \approx 1.48$, which is close to the value predicted by the formula for f^*_{lower} from [79] using the values of our parameters, i.e. $m^* = 1.74$:

$$f^*_{lower} = \sqrt{\frac{m^*+C_a}{m^*-0.54}} = 1.51$$

The time series for $U_r = 8.88$ in figure 4.5(e) shows a characteristic periodic motion of the cylinder in the lower branch, exhibiting again a very low amplitude modulation. The vortex formation mode in the lower branch is a 2P mode in which the vortices are of equal strength in each pair and this mode of vortex formation is observed with flow visualisations carried out at $U_r = 9.22$, leading to a vortex wake such as

presented in figure 4.6(b). The reduced velocity where desynchronisation occurs is

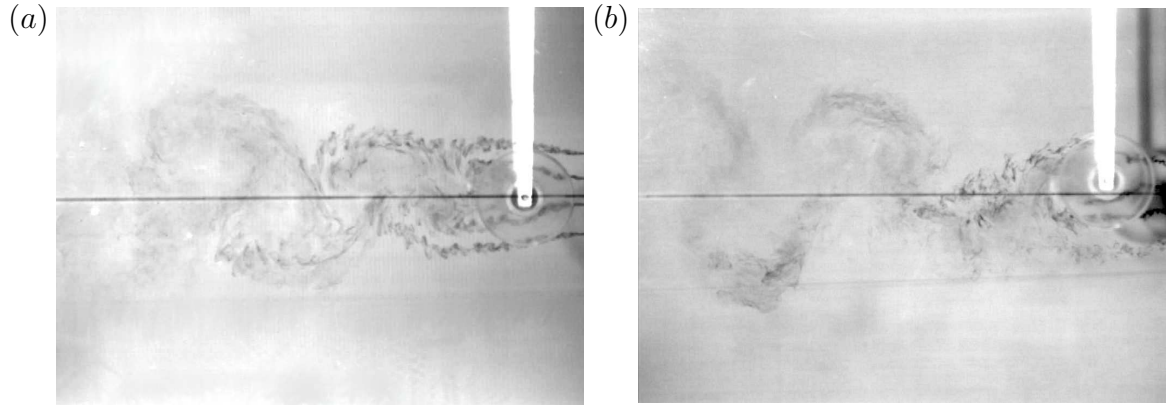

Figure 4.6: Flow visualisations of 2S and 2P modes. (a) : Flow visualisation made at $U_r = 4.61$ in the periodic part of the initial branch. (b) : Flow visualisation made at $U_r = 9.22$ in the second branch of excitation.

difficult to distinguish, but another peak, at f_{vs}, appears in the frequency distributions from $U_r = 11.44$. For larger U_r the motion becomes much more complex and disorganised, leading to the presence of several peaks in the much wider frequency spectra, including those at f_n, f_{vs} or f^*_{lower}. Some instabilities can sometimes give rise to few cycles of higher amplitude vibration as the one appearing in the time series in figure 4.5(f) for $U_r = 12.63$ at $t \approx 10$ s.

The response of the cylinder to VIV obtained with our experimental setup shows a good agreement with the literature. When subject to linear structural restraints, the system exhibits characteristic low-mass ratio low-damping amplitude and frequency responses with the different branches of excitation expected in such cases. The nature of the motion in the different branches has been shown to be as described in the literature. It is firstly quasi-periodic in a first part of the initial branch, with peaks at f_n and f_{vs} in the frequency spectra. It is then periodic in the second part of the initial branch and in the upper branch, before presenting some intermittent switches during the transition between upper and lower branches. It is periodic again in the lower branch with a frequency stable at f^*_{lower}, and disorganised after desynchronisation.

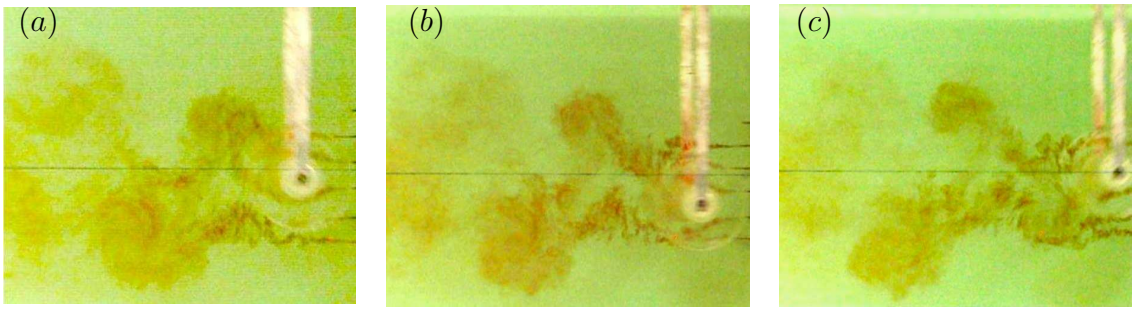

Figure 4.7: Rapid decay of the second vortex in the 2P mode in the upper branch of vibration. Above the line representing the cylinder's rest position, two counter rotating vortices have just been shed in (a). The weaker second one is destroyed by the first one (b) to totally disappear (c). Flow visualisations made at $U_r = 6.14$, $R_e = 5400$.

The experimental setup is therefore accepted as validated in the case of linear restraints, and structural non-linearities can be introduced in the system to investigate their effects on the VIV of a rigid cylinder.

Chapter 5

VIV with symmetric non-linear structural restraints

The design of the present experimental setup allows a non-linearity to easily be inserted into the cylinder's support system. One or two stops, involving discontinuities in the system's stiffness, can be placed to limit the cylinder's cross-flow displacement. The position and stiffness of the stops can be adjusted, such that soft or harder stops placed at a large or small distance from the cylinder's mean position can be obtained.

5.1 Insertion of a jump in the system stiffness

The idea developed is that, in the experimental setup designed, the limitation by a stiff stop of the displacement of one or several of the horizontal beams restraining the cylinder's frame to move only vertically somewhere along its length causes an abrupt change in the stiffness of the cylinder's support system, which implies a non-smooth

discontinuity of the stiffness coefficient of the cylinder'support system.

Experimental difficulties however arose when trying to position several pairs of stops to act in the same way on several beams moving in the same time. It is to solve these problems of positioning of the stops that we chose to have stops acting on only one of the beams restraining the frame holding the cylinder. In a configuration with four horizontal beams restraining the frame in its vertical plane, the use of stops on only one of the four beams however created problems of symmetry in the system during vibrations with impacts.
This configuration with only three beams holding the frame in its plane, particularly with only one beam placed at the top of the frame, and strongly clamped in its middle plane, was designed in order to have the stops to act on only that upper horizontal beam, involving a jump in the stiffness of the cylinder's support system when the beam reaches it without causing any problem of symmetry in the system.

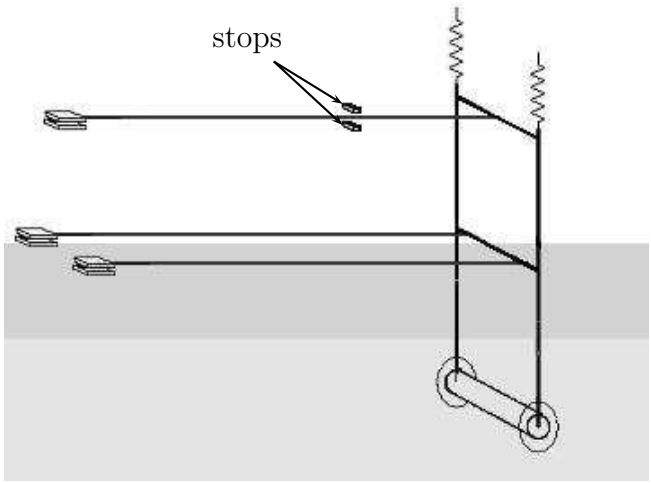

Figure 5.1: Insertion of a symmetrical jump in system stiffness.

With this experimental setup, a symmetrical jump in the system stiffness can for example be achieved in the system stiffness by placing two rigid stops symmetrically on both sides of the upper horizontal beam, as illustrated by figure 5.1. When its moving end is driven by the vertical oscillations of the cylinder at a frequency close to 1Hz, the upper horizontal beam vibrates, as the other ones, in a clamped-clamped 1^{st}

mode of vibration. If the displacement of its moving end, equal to the amplitude of the cylinder, is large enough, the upper beam will come into contact with one of the rigid stops placed at a length L_p from its moving end, and at a distance Y_p from its sides.

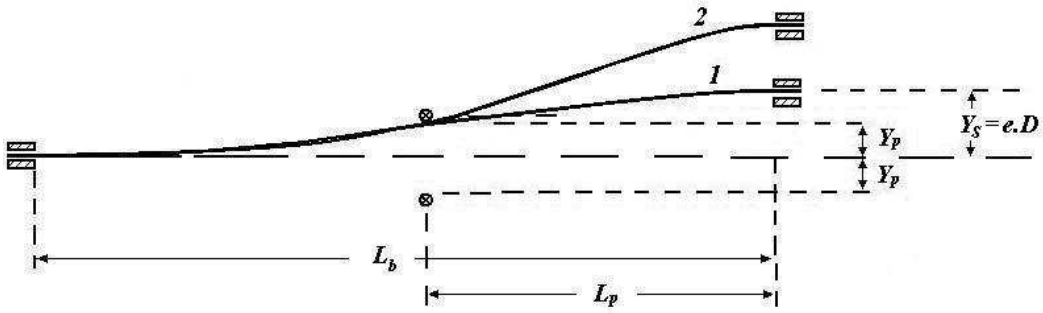

Figure 5.2: Change of the bending mode of the horizontal beam in apparent support stiffness

This is the case in the situation 1 illustrated in the schematic representation in figure 5.2. As shown by this figure, in this situation the vertical displacement Y_s of the moving end is different from the distance Y_p at which the rigid stops are placed from the sides of the beam.

When, during its oscillation driven by the cylinder, the beam reaches one of the stops, its vertical displacement at this point is stopped. If the moving end still goes further, as in the situation 2 in figure 5.2, the beam bends with a different mode depending on the position of the stop. Because of this new mode of bending, the apparent vertical stiffness of the beam at its moving end increases abruptly, and as it contributes to the total stiffness of the cylinder'support system, this latter also experiences an abrupt increase. Tests of static stiffness of the cylinder's support system have been conducted with the stops acting on the upper horizontal beam, for three different configurations of the stops, by applying weights on the cylinder in air. In order to avoid the contacts with the stops from exciting some higher clamped-clamped vibrational modes of the beam during its vibration, the positions of the stops along it

are chosen different from its nodes of vibration for the first higher clamped-clamped vibrational modes, obtained with a structural vibration software. In cases 1 and 2, stops were placed along the beam at $L_s = 0.32L_b$ from its moving end, L_b being the length of the horizontal beam, with an offset Y_p equal to $0.33D$ from each side of the beam in case 1 and $Y_p = 0.5D$ in case 2. In case 3, the stops are placed further from the moving end, at $L_s = 0.45L_b$ from it, with an offset $Y_p = 0.25D$. These tests show the influence of the stops on the system's static stiffness.

Results are presented in figure 5.3, where the vertical displacement of the cylinder is presented as a function of the static vertical force applied on it, for the different different stop settings. For clarity, this plot presents the response of the system on only one side of the cylinder, but, as the system is symmetrical, its response on the other side would be obtained by simple symmetry with respect to the origin point. In

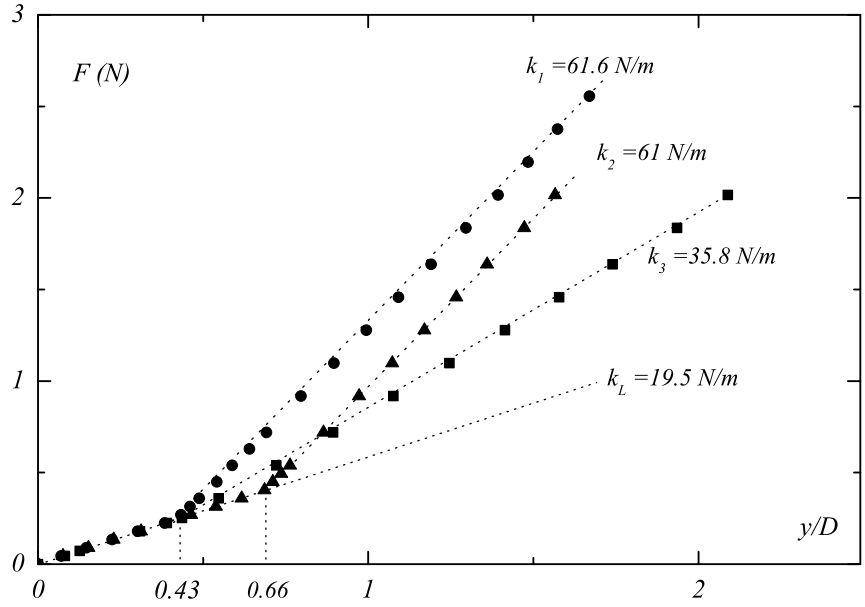

Figure 5.3: Static responses of the system to a load in the different cases of structural restraints, obtention of different jumps in stiffness. (•): case 1, $e = 0.43$, $r_k = 2.15$; (▲): case2, $e = 0.66$, $r_k = 2.15$, (■): case 3, $e = 0.43$, $r_k = 0.83$.

a first part of each plot, starting from the origin, a linear increase of the displacement

of the cylinder with the force applied is observed. The beam is not touching the stop yet, and the slope in this part reveals in all cases the static stiffness of the experimental system in the case of linear restraints k_L, which is measured to be about $k_L = 19.5$ N/m.

For every case, the slope of the plot changes instantaneously at some value of displacement, corresponding to $Y_s = e.D$. At this point, the beam enters in contact with the stop and it bends with another mode of deflection. The plot in this second part is a straight line for all cases, indicating a constant stiffness, and whose slope corresponds to the static stiffness of the system when the stop is acting $k = k_L + k_n$.

Such a plot reveals the piecewise-smooth linearity of the static system response to a load. As the static stiffness of the system corresponds to the slope of this plot, the system stiffness is piecewise-smooth discontinuous function of the cylinder's displacement. A jump in system stiffness is therefore achieved by limiting with a stiff stop the amplitude of the beam along its length. Each jump in stiffness achieved can be characterised by the non-dimensional amplitude of the cylinder when it occurs e , and by a stiffness ratio $r_k = k_n/k_L$.

For cases 1 and 2 where only the offset is changed, the apparent stiffness of the stop is nearly the same at $k_n + k_L \approx 61$ N/m, i.e. $r_k \approx 2.15$. The largest gap between the beam and the stop allows only for a higher offset e. In case 1, the jump occurs for $Y_s = 1.3$ cm, i.e. $e = 0.43$, while in case 2 it occurs for $e = 0.66$. For the case 3, the stiffness of the stop is lower than before, $k_n + k_L \approx 35.8$ N/m, giving $r_k = 0.83$. The amplitude of the oscillation of the cylinder when it experiences the jump in stiffness is about 1.3 cm, i.e. $e = 0.43$, the same as for case 1. This is convenient as we will later obtain from these three settings two sets of data: a first one with cases 1 and 3 with only the stiffness ratio r_k varying, and another one with cases 1 and 2 with only the offset e varying.

The position of the stops along the beam therefore affects the stiffness ratio of the jump in stiffness inserted, while their distance from the beam influences the amplitude of the cylinder where the jump occurs. It is intuitive that the stiffness ratio of the jump inserted increases when the stops are placed closer from the moving end of the horizontal beam holding the frame. The offset e also increases when placing the stops further apart from the horizontal beam. Characteristics of the symmetric jump in stiffness cannot be accurately set, but nevertheless some control on its parameters, e and r_k, is obtained as they can easily be varied.

It can be noted that, during the vibration of the beam, as the contact with the stop affects the shape of the beam, and its apparent stiffness at the moving end, it certainly also affects the damping produced by the bending of this beam, and its contribution to the total damping. However, it is very difficult to estimate the amount by which the damping produced by the beam during its vibration can be affected by the change of its shape induced by the stop.

5.2 VIV of a rigid cylinder impacting on symmetrically-placed soft stops

A jump in stiffness obviously occurs only when the cylinder reaches one of the stops, if it reaches on of the stops. The cylinder's response is therefore identical to the one with linear constraints when its maximum amplitude is smaller than the stops position e. Experiments have been carried out in the 30 m-long towing tank for the three cases of symmetrical jump in stiffness presented in last section. As the stiffness ratio r_k of the symmetrical jumps in stiffness are low in all of these cases, the cylinder's displacement does not show any obvious change when the cylinder experiences the jump in stiffness due to the contact of the horizontal upper beam with the stop. These stops acting on the horizontal beam attached to the frame holding the cylinder can therefore be considered as reproducing the action of soft stops, on which the cylinder impacts when its displacement equals e or $-e$.

5.2.1 Modification of the amplitude and frequency response

In order to compare the response of the cylinder with linear restraints to its response with impacts on symmetrically-placed soft stops, r.m.s amplitudes of oscillation are plotted in figure 5.4 for the case of linear restraints and all three cases of non-linear restraints described before. R.m.s amplitudes are here more representative of the oscillation of the cylinder than maximum amplitudes as these tests have been conducted in the first towing tank, where the heavy carriage could exhibit variations of its velocity involving, as explained before, perturbations in the cylinder's vibration.

The first result from this figure is that the presence of a jump in stiffness results in a shift of the reduced velocity where the maximum vibration amplitude occurs. When

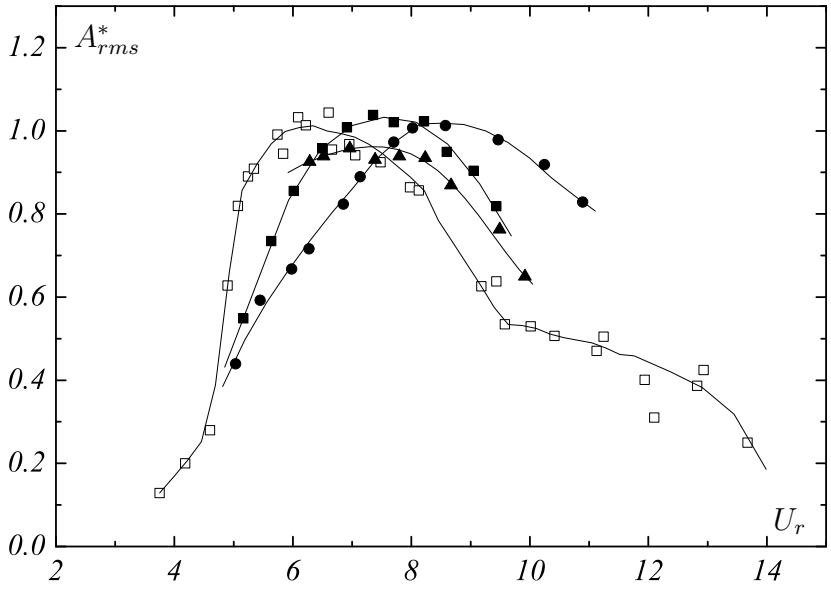

Figure 5.4: R.m.s amplitude of vibration for linear restraints (□) and with impacts on soft stops: (●): case 1, $e = 0.43, r_k = 2.15$; (▲): case 2, $e = 0.66, r_k = 2.15$; (■): case 3, $e = 0.43, r_k = 0.83$.

in the linear case the maximum amplitude of vibration was observed for $U_r = 6.2$, for all cases it occurs at a larger reduced velocity.

By comparing cases 1 and 3 where $e = 0.43$ but r_k is varied, the maximum amplitude is observed to be shifted to larger U_r when increasing r_k. In case 3 where $r_k = 0.83$, the maximum amplitude is found to occur at $U_r = 7.7$ while in case 1 where $r_k = 2.15$, it occurs at a higher value $U_r = 9.46$. The maximum amplitude seems to stay the same though, at $(A^*_{rms})_{max} \approx 1.1$. Comparing cases 1 and 2, where $r_k = 2.15$ but $e = 0.43$ and 0.66 respectively, it can be observed that the shift of the maximum amplitude, as well as the value of the maximum amplitude, increases with the offset e decreasing. In cases 2 and 3, the amplitudes exhibit about the same trend in the same range of reduced velocities, only with slightly lower values for the case 2. This would tend to suggest that these cases are nearly equivalent in terms of strength of non-linearity, the non-linearity in case 3 being just a bit stronger, leading to higher

amplitudes.

This shift of the reduced velocity where the maximum vibration amplitude occurs is similar to that observed in [23], where Stappenbelt et al. show that a shift to a higher reduced velocity occurs in the amplitude response with increasing non-linearity. The non-linearity considered in their paper was different from the one considered here, as they used a third-order polynomial stiffness with zero even index terms, as seen in section 2.4.

A change in the dynamics of the cylinder when in presence of a jump in stiffness is also apparent in its frequency response as illustrated by figure 5.5. The frequency

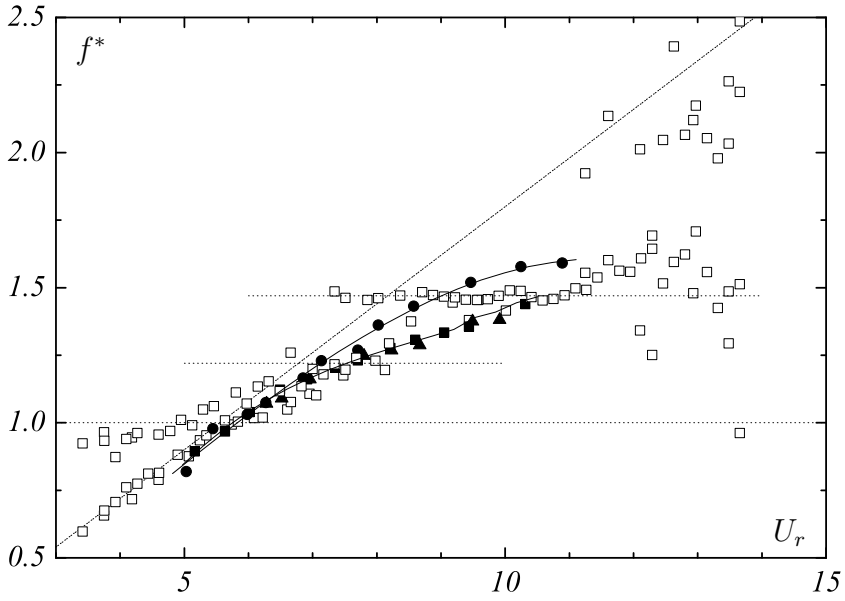

Figure 5.5: Frequency ratio for linear and non-linear cases.(□): linear case; (●): case 1, $e = 0.43, r_k = 2.15$; (▲): case 2, $e = 0.66, r_k = 2.15$; (■): case 3, $e = 0.43, r_k = 0.83$.

response does not follow any more the evolution it had with linear compliances. It does not exhibit the same slight increase to $f_{n_{air}}$ in the upper branch, neither the plateau at f_{lower} it presented in the lower branch. Instead, the oscillation frequency increases progressively for all non-linear cases, staying between its value for the linear

case and the vortex shedding frequency $f_{vs} = 0.18U/D$ represented by a line in figure 5.5. The strength of the non-linearity influences the frequency response, as frequencies measured for case 1, where the non-linearity is the strongest, are above those for the two other cases. In the latter, the frequency response is the same; values are very close, exhibiting the same increase. The oscillation frequency increases with the non-linearity increasing, which did not appear in the data from Stappenbelt et al.

The non-linearities linked to a discontinuity in the system stiffness studied in this section can be considered relatively strong. Indeed, in order to have an idea of the strength of the non-linearities, the system stiffness responses are approximated by third order polynomials as in [23], of the form $k_1 y + \frac{k_1 C_r}{D^2} y^3$. This approximation is made over a displacement of only up to about 1 diameter, as it is the domain where the cylinder oscillates most during VIV.

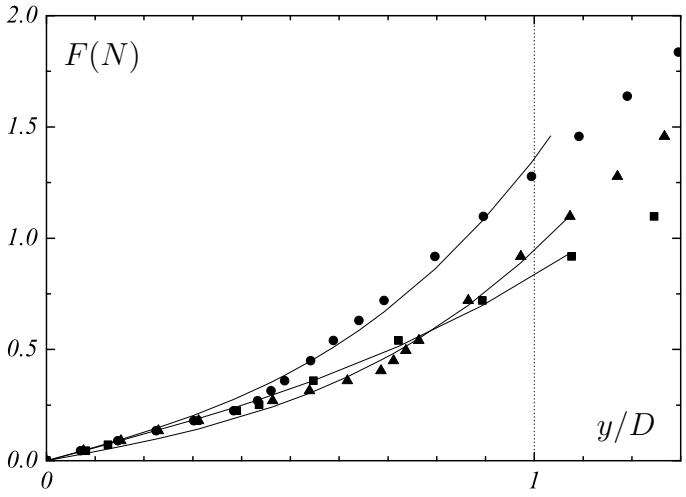

Figure 5.6: Approximation of static stiffness responses up to 1 diameter displacement by third order polynomials.

Curve fitting of the stiffness response based on the same form as in [23], displayed in figure 5.6 of the three different static stiffness responses obtained previously gives for cases 1, 2 and 3 respectively a stiffness k_1 equal to 20.24, 13.52 and 19.45, and C_r equal to 1.23, 1.32, and 0.42. These approximations by third order polynomials do not exactly fit the present stiffness responses, and modifications of the dynamics of the cylinder caused by impacts on soft stops are different from those caused by

smooth non-linearities of the system stiffness and these problems are different. But these approximations show that even in the case 3, in which the non-linearity is the weakest of the three cases studied, it is lot stronger than that of a typical shallow-water catenary moored structure usually presenting a maximum compliance ratio of about 0.1 [23]. Here fits of the stiffness responses lead to compliance ratios much larger than 0.1.

But even stronger non-linearities can be encountered by structures subject to VIV, as contacts with structural parts specially designed to limit their vibration, or with other moving parts. Contacts in vibrating systems have received a lot of interest as seen in section 3.2. The limitation of the amplitude of vibration of sinusoidally-excited systems can imply changes in their dynamics, leading to unwanted behaviour and ultimately to failure. In the case of a structure experiencing free vortex-induced vibrations, the problem is thought to be even more complex as the driving force acting on the structure is strongly related to its displacement. Limitation of the amplitude of oscillation of the structure could therefore affect the strong interaction fluid-structure present in this problem, and modify the vortex shedding phenomenon driving the oscillation.

5.3 VIV of a rigid cylinder with impact on symmetrically-placed stiff stops

The case of a rigid cylinder experiencing VIV, and whose amplitude is symmetrically limited on both sides by the presence of very stiff stops is investigated. As the clearance is the most important system parameter for a two-degree-of-freedom harmonically-excited system with symmetrical rigid stops [66], the effect of the strength of limitation is investigated by setting the offset e between the rest position of the cylinder and the stops at different values. From the displacement of the cylinder recorded for each offset value at different flow velocities, its dynamics can be studied and compared to the one it exhibited with linear restraints. Modifications of the dynamics are shown to occur when the non-linearity is strong. The symmetric limitation of the amplitude of vibration of a cylinder experiencing VIV affects the fluid-structure interaction as these changes in the dynamics are accompanied by changes in the vortex-wake dynamics as shown by the flow visualisations.

5.3.1 Amplitude limitation

To limit the amplitude of vibration of the cylinder experiencing VIV on both sides, a symmetric jump to a very high stiffness is introduced in the system, at an offset e from the cylinder's rest position. To achieve this experimentally, the stops acting on the upper horizontal beam are placed at about 2 cm, i.e $0.02L_b$, from its moving end attached to the frame holding the cylinder. The displacement of the beam being stopped so close to its moving end, its bending if trying to move further the moving end is very hard, but still possible. The stop acting on the beam changes the latter to a very stiff hardening spring, inserting a jump to a high value in the system stiffness when the cylinder reaches it. As previously done, tests of static stiffness of the system

in air were conducted by placing weights on the cylinder, including therefore in the measure the plausible bending of all parts of the aluminium rod holding the cylinder. The static response of the system to a load obtained with the stop placed that close from the moving end at an offset of about 0.65 D is displayed in figure 5.7, with those obtained with the previous stop settings for comparison.

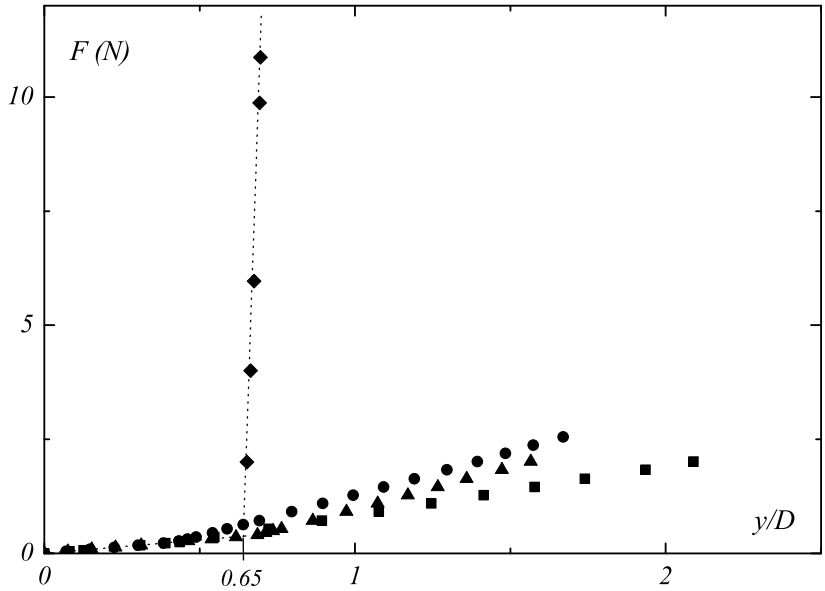

Figure 5.7: Static response of the system to a load when in presence of a stiff stop; (◆) : $e = 0.65$, $r_k = 344$. Others: Data from figure 5.3.

Here again, a first part of the graph shows the displacement increasing linearly with the load, and the slope of the plot in this graph reveals the constant stiffness of the system when the stop are not acting, $k_L = 19.5$ N/m. When the cylinder's amplitude reaches $Y_s = e.D$, here equal to $0.65D$, the static response exhibits a first order singularity, and the plot displays a line with a larger slope for larger displacements. The system experiences when reaching a stop a considerably high jump in stiffness; much more force is needed to push it just a bit further. The total system stiffness when the stop is acting is measured here to be about 6701 N/m, which gives $r_k \approx 344$. The stop cannot be considered as rigid as its stiffness is not infinitely large, but the value of its stiffness ratio is high enough to identify this structural non-linearity as a very stiff stop, strongly limiting the amplitude of the cylinder.

Moreover, in the experimental tests of VIV of the rigid cylinder with impact on these stops carried out in this project, impact times are not nil and can be measured. They therefore cannot be considered negligible as they are with rigid stops.

Double-sided impacting motions are first achieved by placing stops symmetrically on both sides of the upper horizontal aluminium beam, at 2cm from its moving end, resulting in a symmetric jump in stiffness of stiffness ratio $r_k \approx 344$ when $|y| = e$. The introduction of such a strong amplitude limitation involves the appearance of repetitive impacts between the cylinder and the stop, revealed, as will be seen in next section, by strong singularities of the displacement function at moments of impact. Experimentally, contacts between the physical stop and the horizontal beam were long enough during the first cases with smaller jumps in stiffness to observe the gradual bending of the horizontal beam. In this case, with the stops placed that close to the moving end of the beam, contact times were very small and impact noises between the stops and the beam could be clearly be heard even at low velocity. Such non-linearity appearing in the system raises for the experimenter some practical problems, particularly in the post-processing of the recorded data of displacement.

5.3.2 Post-processing of the data

In the case of the symmetric non-linear restraints considered in this project, the system stiffness k is not continuous, and can be expressed as a piecewise-constant discontinuous function of the position of the cylinder Y, such as:

$$\begin{cases} k = k_L & \text{if } -Y_s > Y > Y_s \\ k = k_L + k_s & \text{if } -Y_s \leq Y \quad \text{or} \quad Y \geq Y_s \end{cases} \tag{5.3.1}$$

where k_L is the linear stiffness of the system, k_s is the stiffness of the stop and Y_s is the symmetric offset between the stops and the cylinder, $Y_s = e.D$. Equation 4.1.1

can be rewritten as:

$$m\ddot{Y} + c\dot{y} + kY + \Delta\left(k_s(|Y| - Y_s)\right) = F(t) \tag{5.3.2}$$

Where $\Delta(x)$ is a function equal to x for $x \geq 0$ and to zero for $x < 0$. When the cylinder reaches the stop, i.e. when $Y = Y_s$, Δ is continuous and so is the acceleration. However, the derivative of the acceleration is not continuous at this point as the derivative of Δ is not continuous. $\ddot{Y}$ is therefore of class C^0, and exhibits singularities each time $|Y| = Y_s$. By integration, the velocity $\dot{Y}$ and displacement Y, respectively of class C^1 and C^2, also exhibit singularities at the moments of impact.

The small values of r_k set for the jump in stiffness in the previous section, with $r_k = 0.83$ and 2.15, resulted in a very weak non-linearity of the displacement at impact, so weak that the instant of impact was imperceptible in the time series. The recorded signal of displacement could therefore be filtered in the same way as with linear constraints, i.e. by applying to it the low-pass filter using the Shannon-Whittaker interpolation formula with a cut-off frequency of five times the vortex shedding frequency for a fixed cylinder $f_{vs} = 0.2U/D$. Obtained SNR values were about the same as for linear constraints.

However in the present case of very high stiffness ratio, impacts on the stops are clearly observed in the time series of displacement. A typical example of the raw signal of displacement of the cylinder undergoing VIV when impacting on a stop is presented in figure 5.8(a). The impact occurring at $t \approx 10.75$ s, revealed by singularities of the signal of displacement displacement, is clearly apparent in this figure. The close-up on the moment of impact presented in figure 5.8(b) displays many features of the measured raw signal. It can be observed that often two consecutive points at least are measured successively at the same value of displacement. This is due to the fact that the 12-bit acquisition board used records a signal varying between -10 and +10V over with a precision of 2.5 mV. To be sure to capture large-amplitude motions, the calibration factor was usually about 0.013 m/V, leading to an accuracy

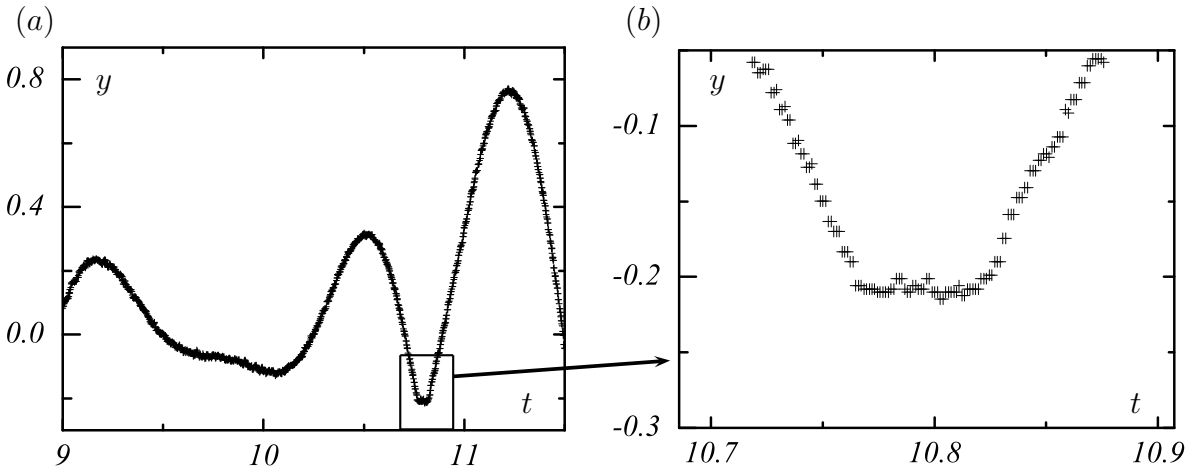

Figure 5.8: Time series of displacement with occurrence of a contact. (a): raw signal of displacement with impact on a rigid stop placed at $y_s = 0.22D$. (b): Close-up on the moment of impact.

on the displacement signal recorded by the PC of 0.0325 mm, or 1.08×10^{-3} D.

The high rate of acquisition set was chosen to capture accurately the singularities of the displacement function at moments of impact. With this rate of acquisition and the calibration factor used, two values of displacement should consecutively be measured at the same value of displacement if the instantaneous velocity of the cylinder is less than 0.87 D/s, which is a very large velocity for the cylinder. Several consecutive points are therefore very often measured at the same value of displacement.

Such an accuracy on the measurement of the position of the cylinder allows one to obtain a good knowledge of the dynamics of the cylinder when not in contact with the stop. However, the high local Signal-to-Noise Ratio during contacts limits the information on the dynamics of the cylinder during the contact with the stop. This could have been improved by adjusting the output signal of the PSD with an amplifier to match for each test the expected extremes values of displacement with the extreme values of the voltage range captured by the acquisition board. The

calibration factor could in that way have been decreased, increasing the accuracy of the measurement of the displacement. Better accuracy could also have been reached by using a more powerful acquisition board.

The raw measure of displacement includes also some electrical noise and experimental errors due for example to the positioning of the LED during calibration of the position sensor displacement, or to the small defaults of alignment of the different components of the experimental setup. Precision of the numerical variables used during the post-processing is another source of error, but the displacement $Y(t)$ is nevertheless estimated to be obtained with a precision of less than 0.1 mm, i.e. about 3.3 10^{-3} D.

On this raw signal, post-processing was conducted to remove some of the noise from the data, and obtain a clean velocity function. A problem arises in the post-processing of these data due to the discontinuity in stiffness. The signal contains high frequency components, but only at the moments of impact. Filtering of the recorded data of displacement is not straightforward as noise-created high frequency components have to be removed from the signal everywhere else, but not at the moments of impact.

Applying a low-pass filter to these time series did not prove to be a useful way to process the data. In choosing a high cut-off frequency to accurately capture the moment of impact, one does not eliminate the unwanted high frequency components in the signal between impacts. In choosing a low cut-off frequency to remove the noise and discard high frequency components appearing in the motion between impacts, the displacement of the cylinder around impact times is smoothed, and even more is its velocity, obtained from differentiation of the displacement. This results in an abrupt decrease of the velocity of the cylinder, and therefore an abrupt variation of its acceleration, before the cylinder even reaches the stop, which obviously makes no sense and is due to inappropriate processing. Phase portraits, presenting the velocity of the cylinder as a function of its displacement, proved to be very useful in evaluating in a glance the smoothing close to an impact induced by the signal processing used on

the data. Indeed, the very rapid change of sign of the velocity at a quasi constant position, resulting from an impact of the cylinder on the stop appears in a phase portrait as the trajectory describing a nearly straight vertical line placed at the stop position on the axis going from the value of the velocity before impact to its value after impact. The trajectory should present very abrupt singularities at both ends of this line. Smoothing of the displacement or velocity induced by the signal processing causes in the corresponding phase portrait a rounding of the trajectory close to the impact position. Moreover, as the acquisition frequency is fixed, smoothing induced by a window averaging or low-pass filter increases with the velocity of the cylinder.

To avoid this smoothing of the displacement around impact caused by the application of a continuous low-pass filter on the data, some specific signal processing has to be used. As no literature concerning the post-processing of experimental data from vibrating systems containing such a non-linearity could be found, this specific signal processing has been thoroughly developed.

From the basic observation that the system is not continuous only at the impact times, it follows that it is therefore continuous in the domains where the cylinder does not touch the stop, and in the domains where it is in contact with the stop. Obtaining the contact times makes it possible decompose the recorded displacement into successive parts where the system is continuous.

Individual reconstruction of the signal with the Shannon-Whittaker interpolation formula on these domains did remove the noise from the signal in these parts, but problems arose in reassembling the different domains to obtain the whole time series again.

In order to keep high frequency components only at impact, an ‘adaptative window filtering’ was developed, in which the window width is smaller in the domains where contact occurs compared to those where there is no contact. However, reducing the

window width when approaching an impact allows high frequency components to appear just before impact, in the displacement and in the velocity, falsifying therefore the important impact velocities.

The algorithm finally adopted to filter the time series of displacement uses the decomposition of the time series in domains where the system is continuous, and applies a window filtering on them, but avoids the problem due to boundary conditions by creating fictive points at each ends of these domains. It is described here in more detail.

The raw signal recorded is first of all converted into non-dimensional displacement using the calibration factor of the PSD and the value of the signal when the cylinder is in its rest position, read at the beginning of each record. A simple moving window averaging of the displacement data, with a 3-point window, is first of all conducted. This principally changes the values of successive points presenting the same amplitude, and removes some of the noise from the data. The width of the window is small enough not to smooth the moment of impact, nor involve any significant amplitude loss. A first estimation of the stop position is made using the peaks of displacement, averaging those identified as belonging to a contact. A rough estimation of the successive impact times, when the cylinder reaches and leaves the stop, is then made using the average value of the stop position. Statistics on the impact position and a rough test on the acceleration are performed to identify grazing cases. As will be seen, the average position of the cylinder during an impact does vary slightly at each impact. Therefore, a more accurate determination of the impact position is carried out for each impact, and, using these individual stop positions, a more accurate determination of the contact times is then performed.

With this method, contact times are obtained with a good accuracy, roughly estimated to around ± 3 ms and the time series can be segmented into intervals where the cylinder is in contact with the stop and intervals where it is not, these latter

carrying most of the information about the dynamics of the cylinder.

Considering one by one these intervals where the cylinder is not in contact with the stop, fictive data are created at each boundary outside the considered domains, by transposition of the last extreme points. This makes it possible to apply a low-pass filter on these extended intervals, without having high frequency components appearing close to impacts.

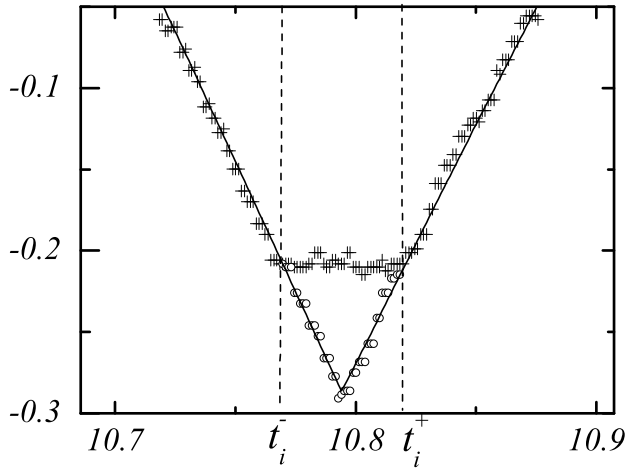

Figure 5.9: Processing of the signal around impact. (+): raw data; (∘): added fictive points; (——): filtered fictive displacement data.

This method is illustrated by figure 5.9 displaying the same raw signal of displacement as in figure 5.8. In this figure, three parts of intervals appear: the end of a first interval $t_{i-1}^+ < t < t_i^-$ where the cylinder is not in contact with the stop, and therefore approaching the stop, an interval between impact times $t_i^- < t < t_i^+$ where it is in contact with the stop, and the beginning of the next interval for $t_{i+1}^- > t > t_i^+$ where the cylinder has left the stop and is again not in contact with it any more.

Considering only the intervals where the cylinder is not in contact with the stop, fictive points, displayed here with circles, are added at the end of the first interval and at the beginning of the second one, by transposition of the extreme points. Continuous window averaging is performed on these domains extended by fictive points, resulting in the continuous lines on the graph. For the reconstruction of the time series, fictive data are then replaced by the original data points belonging to the domains where impact occurs, and averaging in a small window is then carried out over these domains, widened on each side by two adjacent points to ensure the

continuity of the signal at impact. Artificial smoothing of the displacement around impact is therefore much reduced. The obtained filtered time series of displacement are, everywhere outside of contacts, removed from noise and high frequency components.

The velocity of the cylinder is obtained by derivation of the filtered displacement with a 5-point centred difference scheme. This involves a very weak smoothing of the velocity around impact, but velocities of the cylinder just before and after impact are measured just a bit further from their respective impact times t_i^- and t_i^+, and are not affected by this weak smoothing. Phase portraits presented later in this work, and obtained using the above-described post-processing, exhibit the abrupt change of sign of the velocity due to the impact, without displaying any strong smoothing around impact. This result allowed us to adopt this technique for the post-processing of the recorded time series of displacement of the cylinder oscillating under vortex shedding excitation and impacting on one or two stiff amplitude limiting stops. Results presented in the following parts of this work have been obtained using this specific signal processing on the recorded signal of displacement.

It has to be noted that during some tests with impacts, higher modes of vibration were observed to be excited in the horizontal beams. These higher modes of vibration appeared at high reduced velocities with linear restraints, but were also clearly excited by impacts on the stops. A very low-amplitude high-frequency component appeared indeed in the time series of displacement when these high modes of vibration of the beams were excited. These modes certainly gave rise to vertical oscillating forces on to the frame supporting the cylinder, in which some of it was dissipated, but whose other part was also certainly transmitted to the cylinder. This high frequency component certainly slightly affected the fluid-structure interaction, but it is considered to be of such low amplitude that its effect on the fluid-structure interaction can be neglected, and is therefore removed during signal processing.

5.3.3 Observation of time series of displacement

The symmetric offset e between the cylinder's rest position and each stop was set at e=0.75, 0.34 and 0.23 during the first set of experiments carried out in the 30m-long tank, and at 0.65, 0.47, 0.30 and 0.20 in the second set carried out in the 13m-long glass-walled tank.

Experimentally it is very difficult to position the stops exactly symmetrically. In fact as the stops act on the 1.5 mm-thick upper horizontal beam attached to the frame holding the cylinder, they have to be both placed at exactly the same distance from the side of the beam they face. Given the dimensions of the cylinder, an error of 0.3 mm on the positioning of a stop corresponds to an error of $0.01D$ from its position. Verification of the symmetry of the positioning of the stops could experimentally be done by running the experiment at the lowest reduced velocity where impact occurs, to check that it occurs symmetrically on each side. Small errors of positioning have nevertheless occurred and in some cases, as in the case for $e = 0.20$, the limits are in fact slightly asymmetric. This asymmetry is considered small enough not to affect too much the nature of the vibration, in comparison with the same exactly symmetric case.

As in the case of impact oscillators with symmetric stops, the motion of the cylinder, here driven by the oscillating fluid force resulting from vortex shedding, can be very complex and can display different kind of regular patterns. It can for example impact once on each stop during one oscillation cycle, or repeatedly on only one of the stops during one or several oscillation cycles, or not reach any of the stops during some oscillation cycles. A notation $p - l - u$ similar to the one used in [66] can be used here to classify observable periodic motions, with u and l the number of impacts on the upper and lower stop, occurring in p periods. This notation is here based on the main oscillation frequency, which is equivalent in these cases of double-sided

impacting motions to the vortex shedding frequency, which could be considered as the forcing frequency.

A first indication of the effect of the symmetric amplitude limitation of a cylinder undergoing VIV on its dynamics can be given by a simple comparison between the time series of displacement for the same conditions with only the offset e between the cylinder and the stops varying. Figure 5.10 displays time series recorded during the second set of experiments at $U_r = 5.12$ in the case of linear constraints, i.e. in the upper branch of excitation, and for double-sided impacting motions with the four gap values set in this case. On each graph, the stops, when present, are identified by horizontal lines whose positions are given on the displacement axis.

The first result appearing from the comparison of the presented time series is that a change in the dynamics of the cylinder clearly seems to occur, at U_r=5.12, when the amplitude of the cylinder is strongly limited by the stops. For $e = 0.65$ or 0.47, the cylinder describes a remarkably stable motion with impact on each stop during one period, describing a stable symmetric period-1 double-impact motion, or *1-1-1* motion. The period of the motion seems constant, and the motion periodic. The limitation of the cylinder's amplitude in this case does not seem to change the periodic nature of the motion; it changes the high-amplitude periodic oscillation existing at this reduced velocity into a periodic motion impacting once on each stop during each cycle.

When the symmetric offset is reduced, here to $e = 0.30$ or 0.20, the cylinder's displacement exhibits periods of nearly periodic *1-1-1* motions, but also moments where it impacts successively on the same stop or moments where it marks a brief oscillation around some apparently random value of displacement. The motion in these cases is much more affected by the amplitude limitation, and the response is more complex without any distinctive periodic pattern. The dynamics of the cylinder therefore seems to be greatly affected by a symmetric amplitude limitation when this

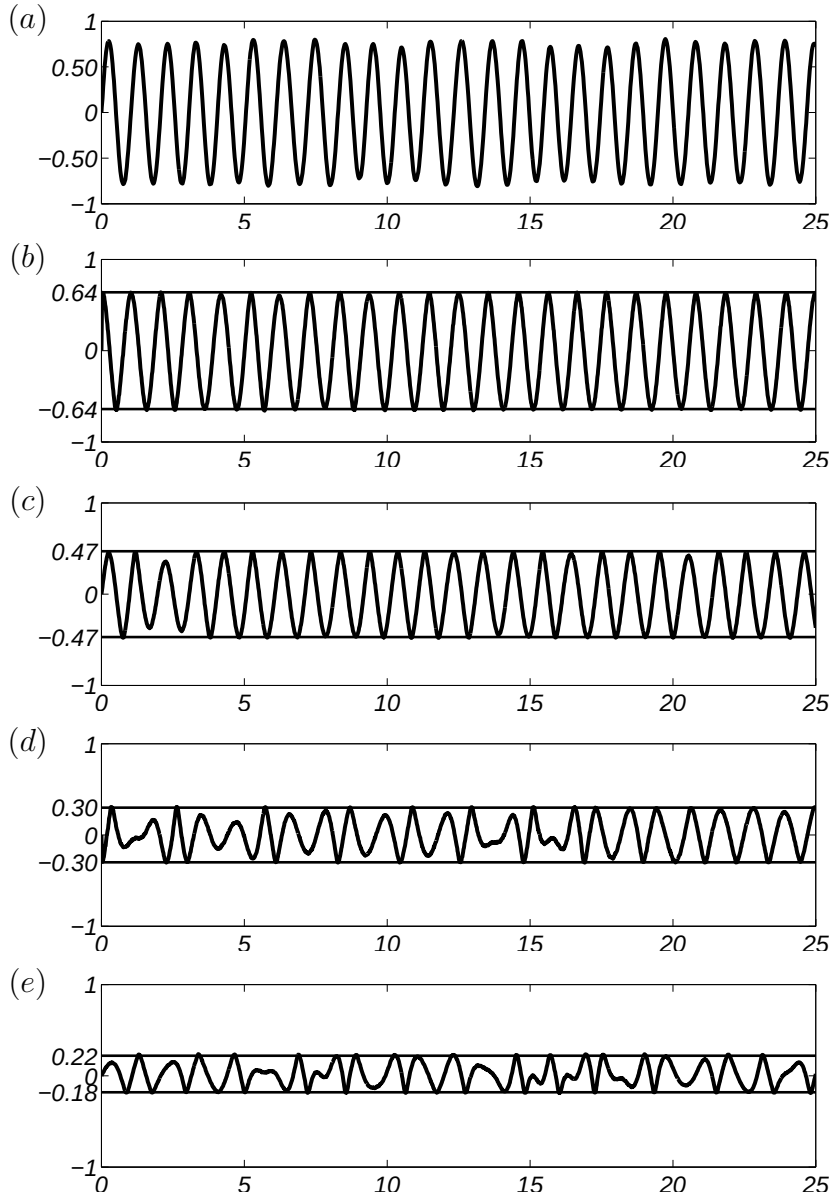

Figure 5.10: Time series for linear constraints (a) and double-sided impacting motions for $U_r = 5.12$. (b): $e = 0.65$, (c): $e = 0.47$, (d): $e = 0.30$, (e): $e = 0.20$

latter is strong.

It can hardly be seen on the time series plotted with this scale, but the cylinder's recorded position goes beyond the stop position, even if it is by a very small distance, during some impacts. The stops being springs of high but finite stiffness, but still

springs, the cylinder can push them and reach slightly beyond. In fact, as will be seen in section 5.3.5, impact velocities and impact forces vary at nearly every impact and therefore the extreme position of the cylinder during impact varies slightly at each impact.

5.3.4 Amplitude and frequency response

Naturally, amplitude limitation only takes place when the cylinder's maximum non-dimensional amplitude in the linear case A^*_{max} reaches the stop position e. As A^*_{max} depends on the reduced velocity U_r, the range of reduced velocities where the cylinder impacts on the stop, more simply called impacting domain, depends on e.

The plot of the extreme positions presented in figure 5.11 shows the width of the impacting domain for each case of symmetric amplitude limitation investigated during the more accurate second set of experiments. Figure 5.11 presents the extreme amplitudes reached by the cylinder on the side $y > 0$, or upper peak excursions ${A^*_{max}}^+$, and the lower peak excursions ${A^*_{max}}^-$ on the side $y < 0$, plotted against the reduced velocity U_r for the four different offset values investigated.

For the largest offset value set here, symmetric amplitude limitation occurs only in the range of reduced velocities corresponding to the upper branch of excitation in the linear case. When the offset is reduced such as impact can occur in the lower branch, impact occurs from the flow velocity where the cylinder's amplitude in the linear case equals the stop position, up to the highest flow velocity safely reachable with the present experimental setup.

Another feature of the system appearing in this figure, even if very slightly when presented with this scale, is the increase of the absolute value of ${A^*_{max}}^+$ and ${A^*_{max}}^-$ with U_r. As mentioned before, the cylinder reaches slightly beyond the stop position

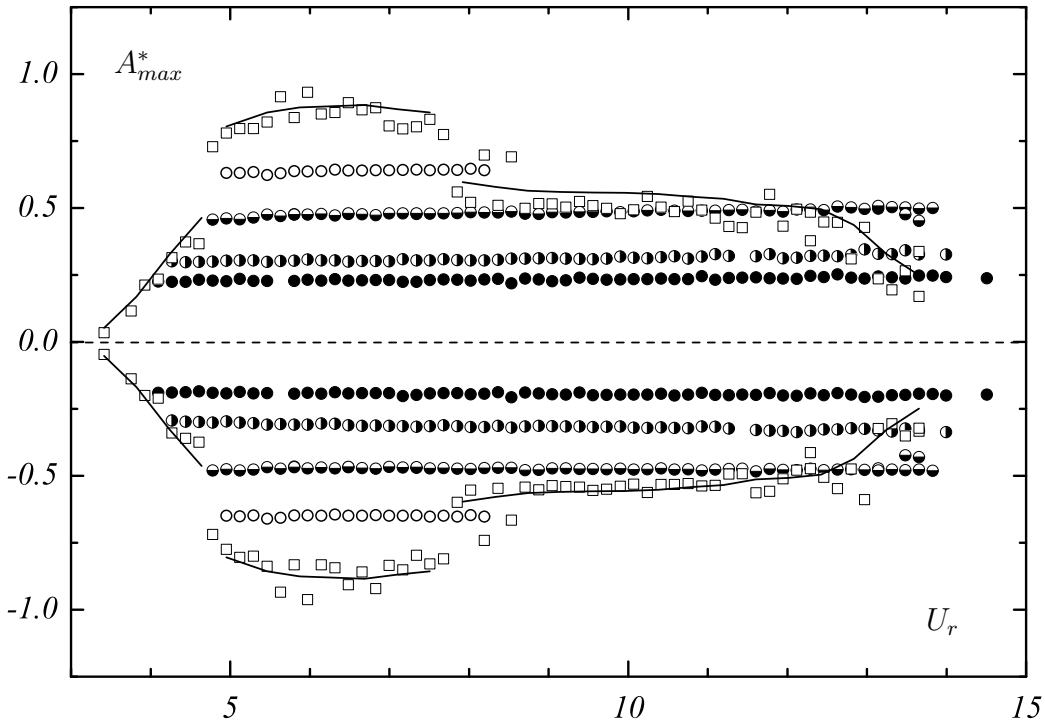

Figure 5.11: Extremes of displacement for the linear case (□) and double-sided impacting motions: (○): $e = 0.65$; (◒): $e = 0.47$; (◑): $e = 0.30$; (●): $e = 0.20$.

when impacting on it, and the extreme position of the cylinder during impact depends on the impact velocity. The increase of the extreme positions reached by the cylinder occurring in any case of symmetric amplitude limitation with U_r reveals an increase of the maximum impact velocity with U_r, which will be investigated later in section 5.3.5.

Another indication of the modification of the dynamics of the cylinder caused by amplitude limitation can be given by comparing its frequency response when its amplitude is symmetrically limited on both sides to that it exhibits with linear restraints. As will be seen later the frequency response of the cylinder becomes much more complex when impacts occur, but frequency distributions always contain a distinctive main peak higher than the other ones. Figure 5.12 displays the frequency ratio of the main peak in the frequency ratio distributions obtained by Fast Fourier

Transform on the post-processed time series of displacement as a function of U_r, for the three different offset values investigated.

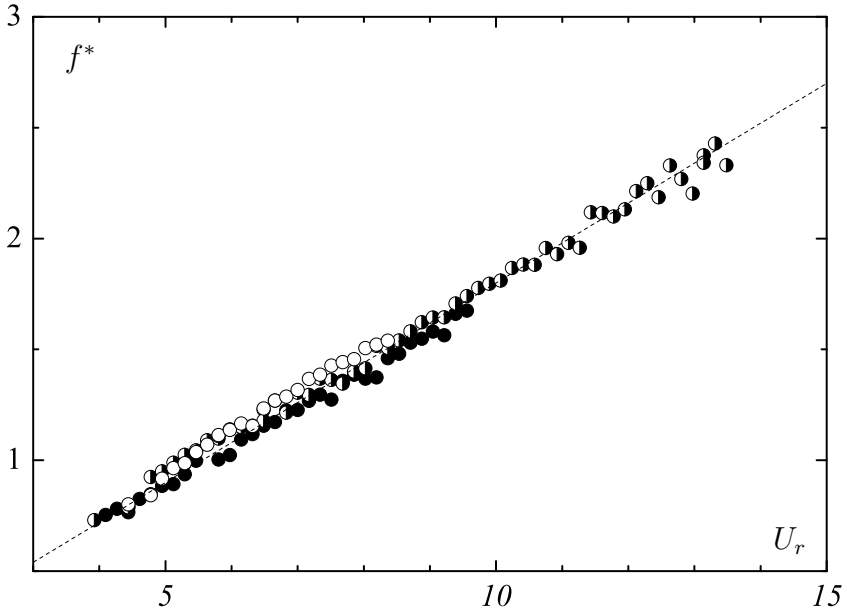

Figure 5.12: Main frequency ratio peaks for double-sided impacting motions. (○): $e = 0.65$; (◑): $e = 0.30$; (●): $e = 0.20$.

The first observation from this graph is that the main frequency f^* does not follow any more the evolution it presents with linear restraints. In all cases of symmetric amplitude limitation, the main frequency of the motion increases nearly linearly with U_r over the respective impacting domain, staying close to the vortex shedding frequency $f_{vs} = 0.18\ U/D$ plotted with a dashed line in figure 5.12.

It is interesting to note that whereas with linear restraints the reduced frequency of the cylinder presents jumps in frequency, as from f_{vs} to f_n during the initial-upper transition or from f_n to f_{lower} during upper-lower transition, here when amplitude limitation acts no jump is to be observed over the whole impacting domain. Obviously, if the offset is large enough for the stops to act only in the upper branch, as for $e = 0.65$, the frequency of the motion exhibits a jump to f^*_{lower} at the end of the impacting domain.

Before further investigating the changes in the dynamics of the cylinder induced by its symmetric amplitude limitation, attention is drawn to the impact velocities and impact forces, as these are particularly important factors in the design of structures.

5.3.5 Impact velocities and impact forces

The impact velocity, being the velocity of the cylinder when it comes into contact with a stop, can be recorded for every impact from the recorded data using the algorithm previously described. Values of the cylinder's velocity are taken just before every impact on the upper and lower stop; the impact velocity varies at nearly each impact, but its average and maximum values over each record shows interesting features. For the presentation of these data, dimensional impact velocities $\dot{Y}_i$ are normalised by a characteristic velocity of the system, chosen equal to the maximum velocity of the cylinder oscillating at its natural frequency with an amplitude of one diameter, i.e. $U_c = 2\pi f_n D$.

Average and maximum values $\overline{V_i}$ and V_{imax} of the reduced impact velocities $V_i = \dot{Y}_i/U_c$ obtained from the recorded time series of displacement are presented in figure 5.13 as functions of U_r for double-sided impacting cases with different offset values.

Obviously, as impact occurs on a range of flow velocities depending on e, values of impact velocity can only be presented on the respective impacting domain corresponding to the value of e.

The average impact velocity $\overline{V_i}$ is about the same for all gap settings at low U_r, and it increases nearly linearly with U_r in every case over each respective impacting domain. Its increase depends highly on the offset e as the four sets of data plotted form four distinctive lines with four different slopes, decreasing as e decreases. The maximum

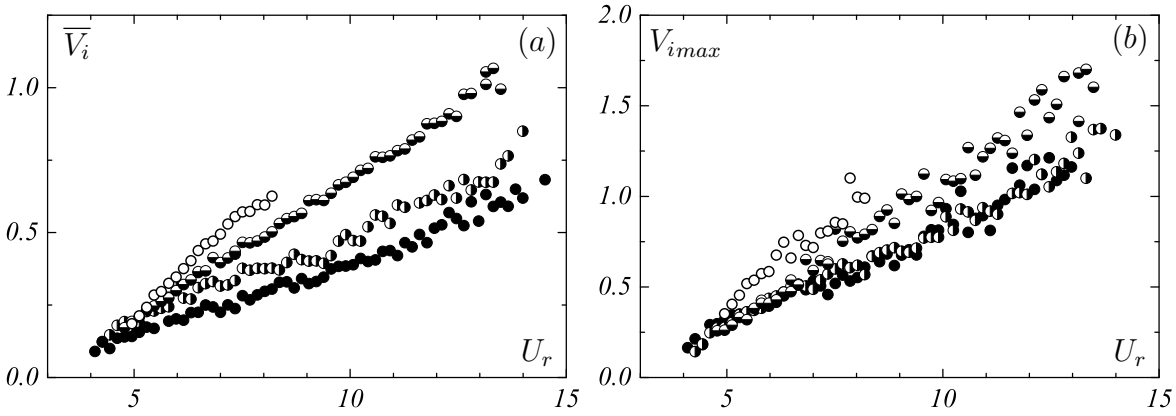

Figure 5.13: Average (a) and maximum (b) reduced impact velocities for double-sided impacting motions. ($\circ$): $e = 0.65$; ($\fisheye$): $e = 0.47$; ($\circlehalfright$): $e = 0.30$; ($\bullet$): $e = 0.02$.

value of the impact velocity follows the same trend, with the largest offset case leading to the largest maximum impact velocities. V_{imax} decreases with e decreasing for any U_r, but not when reaching the smallest value $e = 0.20$ as it stays in this case at about the same value as for $e = 0.30$.

However maximum values of impact velocities are highly dependent on the post-processing and are certainly less accurate than their average value. The post-processing of the displacement is not perfect and can still in some cases lead to erroneous impact velocities; difficulties particularly arise when impact velocity is low, in close-to-grazing cases, where the condition of symmetry used on the boundary conditions during post-processing can lead to a slight overestimation of the impact velocity. For such cases, a different boundary condition, keeping constant the velocity to create the fictive points, might have given better results. But this method generates false large impact velocities and a threshold at which to change method, very difficult to set, would have been to be determined.

When reducing the gap between the cylinder and the stops, the impacting domain increases, but the average and maximum impact velocities can be strongly decreased. As the impact force depends a lot on the impact velocity, reducing the offset has the

same effect on the impact force.

The extreme position of the cylinder during impact varies by some few tenths of a millimetre at nearly each impact in every time series of displacement. On each time series, it is then difficult to determine exactly the stop position and so the distance the cylinder pushes the stop. Therefore, instead of obtaining the impact force using the stop stiffness and the displacement of the cylinder during contact, or by the means of the impulse of force involving the computation of the acceleration of the cylinder at moments of impact, the determination of impact forces is done using the change of momentum of the cylinder.

The mean force acting on the cylinder during an impact F_i can be expressed as the variation of momentum of the cylinder over the impact time:

$$F_i = \frac{\Delta(mV)}{\Delta t} \approx m\frac{V_i^+ - V_i^-}{t_i^+ - t_i^-} \tag{5.3.3}$$

where V_i^- and V_i^+ are the velocities of the cylinder respectively just before and after the impact, at the respective times t_i^- and t_i^+; V_i^- corresponds to the impact velocity noted earlier V_i. It is assumed here that the oscillating mass, including the added mass, does not vary during impact. As the contact time is small, it seems reasonable to assume that the variation of the added mass is very small. However as no expression can be used for determining the instantaneous added mass during impact, a rougher assumption is made on the value of the added mass during impact. It is here considered for every impact equal to its ideal value of 1.

Like the impact velocity and other parameters of the oscillation, the impact force F_i varies at nearly each impact. Its average value over each record, $\overline{F_i}$, plotted as function of U_r for all double-sided impacting motion and all gap settings in figure 5.14, exhibit about the same behaviour as that for the impact velocity.

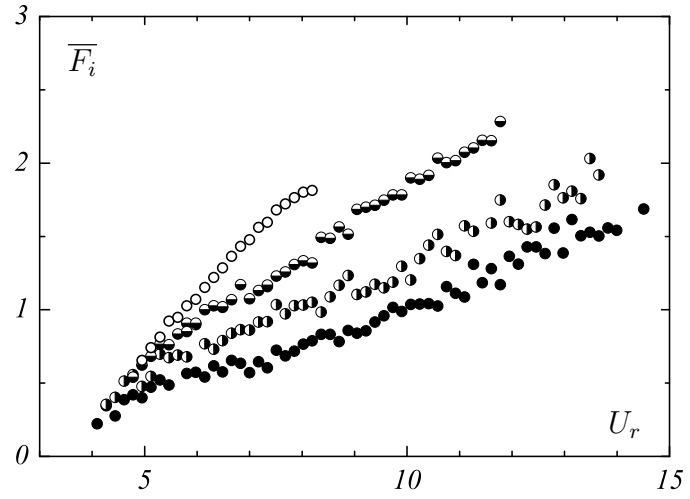

Figure 5.14: Average impact forces for double-sided impacting motions.
(○): $e = 0.65$; (◒): $e = 0.47$; (◑): $e = 0.30$; (●): $e = 0.20$.

The average impact force takes about the same low value for every offset in the beginning of their impacting domains, and it increases nearly linearly with U_r for every case of symmetric amplitude limitation. Its increase also clearly depends on the offset e, the largest offset leading to the largest impact forces. As impacting domains extend up to very high flow velocities for the three smallest values of e, at high U_r the case $e = 0.47$, close to the largest one at which impact can still occur, leads to the highest impact forces. Decrease of the offset induces then a decrease of the impact force, and this for any flow velocity.

These nearly linear increases of the average impact velocities and impact forces with U_r are clearly dependent on the offset e, and are certainly related to the nearly linear increase of the main oscillation frequency in each case. However the frequency response can be very complex when impact occurs. The strong non-linearity caused by the symmetric amplitude limitation of the cylinder can bring significant changes to the frequency distributions of the motion.

5.3.6 Modification of the frequency distributions

The frequency distributions obtained by Fast Fourier Transform of the time series of displacement reveals more features of the dynamics of the cylinder, and selected frequency ratio distributions of recorded data for cases with symmetric amplitude limitation are presented in figure 5.15.

In this figure, the first column corresponds to cases with linear restraints and the others to cases with symmetric amplitude limitation with the stop brought closer from the cylinder's rest position when going on the right. The reduced velocity increases when descending each column. This template is useful for comparing data in a glance for a fixed U_r and different offsets or for the same offset at different reduced velocities, and it will be used later in this work to present other types of data. As for these cases with symmetric amplitude limitation, the main frequency of the motion follows the Strouhal frequency in the impacting domain, and for the purpose of identifying harmonics here, each of these graphs presents the distribution of energy over the frequency normalised by the Strouhal frequency.

As seen in section 4.1.3, frequency ratio distributions obtained from the time series of displacement recorded in the case of linear restraints, presented here in the first column, reveal the nature of the motion in the different parts of the lock-in domain. In the first part of the initial branch, they contain two peaks revealing the semi-periodic nature of the motion. They contain only one narrow peak in the second part of the initial branch, and in the upper branch before the start of intermittency, revealing the periodic nature of the VIV in this domain. During the transition between upper and lower branches, two very close peaks appear, one at f^*_{lower} and one at f_{vs} revealing the intermittency between upper and lower modes of vibration. In the lower branch, frequency distributions contain only one distinct peak at f^*_{lower}, and the motion is periodic. In the desynchronisation regime, many peaks are present

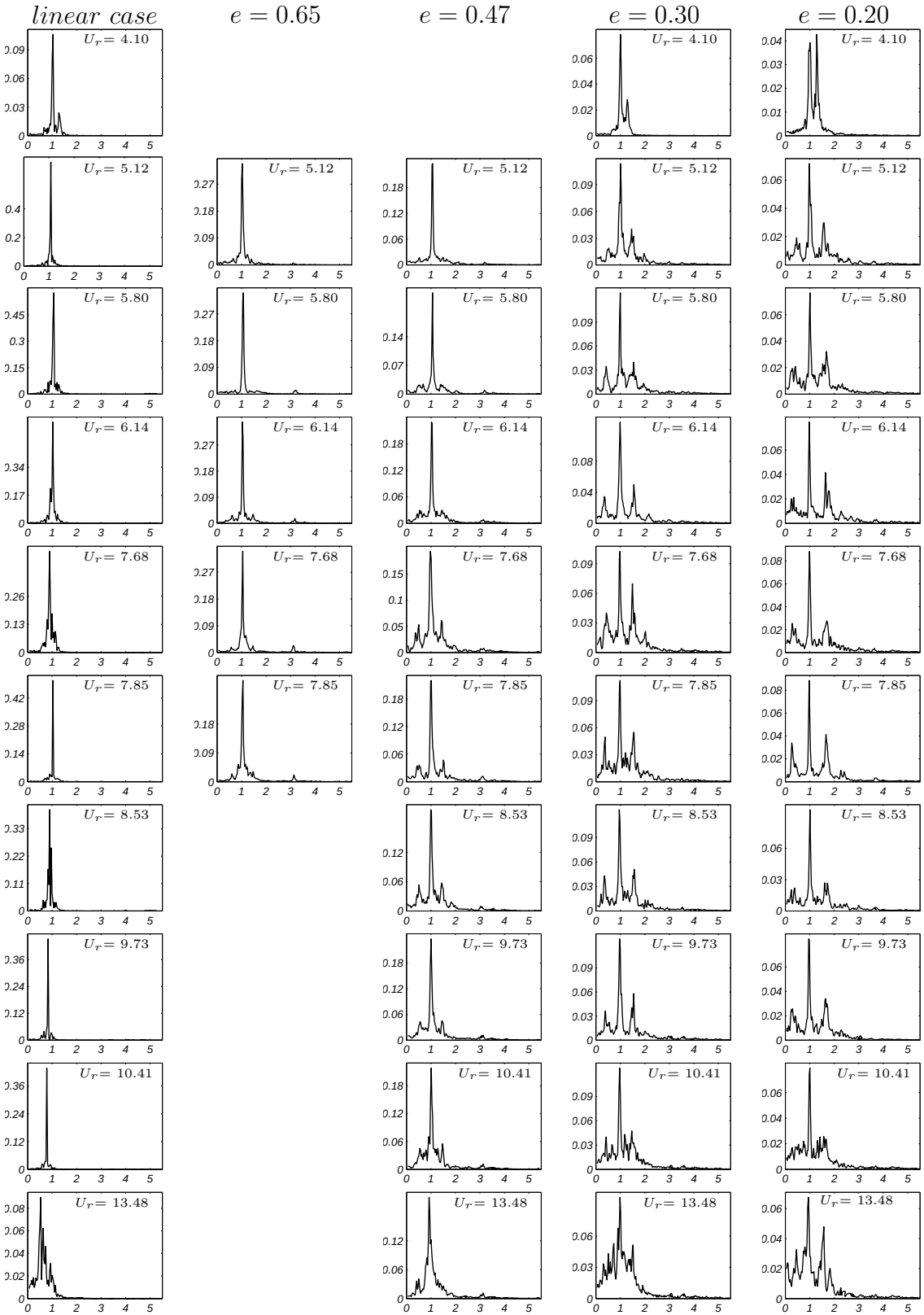

Figure 5.15: Reduced frequency ratio distributions for linear restraints and double-sided impacting motions. *The x-axis represents* f/f_{vs}.

in the frequency distributions including some at f_{vs}, or f_n, but those at f^*_{lower} and f_n often present also a large magnitude. This would suggest that the lower branch mode of oscillation is still sometimes present at large flow velocity in this experiment, even if very unstable, and that would explain the occurrence of rare high-amplitude cycles at large U_r.

When comparing graphs in line from left to right in this figure, corresponding to cases with linear restraints and cases with symmetric amplitude limitation with the offset reducing, the perturbation of the frequency ratio distributions induced by the presence of the stops is clear. For any reduced velocity apart from the largest, the magnitude of the main peak decreases when limiting the amplitude of the cylinder with a large offset and decreases even more when decreasing further the offset. The frequency distributions become more complex with subharmonics and harmonics appearing and noise increasing; energy is distributed over wider ranges of frequencies.

For e=0.65, frequency ratio distributions still present a distinctively organised structure. They always contain a distinctive main narrow peak at the oscillation frequency f, close to f_{vs}, i.e. at $f/f_{vs} = 1$ as mentioned above. They also contain subharmonics and harmonics of this main frequency, as peaks appear at 0.5, 1.5 and even 3 times the oscillation frequency. As U_r is increased the magnitude of the main peak stays about the same while the magnitudes of the harmonics increase.

Frequency ratio distributions for $e = 0.47$ also display this same structure with one main peak, its strong harmonics at 0.5 and 1.5, and some higher harmonics. For any flow velocity, the magnitude of the main peak is decreased compared to the case $e = 0.65$, and those of the subharmonics and harmonics are increased. Peaks at 0.5 and 1.5 times f, whose magnitudes increase with U_r at the beginning of the impacting domain, are more evident.

For most of impacting motions with both offset values $e = 0.30$ and $e = 0.20$,

frequency distributions exhibit still the same structure with one main peak at $f \approx f_{vs}$ and strong subharmonics and harmonics at 0.5 and 1.5 times f, but they are much more noisy as energy is distributed over a wide range of frequencies. Magnitudes of the subharmonics and harmonics are again increased compared to the case $e = 0.47$ for any U_r. Some other harmonics at 2, 2.5, 3 and even 3.5 times f can also be observed in some frequency distributions. In both cases, frequency distributions are more complex for large flow velocities; the peaks become wider as energy is very widely distributed over frequencies.

The input signal of the system here is the lift force on the cylinder, which should have a frequency close to the vortex shedding frequency. In the double-sided impacting cases with a large offset, the cylinder′s energy distribution exhibits a dominant main peak at this frequency, and little energy is transferred to harmonics. The system in these cases seems to respond nearly linearly to the excitation. However when the motion is limited on both sides with a smaller gap, strong sub-harmonics at f/n and harmonics at nf, with n integer, appear. And that is a precursor sign for the appearance of chaos [38].

To investigate more deeply, qualitatively and quantitatively, the effect of the symmetric amplitude limitation of a cylinder undergoing VIV on its dynamics, non-linear dynamics tools can be used, as they already proved themselves useful in the study of vibrating systems subject to non-linear compliances.

5.3.7 Changes in the dynamics of the cylinder

Equation of motion 4.1.1 can be rewritten as a system of first order differential equations:

$$\begin{cases} \dot{y} = x \\ \dot{x} = (F(t) - cx - ky)/m \end{cases} \tag{5.3.4}$$

where in the present case of non-linear structural restraints, the stiffness of the system is a piecewise function of the cylinder's displacement. This system is non-autonomous as the time is explicitly present in the equations. The presence of the time variable in the equations means that part of the physical process is not totally described in terms of forces. Indeed no expression for the oscillating force F resulting from the oscillating pressure field around the cylinder during vortex shedding can be given. It is therefore just expressed as depending on the time t, which appears as one of the dynamic variables of the system. The usual approach of this type of system is to use a phase space of dimension $\mathbb{R}^{2+1} = \mathbb{R}^2 \times \mathbb{S}$, the topological product of $\mathbb{R}^2(x, y)$ by a circular space associated to time $t^* = t \bmod(T)$ where T is the period of the forcing. In this case, the system 5.3.4 can be expressed as:

$$\begin{cases} \dot{y} = x \\ \dot{x} = (F(t) - cx - ky)/m \\ \dot{t} = 1 \end{cases} \tag{5.3.5}$$

This approach has the feature of supposing that the evolution of the system is synchronised with the external constraint, which is not necessarily true [81]. Another solution would be to describe the external constraint as a system of differential equations. If $F(t)$ could be expressed in the form of $sin(\omega t + \phi)$, as it can be for impact oscillators, the system 5.3.4 could be expressed as:

$$\begin{cases} \dot{y} = x \\ \dot{x} = (u - cx - ky)/m \\ \dot{u} = v \\ \dot{v} = -\omega^2 u \end{cases} \tag{5.3.6}$$

as $u = sin(\omega t + \phi)$ is solution of $\ddot{u} + \omega^2 u = 0$. However the phase space associated would then be of dimension 4, which results in a much more difficult analysis as, as Poincaré stated, "*A man who devoted his life to it could perhaps succeed in picturing himself the fourth dimension*" [82].

In the analysis of the experimental data of a cylinder subject to free vortex-induced vibrations, and supported by linear or non-linear restraints, the external forcing cannot be analytically expressed and its period, if periodic, is a priori not known. In the present system the time variable can not be withdrawn from the system as no expression can be used for the hydrodynamic forcing. The phase space to use for the analysis of the dynamics of the cylinder at one value of flow velocity is then $\mathbb{R}^3(y, \dot{y}, t)$.

For the analysis of the response of the system over a range of flow velocity, one can consider the hydrodynamic force F as depending on the time t but also on the flow velocity, which it is obviously but in such a complex way that one can only mention it using $F(t, U)$. This adds a dynamic variable to the system and the phase space for the analysis of the response of the cylinder to VIV over a range of flow velocity becomes $\mathbb{R}^4(y, \dot{y}, t, U)$ or $\mathbb{R}^4(y, \dot{y}, t, U_r)$.

The recorded time series of displacement are projections of the trajectory of the system evolving for a fixed flow velocity in the phase space $\mathbb{R}^3(y, \dot{y}, t)$, on the plane (y, t). The determination of the cylinder's instantaneous velocity $\dot{y}$ by derivation of its position y with respect to time t allows one to use other projections of the attractor to investigate the dynamics of the motion. Phase portraits for example are projections of the trajectory on the plane $(y, \dot{y})$. They are useful in determining the nature of a motion as the orbit formed by a periodic motion is a closed curve repeating itself, whereas for chaotic motions the orbit does never close or repeat and then fills a large surface of the phase space projection.

5.3.7.1 Identification of characteristic motions

Phase portraits for double-sided impacting motions obtained from the second set of experiments are described in order to gain an insight into the nature of the motion of the cylinder, and some are presented in figure 5.16 for the different gap settings at

some chosen values of U_r, using the template already used. Data plotted in each graph of figure 5.16 are the instantaneous velocity of the cylinder in m/s reduced by the characteristic velocity U_c against its non-dimensional position y. All graphs are presented here with an adapted scale for each motion to fill the whole window, in order to compare the nature of the motions without accounting for their amplitude. Each of these graphs presents the recorded trajectory described by the cylinder, in the clockwise direction, in the plane $(y, \dot{y})$.

Looking at the phase portraits corresponding to the case with linear restraints presented in the first column of figure 5.16 allows one to become more familiar with this representation of the trajectory, and to identify phase portraits corresponding to different natures of motion. As seen already, the cylinder, when subject to linear restraints, exhibits under VIV semi-periodic, periodic, intermittent and chaotic motions depending on the reduced velocity.

When the motion is a pure periodic oscillation, as existing in the beginning of the upper branch at $U_r = 4.95$, the trajectory follows an oval-shaped cycle in the plane $(y, \dot{y})$. If it contains some modulation, as for $U_r = 5.80$ or $U_r = 10.41$, the outline forming the oval shape widens.

For semi-periodic oscillations like those occurring in the first part of the initial branch, for example at $U_r = 4.10$, the phase portrait displays many oscillation cycles with varying amplitude, and the ovaloid area between the smallest and biggest oscillation cycles is ultimately filled by intermediate cycles, as these latter are experimentally not perfectly identical.

As illustrated by the phase portraits for $U_r = 7.68$ or 8.53, intermittent motions presenting two periodic limit cycles display only a large oval-shaped band as transitions between these modes fills the phase-space they enclose.

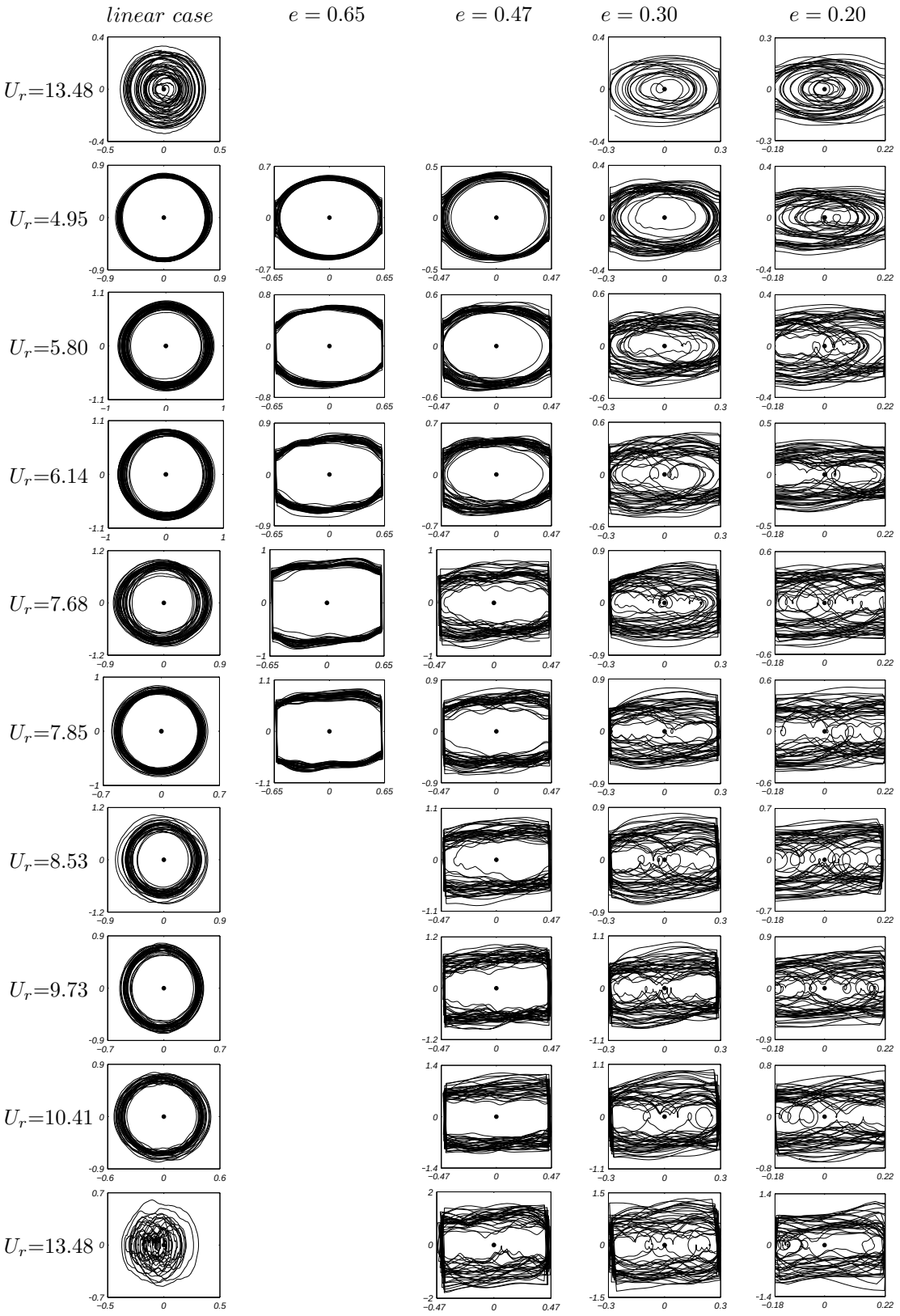

Figure 5.16: Phase portraits for linear restraints and double-sided impacting motions.

It can be noted that, as the temporal aspect of the evolution of the system is lost in these projections of the attractor, they are not sufficient to distinguish for example intermittent motions as occurring for $U_r = 7.68$ and 8.53 from nearly periodic motions with high amplitude modulation as occurring for $U_r = 10.41$.

After desynchronisation, the motion does not present any apparent structure; its trajectory ultimately fills the phase space enclosed by its widest cycle, as for $U_r = 13.48$, which is a strong sign of chaotic motion.

For double-sided impacting cases, the post-processing previously described and applied to the recorded time series of displacement results in a good restitution of the rapid change of sign of the velocity occurring during an impact. But as the dynamics of the cylinder are not well known during impact due to the high local SNR, moments where the cylinder is in contact with the stops are not displayed on these graphs. This representation also allows one to better judge the velocities before and after impact.

For the largest offset $e = 0.65$, when impact starts to occur at $U_r = 4.95$, the cylinder impacts on both stops at nearly each oscillation cycle. At this flow velocity, it happens that the cylinder sometimes does not reach one of the stops but gets close to it, or grazes the stops. For larger flow velocities, the cylinder impacts at every cycle on both stops, describing a stable symmetric *1-1-1* motion; the system does not seem much affected by the amplitude limitation as its nature is still periodic, as it was in the upper branch without the stops, and this for all reduced velocities. However, phase portraits lose all information related to the variable time t, and one has to remember that the frequency of oscillation has changed compared to the linear case.

When the symmetric offset is reduced to $e = 0.47$, the contact on the stops has more effect on the dynamics of the cylinder. At the lowest reduced velocity where contact occurs, $U_r = 4.95$, the cylinder reaches the stops most of the time but sometimes after an impact it describes some oscillation cycles without impact, before reaching a stop

again. For larger U_r, the cylinder impacts most of the time at every cycle on both stops, describing a *1-1-1* motion. This motion nearly always presents some modulation as borders of the phase portraits are wider than for $e = 0.65$, and this modulation seems to increase with U_r.

With a smaller offset value, motions seem very disorganised and phase portraits for $e = 0.30$ and $e = 0.20$ are much more complex as the trajectory fills most of the phase space projection for any reduced velocity. Lines nearly always present on their outside going from one stop to the other correspond to *1-1-1* motions with high velocity. Out-of-phase oscillations represented by the trajectory marking small circles around $\dot{y} = 0$ and any value of displacement also occur often. At high U_r quick double bounces on a same stop can also be observed. One occurring on the upper stop is clearly visible in the phase portrait for $e = 0.20$ and $U_r = 8.53$. The strong symmetric limitation of the oscillation amplitude introduced by the stops in these cases seems to strongly change the dynamics of the motion. In these phase portraits, no pattern is recognisable, the trajectory does not seem to repeat itself but fills most of the phase space projection enclosed by its widest cycle. This would confirm the chaotic nature of the motion in these cases, already suggested by the wide distribution of energy in frequency in these cases.

With the observation of phase portraits for double-sided impacting cases, several types of motion have been observed.

Symmetric *1-1-1* cycles seems stable for large offset values over most of the impacting domain. An example of a typical *1-1-1* cycle occurring at $U_r = 5.80$ for $e = 0.65$ is given in figure 5.17(a). At low flow velocities in the impacting domain, the cylinder sometimes presents some characteristic periodic pattern. After an impact on a stop, the amplitude of vibration of the cylinder can be strongly decreased such as the cylinder describes then some oscillation cycles without impact, during which its amplitude of vibration increases until the cylinder impacts on a stop again.

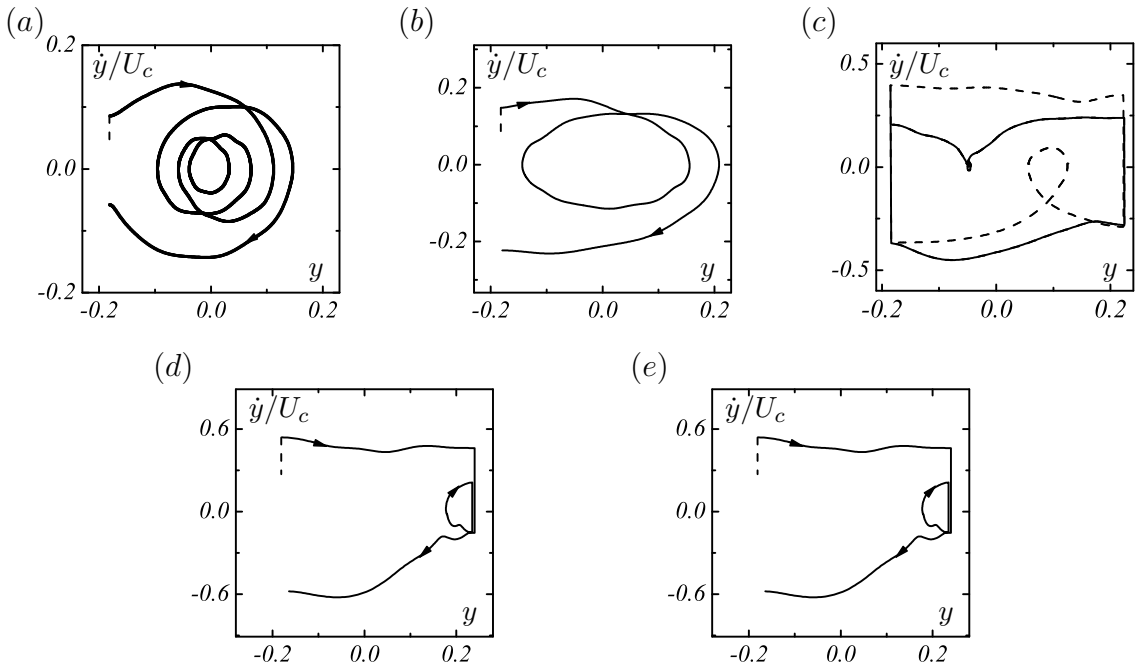

Figure 5.17: Phase portraits of typical characteristic motions. (a): symmetric *1-1-1* cycle; (b): *4-0-1* cycle; (c): *2-0-1*; (d): Pair of antisymmetric *1-1-1* cycles; (e): double bounce on upper stop.

Experimental examples of such motion are given in figure 5.17(b) and 5.17(c) for $e = 0.20$. The cycle presented in figure 5.17(b) extracted from the time series for $e = 0.20$ and $U_r = 4.44$ shows the cylinder describing after an impact on the lower stop four oscillation cycles without impact before reaching the lower stop again; this is a *4-0-1* motion. In figure 5.17(c) for the same offset value and $U_r = 4.78$, the cylinder describes only two oscillation cycles before impacting on the lower stop again; this is a *2-0-1* cycle. These *k-1-0* or *k-0-1* motions will be given more attention in the next section.

In cases with small offsets, the dynamics of the cylinder are often more complex and other characteristic motions can be observed, as those in which the cylinder oscillates once after an impact, before impacting on the other stop. Motions similar as those, appearing in the different phase portraits as small circles around some value of

displacement, have also been observed in the case of a harmonically excited two-degree-of-freedom system with symmetric amplitude limitation. Luo & Xie observe in [66] a pair of antisymmetric cycles, after pitchfork bifurcation of the symmetric *1-1-1* cycle. In their system, the impacting mass stabilises on one of these antisymmetric period-1 double-impact motion or the other depending on the initial conditions. In the experimental tests conducted here in which the forcing term is due to the shedding of vortices by the cylinder, both cycles are observed simultaneously at the same flow velocity. The phase portrait presented in figure 5.17(d) displays the trajectory of the cylinder for e= 0.20 and $U_r = 7.51$ between $t = 2.80$ s and $t = 4.5$ s; the cylinder describes both antisymmetric *1-1-1* cycles, the first one represented with a solid line, and the second just after, represented with a dashed line.

Phases with two quick successive bounces on the same stop occur also for cases with a small offset and at high reduced velocity. A phase portrait of such a cycle, recorded during the test for $e = 0.20$ and $U_r = 10.92$, is presented in figure 5.17(e). These motions involved difficulties during post-processing, mainly because of the short time of oscillation between impacts; these were solved by adjusting individually the threshold for impact detection for each of these time series. Cycles with phases of quick bounces on the same stop, as the *2-2-3* or *2-2-4* antisymmetric cycles presented in [66], are also observed for a harmonically-excited two-degree-of-freedom system with symmetric amplitude limitation.

Because of the projection used, one other kind of motion cannot be observed using phase portraits. Chattering of the cylinder on a stop, for which the system's trajectory stays at about the same point in the plane $(y, \dot{y})$, also does occur in some conditions. Measurements of times of impact ${t_i}^-$ and ${t_i}^+$ can be used to detect the occurrence of chattering motions. Average and maximum values of times of contact are recorded for each time series of displacement but chattering is only observed in the case of double-sided impacting motions with a small offset value, and at high flow

velocity, i.e. when the dynamics are strongly perturbed by the stops.

Figure 5.18 presents the average and maximum values of the time of contact for this case of structural restraints as functions of the reduced velocity. The average value of the contact time slightly varies with the flow velocity but generally stays at around 0.05 s for this case of structural restraints. Maximum contact time is measured at about twice its average value for $U_r < 11$, but for larger flow velocities maximum contact time is about four or five times larger than its average value, revealing the occurrence of chattering motions. Time series of displacement of the cylinder do exhibit in these cases chattering motions during which the cylinder impacts many times on a stop in a short time. In figure 5.19, presenting the time series of displacement for $e = 0.20$ and

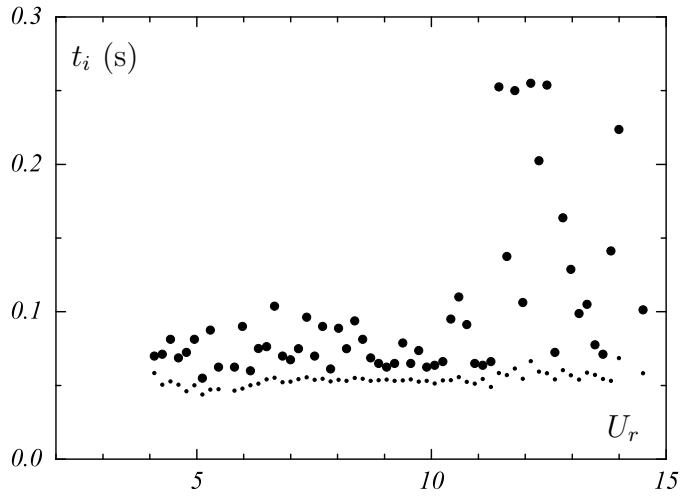

Figure 5.18: Maximum (•) and average (·) contact times for double-sided impacting motions with $e = 0.20$. *High values of t_i correspond to chattering motions.*

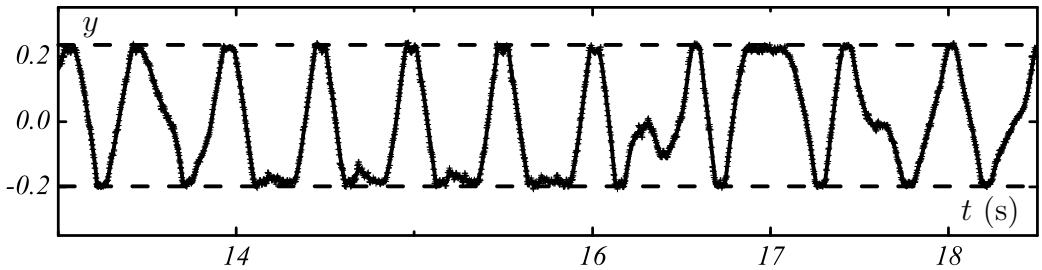

Figure 5.19: Time series of displacement for double-sided impacting motion for $e = 0.20$ and $U_r = 11.95$. *Double bounces on the lower stop, as well as chattering on the upper stop, occur when the dynamics are strongly perturbed by the stops.*

$U_r = 11.95$, the cylinder clearly marks three successive double bounces on the lower stop after $t = 14$ s. Chatter occurs on the upper stop at $t \approx 17$ s. It is unclear however whether the cylinder stays in contact with the lower stop at $t \approx 15.6$ s.

In order to investigate more deeply the dynamics of the system, further analysis is conducted to identify the nature of the motion of the cylinder in the different cases of amplitude limitation all over their respective impacting domain.

5.3.7.2 Stabilisation and stability of a *1-1-1* cycle

Bifurcation diagrams of dynamic variables of a system can be used to study its dynamics. Interesting bifurcation diagrams in the present system are those made by the projection of all upper or lower peaks of oscillation on the plane (y, U_r). These points are intersections of the trajectory with the Poincaré section $(y, \dot{y} = 0, t, U_r)$ when crossing from the domain $\dot{y} > 0$ to $\dot{y} < 0$ or $\dot{y} < 0$ to $\dot{y} > 0$. Such a bifurcation diagram gives information on the nature of the motion at a specific value of a varying parameter, here the flow velocity through U_r, but also on its bifurcations with variations of the reduced velocity.

In the case of oscillation with impacts on symmetric stops, bifurcation diagrams of a dynamic variable concerning both upper and lower stops are needed to distinguish asymmetric motions having different frequencies of contacts on each stop. However, as seen with the phase portraits of double-sided impacting motions presented in figure 5.16, motions recorded in this case where the cylinder is driven by vortex shedding are all nearly symmetric, with impacts occurring at about the same frequency on both stops. Sequences of consecutive impacts on the same stop, as double bounces on the same stop or short phases of chatter, occur sometimes with a small offset for high reduced velocities. But even in these cases, consecutive impacts on the same stop do occur in a symmetric way on both stops.

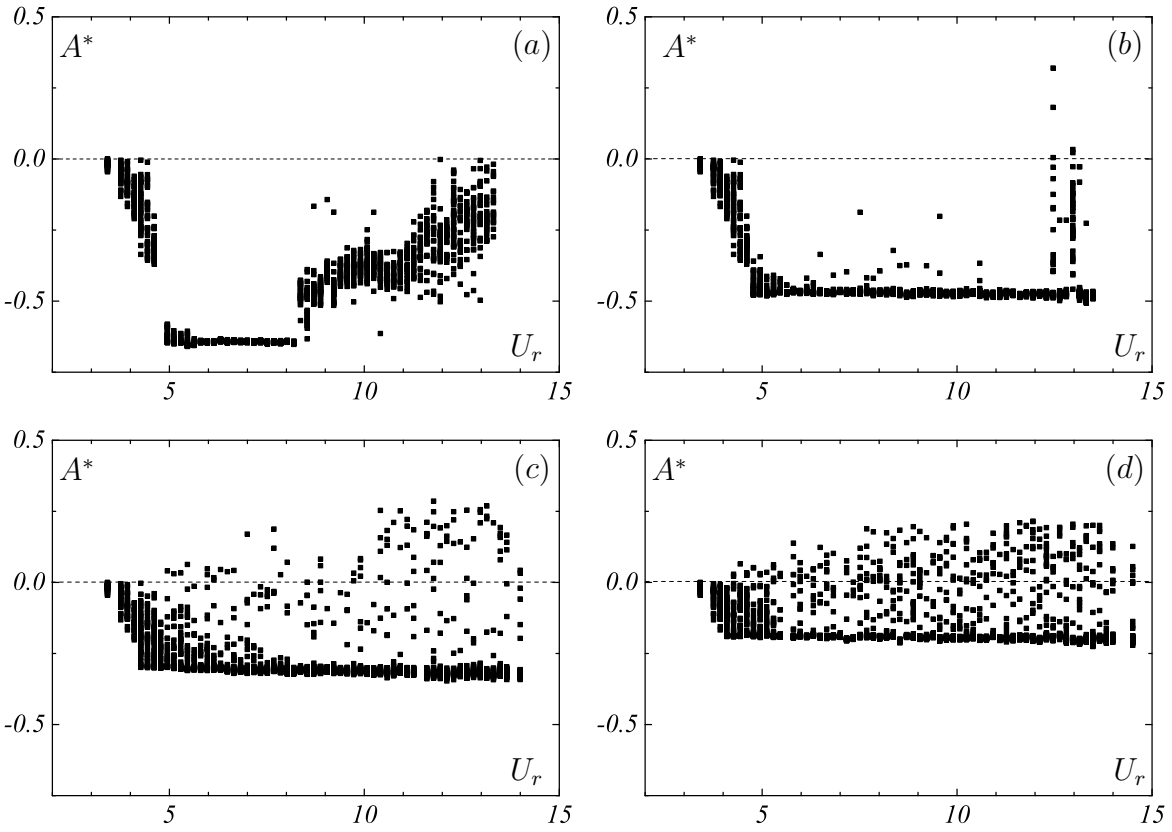

Figure 5.20: Bifurcation diagram of lower peak excursions for double-sided impacting motions. (a): $e = 0.65$; (b): $e = 0.47$; (c): $e = 0.30$; (d): $e = 0.20$.

The dynamics of the system can therefore be presented using only one of the two bifurcation diagrams of peak excursions. As lower peaks excursions will be used in the case of asymmetric amplitude limitation presented later in this work, bifurcation diagrams of lower peak excursions also are presented here in figure 5.20 for the different cases of symmetric amplitude limitation investigated.

In this figure, and to clearly identify impacting cases, data are plotted with crosses when impact does not occur, and with squares when it does. Bifurcation diagram of lower peak excursions for the case with linear restraints is presented for comparison, but only later in figure 6.7(a), at page 143.

When the stops are symmetrically placed at $e = 0.65$, the bifurcation diagram presented for this case in figure 5.20(a) exhibits over most of the respective impacting domain nearly only points at the stop position, meaning that the cylinder reaches the stop at every cycle, therefore describing a stable *1-1-1* motion.

As shown in figure 5.20(b), when the offset is reduced to $e = 0.47$, points close to the stop position indicating an oscillation cycle without contact are present also at the beginning of the impact domain, and as the flow velocity is increased they get closer to the stop and disappear totally at $U_r \approx 6$. For $6 < U_r < 13$, lower peak excursions are only present at the stop position indicating the stability of a *1-1-1* motion over this whole window. The few points out of the stop position in this domain are certainly due to experimental disturbances. At large flow velocities, points spread over the domain $A^* < 0$ indicate the start of desynchronisation, but the *1-1-1* is still quite stable as present at the largest flow velocity $U_r = 13.82$.

When reducing the offset to $e = 0.30$, the same structure is still appearing in the bifurcation diagram in figure 5.20(c), but points at the beginning of the impacting domain are spread over the whole domain $0 > A^* > -e$. In this case, points indicating a lower peak of amplitude are much more spread over the projection of the attractor, as some lower peaks of oscillation appear even at amplitudes greater than zero, indicating a stronger perturbation of the system. Amongst them, some indicate the occurrence of antisymmetric *1-1-1* cycles, and for $U_r > 10.41$ those close to $A^* = +e$ reveal quick double bounces on the upper stop.

When reducing again the offset to $e = 0.20$, the perturbation of the system seems even stronger as lower peaks of oscillation are very widely spread over the whole domain $-e > A^* > e$ in figure 5.20(d). Points widely spread over the domain $A^* < 0$ at the beginning of the impacting domain disappear more abruptly than for larger offset values at $U_r \approx 6$. Points close to $A^* = e$ revealing quick double bounces on the upper stop, as presented in figure 5.17(e), appear from a smaller reduced velocity

than with $e = 0.30$. For $U_r > 10$, some of these points close to $A^* = e$ reveal also chatter on the upper stop.

With the phase portraits and the bifurcation diagrams presented, the dynamics of the cylinder at the beginning of the impacting domain can be further investigated.

At the beginning of the impacting domains of the bifurcation diagrams for $e = 0.65$ and $e = 0.47$, some points appear close to the stop position indicating an oscillation cycle without contact, and disappear as they get closer to the stop position with U_r increasing. Similar observations can be made for $e = 0.30$ and $e = 0.20$, but in these cases, these points are much more spread over the whole domain $A^* < 0$.

These points correspond to motions in which the cylinder's amplitude of vibration is decreased after an impact, and it increases back during some cycles without impact, before the cylinder reaches a stop again. Such *k-1-0* or *k-0-1* motions were observed with the phase portraits presented in figure 5.17(b) and (c). In this sort of motion, the contact with a stop can be seen as sending back the system into the attraction basin of the attractor existing with linear restraints, and the rest position of the cylinder, singular point of the system, appears to act as a source here.

During experimental tests at low U_r, k can widely vary as, for $e = 0.20$ and $U_r = 4.10$ for example, k varies between 2 and 10. The bifurcation diagrams show these points getting closer from the stop position as U_r is increased and disappearing after some value of U_r. This shows that, as U_r is increased, the contact with the stop sends the trajectory back into the attraction basin closer from the stop position, and therefore fewer cycles of amplitude growth are, in average, needed for the cylinder to impact on a stop again. At some value of flow velocity, the contact with a stop can not any more send back the system in the attraction basin of the original attractor; after impact, the cylinder still presents an amplitude high enough to reach the opposite stop straight away, and the symmetric *1-1-1* motion becomes stable. This happens at

different flow velocities depending on e.

These windows in which *k-0-1* and *k-1-0* cycles occur, and over which the average value of k decreases, finish with the stabilisation of a *1-1-1* cycle, more stable with large offset. These windows are similar to the succession of grazing bifurcations occurring in mechanical impacting systems at the start of the impacting domain. It is believed that the same phenomenon occurs here, i.e. that at the beginning of the impacting domain, the system undergoes a succession of subcritical grazing bifurcations, which finishes with the stabilisation of the *1-1-1* cycle. In impacting mechanical systems grazing bifurcations usually produce a large number of unstable periodic orbits [62], and this clearly has importance for the global dynamics of the system. As for the one-degree-of-freedom impacting system studied in [64], the system is in such a window chaotic, because the intensity and the instant of additional impact are unpredictable.

The bifurcation diagrams show an increase of the dispersion of lower peaks of oscillation over the domain $-e > A^* > e$ when e decreases, which suggest a perturbation of the system increasing with e decreasing. This qualitative observation can be verified using a quantitative measurement of the nature of the motion, the Lyapunov exponent, introduced in section 3.1.4.

5.3.7.3 Existence of chaotic motions

As seen in section 3.1.5, the determination of the main Lyapunov exponent of a non-linear system from its experimental time series is very difficult as developed methods depend on many parameters, which have to be carefully set by the experimenter. Estimation of the Lyapunov exponent from the experimental time series of displacement recorded in this project for different cases of structural restraints and different flow velocities has been undertaken using both the method of

Wolf et al. [50] and that of Kantz & Schreiber [47].

In both methods, time delay τ and embedding dimension m_e are very important for the attractor reconstruction, and the neighbourhood size ϵ influences greatly the determination of the Lyapunov exponent.

Estimates of the Lyapunov exponent obtained with the method of Wolf & Al. applied to an experimental time series proved to highly depend on the time delay τ and the dimension m_e for the attractor reconstruction, but also on the time used for the evolution of found neighbours. As this method follows the trajectory of the system, the number of measurements of the divergence of neighbour points along the trajectory is limited by the length of the record. Tests also show that the estimate of the Lyapunov exponent is for one time series dependent on the amplitude of the motion, which becomes a problem when aiming to compare the nature of time series of different amplitudes. Non-dimensionalisation the time series using the maximum of amplitude, its r.m.s value or its dispersion did not solve this problem and results obtained with this algorithm applied to the experimentally-recorded time series did not present any specific trend, or any information on the dynamics of the system. Recorded time series could be too short in time, but, as mentioned in [47], this algorithm is not very robust and one can easily obtain erroneous estimates of the Lyapunov exponent.

Information about the dynamics of the cylinder has however been obtained when using the method developed by Kantz & Schreiber [47]. When using their algorithm on a time series of displacement, the experimenter first has to test for exponential divergence by measuring the average growth of the distance between nearby trajectories. He then has to judge if exponential divergence, and therefore chaos, occurs, then, if this is the case, measurement of the exponential rate of divergence of trajectories can be conducted. The obtained average growth in distances depends strongly on the embedding dimension m_e and on the neighbourhood size ϵ, and

several tests with different values of these parameters are needed to test the robustness of the exponential growth and judge the rightfulness of the calculation of a Lyapunov exponent. Estimation of value of the Lyapunov exponent is left to the appreciation of the investigator, and experience is needed. It is mentioned in [47] that the determination of such characteristics is sometimes an art.

However more than four hundred experimental tests have been conducted in this project, for which time series have been recorded, and from which measurement of the Lyapunov exponent is to be conducted. Long and individual verification first of the exponential aspect of the average growth of distance, and determination of the Lyapunov exponent through multiple tests with embedding dimension and neighbourhood size varying to judge the convergence of the result, would have been too long to conduct for such a large number of tests.

Average growth of the distance between neighbours is therefore computed for every time series, from which an exponential growth rate λ_K is measured, even if the exponential aspect of the growth, or its robustness are not tested against variations of the embedding dimension and the neighbourhood size. The measurement obtained does not represent an estimate of the Lyapunov exponent of the system for the cases in which exponential divergence does not occur. It is nevertheless in these cases a measure of the divergence of close experimental trajectories and reveals the aptitude of the system to stabilise on a limit cycle in response to experimental disturbances. For the cases in which exponential divergence takes place, this measurement λ_K is an estimate of the Lyapunov exponent of the system λ. Error on this measurement can not be known, as λ is not known. This algorithm does not give an exact value when applied to numerically-generated long and noiseless time series issued from a two-dimensional system, and the error may also be increased when applying this algorithm to experimentally-recorded, noisy, and relatively short time series issued from a non-linear system of larger-dimension such as that considered here.

For every time series, the attractor is reconstructed using the embedding dimension m_e set to the value of 3 as this algorithm has been shown to give good estimates of the Lyapunov exponent of chaotic systems even for m_e smaller than $2N+1$, and the time delay τ is chosen equal to the first zero of the autocorrelation function, i.e. the time where it decays to $1/e$. The use of a box-assisted method to find neighbour points allows to control the number of neighbours by varying the neighbourhood size ϵ, and to adjust the neighbourhood size to obtain a reasonable number of neighbours. ϵ is set for each time series in such a way as to obtain a maximum of 50 neighbours for every point considered.

The Lyapunov exponent carries the units of an inverse time, and characterizes the typical time scale for the divergence or convergence of trajectories, and so, in order to compare the chaotic aspect of the time series recorded with the same conditions of structural restraints but at different flow velocities, the value of its estimate is normalised using the vortex shedding frequency.

In order to judge the influence of the structural non-linearities on the nature of the system, estimation of the growth rate of the separation between neighbour points is first conducted with this algorithm for the case of linear restraints, from every time series of displacement recorded in this case at different flow velocities. It is already known that the system is not chaotic in these conditions over most of the impacting domain; this measurement cannot be considered as a Lyapunov exponent of the system, as chaos, implying exponential growth of the separation, does certainly not occur in these cases. However, these results, presented in figure 5.21, make it possible to judge the accuracy of the algorithm used for the estimation of the Lyapunov exponent when applied to experimental time series, of which the nature is already known. At the lowest flow velocity investigated, before the lock-in domain, VIV are desynchronised and the motion is disorganised, and λ_K is positive. With the flow velocity increased, some structure appears in the motion as it is semi-periodic in the

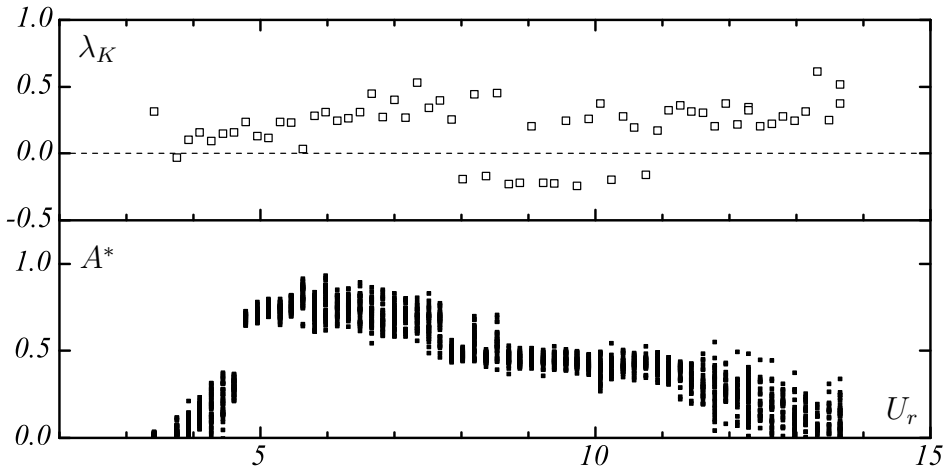

Figure 5.21: Lyapunov exponents in the case of linear structural restraints.

first part of the initial branch. This is revealed in the results as λ_K decreasing, here to a negative value for $U_r = 3.75$. λ_K becomes positive at the next flow velocity investigated, and increases slowly then up to the end of the upper branch of vibration. Some of the motions exhibited by the cylinder over this range of flow velocity are however known to be periodic, and some of these, particularly at the beginning of the upper branch, even present a low amplitude modulation. The Lyapunov exponent for these cases was therefore expected to be negative. However as the system is periodic in these cases, growth of the separation between neighbour points may strongly not be exponential, and measuring an exponential growth rate certainly does not makes sense in these cases. Noise in the time series could be increasing the result given by the algorithm, but these measurements nevertheless represent some measurement of the chaotic nature of the motion as they increase when the dynamics of the cylinder become more complex, over all the upper branch of oscillation when increasing U_r.

Encouragingly, λ_K takes negative values over most of the lower branch of oscillation, where the cylinder describes periodic motions. Values for $U_r = 8.19$ and 8.53 are positive revealing, as reminded by the bifurcation diagram of peak excursions also plotted in figure 5.21, the intermittent nature of the motion in these cases still belonging to the transition between upper and lower modes. λ_k is positive for some

other flow velocities in this range, for which it is expected to be negative, and these values mainly reveal the difficulty in conducting such measurement.

For large flow velocities corresponding to the desynchronisation regime, λ_K is positive, and about constant, increasing only for the largest flow velocities.

The trend of these measurements of the average growth rate of the separation between neighbour points, in an exponential form, conducted with the method developed by Kantz & Schreiber is consistent with the nature of the motions observed with linear restraints. Values of λ_K certainly do not always represent the Lyapunov exponent of the system, but they are a form of measurement of the chaotic nature of the system, of its predictability. They also provide a basis for the interpretation of results obtained in the cases of non-linear structural restraints, allowing to obtain some information on the perturbation of the dynamics of the system implied by the presence of stops.

With the same algorithm using the same values for the different parameters, estimation of the exponential growth rate of the separation between neighbours is performed on the time series of displacement recorded in the different cases of symmetric amplitude limitation, all over their respective impacting domains. Results obtained in the different conditions of structural restraints investigated are presented in figure 5.22. A general increase of λ_K is observed at any flow velocity when limiting the motion of the cylinder. However when amplitude limitation is weak, as for $e = 0.65$ and $U_r = 4.95$, r_K is just slightly larger than its value in the linear case, revealing as previously seen the weak perturbation of the cylinder's response in this case. For low flow velocities, λ_k increases with the offset decreasing, indicating the increased perturbation of the dynamics with small offsets. For all offset values, λ_K increases with U_r at the beginning of the impacting domain. For $e = 0.65$, it seems to reach a plateau for $U_r \approx 7$, which is about the start of the upper⇌lower transition in the case of linear restraints, and it increases back for the last values of flow velocity

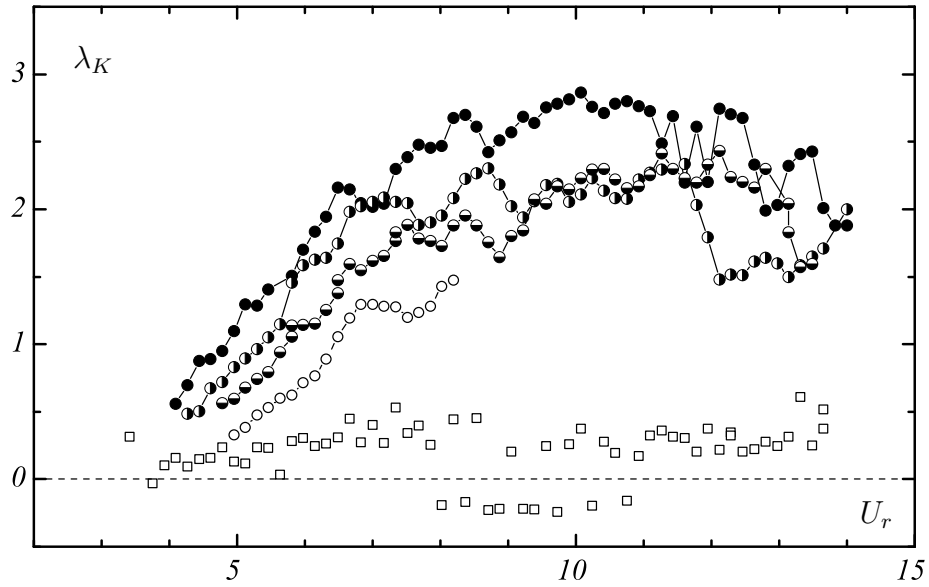

Figure 5.22: Lyapunov exponent from the linear case (□) and for double-sided impacting motions. (○): $e = 0.65$; (◒): $e = 0.47$; (◑): $e = 0.30$; (●): $e = 0.20$.

where impact still occurs in this case. At these flow velocities, impact occurs in a very unpredictable breathing-type way, i.e. in apparently randomly long phases of successive impacts between phases of non-impacting oscillations.

For smaller offset values, λ_K increases with U_r for low flow velocities, and then seems to reach a plateau, at a value apparently depending on the offset even if values are very close for $e = 0.47$ and $e = 0.30$ between $U_r = 9$ and $U_r = 11.5$. λ_K decreases then for every case for the largest flow velocity at the end of the impacting domain when desynchronisation seem to occur.

These measurements of the exponential growth rate of the distance between neighbours quantify the predictability of the system, as results obtained for the case of linear restraints are consistent with the nature of the motion in this case. Even if they are not very accurate estimates of the Lyapunov exponent of the system, values of λ_k do reveal the more complex nature of the motion in the case of symmetric amplitude limitation, with its unpredictability increasing with e decreasing, and U_r

increasing. Large values obtained do also certainly reveal the chaotic nature of the motion in the corresponding cases.

5.3.8 Modification of the vortex wake

As seen in section 4.1.3, flow visualisations have been conducted in the case with linear restraints at some specific values of U_r to observe the different modes of vortex formation that exist in the 2S and the two 2P modes.

Flow visualisations have also been conducted for some tests of VIV with symmetric amplitude limitation, at some specific values of flow velocity and with different offsets. Observation of shedding and evolution of the vortices present in the wake of the structure provides an insight on the fluid-structure interaction existing in these double-sided impacting cases.

As the video recording system could not be mounted on the carriage to film the totality of the test, only a fixed window of the motion, of only about 40 cm wide, could be captured. The chaotic nature of some motions involving the need to conduct several tests for the same conditions therefore limited the number of cases investigated in this project. Flow visualisations have mainly been conducted for two flow velocities, one corresponding to the middle of the upper branch existing with linear restraints, at $U_r = 6.14$, and one in the middle of the lower branch, at $U_r = 9.22$. For these two flow velocities, tests have been conducted with linear restraints, and with stiff stops symmetrically-placed at $e = 0.47$ and $e = 0.30$.

At $U_r = 6.14$, i.e. in the upper branch with linear restraints, the cylinder exhibits periodic high-amplitude oscillations with $A^* \approx 0.9$ and $f^* \approx 1.13$. It sheds two pairs of vortices per oscillation cycle, in which the second vortex shed is weaker than the first one.

When, for the same flow velocity, the amplitude of the motion is restricted symmetrically on both sides by stops placed at a large offset, the cylinder describes a stable *1-1-1* motion with a main frequency close to $f_{vs} = 0.18U/D$, which is for this value of U_r equal to $1.10f_n$ and therefore close to the frequency of the motion with linear restraints. In a video of the flow visualisation recorded with the high speed camera for $U_r = 6.14$ and $e = 0.47$, the cylinder is seen to impact on the stops five times alternately, and appears to shed only one single vortex at each extreme of displacement. This is illustrated by the picture in figure 5.23 extracted from the video. On this picture, the horizontal black line that was traced out on the glass of

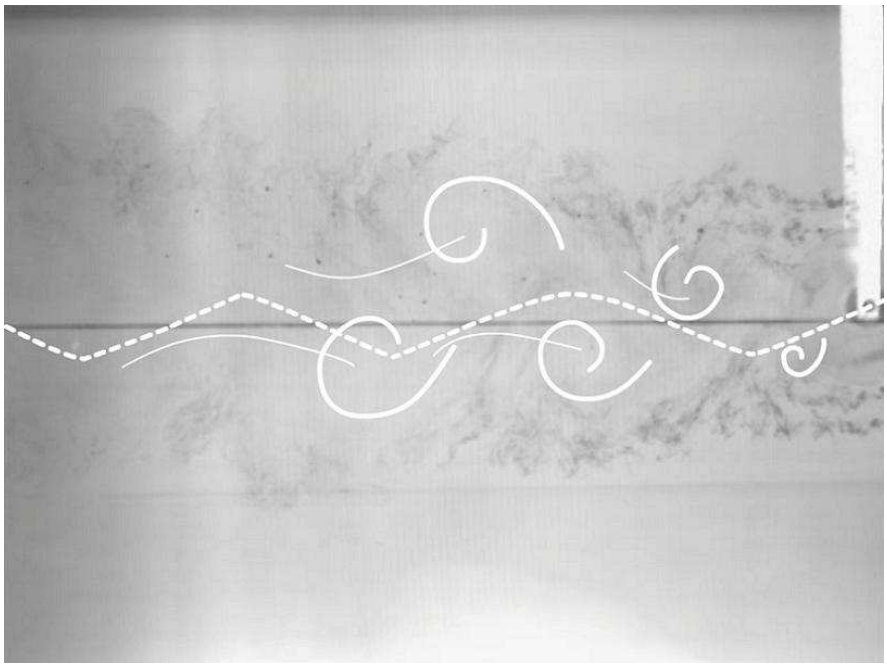

Figure 5.23: Vortex wake for double-sided impacting motion with $e = 0.47$ at $U_r = 6.14$. $R_e \approx 5400$.

the tank represents the rest position of the cylinder, and the thick dashed white line shows the trajectory the cylinder exhibits during the video. Positions of vortices at the moment of the picture are highlighted by thick white lines, with the approximative displacement of their centres of vorticity during the record drawn with light white lines. The cylinder does clearly not shed two vortices per cycle as it does

at this value of U_r with linear restraints.

The 2P mode of vortex formation existing in the lower branch of excitation when the cylinder is subject to linear restraints is clearly recognisable also. During the flow visualisation made at $U_r = 9.22$, i.e. in what was the lower branch of excitation with linear restraints, with $e = 0.47$, the cylinder describes a *1-1-1* motion and hits the stops four times within the field of view. In this case it clearly sheds only one single vortex just after hitting a stop. The vortex wake displayed in figure 5.24 extracted from this video, with the path of the cylinder and the vortices highlighted as before, is very different from a 2P-type vortex wake as presented in figure 4.6(a) at page 67. The resulting vortex wake looks again like that resulting from a 2S mode of vortex

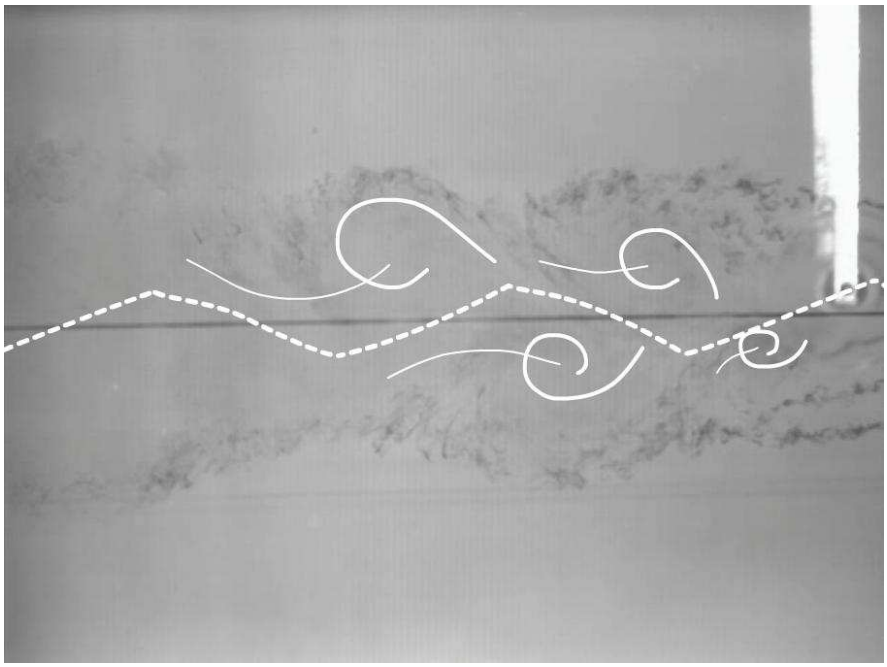

Figure 5.24: Vortex wake for double-sided impacting motion with $e = 0.47$ at $U_r = 9.22$. $R_e \approx 8100$.

formation. However the vortex formation seems to be based on a different process.

The vortices do not appear to be shed by the cylinder in the same way as with linear

restraints. In the 2S-mode existing when the cylinder is subject to linear restraints and U_r is situated in the initial branch, the vortices form behind the cylinder and build up in strength before being shed. When the cylinder's amplitude is limited, its motion during a contact on a stop is caused by the impact changing nearly instantaneously the sign of its velocity. It is believed that just after the change of direction of the cylinder, the shear layer that is on the side of the cylinder opposite the stop joins that from the opposite side and forms a vortex.

In the case of vortex shedding of a cylinder subject to linear restraints, researchers have commented that "*the wake of the circular cylinder seems to be paced by a vortex formation time.*" [21]. In this case, it is believed that the amplitude limitation interrupts the build-up of the shear structure behind the cylinder and that vortices are formed because of the rapid change of direction of the cylinder due to impact. In these cases, the secondary roll-up observed in the 2P modes occurring with linear restraints does not have time to build up and only a single vortex is shed by the cylinder after an impact.

When reducing the offset between the stops and the cylinder at $e = 0.30$, the vortex formation seems to be based on the same process as with a larger offset. The cylinder still sheds one single vortex just after each impact on a stop, through the same mechanism, i.e. the amplitude limitation interrupting the build-up of the shear structure behind the cylinder, forcing it to be shed.

In the snapshot taken from the video made with $U_r = 9.22$ and $e = 0.30$, presented in figure 5.25, the cylinder first hits alternatively the stops once, shedding one single vortex after each impact. It then slows down and does not reach the lower stop. In fact the strong vortex formed after hitting the upper stop seems to stay longer close to the cylinder and preventing it from reaching the lower stop. After some time, the shear layer below the cylinder has built up and a clockwise vortex is shed when the shear layer on its upper side starts to grow, leading the cylinder to reach the upper

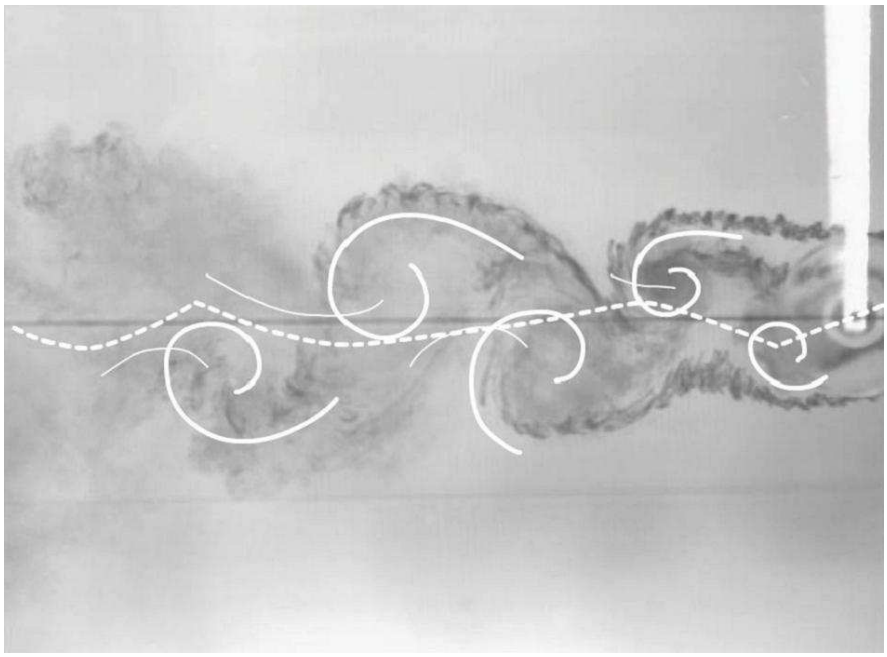

Figure 5.25: Vortex wake for double-sided impacting motion at $U_r = 9.22$ and $e = 0.30$. $R_e \approx 8100$.

stop again. This impact results in a change of direction of the cylinder, stopping the build-up of the shear structure and leading to the shedding of an anticlockwise vortex. It has also to be noted that in this case, with $e = 0.30$, the vortices are shed on each side of the cylinder closer to its rest position than with $e = 0.47$, and therefore the resulting wake is narrower than with $e = 0.47$.

5.4 Conclusions

When the cylinder impacts on stiff symmetrically-placed stops, its amplitude of vibration is strongly limited. This affects the fluid-structure interaction as the 2P modes of vortex shedding observed during large amplitude oscillations of the cylinder with linear restraints are not observed any more. It is believed that the amplitude limitation of the cylinder interrupts the build up of the shear structures behind the

cylinder, and that the vortex formation modes necessitating long build-up times cannot occur. The flow visualisations show in every case that only one single vortex is shed after an impact on a stop. It is believed that this vortex is created by the rapid change of direction of the cylinder due to the impact.

The dynamics of the cylinder are only slightly affected when the amplitude limitation is weak. With a large offset e, impacts occur over all the range of flow velocities corresponding to the upper branch of excitation in the linear case. Over most of this impacting domain, the cylinder exhibits symmetric *1-1-1* motions, with a frequency increasing with U_r close to the Strouhal frequency. This shows that the vortex shedding process leading to 2S-like vortex wakes takes place at the same frequency as in a 2S mode of vortex shedding. As shown by the frequency distributions, in this case the system responds linearly to the excitation. When impact occurs at low flow velocities, it has the effect of decreasing the cylinder's amplitude of vibration so that the cylinder describes *k-0-1* and *k-1-0* cycles, making its motion chaotic due to the unpredictability of the impact times and forces, over a narrow range of flow velocities at the beginning of the impacting domain.

With the offset decreased, impact occurs on wider ranges of flow velocities. In a first time, the chaotic window at the start of the impacting domain widens, and *1-1-1* motions are stable until the end of the impacting domain. Perturbation of the dynamics become much clearer as e is further decreased, the chaotic window at the start of the impacting domain becomes wide, and symmetric *1-1-1* motions less stable as many other motions can be observed, like double bounces on a stop at large flow velocities. With a very small offset, the chaotic window with *k-0-1* and *k-1-0* cycles is much smaller, but the dynamics of the cylinder are very complex for any flow velocity; chatter on the stops even occurs at large flow velocities. For any flow velocity, the average impact velocity, and the average impact force, increase with U_r increasing, and decrease with e decreasing.

Chapter 6

VIV of a rigid cylinder with impact on one stiff stop

As seen in section 3.2, in some applications part of a structure experiencing VIV can be subject to a limitation of its motion on only one of its sides. The case of a rigid cylinder experiencing VIV whose amplitude is limited on one side by a stop involving an asymmetric jump to a high value in the system stiffness is investigated here. The offset e between the rest position of the cylinder and the stop position is set at different values. The displacement of the cylinder is recorded for each offset at different flow velocities, and data processing is performed to obtain information on the dynamics of the cylinder, such as bifurcation diagrams of peak excursions or impact velocities. Changes in the dynamics of a cylinder experiencing VIV are shown to occur when amplitude limitation acts. These changes are accompanied by changes in the vortex-wake dynamics, as shown by flow visualisations.

To limit on only one side the amplitude of the rigid cylinder undergoing VIV, only one stop is placed at the moving end of the upper horizontal beam. As in the case of symmetric amplitude limitation, the stop is placed at about 2 cm from the moving

end, underneath it. The cylinder is in this way subject to an asymmetric jump in stiffness characterized by $r_k \approx 344$, when its non-dimensional displacement y equals $-e$.

As mentioned previously, results from the first set of experiments published in [78] showed interesting features that were further investigated during the second set of experiments carried out in the glass-walled tank.

As for the case with linear restraints, results obtained during our second set of experiments are more reliable, and contain more information about the dynamics of a low-mass ratio low-damping rigid cylinder experiencing VIV and subject to asymmetric amplitude limitation. Maximum amplitude reached by the cylinder when subject to linear restraints is about $0.9D$, and the stiff stop is in this case first placed at $e = -0.65$, and brought closer to the stop at $e = -0.47$ and $e = -0.22$.

In order to test the repeatability of these measurements, another set of tests with an offset e equal to -0.47 has been carried out some days after the first one. During this lapse of time the experimental setup had been changed and then readjusted to reproduce the same experimental conditions. Repeatability of these tests with $e = -0.47$ is good, as will be seen in section 6.5, and the repeatability of the other sets with different values of e is accepted to be as good, as the experimental setup and procedure were the same.

As in the case of symmetric amplitude limitation, a first indication of the effect of an asymmetric amplitude limitation of a cylinder undergoing VIV on its dynamics can be given by a simple comparison between the time series of displacement for the same conditions with only the stop position varying.

6.1 Observation of time series of displacement

In figure 6.1, time series of displacement of the cylinder in the case with linear restraints and for single-sided impacting motions with three different offset values are presented. In each case, the reduced velocity U_r is equal to 5.12, and the stop position is identified by the position of the time axis.

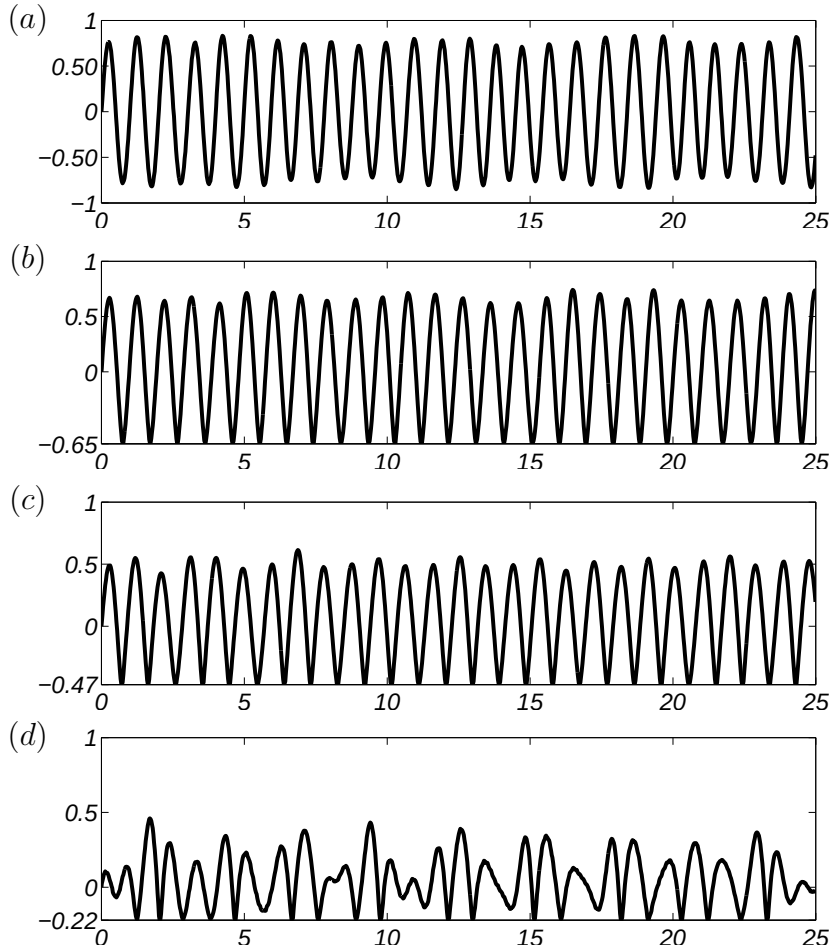

Figure 6.1: Time series for linear constraints (a) and single-sided impacting motions for $U_r = 5.12$. (b): $e = -0.65$, (c): $e = -0.47$, (d): $e = -0.22$

A change in the dynamics of the cylinder caused by the presence of the stop is clearly apparent with a small offset. With linear restraints, the cylinder describes a periodic

oscillation of frequency $f \approx f_n$ and of amplitude about $0.8D$. With a stop at e=-0.65, the response does not seem much affected as the motion still seems periodic. The cylinder impacts on the stop at each oscillation cycle, describing a seemingly stable 1-impact-per-period motion. The amplitude reached between impacts is at about $0.65D$, and it presents only small variations. The frequency of oscillation is at this reduced velocity very close to the vortex shedding frequency f_{vs}, but also close to f_n as f_{vs} equals 0.92 for $U_r = 5.12$.

With the stop placed at $e = -0.47$, the cylinder exhibits the same type of response, but the amplitude between impacts is reduced to about $0.48D$, and presents more modulation than for $e = -0.65$. The frequency of this 1-impact-per-period motion seems unchanged compared to $e = -0.65$.

With e reduced to -0.22, the motion is much more affected. The response is more complex without any distinctive periodic pattern. The contact with the stop can sometimes, as here at $t \approx 10$ s, result in an abrupt decrease of the oscillation amplitude followed by a phase of one or several cycles of amplitude growth before reaching the stop again. Some other times, successive impacts with the stop occur during many cycles, regularly or not.

6.2 Amplitude and frequency response

As seen with the time series presented in figure 6.1, oscillations of the cylinder can present very large variations for a fixed flow velocity when amplitude limitation acts on one of its sides. However the extreme, i.e. minimum and maximum, displacements of the cylinder during a test, respectively noted ${A^*_{max}}^-$ and ${A^*_{max}}^+$, give some first information on the dynamics of the cylinder.

Figure 6.2 presents the extreme values of displacement reached by the cylinder for the different offset values investigated, in the respective impacting domains. Data are here presented for the two sets of experiments conducted, with circles for those from the first, and with triangles for those from the second. For both cases, data are shown with empty symbols for the largest offset, fully-filled symbols for the smallest value of e, and half-filled symbols for the intermediate value.

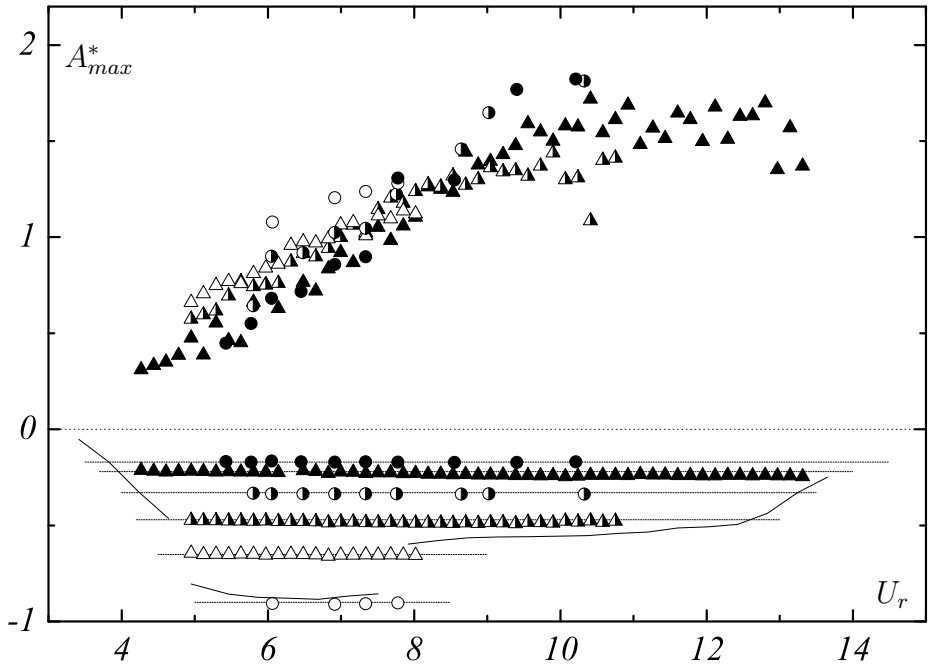

Figure 6.2: Extremes of time series of displacement for single-sided impacting motions.

In the lower part of the plot, the amplitude response in the linear case (from the more reliable second set of experiments) is shown with a line. Lower extremes of displacement plotted for each case with their respective symbols, illustrate the amplitude limitation by the corresponding stop, whose position is indicated by a horizontal line. They also indicate the width of the impacting domain in each case.

In figure 6.2, the negative extreme amplitudes for $e = -0.91$ seem lower than the cylinder vibration amplitude in the linear case, which would make no sense. These are from the first set of experiments where the cylinder experienced, certainly because

of fluctuations of its velocity, oscillations of larger amplitude than in the second case. The cylinder did impact on the stop placed at $e = -0.91$ in these tests. However, as few tests have been carried out during the first set of experiments, their results will not be discussed any further as they only confirm those obtained later.

As in the case of double-sided impacts, it can be observed that the absolute value of ${A^*_{max}}^-$ increases with U_r in all cases. As will be seen later, this is due to the increase of the maximum impact force with U_r. The cylinder impacting harder with U_r increasing on the non-perfectly rigid but stiff stop pushes it further.

In the upper part of the plot, the maximum amplitude reached between impacts ${A^*_{max}}^+$ is minimum for every gap setting at the lowest reduced velocity where the cylinder starts impacting on the stop. For the smallest gap value investigated here this happens in the initial branch, while for the others it starts at the beginning of the upper branch of oscillation. For all gap settings, ${A^*_{max}}^+$ firstly increases with U_r, and seems to reach a limit.

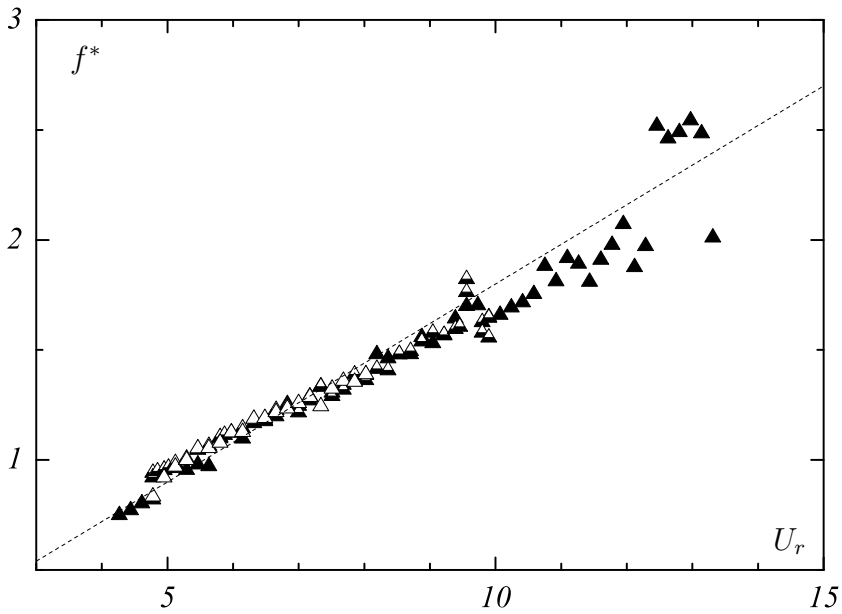

Figure 6.3: Main frequency ratio peaks for single-sided impacting motions.

As before, the frequency response of the cylinder can be complex when impact occurs,

but frequency distributions obtained by FFT of the displacement signal again always contain one main dominant peak, whose frequency increases with U_r. Figure 6.3 displays the frequency ratio of the main peak in the distributions as functions of U_r for the different offset values using the nomenclature for symbols described previously.

The first indication given by this plot is that the main peak frequency does not seem to depend much on the offset as all cases present about the same value at fixed U_r, and therefore the same increase with U_r. For $U_r \approx 5$, the main frequency is close to f_{vs}, which is close to f_n. In all cases, it increases with U_r, marking a slight discrepancy from f_{vs}. For the case $e = -0.22$, the main frequency jumps to a value close to fvs at $U_r = 12.46$. Desynchronisation has occurred, but impacts still occur leading to high maximum amplitude between impact as seen in figure 6.2.

6.3 Impact velocities and impact forces

During these single-sided impacting cases also, the impact velocity $\dot{y}_i$ varies from impact to impact. Nevertheless, as for symmetric cases, its average and maximum values over each record show interesting features. As before, contact velocities are normalised by $U_c = 2\pi f_n D$. Average and maximum values, $\overline{V_i}$ and V_{imax}, of the reduced impact velocity $V_i = \dot{y}_i/U_c$ are presented in figure 6.4 as functions of U_r, for single-sided impacting cases with different offset settings, using the nomenclature described before.

At low reduced velocities, maximum impact velocities presented in figure 6.4(b) do not seem to depend on the offset e as they present the same increase with U_r up to $U_r \approx 8$ where they are at about 1 U_c. For higher U_r, impact has stopped for $e = -0.65$; V_{imax} decreases gradually with U_r increasing for $e = -0.47$. V_{imax} reaches a maximum for $e = -0.22$ at about 1.2 U_c at $U_r \approx 9$ and decreases then very slowly

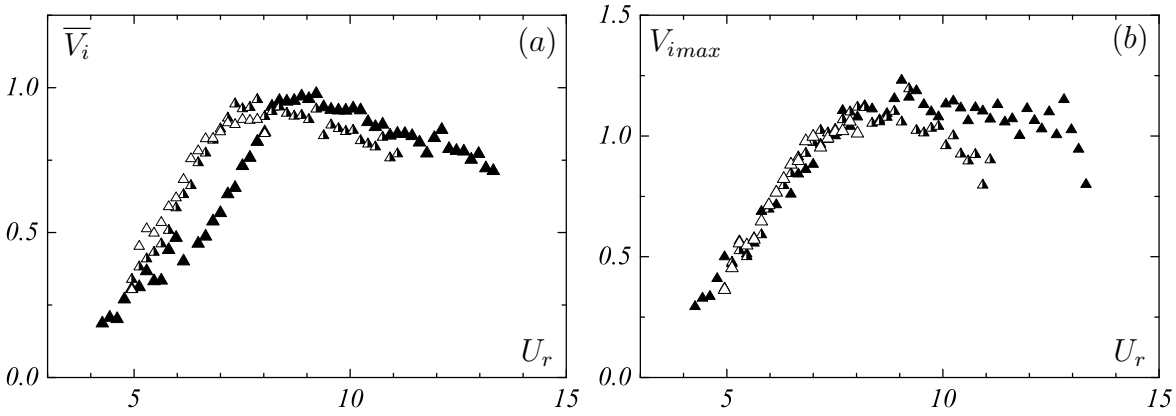

Figure 6.4: Average (a) and maximum (b) reduced impact velocities for single-sided impacting motions. △: $e = -0.65$; ◮: $e = -0.47$; ▲ : $e = -0.22$.

with U_r increasing, staying at about $1.1U_c$ for $U_r \approx 13$.

Average impact velocities presented in figure 6.4(a) are at their lowest value for all gap setting at the beginning of the impacting domain. In the two cases with the largest offsets, it increases nearly linearly with U_r to reach a maximum for $U_r \approx 8$, and it then decreases slowly until the end of the impacting domain. $\overline{V_i}$ mark a different increase for $e = -0.22$, as it increases slowly first, and more strongly then with U_r increasing until it reaches a maximum for $U_r \approx 9$ before decreasing then gradually up to the end of the impacting domain.

As could have been expected, increases in the maximum amplitude between impacts and of the main frequency of the motion with U_r result in an increase of the average impact velocity. The mean impact force, obtained using the change of momentum of the cylinder can here again be obtained from the time series of displacement recorded using the post-processing described earlier. As other parameters of the vibration of the cylinder, the impact force varies at nearly each impact. Its average and maximum values, $\overline{F_i}$ and F_{imax}, presented in figure 6.5 as functions of U_r, show that the force of impact follows the same general evolution as the impact velocity.

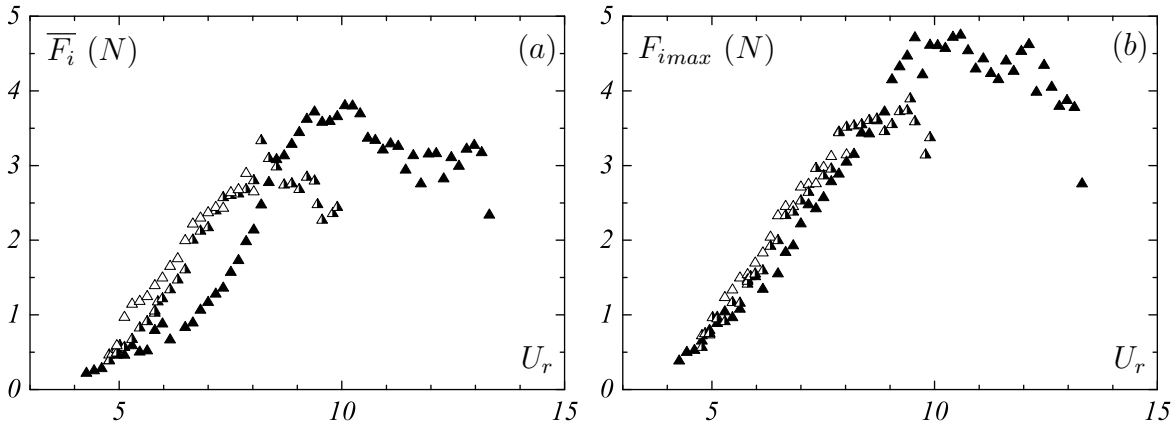

Figure 6.5: Average (a) and maximum (b) impact forces for single-sided impacting motions.

Similarity of the evolutions of the impact velocity and the impact force for the two largest offset suggest a similar response to the presence of the stop. However, the different evolutions of these parameters observed for $e = -0.22$ suggest a change in the dynamics of the cylinder.

6.4 Change in the dynamics

In the time series presented in figure 6.1 for $U_r = 5.12$, the dynamics of the cylinder do not seem too much affected by the amplitude limitation on one side when the offset is large. The periodic oscillation observed with linear constraints becomes a periodic motion with impact at each cycle, i.e. a 1-impact-per-period motion. But when bringing the stop closer to the cylinder, the motion becomes more complex.

6.4.1 Observation of phase portraits

Phase portraits of single-sided impacting motions are compared in figure 6.6 to those obtained with linear restraints at the same U_r. In this figure, composed of four columns, the first column corresponds to the linear case. Cases corresponding to single-sided impacting motions are presented in columns to the right, with the stop brought closer from the cylinder's rest position, itself marked by a dot on each graph. The reduced velocity increases while descending each column. Data plotted here are, as in figure 5.16, the instantaneous velocity of the cylinder $\dot{y}$ normalised by $U_c = 2\pi f_n D$ plotted against its non-dimensional displacement y. All graphs are also presented here with a scale adapted for each motion to fill the whole window, in order to compare the nature of the motions without accounting for their amplitude.

The change in the nature of the motion resulting from the introduction of an amplitude limiting stop on one side of the cylinder can clearly be observed by looking at the different phase portraits corresponding to the same value of U_r.

For $U_r = 4.95$, the cylinder on linear restraints is in the beginning of the upper branch of oscillation and exhibits a periodic oscillation with r.m.s amplitude equal to $0.72D$ at a frequency equal to its natural frequency. When for this flow velocity a stop is placed at $e = -0.65$, contacts occur, strongly limiting on one side the amplitude of the cylinder. The cylinder reaches the stop nearly every cycle, or at least getting very close to it, and always reaches about the same amplitude between impacts.

When this stop is brought closer to the cylinder's rest position, to $e = -0.47$, the dynamics of the cylinder are more affected by the stop. It still presents the same shape as for $e = -0.65$ but shows much more modulation. Cycles without impact present lower amplitudes, dispersion of the impact velocity and of the amplitude between impacts are increased.

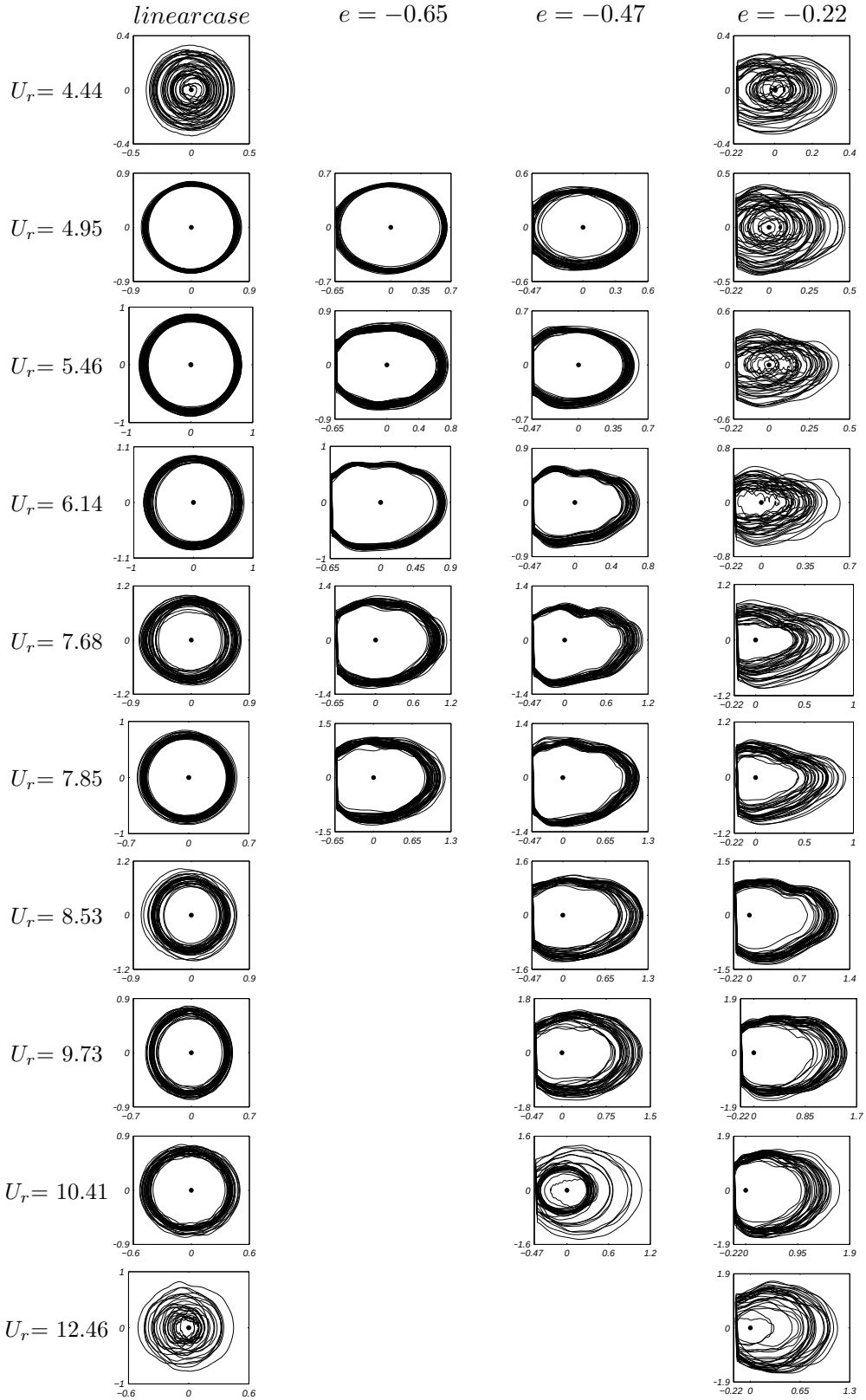

Figure 6.6: Phase portraits for linear and single-sided impacting cases from the second set of experiments.

When the stop is brought even closer, to $e = -0.22$, the motion does not seem any close to periodic any more. The phase portrait shows a very complex trajectory, with bounces on the stop having an amplitude between impacts varying strongly, some cycles without impact, and even some where the cylinder oscillates close to its equilibrium position. In this phase portrait no pattern is recognisable, the trajectory fills most of the space enclosed by its widest cycle, which suggests a chaotic nature of the motion.

The original high amplitude periodic vibration existing in the beginning of the upper branch is therefore perturbed when its amplitude is limited. The limitation has more and more effect on the nature of the motion when reducing the offset for a fixed flow velocity, the motion becoming apparently disorganised at low flow velocities with a small offset.

The dynamics of the cylinder become also more complex when the reduced velocity increases. For $e = -0.65$, the periodic 1-impact-per-period motion, stable at $U_r = 5.80$, seems to lose in stability as U_r increases as the borders of the phase portraits, formed by the superposition of the many cycles measured, widen with U_r increasing. The same observation can be made for $e = -0.47$. In this case, impact occurs at large flow velocities, at which modulation of the 1-impact-per-period motion is large. For $e = -0.22$, phase portraits are very complex for low reduced velocities, the trajectory filling most of the phase space. A 1-impact-per-period motion seems to become more stable with U_r increasing, but it always presents a large modulation, with amplitudes between impacts distributed over a large range of values.

The 1-impact period-1 motion observed in some ranges of reduced velocity with all offset values implies the occurrence of repetitive impacts. As this can be of major concern in applications, this periodic motion is given more attention. As seen in section 3.1.3, periodic orbits and their stability can be studied with the use of Poincaré sections and bifurcations diagrams. They are useful to identify windows of

stability of periodic motions, or chaotic windows, but help also in understanding the transitions between the different states of the system under variation of a parameter.

6.4.2 Stability of a 1-impact-per-period cycle

Interesting bifurcation diagrams in our system are those made by plotting the lower peak excursions, intersections of the trajectory with the Poincaré section $(y, \dot{y} = 0, t)$ when crossing it from the domain $(y, \dot{y} < 0, t)$ to $(y, \dot{y} > 0, t)$, as a function of the reduced velocity. Experimental bifurcation diagrams of lower peak excursions, presented for the unconstrained case and for single-sided impacting cases with $e = -0.65$, -0.47 and -0.33 in figure 6.7, are preferred here to those of upper peaks excursions as they provide information in the region where the non-linearity acts.

In the bifurcation diagram presented for the unconstrained case in figure 6.7(a), the first bifurcation, through which the initial branch of oscillation appears, occurs at $U_r \approx 3$. The upper branch of oscillation appears through a second bifurcation causing a jump in amplitude at $U_r = 4.77$. Periodic motions at the beginning of the upper branch present low amplitude modulation, but this latter increases with U_r until some peaks appear at about the amplitude of the lower branch at the start of the intermittent transition between upper and lower branches. In the lower branch which therefore appears through a different kind of bifurcation, the motion is periodic with some amplitude modulation. In the desynchronisation regime, lower peak excursions are spread over wide ranges of values; the cylinder exhibits aperiodic oscillations with a lot of amplitude modulation.

As observed in figure 6.7(b), the introduction of an amplitude-limiting stop at $e = -0.65$ implies the transformation of nearly all the upper branch of oscillation in a window of stability for a 1-impact-per-period cycle. It is only at the very beginning and very end of the impacting domain that lower peaks outside the stop position, but

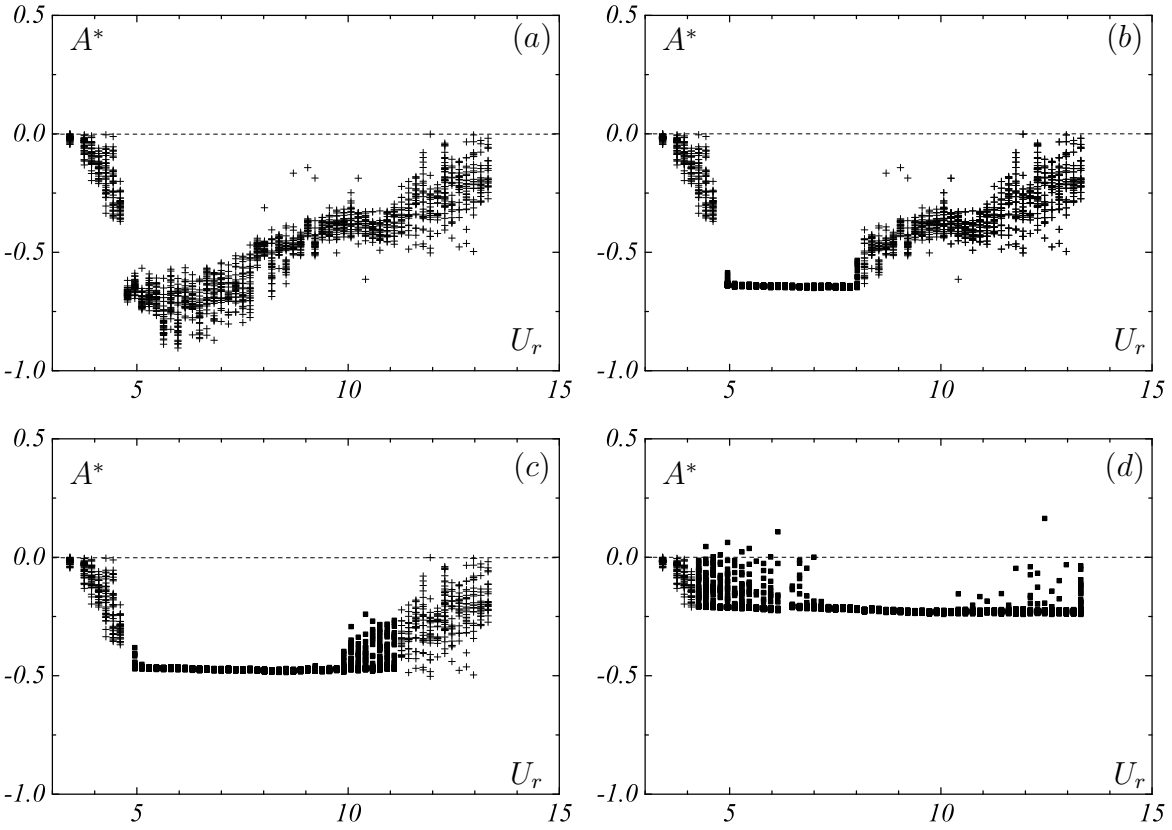

Figure 6.7: Bifurcation diagram of lower peak excursions for unconstrained motions (a), and motions limited on one side. (b): $e = -0.65$; (c): $e = -0.47$; (d): $e = -0.22$.

close to it, appear, revealing cycles without impact. In the lower branch and desynchronisation regime, amplitude of oscillation is too small for the cylinder to reach the stop and impact does not occur.

Figure 6.7(c) shows that when e is decreased to -0.47, the width of the window of stability of the 1-impact-per-period cycle is increased. It still starts at the beginning of the impacting domain, but finishes before the end of it, at $U_r \approx 10$. At the beginning of the impacting domain, a narrow transition region where some lower peaks appear out of the stop position is also apparent, as for $e = -0.65$. At $U_r \approx 10$ a bifurcation occurs through which the 1-impact-per-period cycle loses its stability. Impact still occurs but cycles without impact on the lower stop also occur. Lower peaks become widely spread between the cylinder's rest position and the stop

position. For $U_r > 11.09$, the cylinder does not reach the stop any more.

As illustrated by figure 6.7(d), when the stop is moved to $e = -0.22$, impact starts earlier, at $U_r \approx 4$, and what seems to be a chaotic window appears. In this window, which ends at about $U_r = 6.82$, lower peaks of oscillation are spread over wide ranges of values; some lower peaks even occur at $A^* > 0$, revealing the strong perturbation of the dynamics. A transition to a stable 1-impact-per-period cycle seems to occur, and the cycle stays stable until the very largest reduced velocity set. Few peaks elsewhere than the stop position then appear at large reduced velocities, revealing some short destabilisation of the 1-impact-per-period cycle.

It can be noted that, in the chaotic window at the start of the impacting domain for $e = -0.22$, the system exhibits a process similar to that observed for double-sided cases. At low flow velocities, with $e = -0.22$, the impact on the stop has the effect of reducing the cylinder's amplitude of oscillation. The cylinder describes then some oscillation cycles during which its amplitude increases, until it reaches the stop, and starts this whole process again. This process is about stable at very low flow velocities as the cylinder only describes such 1-impact period-k cycles. With U_r increasing in the chaotic window, some consecutive impacts occur, this process loses its stability while that of the 1-impact-per-period cycle increases.

The same process of reinjection of the trajectory in the attraction basin of the original attractor after an impact also explains the cycles without impact occurring for larger offset values at the very beginning of their impacting domain. It is believed that, as for double-sided cases, the oscillation is more perturbed by the impact on the stop as e is decreased.

6.4.3 Modification of the frequency distribution

The frequency distributions provide also some information on the nature of the motion of the cylinder. Selected frequency ratio distributions of recorded time series for cases with linear constraints and with one amplitude-limiting stop are presented in figure 6.8 using the template described before. On this figure, the perturbation of the energy distribution over frequencies induced by the presence of the stop is clearly apparent.

For $U_r = 6.14$ for example, for which the largest amplitude is observed in the case of linear restraints, the frequency distribution contains only one main peak at f in the linear case. When a stiff stop limits weakly on one side the amplitude of the cylinder to $e = -0.65$, some energy is transferred to the harmonics of f as peaks appear in the corresponding frequency distributions at 2, 3 and even 4 times f. When approaching the stop from the cylinder, here at $e = -0.47$, the same structure appears in the frequency distribution, only more energy is transferred to the same harmonics, and, as a result, the magnitude of the main peak drops compared to its value for $e = -0.65$. However, when the stop is brought even closer from the cylinder, the frequency distribution does not present the same structure. Energy is distributed over a wide range of frequencies, as the frequency distribution is very noisy. The peak at $f \approx f_{vs}$ is larger than the other ones but distinct peaks at 0.5, 1.5, 2, 2.5 and 3 times f can also be observed.

When looking at the frequency distributions corresponding to the case $e = -0.65$, the same structure, with only one main peak at $f \approx f_{vs}$ and its harmonics, always appears in nearly noiseless frequency distributions. The magnitudes of the harmonics increase with U_r. In these cases, the cylinder exhibits periodic 1-impact-per-period motions.

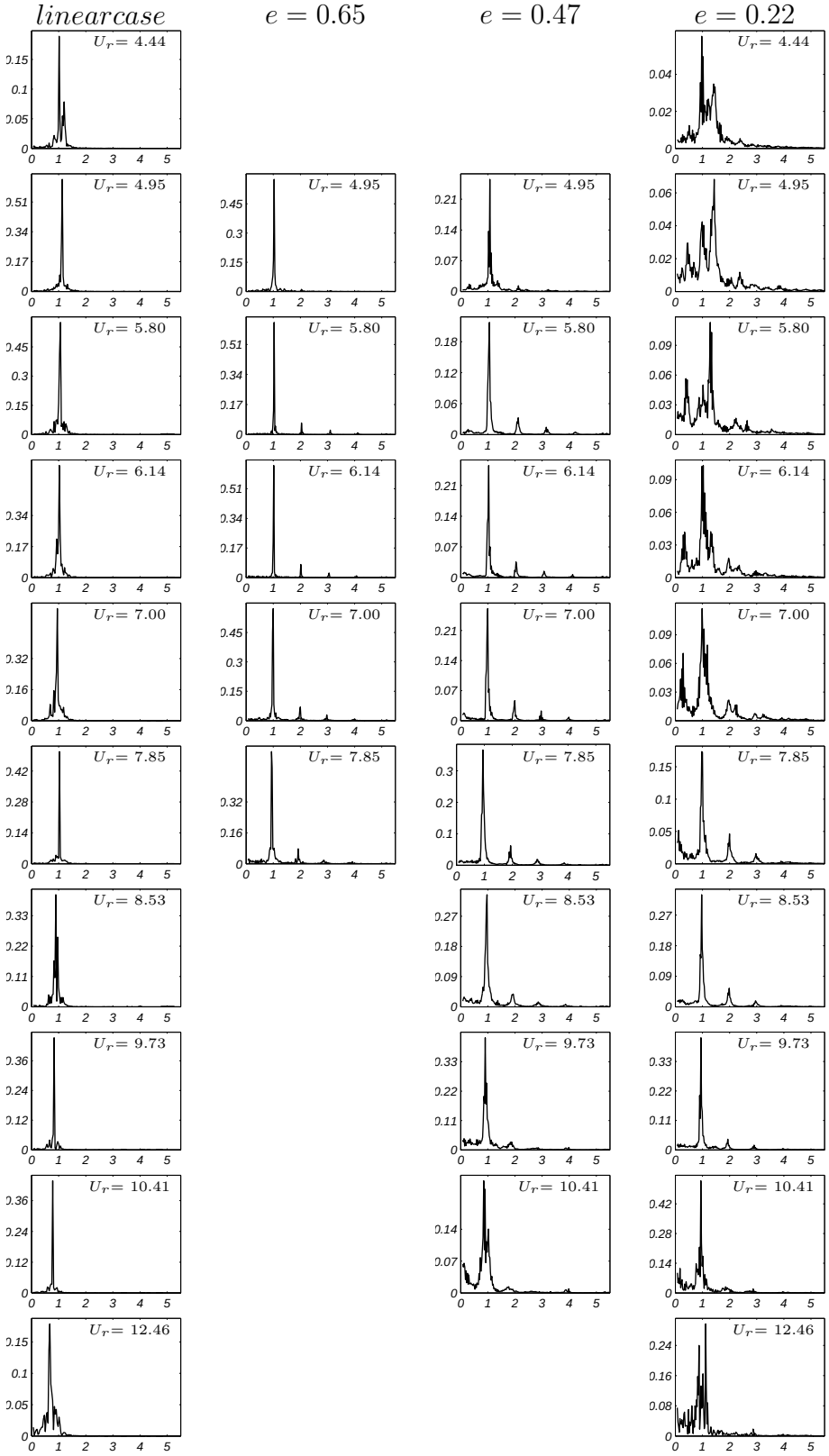

Figure 6.8: Frequency ratio distributions for linear and 1 stop cases from the second set of experiments. *The x-axis represents* f/f_{vs}.

With e reduced to -0.47, frequency distributions still present this same structure at low U_r, characteristic of the 1-impact-per-period motions observed stable for this case in this range of flow velocity. Magnitudes of the harmonics increase with U_r, until at some point they start to decrease. Frequency distributions become more noisy, with wider peaks for large flow velocities.

For $e = -0.22$, frequency distributions are very complex, with many peaks but always one larger peak at f, for low U_r. Some organisation seem to appear with U_r increasing as frequency distributions presenting the same structure as observed for 1-impact-per-period motions with larger offset values can be observed. Magnitudes of the harmonics, large at low U_r, seem to be decreasing with U_r increasing. At very large U_r, frequency distributions are complex, with many peaks and some noise.

More information can be obtained from these sets of frequency distributions by plotting the frequencies of all the significant peaks as a function of the reduced velocity. For each of the frequency distributions obtained, as those presented figure 6.9, frequencies of all the peaks having a magnitude larger than 2% of the one of the main peak can be recorded and plotted as a function of U_r.
The plot for linear constraints presented in 6.9(a) had already been presented in section 4.1.3, but it is displayed here again to allow for comparison. In the graphs corresponding to cases with amplitude limitation, dashed vertical lines point out the impacting domain. The vortex shedding frequency $f_{vs} = 0.18U/D$ and its harmonics are also plotted with dashed lines when needed to help for interpretation.

The plot for the case $e = -0.65$ in figure 6.9(b) confirms the structure observed with the frequency distributions all over the impacting domain.

The plot for $e = -0.47$ presented in figure 6.9(c) reveals the same structure over the range of flow velocities where 1-impact-per-period motions have been observed to be stable, for $U_r < 10$ in the impacting domain. They show also that, in these frequency

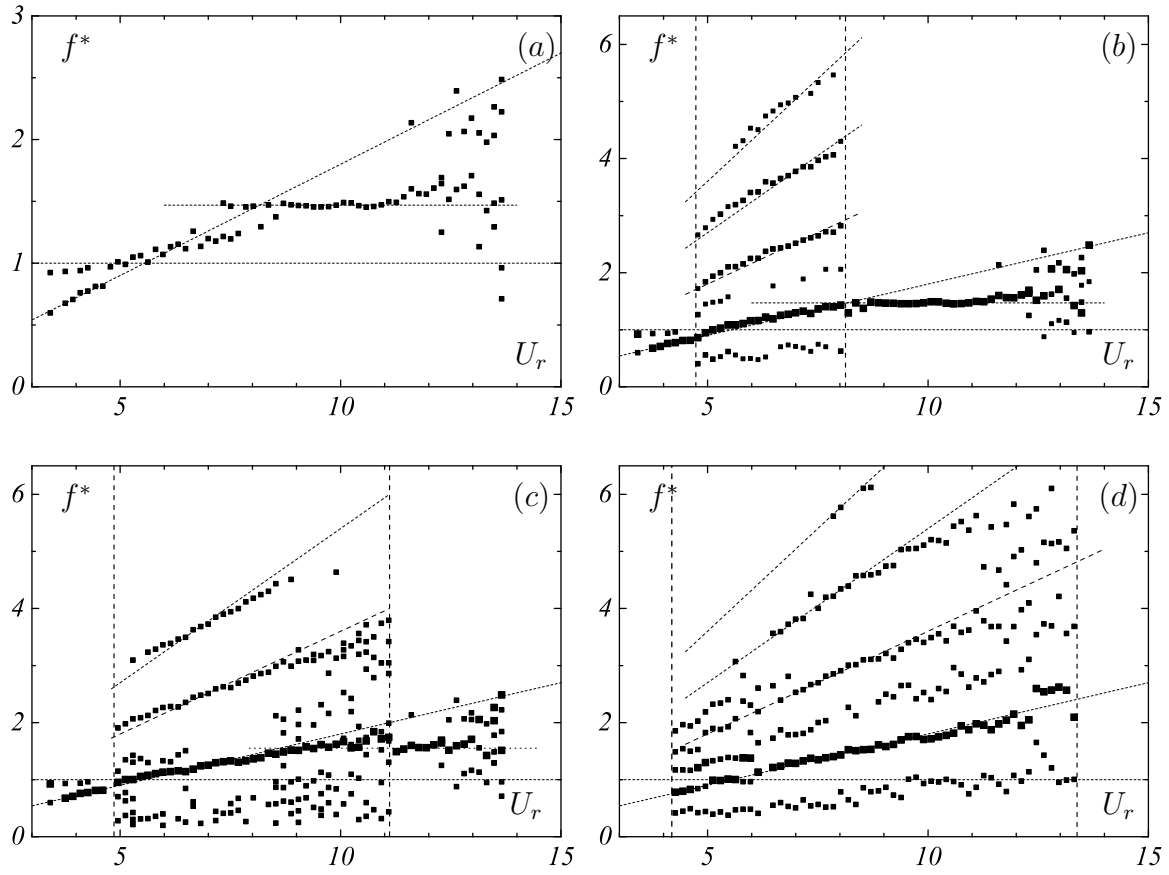

Figure 6.9: Peaks in frequency ratio distributions. (a): linear case; single-sided impacting motions with (b): $e = -0.65$; (c): $e = -0.47$; (d): $e = -0.22$.

distributions, the subharmonics and harmonics at 0.5 and 1.5 f are present moreat the beginning of the impacting domain and disappear with U_r increasing. With its harmonics also displayed, the trend that the main frequency follows becomes clearer. It does take values slightly larger than f_{vs} at low U_r, and it increases with a slope slightly smaller than $S_t = 0.18$ to finish at values lower than f_{vs} for large U_r, in the window of stability of the 1-impact-per-period cycle. At large U_r in the impacting domain, the largest peak becomes that corresponding to f_{vs}, and the many peaks present in the frequency distributions reveal a wide energy repartition.

Figure 6.9(d) exhibits features that were not observed before. It reveals that, in the chaotic window at the beginning of the impacting domain, the main peak frequency is

about the same as in the case of linear restraints. In this window, 1-impact period-k motions are observed. The impact on the stop interrupts the growth of oscillations, resulting in the cylinder spending most of its time subject to linear structural restraints, explaining the large energy distribution over the dominant frequency in the linear case. The main peak frequency seems to mark a discontinuity at $U_r \approx 6.5$ where the 1-impact-per-period cycle is seen to become more stable in the bifurcation diagram in figure 6.7(d). Some organisation reappears for $U_r \approx 7$, as many harmonics disappear, and the frequency distributions present the structure previously observed for 1-impact-per-period motions. In the window of stability of 1-impact-per-period motions, the main frequency follows f_{vs}, marking only a very slight discrepancy from it at large U_r. Discontinuity of the main peak frequency is observed at larger flow velocity, as f^* takes values slightly larger than f_{vs} at the end of the impacting domain. Frequency distributions were much more disorganised in these cases, in which the occurrence of oscillation cycles without impact shows the destabilisation of the 1-impact-per-period cycle.

To know more about the nature of the perturbation of the dynamics of the cylinder involved by the presence of a stiff stop limiting its amplitude, quantification of the predictability of the system can be done by estimation of its main Lyapunov exponent.

6.4.4 Chaotic nature of the motion

As for the cases of symmetric amplitude limitation, quantification of the chaotic nature of the system in the different cases of asymmetric amplitude limitation of the cylinder can be done using the algorithm developed by Kantz & Schreiber. With parameters set at the same values as previously, this algorithm is applied to every recorded time series of displacement of single-sided impacting motions, and estimates

λ_K of the Lyapunov exponent of the system are obtained for every case of asymmetric amplitude limitation over their respective impacting domain. Results obtained for these cases are presented in figure 6.10, along with results from the case with linear restraints for interpretation. With a weak asymmetric limitation

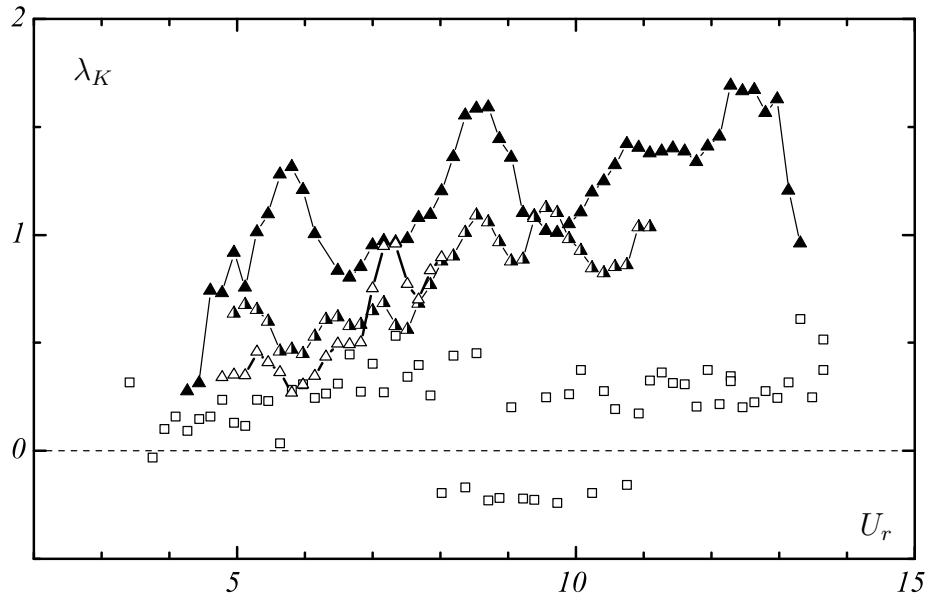

Figure 6.10: Lyapunov exponent from the linear case (□) and for double-sided impacting motions. (△): $e = 0.65$; (◭): $e = 0.47$; (▲): $e = 0.22$.

of the motion, here at $e = -0.65$, λ_K is only slightly increased compared to its value with linear restraints nearly all over the corresponding impacting domain, revealing the weak perturbation of the dynamics in this case. It is only for $U_r > 7$ that values of λ_K are much larger. At these flow velocities the 1-impact-per-period motion becomes less stable as dispersion of the maximum amplitude between impacts or of the impact velocity increase also. This would tend to confirm that the flow-structure interaction existing with linear restraints over this range of flow velocities, corresponding to the upper⇌lower transition, leading to intermittent motions in the linear case is still present in this case and only slightly affected by this weak asymmetric amplitude limitation. Of the two modes of vibration existing with linear restraints, the upper branch mode should be changed into a 1-impact-per-period

motion, while the lower mode, having an amplitude smaller than the stop position would be unchanged. It is believed that at the start of the transition, for $U_r \approx 7$, the system does not stabilise on the lower mode of excitation by long enough phases to lead to the non-occurrence of an impact, but that its presence leads to the loss of stability of the 1-impact-per-period motion revealed by this increase of λ_K at $U_r \approx 7$. The time series of displacement for $e = -0.65$ and $U_r = 8.02$, corresponding to the largest flow velocity where impact occurs in this case, contains only two phases of cycles without impacts occur, one about three oscillation cycles long, the other six oscillation cycles long, which is characteristic of intermittent motions.

For smaller offset values, λ_K generally increases with U_r over all the impacting domain, revealing the decreasing predictability of the system with the flow velocity increasing. All over the impacting domain, λ_K also increases with the offset decreasing, revealing the increased complexity of the dynamics of the system with e decreasing. Values of these estimates of the Lyapunov exponent do certainly not correspond exactly to the actual Lyapunov exponent of the system as this algorithm with these parameters can give positive values for known periodic motions as occurring for example with linear restraints. They however are a measurement of the predictability of the system, and of its chaotic nature. Values of λ_K obtained for small offset values at large flow velocities are much larger than for those for the linear case, and they therefore do certainly reveal the chaotic nature of the motion in these cases.

6.5 Repeatability of the tests

To investigate the repeatability of the experimental results obtained, another series of tests was carried out with one stop placed at $e = -0.47$, three days after the first one. Other tests had been conducted between both series, and the stop, which had been moved, was placed at the same offset from the cylinder's rest position.

The dynamics of the cylinder in these two sets of tests of with $e = 0.47$ are presented with the bifurcation diagrams of peak excursions from both series in figure 6.11. In

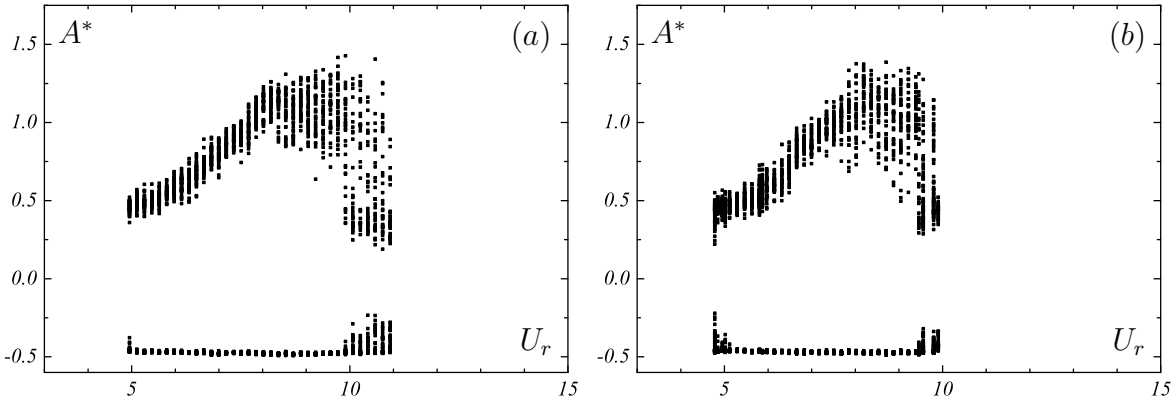

Figure 6.11: Bifurcation diagram of peak amplitudes for motions limited on one side with $e = 0.47$.

both cases, the contact with the stop starts at $U_r \approx 5$. After a small transition window, the 1-impact-per-period motion is stable over most of the impacting domain in both cases. The maximum amplitude reached between impacts increases with the exact same trend, and the exact same dispersion in both cases. Stability of the 1-impact-per-period cycle ends in both cases at $U_r \approx 10$ with the appearance of cycles without impact. In the first series of tests, impact occurred up to $U_r \approx 11$. In the second series of tests, certainly because of a small difference in the stop position, destabilisation of the 1-impact-per-period cycle occurs at a slightly lower flow velocity than in the first series, and impact did not occur any more for $U_r > 10$.

Frequency response from both of tests series are similar also. In both series, the main frequency of the motion takes the exact same values all over the impacting domain, increasing with U_r. Its exact same harmonics are found at two and three times the oscillation frequency.

The average reduced impact velocity $\overline{V_i}$, and maximum mean impact force F_{max} presented in figure 6.12 as functions of U_r, presents the exact same trend in both

series of tests. They increase quasi linearly with U_r first, and decrease slowly after reaching a maximum for $U_r \approx 8$.

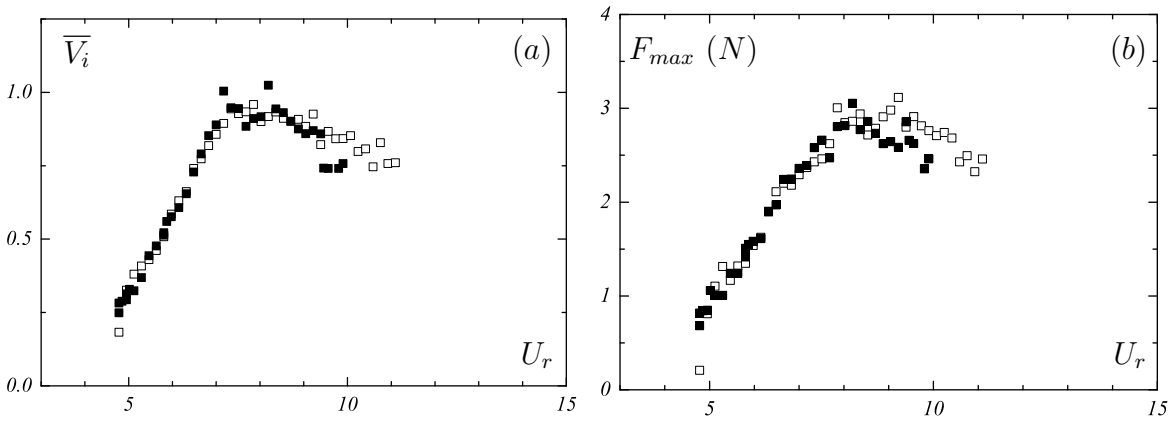

Figure 6.12: Average impact velocities (a) and maximum impact forces (b) for single-sided impacting motions with $e = 0.47$. □ : Results from first series of tests. ■ : Results from second series of tests.

Equivalent results concerning the dynamics of the cylinder for this case of VIV with an amplitude limiting stop placed at $e = -0.47$ have been found when carrying another series of tests three days after the first one. Results obtained concerning the tests presented with $e = -0.47$ are therefore repeatable, and so are thought those with other offset values presented earlier.

6.6 Modification of the vortex wake

To investigate how the fluid-structure interaction is affected by the limitation of the cylinder's displacement on one side, flow visualisations have also been conducted in this case at some specific values of U_r, and with different offset values e.

For $e = -0.47$, the cylinder impacts between $U_r \approx 5$ and $U_r \approx 10$, i.e. over all the upper and lower branch of vibration in the linear case where the two 2P modes of

vortex formation were observed.

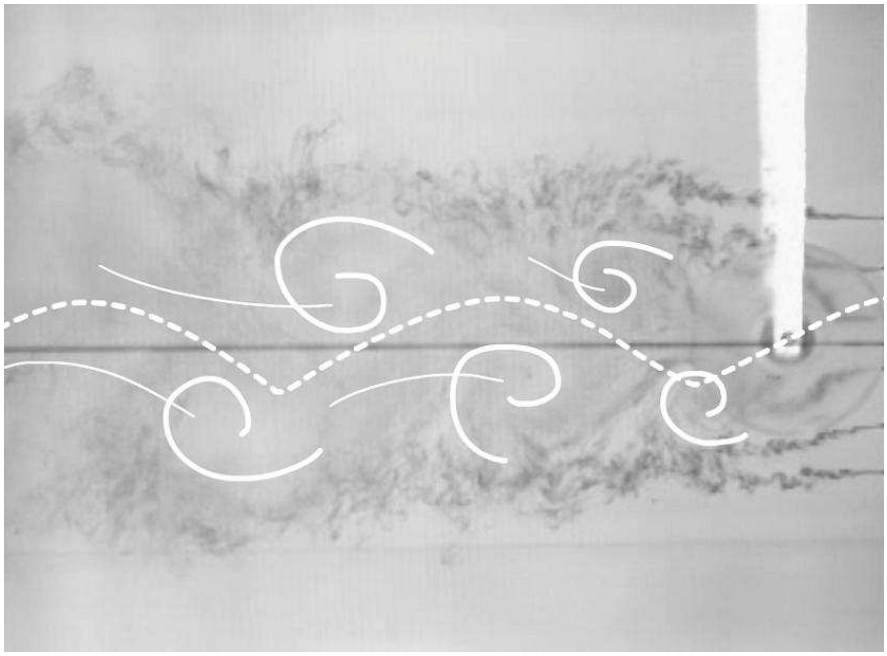

Figure 6.13: Vortex wake for single-sided impacting motion with $e = -0.47$ at $U_r = 6.14$. $R_e \approx 5400$.

For $U_r = 6.14$, i.e. in what was the upper branch of vibration, the cylinder exhibits a stable 1-impact-per-period motion, with an average amplitude between impact of $0.65D$. Flow visualisation conducted in these conditions show the cylinder shedding one single vortex when impacting on the stop and one single vortex when reaching a maximum amplitude between impacts. On the picture presented in figure 6.13, the horizontal black line that was traced out on the glass of the tank shows the cylinder's rest position, and the thick dashed white line shows the trajectory the cylinder exhibits during the video. Positions of vortices at the moment of the picture are highlighted by thick white lines, with the approximative displacement of their centres drawn in light white line. The asymmetry of the motion being low at this reduced velocity, the five vortices shed by the cylinder while crossing the recording window form a wake nearly symmetric with respect to the rest position of the cylinder.

Flow visualisation is made also at $U_r = 9.22$, in the plateau of ${A^*_{max}}^+$. During the movie recorded, the cylinder clearly sheds only one single vortex when hitting the stop. However it is unclear what happens at the top of its oscillation. A pair of vortex seems to be shed, with the second vortex of the pair weaker than the first. As in the 2P mode in the linear case, the second vortex seems to disappear quickly, leaving only one single vortex in the wake of the cylinder. The snapshot extracted from the video recorded and presented in figure 6.15 shows that the resulting wake is not symmetric any more as vortices shed when hitting the stop are convected close to the cylinder's rest position while the others are much further from it.

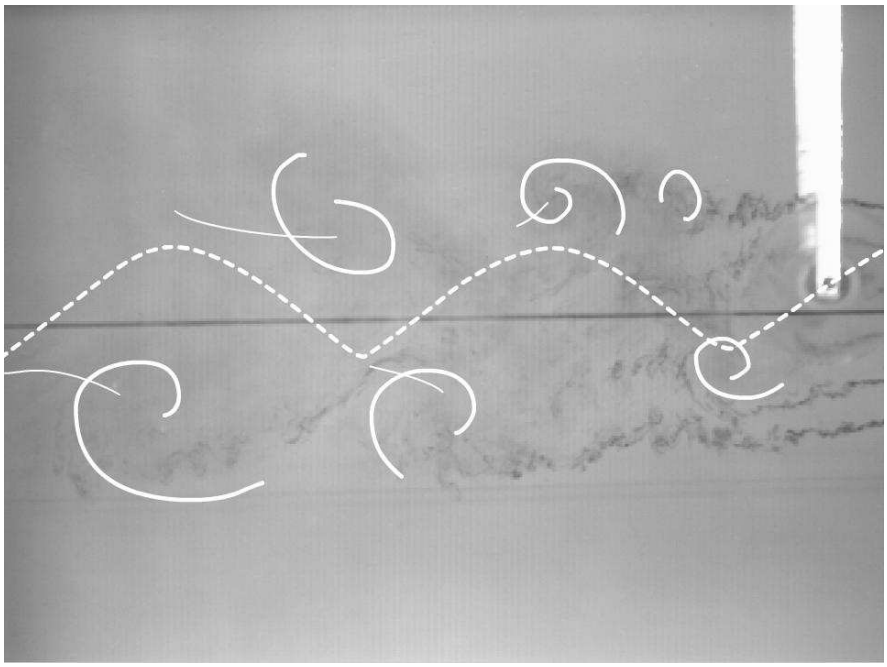

Figure 6.14: P+S mode of vortex formation for single-sided impacting motion with $e = -0.47$ at $U_r = 9.22$. $R_e \approx 8100$.

This result however is uncertain and other tests would be needed to further investigate the exact dynamics of the wake with motion limited on one side.

As the stop is brought closer to $e = -0.30$, two single vortices are shed in an oscillation cycle, as with $e = -0.47$. At low flow velocities, the motion of the cylinder

is slightly asymmetric, and the vortices shed when hitting the stop are closer to the cylinder's rest position.

When increasing the reduced velocity, the maximum amplitude between impacts increases and reaches large values. At $U_r = 9.22$ with $e = 0.3$, A^*_{max} is measured at $1.42D$; the motion is then strongly asymmetric. Flow visualisation made during this test still show one vortex being shed when impacting and one at the top of the oscillation cycle, but the resulting wake is therefore very asymmetric with respect to the cylinder's rest position.

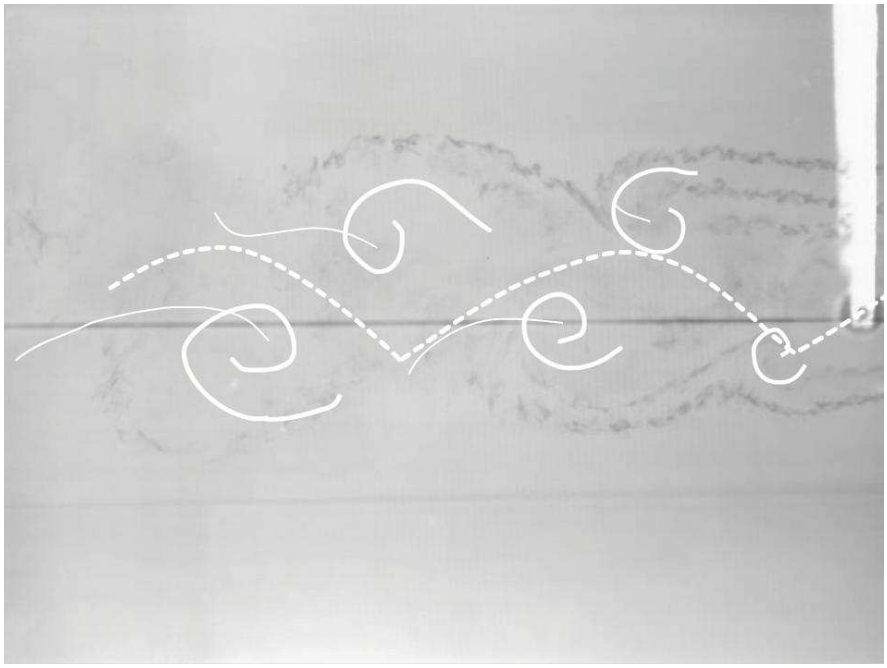

Figure 6.15: Asymmetric 2S wake for single-sided impacting motion with $e = 0.3$ at $U_r = 9.22$. $R_e \approx 8100$.

The vortex formation process is then much affected by the limitation of the cylinder's motion. In the linear case in the upper branch of vibration, the amplitude of vibration is high and a 2P mode with the second vortex weaker than the first one is observed. In this range of reduced velocity, only two vortices are shed per oscillation cycle when

the motion is limited on one side, one when hitting the stop and one when reaching its maximum amplitude between impacts. The frequency of the motion is close to the Strouhal frequency suggesting that the modified fluid-structure interaction drives the cylinder through forces resulting from this 2S mode of vortex shedding.

6.7 Conclusions

In the case of impacts on only one stiff stop, the fluid-structure interaction is again affected by the limitation of the amplitude of motion of the cylinder. In the same way, the contact with the stop interrupts the build up of vortices and only one single vortex is shed after an impact. 2P modes of vortex formation are not observed when impact occurs. With a large offset, dynamics of the motion are affected as the cylinder exhibits 1-impact-per-period periodic motions at a frequency f close to f_{vs} over most of the impacting domain. The maximum amplitude reached between impacts in these motions increases with U_r, as the impact velocity and the impact force. In a similar way as for the case of impacts on two stops, chaotic 1-impact period-k motions occur on a narrow window at the start of the impacting domain.

When the offset is decreased, the width of this window slightly increases. 1-impact-per-period motions are stable over a wide range of reduced velocity, with their amplitude between impact increasing with U_r. At large flow velocities, ${A^*_{max}}^+$ reaches a plateau at its maximum value, and destabilisation of the 1-impact-per-period cycle occurs.

With a very small offset value, the chaotic window at the beginning of the impacting domain becomes wide, and 1-impact-period motions become stable at larger flow velocities. In the chaotic window, the frequency of the main peak, appearing in very disorganised frequency distributions, is equal to its value in the case of linear

restraints. Maximum amplitude between impacts, average impact velocity and average impact force increase slowly in this window. A change in the frequency response seems to occur at the transition to the window of stability of 1-impact-per-period motions, as f, present in much more organised frequency distributions, takes values close to f_{vs}. The maximum amplitude between impacts, the impact velocity and the impact force increase first strongly with U_r in this window, but at large flow velocity they reach a plateau as destabilisation of the 1-impact-per-period cycle occurs.

Chapter 7

Numerical simulation of VIV with non-linear restraints

Industrial applications highlight the current inability to predict the dynamic response of structures to fluidstructure interactions. Numerical codes for prediction of VIV of structures require the input of the in-phase and out-of-phase components of the lift coefficients, in-line drag coefficients, correlation lengths, damping coefficients, relative roughness, shear, waves, and currents, among other parameters, and thus also require the input of relatively large safety factors. The estimated cost of countering VIV in the recent multi-billion pounds projects of offshore platforms is estimated to approximately 10% of the cost of the project itself.

Chaplin et al. have gathered in [83] blind predictions of experimental tests of VIV of a tensioned riser from eleven different numerical codes, using for example a vortex-tracking model, a wake oscillator model, a finite element method, and CFD computations. Results given by the wake oscillator model show in some cases good agreement with experimental data, which is interesting considering their simplicity.

7.1 Wake oscillator models

Bishop & Hassan [84] developed the idea of Birkhoff [85] of using a non-linear equation modelling the effect of the wake on the transverse vibration of the cylinder. They created the first wake oscillator model by coupling the equation of motion for the cylinder with another equation for its lift coefficient, and several other wake oscillator models have been developed since. These models, generally self-exciting and self-limiting, consider the flow as two-dimensional and mostly predict only the cross-flow vibration of the structure. They are semi-empirical as calibrated by fits with experimental data, but present the advantage of being low in computation cost.

In 1970, Hartlen & Currie [86] formulated an equation for the lift coefficient C_L to make it meet the requirements for cases of a fixed cylinder, a forced cylinder and a cylinder undergoing VIV. Their equation for the lift coefficient is coupled with the cylinder's velocity $\dot{y}$:

$$\ddot{C_L} - A\Omega_s \dot{C_L} + \frac{B}{\Omega_s}\dot{C_L^3} + \Omega_s^2 C_L = D\dot{y} \tag{7.1.1}$$

The constant A,B,D of the equation 7.1.1 can be deduced from experiments with fixed and forced cylinders. This equation is of the general Van der Pol (VDP) type [87]:

$$\ddot{y} - \epsilon(1 - y^2)\dot{y} + y = 0 \tag{7.1.2}$$

It exhibits some of some features similar to those encountered in VIV, and is used in other VDP wake oscillator models.

Some wake oscillator models consider lock-in as the synchronisation of the cylinder's oscillation frequency with the cylinder's natural frequency. However this assumption is only true for high mass ratio cases with $m* > O(10)$. For lower mass ratios the fluid has an increased ability to control the cylinder's vibration.

Other wake oscillator models can describe qualitatively and sometimes quantitatively

the main features of the VIV of a structure with low mass ratio and low damping, such as the discrepancy of the oscillation frequency from the natural frequency of the system when the mass ratio is low. It is interesting to investigate if these wake oscillator models are able to model the VIV of a rigid cylinder whose amplitude is limited by stiff stops.

To do so, wake oscillator models developed to predict the VIV of low-mass low-damping structures are chosen to simulate the VIV of a cylinder similar to that studied in the experimental part of this work and subject to limitation of its amplitude. For this study, the main concern in the choice of the models is their ability to present a frequency response that can be associated with low-mass low-damping cases. Two wake oscillator models of different nature have this characteristic, one developed by Facchinetti et al. [88], using a VDP equation, and another developed by Falco et al. [89]. This latter has more physics, as simulating the effect of the wake by a mass attached to the cylinder. These two different wake oscillator models are therefore chosen to investigate the simulation of the VIV of a rigid cylinder whose amplitude is limited. These models are presented in more detail in the next section, as well as their responses first in the case of linear restraints and then when stops are present to limit the cylinder's motion.

7.1.1 The Van der Pol model

In the wake oscillator developed by Facchinetti & al. [88], the cross-flow displacement of the cylinder y is described by a classic equation of motion involving structural mechanical parameters as structural mass m_s, structural stiffness k, and structural damping c. The cylinder's oscillation is driven by a fluctuating lift force resulting from vortex shedding $S = \frac{1}{2}\rho U^2 D C_L$ where C_L is the lift coefficient. A forced Van der Pol equation is used to describe the effect of the wake on the cylinder. It drives a

reduced lift coefficient $q = 2C_L/C_{L_0}$ where C_{L_0} is the reference lift coefficient observed on a fixed cylinder usually taken as $C_{L_0} = 0.3$. Coupling with the cylinder is achieved through the forcing term F_q of the VDP equation, representing the action of the structure on the fluid wake. The model is described by the system:

$$m\ddot{y} + c\dot{y} + ky = S \tag{7.1.3}$$
$$\ddot{q} + \epsilon\Omega_f(q^2 - 1)\dot{q} + \Omega_f^2 q = F_q \tag{7.1.4}$$

in which $\Omega_f = 2\pi S_t U/D$ is the vortex shedding angular frequency, based on a Strouhal number S_t equal to 0.2. In this system, the mass m encompasses the structural mass m_s and the added mass $m_A = C_A\rho\pi D^2/4$ in which $C_A = 1.0$: $m = m_s + m_A$. The linear damping $c = c_s + c_f$ includes the structural damping c_s and the fluid damping $c_f = \gamma\Omega_f\rho D^2$ in which γ is a stall parameter assumed to be constant at $\gamma = 0.8$.

Non-dimensional forms of equations 7.1.3 and 7.1.4 are:

$$\ddot{y} + \left(2\zeta\delta + \frac{\gamma}{\mu}\right)\dot{y} + \delta^2 y = s \tag{7.1.5}$$
$$\ddot{q} + \epsilon(q^2 - 1)\dot{q} + q = f_q \tag{7.1.6}$$

Where $\zeta = c/(2m\Omega_s)$ is the reduced damping, $\Omega_s = \sqrt{k/m}$ the structural angular frequency, $\delta = \Omega_s/\Omega_f$ the frequency ratio and $\mu = (m_s + m_A)/(\rho D^2)$ is the mass ratio. s and f_q are the dimensionless coupling terms, $s = S/(D\Omega_f^2 m)$ and $f_q = F_q/(D\Omega_f^2)$. s is directly linked to q by the relation $s = Mq$ with $M = C_{L_0}/(16\pi^2 S_t^2\mu) = \frac{0.05}{\mu}$.

In [88], the authors consider three modes of coupling for this action: a displacement coupling in which $f_q = Ay$, a velocity coupling in which $f_q = A\dot{y}$, and an acceleration coupling in which $f_q = A\ddot{y}$. Their results show that "*the acceleration coupling model succeeds in modeling all the features of VIV analysed, qualitatively and, in some aspects, quantitatively*" The model exhibits indeed a range of flow velocities where high amplitude vibrations occur, and in which the frequency of the structure, otherwise locked onto the vortex shedding frequency, becomes locked onto the structure's natural frequency.

More interesting to our project is the ability of this model to describe qualitatively the features of the VIV of a rigid cylinder with low m^* and low damping. The maximum amplitude of oscillation increases when the Skop-Griffin parameter is decreased and extension of the lock-in domain is also observed when decreasing m^*. The lock-in domain even becomes unbounded as m^* tends to zero, which is consistent with experimental results. The frequency response at low damping and low mass ratio also reproduces the discrepancy from the natural frequency expected in such cases.

Because of these features, the acceleration coupling model presented in [88] is chosen here to simulate the experimental tests carried out in this project. Implementation of equations 7.1.5 and 7.1.6 is done numerically with a fourth-order Runge Kutta method, using a time step for integration equal to 2.7×10^{-4} s. This value is chosen as, in the case of a sinusoidally-excited mass impacting on both sides, for which the system can be also solved with a semi-analytical method considered as the exact solution, it results in the best simulation of the same system with the RK4 method.

For each flow velocity set, the cylinder is started from rest and, as the model is not self-exciting, a very small initial perturbation is given to start its oscillation. The model describes a transient period before reaching a steady state, but as characteristics of its oscillation are recorded after one thousand seconds of real time computed, this transient period is not taken into account in the results presented in this work.

As this part of the project is concerned with the simulation of the VIV of a rigid cylinder whose amplitude is limited by stiff stops, the amplitude response of the model in the case of linear restraints is to fit experimental data for the same case. However, as noted by its authors, this model underestimates the amplitude of vibration when using the suggested values of A=12 and ϵ=0.3. They comment that the fit may have been done using the total lift magnification, resulting in A=3 and ϵ=0.3, but leading to a lock-in domain symmetric with respect to $1/S_t$.

The model response, with A=12 and ϵ=0.3 and parameters fixed to match the experimental conditions of the present project in the case of linear restraints, i.e. ρ=1000 kg/m^3, m^*=1.74, ζ=0.0079, and $f_{n_{water}} = 0.9765$ Hz is presented in figure 7.1. The amplitude response of the model plotted on the graph exhibits for these

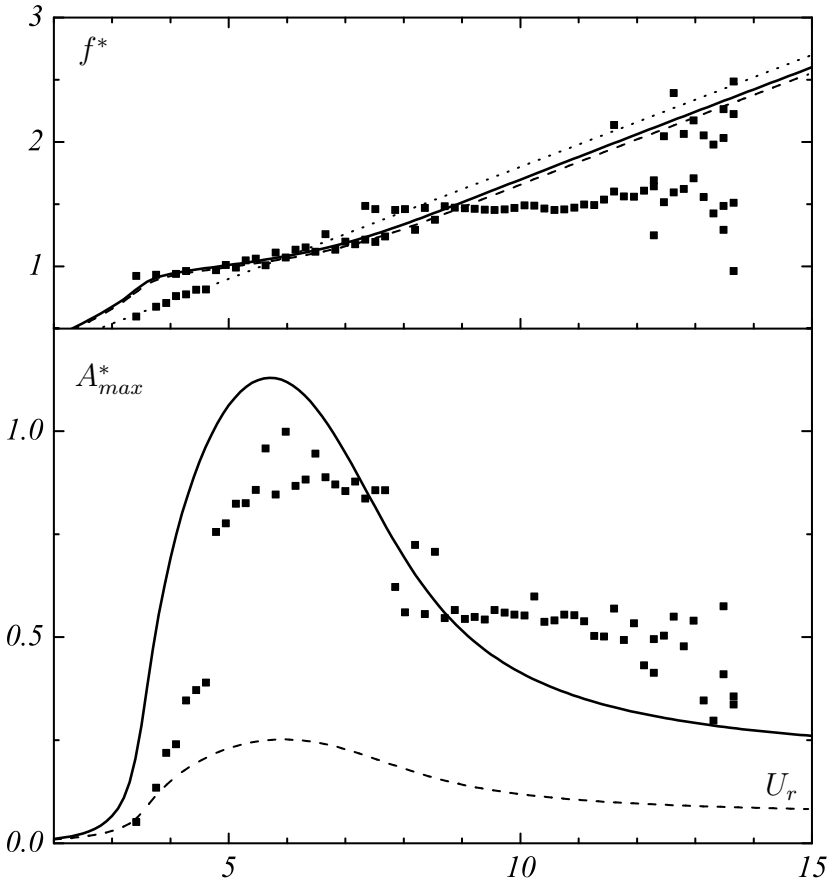

Figure 7.1: Comparison of VDP model responses with A=12, ϵ=0.3 (----) and A=12, ϵ=0.01 (—) with experimental data at low mass-damping: present work (■).

parameters a high amplitude vibration domain starting at about the same value of flow velocity as the experimental data, and extending up to high flow velocities. The frequency before lock-in increases with U_r with a slope of about 0.22; its is larger than experimental data which in this part follow $f_{vs} = 0.18U/D$, plotted on this graph with dots. When f^* reaches a value of about 0.9, a phenomenon of lock-in in

frequency starts. The frequency in the lock-in domain is not locked onto the natural frequency of the cylinder. It increases slowly with U_r, with a slope of about 0.06. Predicted values of f^* are very close to experimental data all over the upper branch of vibration. At $U_r \approx 8$, the frequency, lower than f_{vs}, increases back to present a slope of about 0.18 for larger reduced velocities. The model does not predict the lock-in of the frequency ratio onto f^*_{lower} occurring in the experiments over the lower branch of vibration. The frequency, very close to experimental data everywhere apart in the lower branch, shows overall a good agreement with experimental data.

The amplitude of oscillation is however by underestimated far when setting A=12 and ϵ=0.3, its maximum value approaching only 0.26 D. A really low value of ϵ=0.01 results, as presented in figure 7.1, in a better estimation of the maximum amplitude reached during the experiments, for a reduced velocity close to the experimental value. With this value for ϵ, the VDP oscillator predicts the start of the lock-in domain for a reduced velocity slightly lower than in the experiments, and maximum amplitude of oscillation reaches $1.13D$ for $U_r = 5.70$. The frequency response of the cylinder is unchanged. The lower branch is however still not apparent in the simulations, resulting in the underestimation of the amplitude of vibration between U_r=8 to ≈12. For larger U_r the amplitude of vibration is overestimated as lock-out has occurred in experimental data and maximum amplitude of vibration is small.

This wake oscillator model with acceleration coupling is interesting for the simulation of low-$m^*\zeta$ cases as its frequency response presents the discrepancy from the structural natural frequency expected in such cases, and, with parameters set to match the ones of the present low-mass low-damping experiments and ϵ set to 0.01, its amplitude and frequency responses are close to experimental data.

Another wake oscillator model, the “Milan model”, developed in 1999 in Milan, Italy, by Falco et al. [89] also presents this ability to model some features of the VIV of low-mass low-damping cylinders. This model is used in industrial codes of simulation

of offshore structures, and also presents motivations for investigating its behaviour in the case of limitation of the amplitude of the cylinder.

7.1.2 The Milan oscillator model

The Milan wake oscillator [89] models the effects of vortex shedding on a cylinder oscillating in the cross-flow direction by the action of a mass connected to the cylinder with a system of non-linear springs and dash pots, as shown in figure 7.2. The cylinder of mass m_s is supported by a system with linear stiffness and damping, the oscillator of mass m_o by a system with non-linear stiffness and damping, and their interaction is also made through a system of non-linear springs and dash pots.

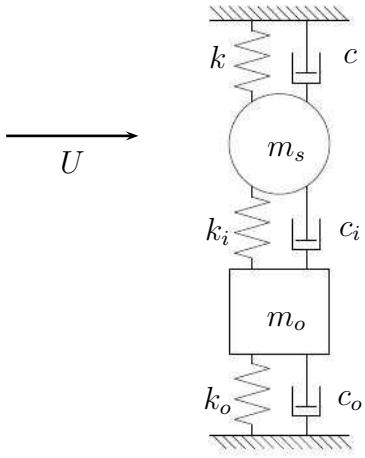

Figure 7.2: Milan oscillator model principle.

The equations of motion for the cylinder and the mass, whose respective displacements with respect to their rest position, denoted y and x, are deducted from Newton's second law:

$$m_s\ddot{y} + c\dot{y} + ky = F_i + F_m \tag{7.1.7}$$

$$m_0\ddot{x} = F_o - F_i \tag{7.1.8}$$

where the dot ($\dot{}$) represents the derivative with respect to time. F_m is the transverse component of a Morrison type force which accounts for the cylinder's hydrodynamic inertial and damping forces [90], F_i is the resultant of forces on the cylinder at its interfaces and F_o of the forces on the oscillator. The non-linearities in these latter two forces are introduced by a third order model in the stiffness and damping terms:

$$F_o = -k_{ol}x + k_{on}x^3 + c_{ol}\dot{x} - c_{on}\dot{x}^3 \tag{7.1.9}$$

$$F_i = -k_{il}z + k_{in}z^3 - c_{il}\dot{z} + c_{in}\dot{z}^3 \tag{7.1.10}$$

where z denotes the displacement of the cylinder with respect to the oscillator, $z = y - x$ and $\dot{z} = \dot{y} - \dot{x}$. The subscripts in the stiffness coefficients $k_{ol}, k_{on}, k_{il}, k_{im}$ and in the damping coefficients $c_{ol}, c_{on}, c_{il}, c_{im}$ indicate the system they refer to by $_o$ for oscillator and $_i$ for interface, and those corresponding to the linear or non-linear contribution by respectively $_l$ and $_n$.

The drag on the cylinder acts in the direction of the relative velocity between the cylinder and the fluid. As the cylinder oscillates, it has a component F_m that is taken into account in the model. The Morison equation is widely used to express the drag on a circular cylinder in a fluid flow of density ρ and velocity U_f. It expresses it as the sum of the cylinder's hydrodynamic inertial and damping forces:

$$F = -C_A\rho\frac{\pi D^2}{4}\ddot{y} - C_D\rho\frac{D}{2}U_f\dot{y} \tag{7.1.11}$$

C_A and C_D being the hydrodynamic inertial and damping coefficients obtained from the literature. In this case, $C_A = 1.0$ as in the case of a cylinder moving in a stationary inviscid fluid, and $C_D = 1.2$. As the cylinder oscillates transverse to the flow, the relative velocity is $U_f = \sqrt{U^2 + \dot{y}^2}$, and then the force F_m is expressed by:

$$F_m = -C_A\rho\frac{\pi D^2}{4}\ddot{y} - C_D\rho\frac{D}{2}[U^2 + \dot{y}^2]^{\frac{1}{2}}\dot{y} \tag{7.1.12}$$

The mass of the oscillator is chosen such as its frequency corresponds to the Strouhal

frequency f_s when the cylinder is not moving. This leads to:

$$f_s = \frac{1}{2\pi}\sqrt{\frac{k_{ol} + k_{il}}{m_o}} \tag{7.1.13}$$

The stiffness and damping coefficients $k_{ol}, k_{on}, k_{il}, k_{im}, c_{ol}, c_{on}, c_{il}, c_{im}$ are made non-dimensional using system characteristic variables:

$$C_{k_{ol}} = \frac{k_{ol}D}{\frac{1}{2}\rho U^2 D} \quad ; \quad C_{k_{on}} = \frac{k_{on}D^3}{\frac{1}{2}\rho U^2 D}$$

$$C_{c_{ol}} = \frac{c_{ol}\omega_s D}{\frac{1}{2}\rho U^2 D} \quad ; \quad C_{c_{on}} = \frac{c_{on}[\omega_s D]^3}{\frac{1}{2}\rho U^2 D}$$

Falco et al. carried out experimental tests of the transverse VIV of a linearly-supported cylinder at mass ratio $m^* = 5.22$ and damping ratio $\zeta = 0.02$, with Reynolds number of some thousands. They used their experimental results, displayed in figure 7.3 to determine the optimum values for the stiffness and damping reduced coefficients, which are listed in table 7.1.

$C_{k_{ol}}$	3.1	$C_{k_{on}}$	0.05
$C_{c_{ol}}$	2.15	$C_{c_{on}}$	0.45
$C_{k_{il}}$	1.364	$C_{k_{in}}$	0.2
$C_{c_{il}}$	5.4	$C_{c_{in}}$	0.0

Table 7.1: Table of coefficients of the Milan oscillator.

The values of $C_{c_{ol}}$ and $C_{c_{il}}$ render the oscillator non-self-exciting, as $C_{c_{ol}} - C_{c_{il}} < 0$. As the VDP model previously presented, this model has to be given a slight perturbation from its equilibrium position at the beginning of the computation to start its oscillation. Time integration of this model was done with a fourth-order Runge-Kutta method, and tested first by comparing results obtained with those published in the original paper. Figure 7.3 displays experimental and numerical results from Falco et al. [89], as well as the results obtained for the same conditions with the RK4 method.

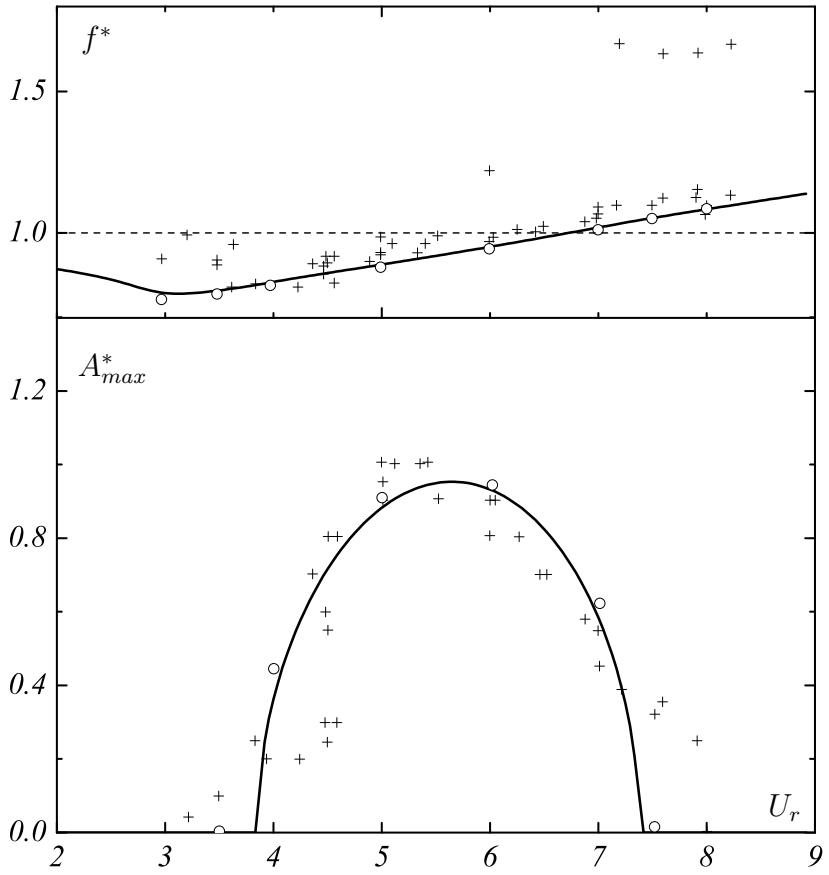

Figure 7.3: Frequency and amplitude responses of the Milan oscillator for $m^* = 5.22$ and $\zeta = 0.02$. (+): Falco's experimental data; (∘): Falco's numerical results; (—): RK4 implementation of the Milan model.

In this figure, the two numerical results agree nearly perfectly. The amplitude response of the Milan model displays high amplitude oscillations over about the same range of flow velocities as the experimental data. However, the experimental data presented in [89] do not exhibit the clear distinction between upper and lower branches usually appearing for such low values of m^* and ζ. In these data, the initial branch of excitation clearly appears, followed by an upper branch as the maximum amplitude reaches about $1D$ at $U_r \approx 5$. Transition to a lower branch seems to occur as soon as $U_r \approx 6$, but this latter is not clearly present. The maximum amplitude and

frequency of oscillation are usually constant over the lower branch, which also usually occurs on a wider range of flow velocities with such parameters. The lower branch is very narrow in these experimental data, as the amplitude of oscillation rapidly decreases after $U_r \approx 7$ with peaks appearing at the Strouhal frequency revealing desynchronisation and vibration dying out for $U_r > 8$. This lock-in domain is a lot narrower than in most experimental results with similar parameters.

The most interesting behaviour of this model is its frequency response. The oscillation frequency does not lock onto the natural frequency but exhibits a slow increase over all the large amplitude domain. It does not follow the Strouhal frequency, as f^* increases with a coefficient of 0.11 in this graph. This behaviour matches the general increase of the experimental points presented in [89], but the frequency f does not present any tendency to get close to f_{vs} out of the lock-in domain. Nevertheless, this slow increase of the oscillation frequency is similar to that of the oscillation frequency of a low-mass ratio low-damping cylinder subject to VIV, in its upper branch of vibration.

Parameters of the Milan oscillator are set to match those of the present experiment, i.e. ρ=1000 kg/m^3, m^*=1.74, $\zeta = 0.0079$, and $f_n = 0.9765$ Hz. Its amplitude and frequency responses are compared to experimental data from the present work in figure 7.4.

With these parameters, the model predicts the high-amplitude domain to start for $U_r \approx 2.8$, which is close to experimental results. However, because of the strong increase of the amplitude of oscillation, A^*_{max} is by far overestimated in the range of flow velocities corresponding to the experimental initial branch of excitation. The model predicts about correctly the maximum amplitude of oscillation of about $1D$ with $1.12D$, even if this maximum occurs for $U_r = 5.2$ instead of 6 experimentally. The predicted high-amplitude domain extends only up to $U_r = 9$, which is much lower than in the experimental data. In fact, the model does not predict the high

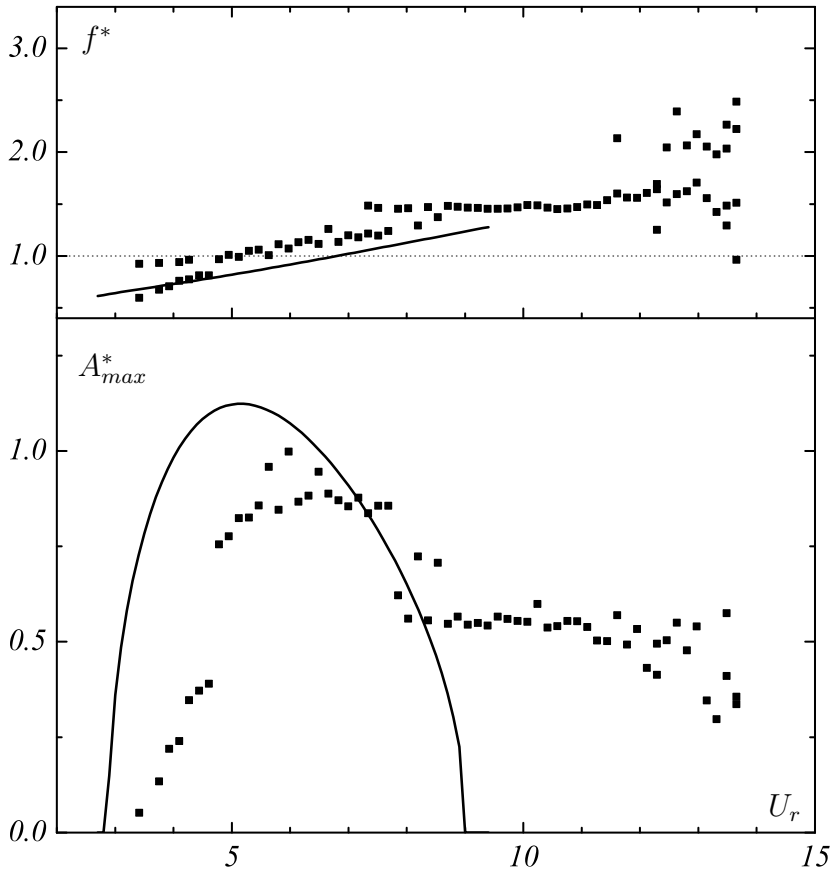

Figure 7.4: Comparison of Milan model response with present experimental data. (—): Milan model, (■): Present data.

amplitude vibrations occurring in the experiments in the range of reduced velocities corresponding to the lower branch of excitation.

It can be noted that between $U_r = 7$ and $U_r = 8.3$ the amplitude of oscillation corresponds accurately to the r.m.s amplitude of experimental results. In experimental data, the decrease of the r.m.s amplitude of oscillation is however due to the intermittent character of the transition between upper and lower modes of excitation. r.m.s values are therefore in this range of flow velocity not representative of the cylinder's dynamics.

With these parameters, predicted oscillations of the cylinder are periodic, of frequency increasing linearly with U_r with a slope of about 0.1 over the whole lock-in domain. The oscillation frequency f is underestimated by the model for $U_r > 5$, but it exhibits the same increase as in the experiments over the whole upper branch of vibration, characteristic of low-mass low-damping systems. It equals its experimental value at $U_r \approx 4$, where amplitude of oscillation is about four times overestimated.

To model an amplitude limiting stop acting on the cylinder, a step change in the system stiffness can be inserted in both of these two wake oscillator models when the simulated cylinder reaches the stop position.

Impact is not considered as occurring on rigid stops with an infinitesimally small contact time and for which condition of impenetrability and restitution coefficient intervene. The cylinder is considered as impacting on stiff stops, characterized by a high stiffness ratio, without loss of energy. Its dynamics during impact, which is of finite time, are computed by implementation of the respective dynamical systems in conditions of contact. Time integration is chosen to be made for both models with a RK4 method as this latter proved, during a preliminary study for the implementation of the motion of a harmonically-excited mass impacting on two symmetrically-placed stops, to be the most accurate when using a time step of 8.10^{-5} s.

In order to compare the response of these models in such cases to experimental data for the same conditions, physical parameters are kept at the same values matching the conditions of the present experiments, and the stop stiffness k_s is set to obtain the stiffness ratio r_k equal to 344. To investigate the effect of the amplitude limitation of the cylinder subject to VIV modelled with each of the two selected wake oscillators, the methodology used during the experimental investigation undertaken in this project can also be used: the effect of amplitude limitation with a large offset is first of all investigated, and the offset is then reduced to appreciate the influence of this parameter on the response of the system. Results obtained with the Milan

oscillator are presented first, followed by results from the VDP oscillator. For both models, response under asymmetric structural restraints involving only one stop is presented first.

7.2 Effect of amplitude limitation on the response of the Milan oscillator

7.2.1 Milan Oscillator with impact on one stiff stop

7.2.1.1 Dynamics of the Milan oscillator with impact on one stiff stop placed at y_s=-0.65D

The bifurcation diagrams of peak excursions obtained with the Milan oscillator for the single-sided impacting case with y_s=- 0.65D and from experimental data for the same case are presented in figure 7.5.
In this figure, the lower peaks are of interest as they give information about the dynamics in the region of the non-linearity. For the Milan oscillator, they show contact with the stop starting at $U_r \approx 3.287$, which is earlier than in the experiments where it starts at $U_r \approx 5$. Contact with the stop is predicted to stop to occur up to $U_r \approx 8$, which is about the same value as in the experimental results. The upper peaks of vibration are of interest in this asymmetrical case, as characteristic of the dynamics of the single-sided impacting motions. Predicted maximum amplitudes between impacts generally increase with U_r, as they do in the experiments. Peak excursions between impacts exhibit even the same trend of increase in both cases. In the range of reduced velocities where impact occurs both in the experiments and with the Milan oscillator, the predicted amplitude of oscillation is close to its maximum experimental value.

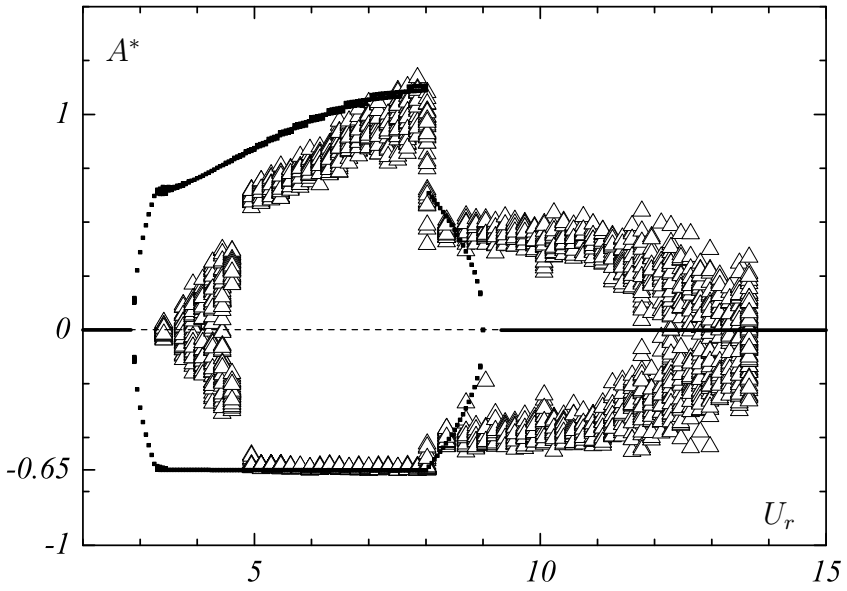

Figure 7.5: Bifurcation diagram of peak excursions for single-sided impacting motions with $e = -0.65$. (—): Milan model; (△): Experimental data

Closer observation of the bifurcation diagram of upper peak amplitude obtained with the Milan oscillator presented in figure 7.6(a) reveals that the cylinder exhibits a succession of long windows of intermittent motions between very narrow windows of stability of *1-1-1* motions. In each of these windows, marked on both sides by discontinuities of the

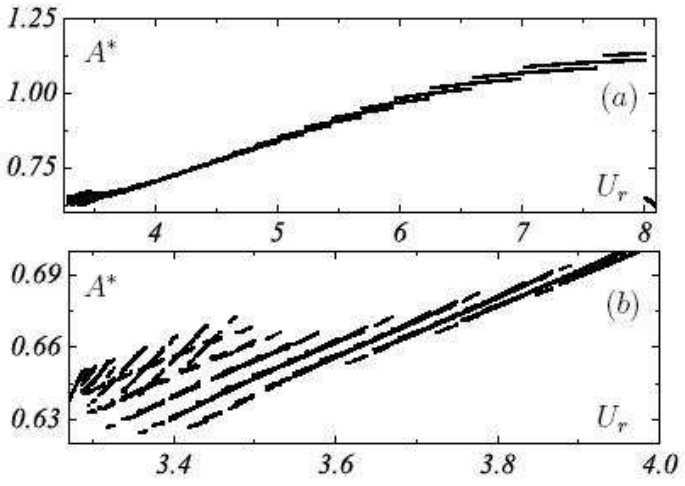

Figure 7.6: Close-ups on the bifurcation diagram of peak excursions for single-sided impacting motions with $e = -0.65$. (a): intermittent windows with amplitude increasing with U_r. (b): Chaotic window at the start of the impacting domain.

bifurcation diagram, the cylinder impacts on the stop at every impact, but bounces intermittently two different maximum amplitudes between impacts, resulting in two points at a fixed U_r on figure 7.5(a), and in two nearly parallel lines when varying U_r.

This is illustrated by the return map of upper peak excursions plotted for one of these motions in figure 7.7. Return maps of upper peak excursions present the upper peak excursion reached by the cylinder during a cycle of oscillation A^*_n as a function of the upper peak excursion it reached during the previous cycle $A^*_{n\text{-}1}$. In such a representation, a purely periodic oscillation is represented by a single point on the line $A^*_n = A^*_{n\text{-}1}$. The two encircled points in figure 7.7 correspond to the two periodic cycles on which the system intermittently switches at this value of U_r. At the beginning of a window of intermittent *1-1-1* motion, as for $U_r = 7.05$, the system spends more time on the mode with the lowest amplitude. The point corresponding to this cycle is encircled twice on the graph to illustrate the dominance of this mode. But as U_r is increased, amplitudes of both limit cycles grow, as well as the relative time spent on the mode with the highest amplitude. At the end of a window, the system finishes in spending all its time on this mode, which is therefore stable, but only over a very narrow range of flow velocities. As U_r is further increased, the system starts to jump intermittently on another higher amplitude *1-1-1* mode, starting another window of intermittent motion.

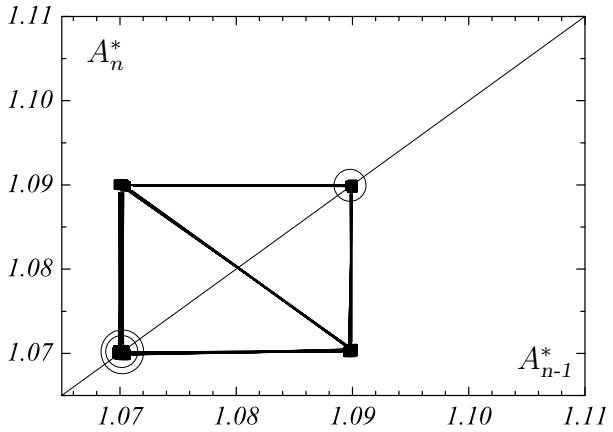

Figure 7.7: Return maps of upper peak excursions for intermittent single-sided impacting motions with $e = -0.65$ for $U_r = 7.05$.

It can be noted that the fact that the amplitudes of both modes present during these

intermittent transitions are so close would have made such a mode of vibration undetected in the experiments and it would have been simply interpreted as a 1-impact-per-cycle motion with some amplitude modulation. This intermittent nature of the motion has been observed after a very long time of computation, but as stabilisation of the system on a limit cycle can be very long, this intermittent nature could be just an artificial feature of the model appearing because of its time integration. This behaviour has also not been tested against variations of the implementation time.

As illustrated by figure 7.6(b), the Milan oscillator predicts a small window of chaotic motion at the beginning of the impacting domain. At the lowest flow velocity where impact occurs, when the cylinder impacts on the stop, its amplitude of vibration at the next cycle is smaller, and impact does not occur. The impact drives the system back into the attraction basin of the limit cycle it would have with linear restraints, and its amplitude of vibration then grows with time, until the cylinder reaches the stop again.

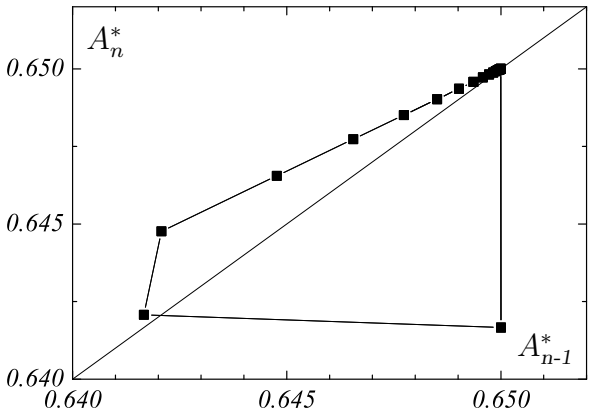

Figure 7.8: Return map of upper peak excursions of the 1-impact period-24 motion for $e = -0.65$ at $U_r = 3.286932$.

For $U_r = 3.286932$, the cylinder describes after an impact 24 periods of amplitude growth during each cycle before reaching the stop again. The limit cycle, of which return map of upper peak excursions is presented in figure 7.8, is therefore a periodic 1-impact period-24 motion.

For this type of periodic motion (noting that time series of

displacement are nearly noiseless with numerical models), k is equal to the number of lower peaks of oscillation between impacts, plus one. The number of cycles between successive impacts, characteristic of these motions, can therefore be recorded for each impact of every time series simulated at all flow velocity. Bifurcation diagrams of the number of cycles k between impacts and of the lower peak excursions, are shown in figure 7.9 in order to identify periodic motions and their bifurcations.

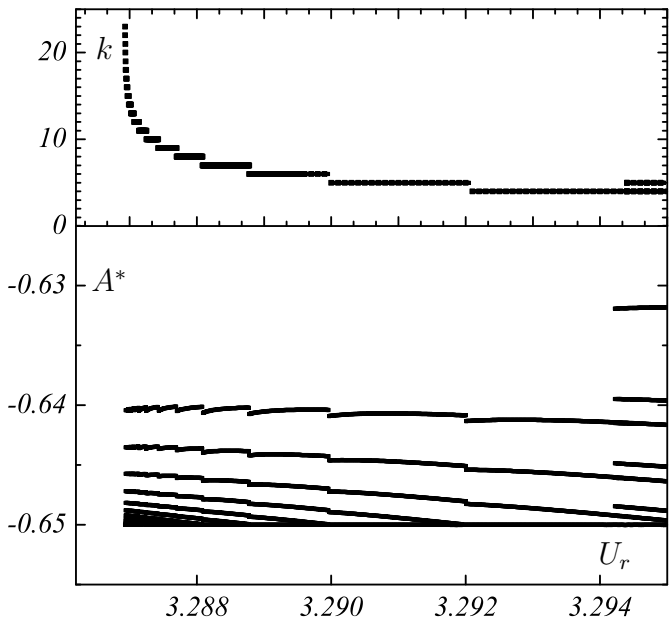

Figure 7.9: Grazing bifurcations of 1-impact period-k cycles at the beginning of the impacting domain

Values of k show that, at the beginning of the impacting domain, many grazing bifurcations occur as U_r slightly increases, changing stable 1-impact period-k cycles into stable 1-impact period-(k-*1*) cycles. It can be noted that the width of the windows of stability of these 1-impact period-k cycles seems to be ruled by an inverse law, suggesting that, by carefully setting U_r and leaving the computation run a very large amount of time, 1-impact period-k cycles with very large k could be observed for U_r slightly lower than 3.286932. For each of these 1-impact period-k cycles, the bifurcation diagram shows that, as U_r increases, amplitudes of the non-impacting cycles between impacts increase. It is when at some value of U_r the amplitude of the last cycle before impact reaches the stop position that a grazing bifurcation occurs.

As illustrated by figure 7.9, the system follows this evolution up to $U_r \approx 3.2943$ where the existing 1-impact period-4 cycle experiences another type of bifurcation, leading this time to the weak stabilisation of a seemingly intermittent 1-impact period-5 cycle.

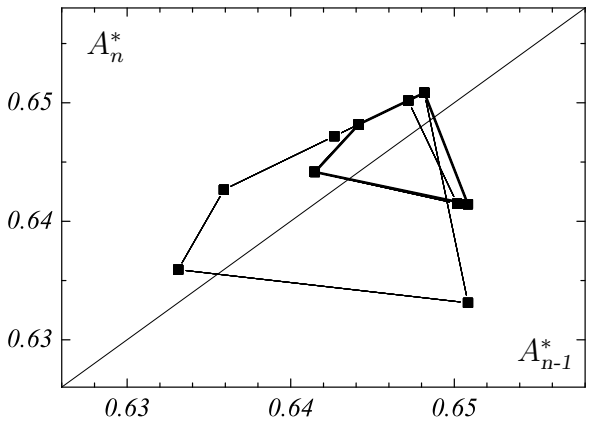

Figure 7.10: Return map of upper peak amplitudes of the intermittent motion between 1-impact period-4 and 1-impact period-5 cycles for $e = -0.65$ at $U_r = 3.295$.

The return map of lower peaks obtained for $U_r = 3.295$ and presented in figure 7.10 illustrates the coexistence of both 1-impact period-4 and 1-impact-period-5 cycles at this value of U_r. In this figure, the 1-impact period-4 mode of vibration is plotted with a thicker line than the 1-impact period-5 cycle to illustrate its predominance, as for this reduced velocity the system spends more time describing the 1-impact period-4 cycle. Such a motion is chaotic because of the intermittency between long-period periodic motions.

For larger reduced velocities up to $U_r \approx 4.25$, many other bifurcations occur. It will be sufficient to just mention here that when looked at even closer, the lines appearing in the bifurcation diagram of figure 7.6(b) appear to be in fact made of of several lines intertwined certainly revealing the presence of torus bifurcations, and the very complex nature of the dynamics of the system in this range of flow velocities. It seems to be through a process of grazing bifurcations of 1-impact period-k to 1-impact period-(k-*1*) cycles that a 1-impact-per-period cycle finds its stability around $U_r = 4.25$, and over a very narrow range of flow velocities only.

The frequency ratios of the main peaks in the frequency distributions and harmonics

whose magnitudes are larger than 1% of the one of the main peak are presented in figure 7.11 with experimental data. In both cases the main peak frequency is shown with wider symbols, to distinguish it from its harmonics. The frequency of the Milan model in the case of linear restraints, as well as the vortex shedding frequency, are also plotted in this graph with dots to help for interpretation.

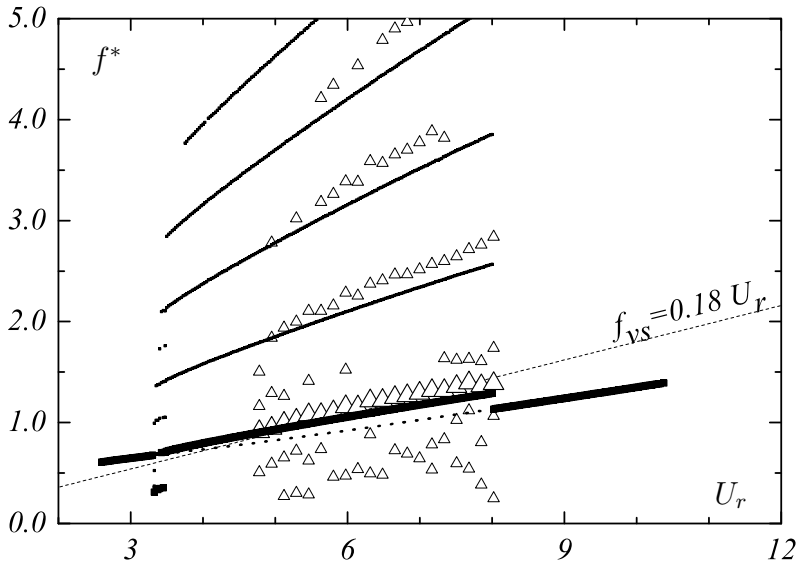

Figure 7.11: Frequency responses for single-sided impacting motions with $e = -0.65$. Milan oscillator: Main peak (▬) and harmonics (—); Experimental data: Main peak (△) and harmonics (▵).

No jump in frequency occurs at the start of the impacting domain. The main frequency of the single-sided impacting motion generally increases with U_r, with a larger slope than without stop, over all the impacting domain. A jump to the lower frequency of the system without stop occurs obviously at the end of the impacting domain.

In the chaotic window at the beginning of the impacting domain, frequency distributions contain a main peak at the oscillation frequency f, harmonics at 2, 3, 4, 5 but also at 1.5 and 2.5 times f and subharmonics at 0.5 times f. This complex but organised structure of the frequency distributions reveals complex motions with some

degree of organisation, as chaotic motions can be. Frequency distributions corresponding to the *1-1-1* motions observed over most of the impacting domain contain a main peak at f and harmonics at 2, 3, 4 and 5 times f, which is similar to those obtained experimentally.

The main frequency is close to experimental data at the start of the range of flow velocities where impact occurs experimentally, but it becomes slightly underestimated with U_r increasing. As a consequence, values of the harmonics present in the frequency distributions are also slightly underestimated by the model.

In order to quantify the chaotic nature of these motions, the main Lyapunov exponent of the system can be calculated by applying to each time series of displacement simulated with the Milan model the algorithms already used on experimental time series.

For both algorithms, the attractor is reconstructed using an embedding dimension equal to 3 as results obtained during the validation of the algorithms showed good agreement with theoretical values for lower embedding dimensions than suggested by Taken's theorem. The first zero of the autocorrelation function of the time series of reduced displacement is used as reconstruction delay, and the neighbourhood size is set to 10^-3. In Wolf's method, the evolution time is set to one twentieth of the vortex shedding period, while exponential growth of the distance is measured with Kantz's method over one eighth of the vortex shedding period.

Values of the main Lyapunov exponent obtained with both methods for all time series computed for the single-sided impacting case with $e = -0.65$ are presented in figure 7.12, with the bifurcation diagram of upper peak amplitudes for the same case to help for interpretation.

Values λ_W of the Lyapunov exponent obtained with the algorithm developed by Wolf

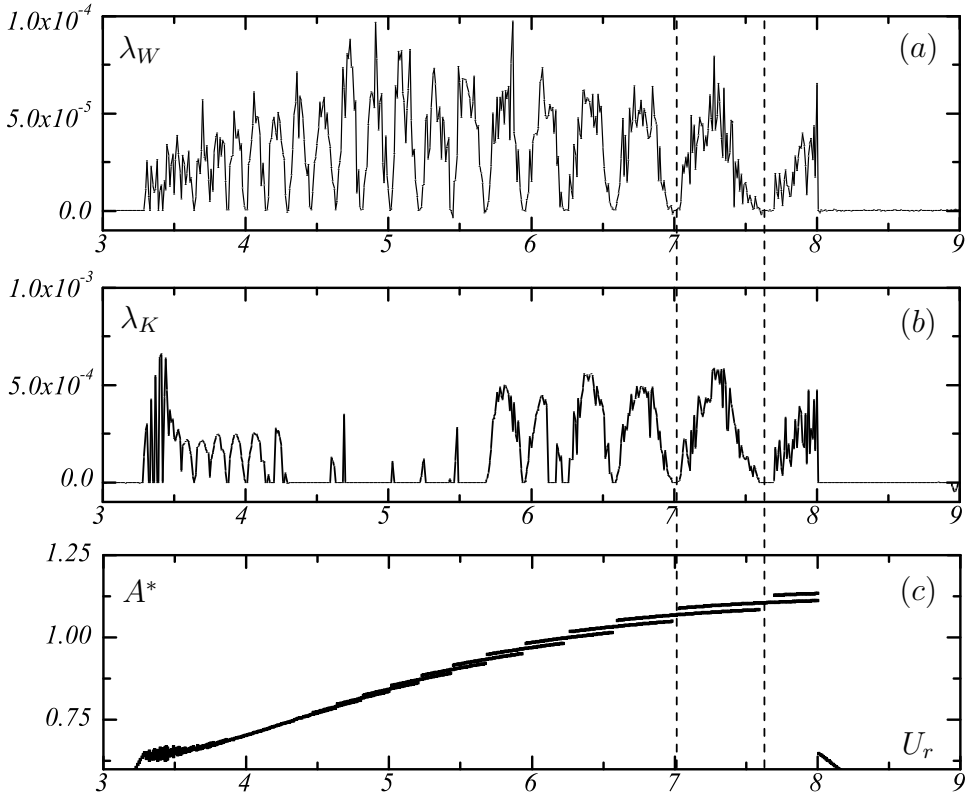

Figure 7.12: Main Lyapunov exponent for single-sided impacting motions with $e = -0.65$; (a): obtained with Wolf's method; (b): obtained with Kant'z method.

et al. are about 10 times smaller than those obtained with the algorithm developed by Kantz et al. but results from both methods exhibit the same trend. The Lyapunov exponent is close to zero outside the impacting domain, and it exhibits a succession of windows of positive values over all the impacting domain. As illustrated by the two dashed lines crossing the graphs, for $U_r > 4.25$ these windows of positive Lyapunov exponent correspond to the windows of intermittent motions observed on most of the impacting domain. The Lyapunov exponent is positive for these intermittent 1-impact-per-period motions presented earlier, demonstrating their chaotic nature, and close to zero for the stable 1-impact-per-period motions existing at both extremities of each window of intermittent motion, showing their periodic nature.

Values λ_K obtained with the method developed by Kantz et al. seem to be influenced

by the amplitude difference between the two modes of vibration present in these intermittent motions as they are close to zero when the amplitude difference is small while λ_W exhibits windows of positive values. λ_K increases when the amplitude difference increases to exhibit for large U_r the same windows of positive values as λ_W.

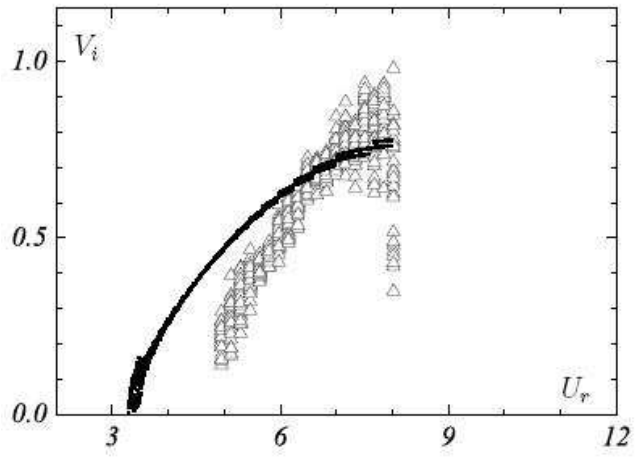

Figure 7.13: Bifurcation diagrams of reduced impact velocities for single-sided impacting motions with $e = 0.65$. (■): Milan oscillator ; (△): Present experiment.

Impact velocities predicted by the Milan oscillator for this case of asymmetric amplitude limitation are also presented here. The bifurcation diagram of reduced impact velocities obtained with the Milan oscillator presented in figure 7.13 exhibits the same structure as that for peak excursions. It also reveals the nature of the system and its bifurcations. At the start of the impacting domain, it is discontinuous due to grazing bifurcations, and reveals intermittent transitions between 1-impact-per-period cycles for larger U_r. Predicted values of impact velocities are overestimated at the start of the range of reduced velocities over which impact occurs also experimentally, for $5 < U_r < 6.5$, and become underestimated for larger U_r.

To investigate the influence of the offset value on the response of the Milan oscillator, its dynamics with smaller offset values are also simulated. In order to compare the response of the model to experimental data, the non-dimensional offset e is set at -0.47 and -0.22.

7.2.1.2 Influence of the offset

For these two cases of asymmetric structural restraints, the Milan oscillator exhibits a dynamic response similar in nature to the one it exhibits for $e = -0.65$. Bifurcation

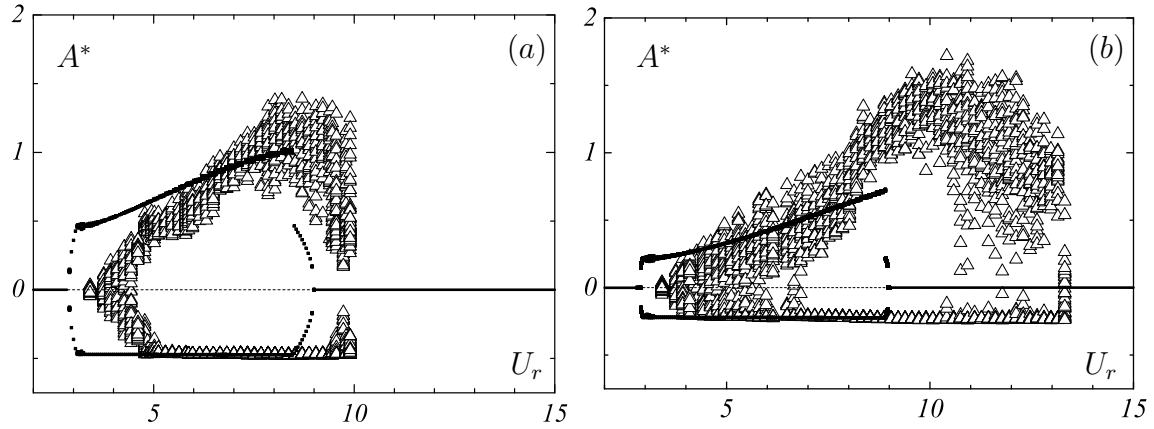

Figure 7.14: Bifurcation diagram of peak excursions for single-sided impacting motions with $e = -0.47$ (a) and $e = -0.22$ (b). (—): Milan model; (△): experimental data.

diagrams of peak excursions obtained with the Milan oscillator with $y_s = -0.47D$ and $y_s = -0.22D$ are presented in figure 7.14 with experimental data.

The amplitude response exhibits the same shape for $e = -0.47$ as for $e = -0.65$, however the shape of the amplitude response is slightly different for $e = -0.22$. As impact occurs earlier in the model than in experiments, ${A^*_{max}}^+$ is overestimated for both offset values by the model for low flow velocities. As for the case $e = -0.65$, in both cases the predicted increaseof ${A^*_{max}}^+$ with U_r takes place at a lower rate than the one occurring in experimental tests resulting in ${A^*_{max}}^+$ to be underestimated for large U_r.

As illustrated by figure 7.15 comparing predicted amplitude responses for the three different offset values investigated, the model exhibits for any reduced velocity a decrease of the maximum amplitude between impacts when decreasing the offset.

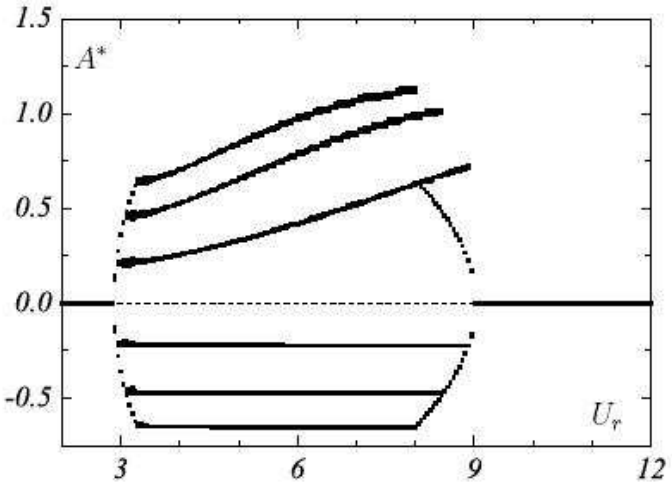

Figure 7.15: Predicted bifurcation diagram of peak amplitudes for single-sided impacting motions with $e = 0.65$, 0.47, 0.22.

This was observed in the experiments at low flow velocities, but not for large flow velocities, as the rate of increase of ${A^*_{max}}^+$ increases with e decreasing in the experimental data displayed in figure 6.2 at page 134, for which ${A^*_{max}}^+$ is about equal for all gap settings at $U_r \approx 8$.

Energy distribution of the system over frequencies is, for both cases $e = -0.47$ and $e = -0.22$, also similar to that the system presents for $e = -0.65$. As illustrated by figure 7.16(a) concerning the case $e = -0.47$, frequency distributions of single-sided motions contain in the chaotic window at the beginning of the impacting domain a main peak at the oscillation frequency f and its

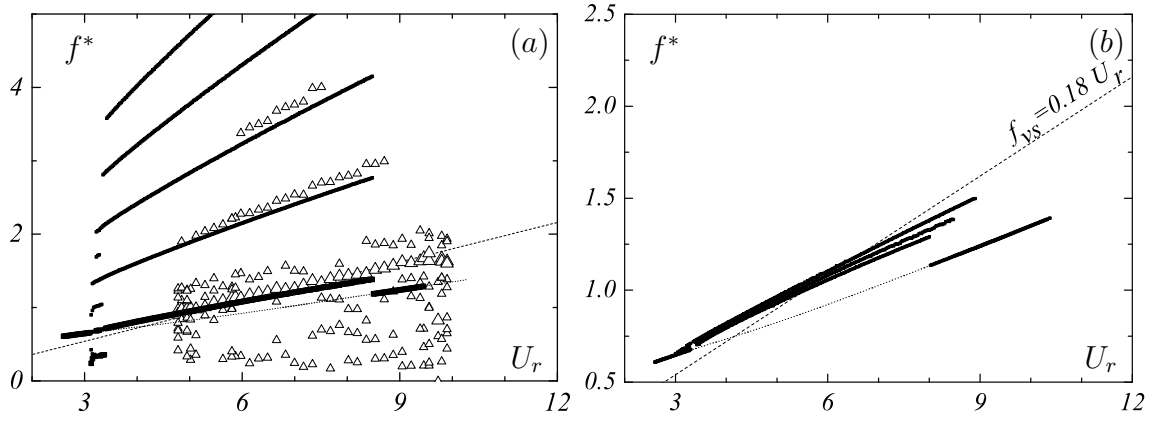

Figure 7.16: (a): Apparition of harmonics for single-sided impacting motions for $e = -0.47$. (b): Increase of the predicted main frequency with e decreasing. (—): Milan model; (△): experimental data.

subharmonics at 0.5 f and harmonics at 1.5, 2, 2.5, 3, 4, 5 times f. This wide energy distribution is a strong sign of the chaotic nature of the system in this window. For the 1-impact-per-period motions existing for larger U_r, frequency distributions present harmonics at 2, 3, 4 and 5 times f. More energy is transferred to these harmonics when the offset is decreased as their magnitude relative to that of the main peak increases when decreasing e.

In the impacting domain, the predicted value of the main frequency, and therefore of its harmonics, increases when decreasing the offset for a fixed U_r. This is illustrated by figure 7.16(b) in which the slope of the line representing the main frequency predicted by the model for the three different offset values investigated increases slightly with e decreasing. This behaviour is different from that in experiments which is close to the vortex shedding frequency all over the impacting domain for any value of the offset. The frequency response of the model in the case of impact on one stiff stop is overall in good agreement with experimental data.

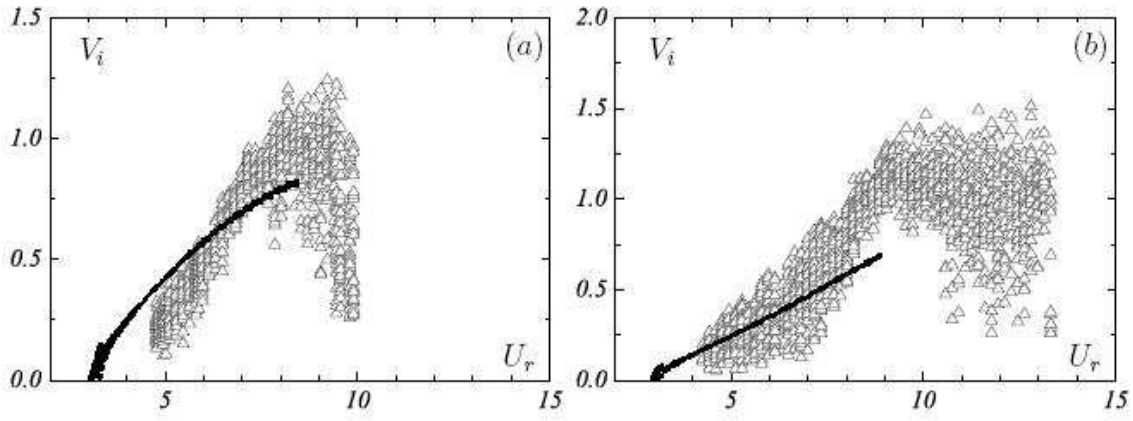

Figure 7.17: Bifurcation diagram of reduced impact velocities for single-sided impacting motions with $e = -0.47$ (a) and $e = -0.22$ (b). (—): Milan model; (△): experimental data.

Reduced impact velocities predicted by the Milan oscillator for the two cases of asymmetric amplitude limitation with $e = -0.47$ and $e = -0.22$ are compared to experimental data for the same cases in figure 7.17.

Predicted impact velocities present for the case $e = -0.47$ the same trend as for $e = -0.65$, overestimating experimental data for low U_r and underestimating it at large U_r. For $e = -0.22$, the increase of V_i is nearly linear over the impacting domain after the chaotic window. For low reduced velocities, V_i is about equal to the average of experimental values, but it underestimate it at large U_r. Predicted impact velocities decrease for any flow velocity when the offset e is decreased; the same trend was observed in experimental results, but only at low flow velocities.

As for these cases of asymmetric amplitude limitation, the Milan oscillator exhibits some features of the VIV of a rigid cylinder subject to the same non-linear restraints, experimentally-investigated cases with two stiff stops limiting the oscillation of the cylinder are also simulated with the Milan oscillator.

7.2.2 Milan Oscillator with impact on symmetric rigid stops

To model the VIV of a rigid cylinder subject to a symmetric restriction of its amplitude of vibration, two stops are inserted in the model symmetrically on each side of the cylinder at a distance e of the cylinder, each of them involving a jump in the system stiffness characterized by $r_k = 344$. The response of the system with symmetric stops is first undertaken with a large value of the offset, set at $e = 0.65$ for comparison with experimental data, and influence of the offset is then investigated by reducing it to the smaller values set in the experiments.

7.2.2.1 Dynamics of the Milan oscillator with stops symmetrically-placed at y_s=0.65D

As the value of the offset is the same as for the asymmetric case presented in section 7.2.1.1, the Milan oscillator predicts impact occurring between $U_r \approx 3.287$ and $U_r \approx 8$

for this symmetric case with $e = 0.65$. Therefore, as in the asymmetric case, the predicted impacting domain starts at a lower flow velocity than in the experiments but finishes at about the same reduced velocity.

The bifurcation diagram of peak excursions is presented in figure 7.18(a) with experimental data.

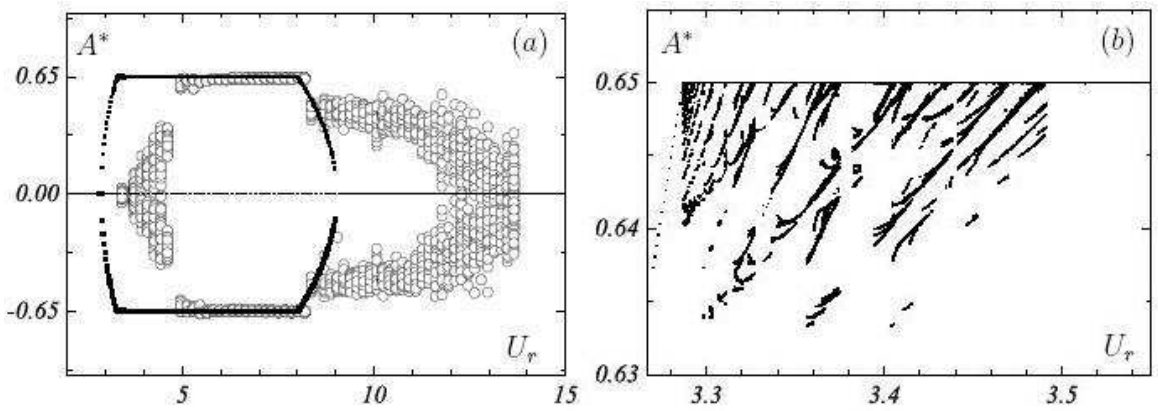

Figure 7.18: (a): Bifurcation diagram of peak amplitudes for double-sided impacting motions with $e = 0.65$. (—): Milan model; (∘): experimental data. (b): Close-up on the chaotic window at the beginning of the impacting domain.

Dynamics of the system with stops symmetrically-placed on both sides of the cylinder are in a way similar to its dynamics with only one stop. A chaotic window in which many grazing bifurcations occur starts at the beginning of the impacting domain. In this window, dynamics of the cylinder are complex but many different *k-0-1* and *k-1-0* cycles can be observed. Through a series of subcritical grazing bifurcations occurring when U_r increases at the end of this window, the system stabilises on a *1-1-1* motion for $U_r \approx 3.50$. With U_r further increased, the system exhibits a succession of windows of *1-1-1* intermittent motions until the end of the impacting domain. As illustrated by the close-up on the bifurcation diagram of upper peak amplitudes in figure 7.18(b), dynamics of the system are however somewhat more complex than in the asymmetric case.

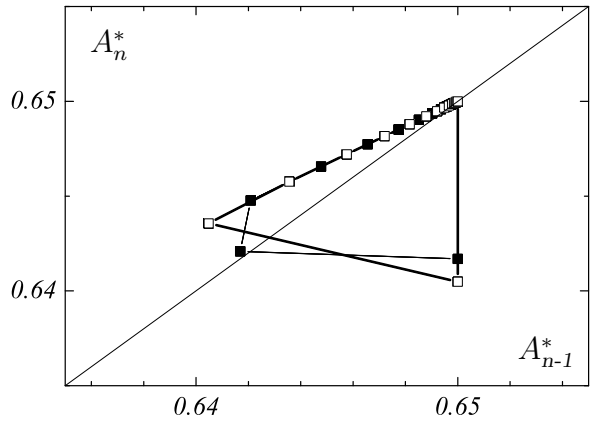

Figure 7.19: Return map of upper peak amplitudes of the *44-1-1* motion at $U_r = 3.286932$

At the start of impact, motions are already more complex than in the asymmetric case because of the presence of two stops. The return map of upper peak amplitudes plotted for $e = 0.65$ and $U_r = 3.286932$ in figure 7.19 reveals the *44-1-1* limit cycle described by the cylinder at this flow velocity. This long-period cycle is made of a *22-1-0* cycle plotted with black squares following by a *22-0-1* cycle plotted with empty squares. As for the asymmetric case, with U_r slightly increasing, several grazing bifurcations occur, reducing quickly the period of the limit cycle. With U_r further increased, many other grazing bifurcations occur, creating very complex motions made of different *k-0-1* and *k-1-0* cycles for $3.287 < U_r < 3.496$.

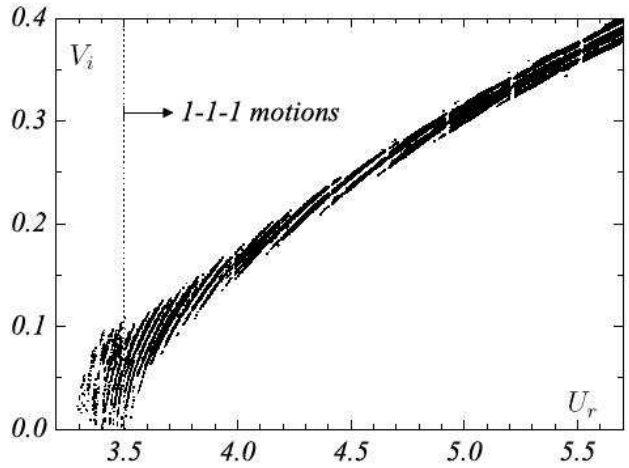

Figure 7.20: Close-up on the bifurcation diagram of reduced impact velocities for double-sided impacting motions with $e = 0.65$.

Even if only one line seems to appear in the bifurcation diagram of peak excursions for $U_r > 3.496$, *1-1-1* motions predicted by the model are rarely periodic. The bifurcation diagram of reduced impact velocities presented for this case in figure 7.20 shows that the system exhibits here again a succession of

intermittent *1-1-1* motions for U_r larger than 3.50.

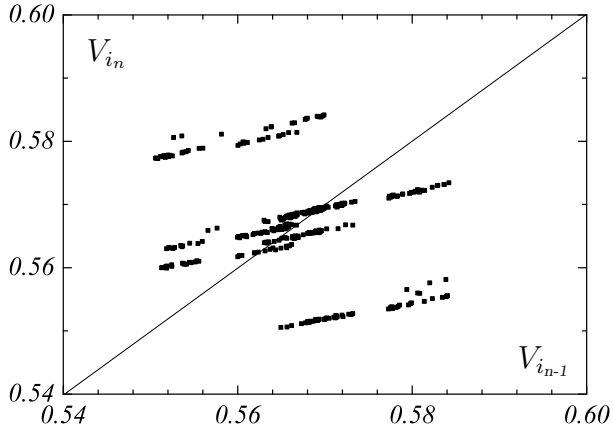

Figure 7.21: Return map of impact velocities for intermittent double-sided impacting motion for $e = 0.65$ and $U_r = 7.50$

These intermittent motions are also more complex than those observed in the asymmetric case. The return map of impact velocities on the upper stop plotted for one of these intermittent motions at $U_r = 7.50$ in figure 7.21 exhibits intermittent channels and four unstable periodic cycles. As U_r is increased, characteristic dynamic variables of these cycles, as the impact velocity on the upper stop, increase until one of the cycles becomes stable, over a narrow range of impact velocities, and before another window of intermittent motion starts.

As for intermittent motions predicted in the asymmetric case, and because of the very small amplitude difference between the *1-1-1* cycles present in these intermittent motions, these latter, if experimentally recorded, would have been identified as periodic *1-1-1* cycles. And indeed, experimental results show for this case of symmetric amplitude limitation with $e = 0.65$ the cylinder describing periodic *1-1-1* cycles over most of the impacting domain. Intermittency might be here also only an artificial feature of the model due to its time integration.

The frequency response of the system presented in figure 7.22(a) with experimental results for the same case shows that the model predicts in this case correctly the structure of the energy distribution of the system. In this case, frequency distributions of motions simulated for $3.267 < U_r < 3.5$ contain one distinct main peak and many subharmonics and harmonics.

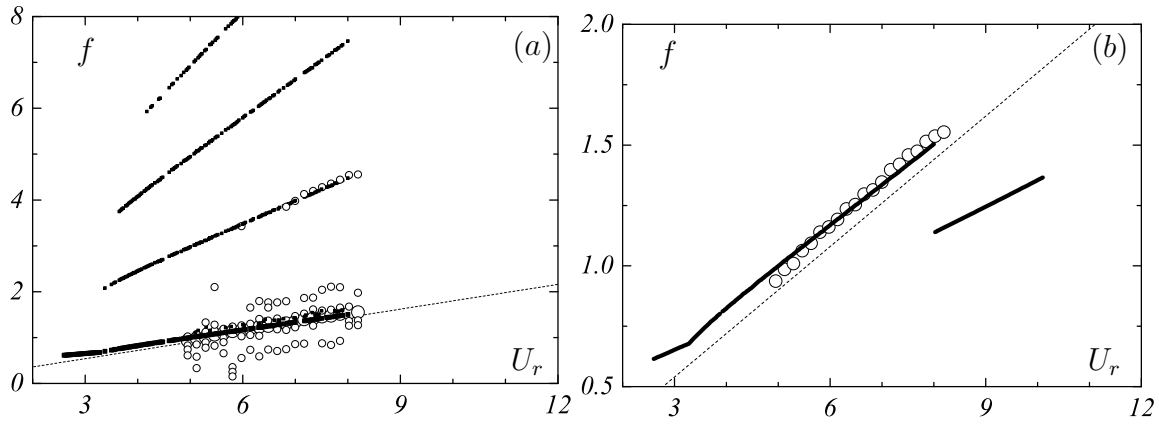

Figure 7.22: Frequency response for double-sided impacting motions with $e = 0.65$. (a): Bifurcation diagram of peak frequencies. (b): Main peak frequency as a function of U_r; (—): Milan model; (∘): experimental data.

For $U_r > 3.5$, frequency distributions contain one distinct main peak and harmonics of it. Frequency distributions of experimental time series contain also a main peak and its first harmonics, but they are more noisy.

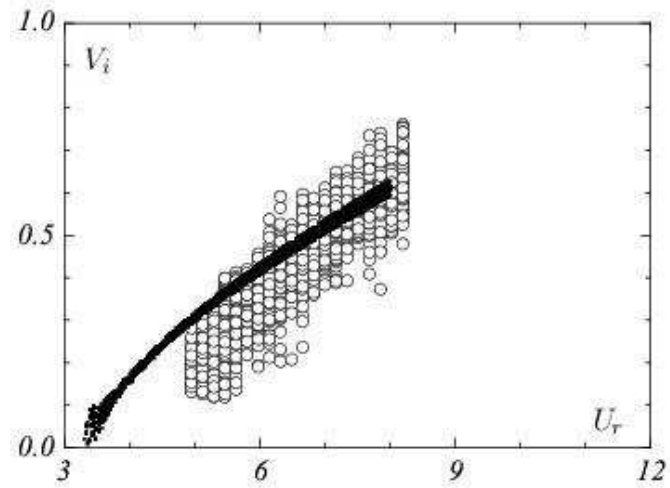

Figure 7.23: Bifurcation diagram of reduced impact velocities for double-sided impacting motions with $e = 0.65$. (■): Milan oscillator ; (∘): Present experiment.

As illustrated by figure 7.22(b), the frequency of the main peak in the frequency distributions of double-sided impacting motions with $e = 0.65$ is accurately predicted by the model.

As shown by the bifurcation diagram of reduced impact velocities on the upper stop presented in figure 7.23, impact velocities predicted by the Milan oscillator in this case are close to experimental values. For $U_r \approx 5$, where impact starts

to occur in the experiments, the predicted impact velocity is close to the maximum impact velocity experimentally recorded. As the rate of increase of the predicted maximum impact velocity decreases with U_r increasing, the predicted impact velocity slightly underestimates the maximum impact velocity at high values of U_r.

7.2.2.2 Influence of the offset

The cylinder's dynamics are investigated with the offset value e set at 0.47, 0.30 and 0.20. As seen before, the first consequence of varying the stop position is the change of the range of flow velocities over which impact occurs. In this case for reasons explained before, the Milan oscillator does not predict correctly the range of flow velocities over which impact occurs.

For all offset values, the model exhibits at the beginning of the impacting domain a chaotic window with many grazing bifurcations of *k-0-1* and *k-1-0* cycles. In every case, this chaotic window finishes with the stabilisation of a periodic *1-1-1* cycle over a very short window of flow velocities. This periodic *1-1-1* cycle quickly loses its stability with U_r increasing and a first window of intermittent motion starts. With U_r further increased, the system exhibits a succession of long intermittent transitions between narrow windows of stability of *1-1-1* cycles, whose impact velocities and main frequency are increasing with U_r.

The amplitude response of the system is in all cases similar to that which it exhibits for $e = 0.65$. As seen in section 5.3, strong perturbations of the dynamics occur in the experiments for small offset values. For these cases, antisymmetric *1-1-1* cycles, double bounces on the same stop as well as chattering motions are observed. These strong perturbations of the dynamics of the cylinder do not appear with the model.

The unchanged nature of the dynamic response of the model is also revealed by the

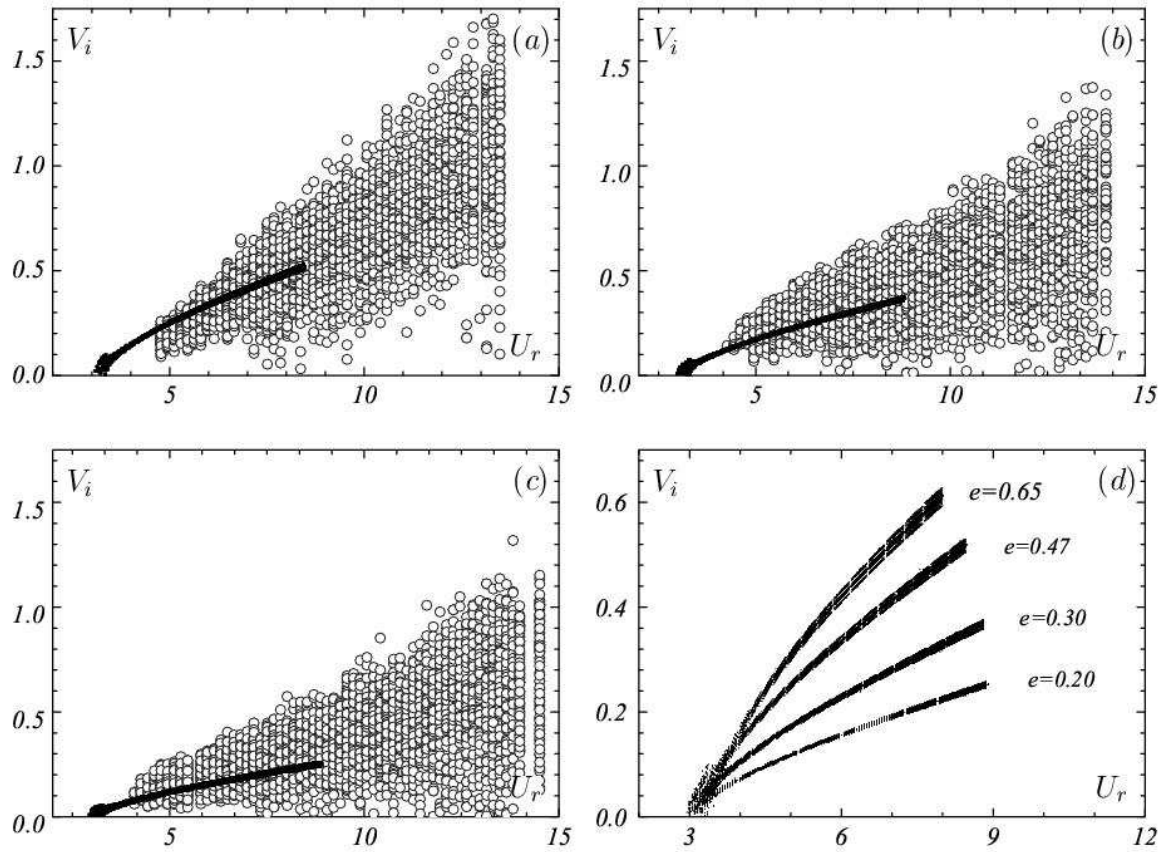

Figure 7.24: Bifurcation diagram of impact velocities on the lower stop for double-sided impacting motions. (a): $e = 0.47$; (b): $e = 0.30$; (c): $e = 0.20$; (d): predicted decrease of the impact velocities with e decreasing.

similarity of the bifurcation diagrams of reduced impact velocities presented in figure 7.24(a), (b), and (c), plotted with experimental data. These graphs show that predicted impact velocity are in all cases about equal to the average value of impact velocity measured experimentally. Figure 7.24(d) shows that the predicted impact velocity decreases for any reduced flow velocity with e decreasing. General decrease of the average impact velocity is also observed in the experiments, as shown in figure 5.13(a), page 97.

Energy distribution over frequencies is similar for any offset value to that it exhibits for $e = 0.65$. *1-1-1* motions predicted over most of the respective impacting domains

exhibit only a main peak and its first harmonics.

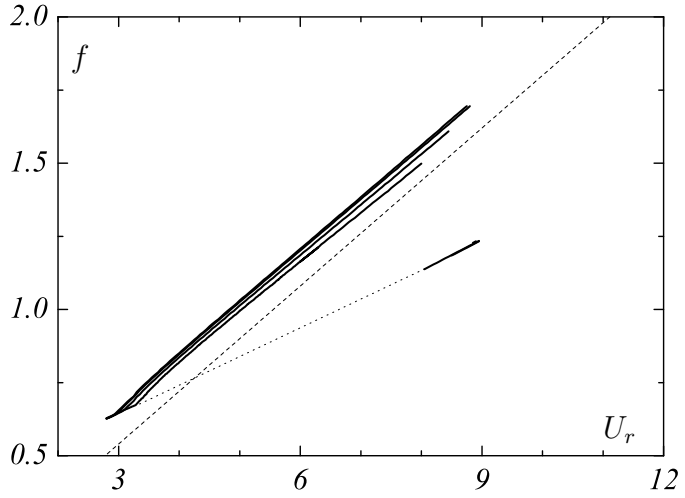

Figure 7.25: Main peak frequency for double-sided impacting motions for $e = 0.65$, 0.47, 0.30 and 0.20.

As illustrated by figure 7.25, the frequency ratio f^* of the main peak increases with U_r over all the impacting domain with a larger rate than in the case with linear restraints, and with about the same slope of 0.18 for all cases. As impact occurs earlier with e decreasing, the frequency of the main peak slightly increases when decreasing the offset. Experimentally, f was observed to be close to f_{vs} for any offset value and any reduced velocity. When looking back at figure 5.12 on page 95 a slight decrease of f with e decreasing, similar to that appearing in the Milan model here, can be seen in the experimental results.

7.2.3 Conclusions

The Milan oscillator exhibits some features observed for a cylinder experiencing VIV and subject to amplitude limitation. Even if it does not predict correctly the width of the impacting domain, The predicted impacting domain, the amplitude response and frequency responses of the model are close to experimental data when the offset is large. The dynamics of the model at low U_r also present similarities with those of the cylinder. For offset values small enough for impact to occur experimentally also over the lower branch of vibration, and because of its amplitude response with linear restraints, the model does not predict impact correctly the range of flow velocities over which impact occurs. The decrease of the impact velocity, and that of the peak

amplitude between impacts in the case of single-sided impacts, occurring with the offset decreasing are similar to those observed experimentally, but only at low U_r.

7.3 VDP oscillator with impact on stiff stops

The response of the VDP model introduced in section 7.1.1 is also investigated, and compared to experimental results, for different configurations of non-linear structural restraints. Structural parameters in the model are set at the same values as in the experiments carried out during this project, i.e. $m^* = 1.74$, ζ=0.79% and $f_n = 0.9765$ Hz. The stiffness of the stops is set such as $r_k = 344$. As seen in section 7.1.2, the VDP oscillator does not present an amplitude response matching the experimental results when the parameters A and ϵ are set to the respective proposed values of 12 and 0.3. However, the amplitude response is closer from experimental results when ϵ is set to 0.01. Changing this parameter may have other consequences in the response of the model to mass ratio or damping variations, but correct amplitude response is here of primary importance.

7.3.1 VDP oscillator with impact on one stiff stop

Dynamic response of the model in the case of asymmetric limitation of the vibration of the cylinder with one stiff stop placed on one of its sides is first presented for a large offset value $e = -0.65$. The offset is then reduced to show the influence of this parameter on the response of the system.

7.3.1.1 Dynamics of the VDP oscillator with impact on one stiff stop placed at y_s=0.65D

The dynamic response of the VDP model for the case of a single stop placed at $e = -0.65$ is presented with the bifurcation diagram plotted in figure 7.26, with experimental data. Predicted impacts start for $U_r \approx 3.93$, and end at $U_r \approx 8.20$,

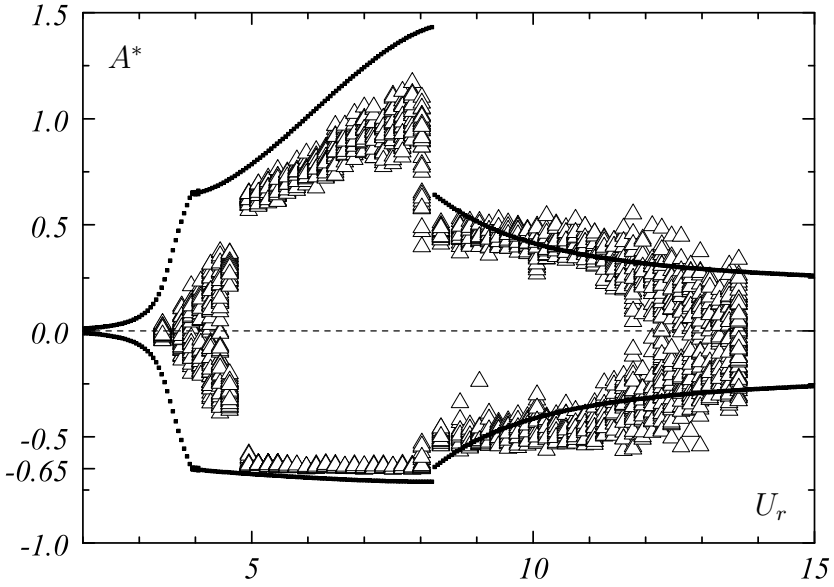

Figure 7.26: Bifurcation diagram of peak amplitudes for single-sided impacting motions with $e = -0.65$.

about the same as in the experiments. The amplitude response predicted by the model is close to that measured experimentally. On most of the impacting domain, from $U_r = 4.09$ until the end of the impacting domain, the VDP model exhibits stable 1-impact period-1 cycles of amplitude increasing with U_r. Experimental results exhibit also 1-impact-per-period motions here, but they display much more dispersion of the peak excursions between impacts. The predicted maximum amplitude between impacts is overestimated, but the increase of A^*_{max} with U_r presents a trend very similar to that of the maximum experimental data.

The close-up on the bifurcation diagram of lower peak excursions at the start of the

impacting domain, presented in figure 7.27(a), displays the narrow chaotic window starting at the lowest reduced velocity for which impact occurs. This chaotic window finishes when, with U_r increasing a 3-impact period-6 cycle undergoes a grazing bifurcation leading to the stability of a 2-impact period-4 cycle at $U_r = 3.979$, which itself undergoes a subcritical Hopf bifurcation to change into a 1-impact period-2 cycle, stable over a relatively wide range of reduced velocities, between $U_r = 3.98$ and $U_r = 4.09$.

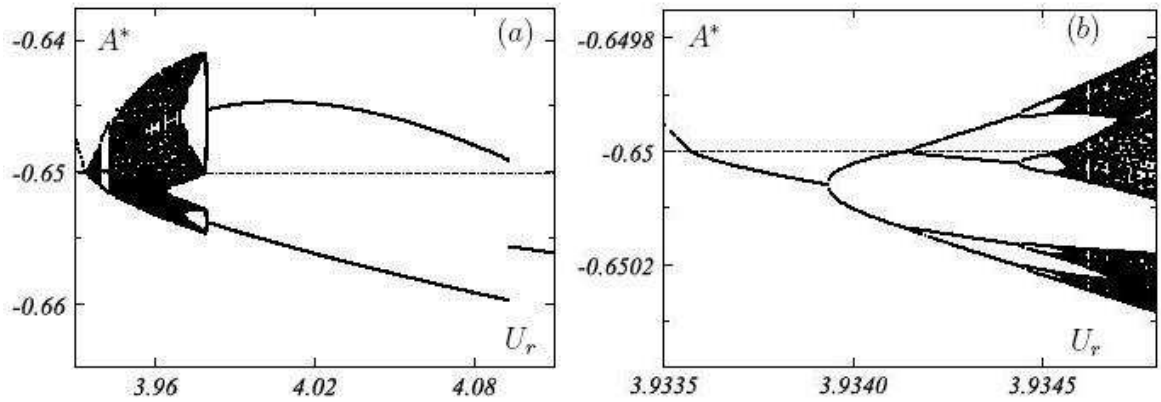

Figure 7.27: Bifurcation diagram of lower peak amplitudes for single-sided impacting motions with $e = -0.65$. (a): Predicted chaotic window and wide window of stability of 1-impact period-2 cycle; (b): Period-doubling route to chaos at the start of the impacting domain.

It can be noted that a short window of stability of 1-impact period-3 impacting cycle appears in the chaotic window in figure 7.27(a) around $U_r = 3.94$. In fact when looking closer at the bifurcation diagram, several other narrow windows of stability of 1-impact period-3 cycles can be observed, and this appearance of narrow windows of stability of periodic motions in larger windows of disorganised motion is characteristic of chaotic systems.

Figure 7.27(b) gives a closer insight on the the destabilisation of the system caused by the stop at the lowest flow velocities where impact occurs. For $U_r \approx 3.9336$, the system just simply stabilises on a 1-impact-per-period cycle with a very low impact

velocity. With U_r increasing, ${A^*_{max}}^-$ increases, and then at $U_r = 3.39392$ the 1-impact-per-period cycle undergoes a Hopf bifurcation to change into a 2-impact period-2 cycle. This bifurcation is followed by a grazing bifurcation similar to a Hopf bifurcation and leading to a stable 3-impact period-4 cycle, which then experiences a period-doubling cascade.

Dynamics of the model at the start of the impacting domain seem to be governed by a different process than taking place in the experiments. With the VDP model, the route to chaos leading to the small chaotic window at the start of the impacting domain, in which cycles without impact do occur, is a period-doubling cascade. This process is different from that observed in the experiments at low flow velocities, where a process of reinjection of the trajectory in the attraction basin of the attractor existing in the linear case occurs after impact, leading to some number of cycles of amplitude growth before the next impact.

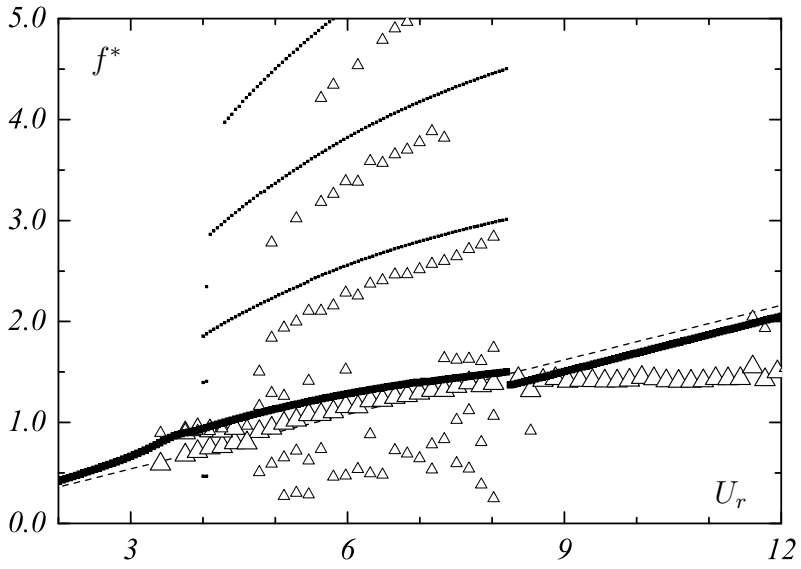

Figure 7.28: Bifurcation diagram of peak frequencies for single-sided impacting motions with $e = -0.65$. (—): VDP model; (△): experimental data.

Bifurcation diagram of peak frequencies in the frequency distributions of simulated

single-sided impacting motions, as used earlier in this work, is presented in figure 7.28 for $e = -0.65$ with experimental data. Over the chaotic window at the beginning of the impacting domain, energy is distributed over a wide range of frequencies.

Frequency distributions of 1-impact-per-period motions exhibit a main peak at the oscillation frequency f, as well as many of its harmonics and subharmonics. For the 1-impact-per-period motions predicted over most of the impacting domain, energy is distributed over a main peak at the oscillation frequency and its harmonics of integer order, which is similar to experimental results.

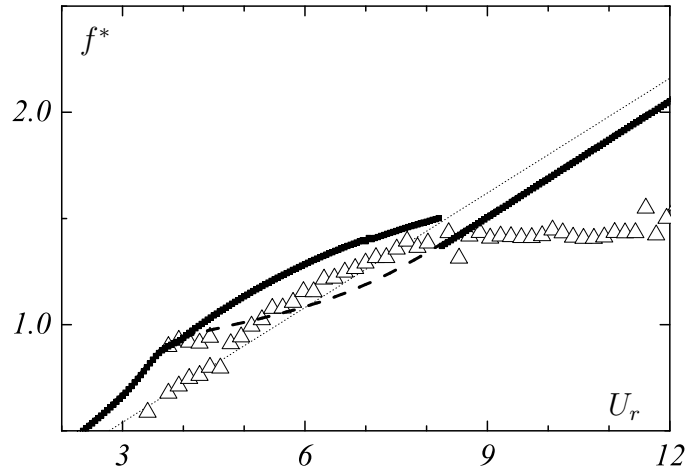

Figure 7.29: Main peak frequency in frequency distributions; (—): VDP model for $e = -0.65$; (----): VDP model with linear restraints; ; (△): experimental data.

When impact starts to occur, the non-impacting periodic cycle stable for $U_r < 3.9336$ simply changes into a periodic 1-impact-per-period cycle with a very small contact velocity. Dynamics of the model are just slightly affected by the stop at the beginning of the impacting domain, and, as illustrated by figure 7.29, the main frequency remains nearly unchanged at the very beginning of the impacting domain. With U_r increasing, f increases and becomes progressively larger than its value with linear restraints. As a result of the overestimation of the main frequency over all the experimental impacting domain, frequencies of its harmonics appearing in figure 7.28 are also overestimated.

At the end of the impacting domain, the predicted oscillation frequency, slightly

larger than f_{vs}, simply jumps back to its value with linear restraints, being for this reduced velocity just lower than f_{vs}. f is overestimated for $U_r > 9$ as it follows f_{vs} with the VDP model while it is equal to f^*_{lower} in the experiments all over the lower branch, in which impact does not occur for this offset value.

Bifurcation diagram of reduced impact velocities obtained with the VDP oscillator for this case of impact on one stop placed at $e = -0.65$ is compared to experimental data in figure 7.30.

Values of impact velocities at a given reduced velocity overestimate experimental values, but the increase of the maximum impact velocity with U_r follows the same trend as in the experiments.

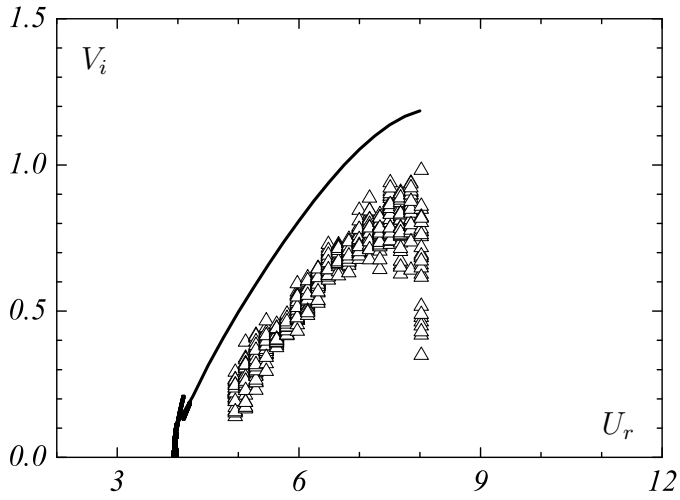

Figure 7.30: Bifurcation diagram of reduced impact velocities on single-sided impacting motions for $e = -0.65$. (—): VDP model; (△): experimental data.

The algorithm described in section 5.3.2 was developed in the aim of decreasing the effect of smoothing of the displacement causing underestimation of impact velocities, which it did, but slight underestimation of the impact velocity can still occur sometimes, contributing to the differences seen in figure 7.30. However, the predicted amplitudes of displacement (in figure 7.26) are below their experimental values, which do not depend so much on the post-processing, suggesting that it is indeed the model that overestimates the actual impact velocity.

The dynamic response of the model for this case of asymmetric amplitude limitation with $e = -0.65$ shows a good agreement with experimental data. The offset value is

now changed to investigate its effect on the system.

7.3.1.2 Influence of the offset

Dynamics of the model with the offset reduced to $e = -0.47$ are first presented, with the bifurcation diagram of peak excursions plotted here in figure 7.31(a) with experimental data. In this case, impact is predicted to occur between $U_r = 3.697$ and

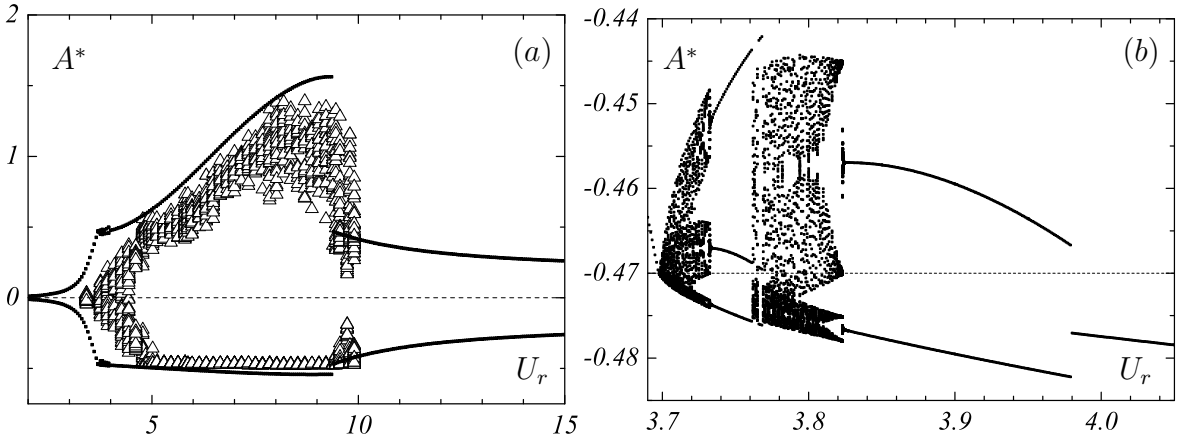

Figure 7.31: Bifurcation diagram of peak excursions for single-sided impacting motions with $e = -0.47$ (a): (—): VDP model; (△): experimental data. (b): close-up on the bifurcation diagram of lower peak amplitudes in the beginning of the impacting domain.

$U_r = 9.35$. The amplitude response of the system for $e = -0.47$ displays the same trend as for $e = -0.65$, which is again very similar to that of maximum experimental data. A^*_{max} is just slightly overestimated by the model, all over the similar impacting domain.

Dynamics of the VDP model are for this offset value also similar to those it exhibits for $e = -0.65$. As illustrated by figure 7.31(b), a chaotic window, similar in structure to that with $e = -0.65$, appears at the beginning of the impacting domain through a period-doubling cascade route to chaos. This chaotic window, in which narrow windows of stability of periodic impacting motions can be observed, finishes with the

stabilisation of a 1-impact period-2 cycle, which itself undergoes with U_r increasing at $U_r = 3.979$ a subcritical bifurcation to change into the 1-impact-per-period cycle stable until the end of the impacting domain. The bifurcation diagram of peak frequencies presented in figure 7.32 shows that energy distribution over frequencies is similar to that with $e = -0.65$. As impact occurs for larger flow velocities in this case, f follows its trend for $U_r > 8.25$ where impact stops to occur for $e = -0.65$. Doing so, it becomes lower than f_{vs} and, as contact does not occur for $U_r > 9.35$, f marks a small discontinuity to jump to its value with linear case.

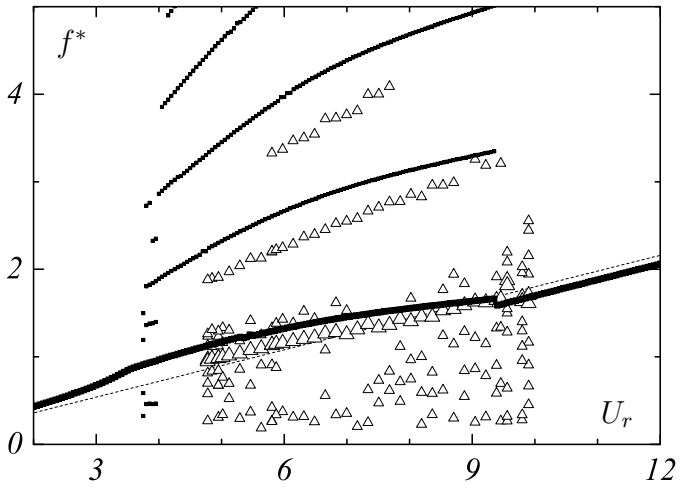

Figure 7.32: Bifurcation diagram of peak frequencies for single-sided motions with $e = -0.47$; (—): VDP model; (△): experimental data.

The impact velocities predicted by the VDP oscillator in this case with impact on a stiff stop placed at $e = -0.47$ are presented with experimental data in figure 7.33. They display the same trend as their maximum experimental values, and provide quantitatively good estimates despite a slight overestimation.

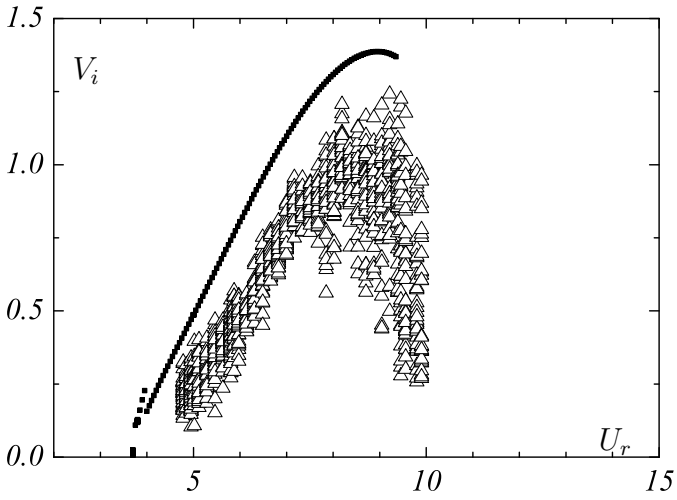

Figure 7.33: Bifurcation diagram of peak frequencies for single-sided motions with $e = -0.47$; (—): VDP model; (△): experimental data.

When the offset is decreased to $e = -0.22$, the VDP model presents some dynamical behaviour it did not present for larger values of e. It predicts for $e = -0.22$ impact occurring between $U_r = 3.40$ and $U_r = 21.95$. This impacting domain starts at a lower flow velocity than in the experiments ($U_r \approx 4.26$), however contact did occur during the experimental tests for large values of U_r, in fact up to the maximum flow velocity safely reachable experimentally. The flow velocity above which impacts cease experimentally is not known but, as seen in section 6.4.2, the experimental test carried out for $U_r = 13.31$ shows disorganised motion with very small impact velocities which suggests that it was near the end of the impacting domain.

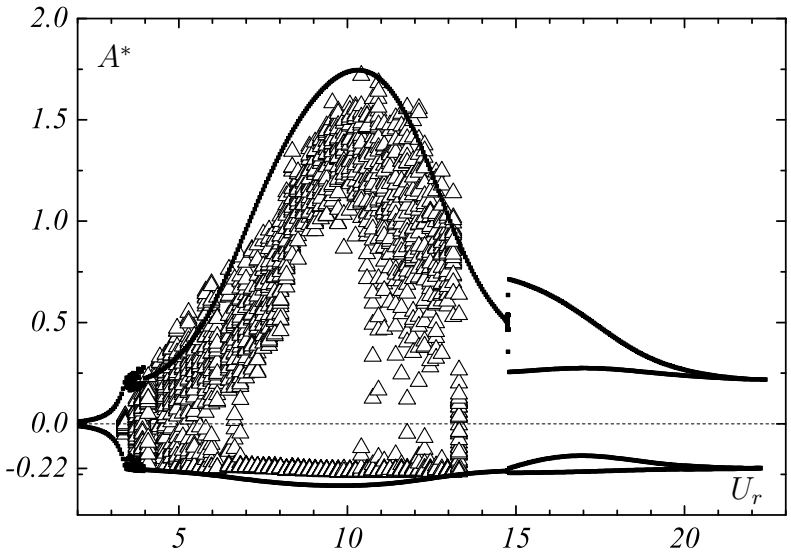

Figure 7.34: Bifurcation diagram of peak excursions for single-sided impacting motions with $e = -0.22$; (—): VDP model; (△): experimental data.

Dynamics of the VDP model, presented in figure 7.34 using the bifurcation diagram of peak excursions and experimental data for the same case shows, as in previous cases, the occurrence, at the start of the impacting domain, of a narrow chaotic window similar in structure to those observed for $e = -0.65$ or -0.47. As for these cases, it finishes with the stabilisation of a 1-impact-per-period cycle. Over the range of reduced velocities where impact occurs experimentally, peak excursions between impacts follow the same trend as the maximum experimental values, reaching about

the same maximum value at about the same flow velocity.

However the 1-impact-per-period cycle is not stable until the end of the impacting domain. At $U_r = 14.70$, it undergoes a Hopf bifurcation, through which a 1-impact period-2 cycle becomes stable, until the end of the impacting domain at $U_r = 21.95$ where it undergoes a grazing bifurcation leading to stable non-impacting cycle of amplitude lower than the stop position.

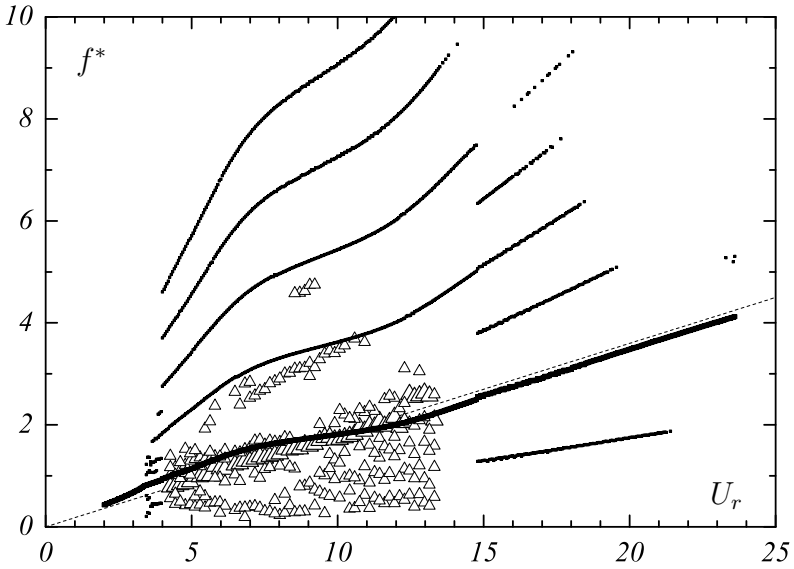

Figure 7.35: Bifurcation diagram of peak frequencies for single-sided motions with $e = -0.22$; (—): VDP model; (△): experimental data.

As illustrated by figure 7.35, energy distributions over frequencies for this case present the same structure as for the other offset values considered. From the start of the impacting domain up to the end of the window of stability of the 1-impact-per-period cycle at $U_r = 14.70$, the main frequency increases with the same trend as for $e = -0.47$. As in this case the 1-impact-per-period cycle is stable for $U_r > 9.35$, the main frequency follows its trend, increasing just below f_{vs}.

Frequency distributions for the 1-impact period-2 cycle existing for $U_r > 14.70$ until the end of the impacting domain contain a main peak at the oscillation frequency f,

one subharmonic at 0.5 f, and harmonics at 1.5,2, 2.5 and 3 times f.

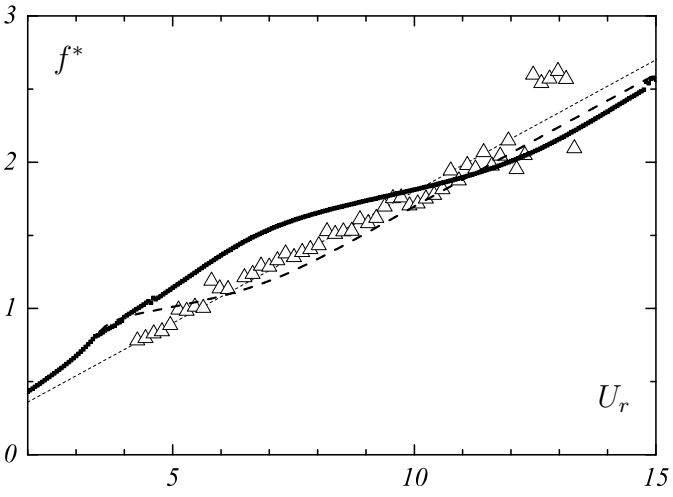

Figure 7.36: Main peak frequency in frequency distributions; (—): VDP model for single-sided impacting motions with $e = -0.22$; (----): VDP model with linear restraints; (△): experimental data.

At the end of the impacting domain, harmonics of f present in the frequency distributions, whose magnitudes decrease with U_r all over the window of stability of the 1-impact period-2 cycle, are very small and just disappear when contact stops.

Figure 7.36 shows that in the range of flow velocities where impact occurs in both experimental and numerical tests, the predicted main frequency of the motion overestimates experimental values up to $U_r \approx 10$. The increase of f with U_r at the beginning of the impacting domain is similar to that of experimental data but predicted variations of the slope of f^* is not observed in the experiments.

The maximum impact velocities presented in figure 7.37 exhibit also in this case the same trend as their maximum experimental value. The predicted maximum impact velocity marks a discontinuity at $U_r = 14.70$, i.e. at the bifurcation between 1-impact-per-period and 1-impact period-2 cycles. With U_r increasing, the impact velocity corresponding to the 1-impact period-2 cycle decreases, to become nil for $U_r = 21.95$, confirming the nature of the grazing bifurcation occurring at the end of the impacting domain.

Variation of the offset e in these cases of asymmetric amplitude limitation of the cylinder does not change the nature of the dynamics of the Milan model. However as shown by figure 7.38, amplitude and frequency responses are affected by the variation of e. At low flow velocities, a reduction of the offset involves a decrease of the peak excursions between impacts, but at $U_r \approx 8$, A^*_{max} is about equal for all cases. The exact same observation was made with experimental data.

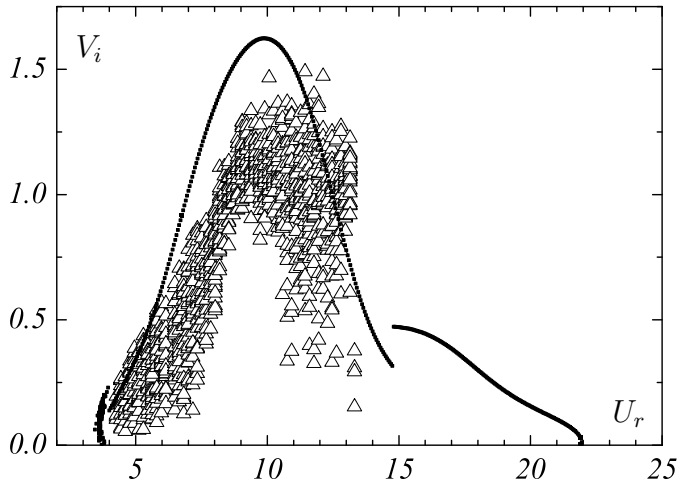

Figure 7.37: Bifurcation diagram of peak frequencies for single-sided motions with $e = -0.22$; (—): VDP model; (△): experimental data.

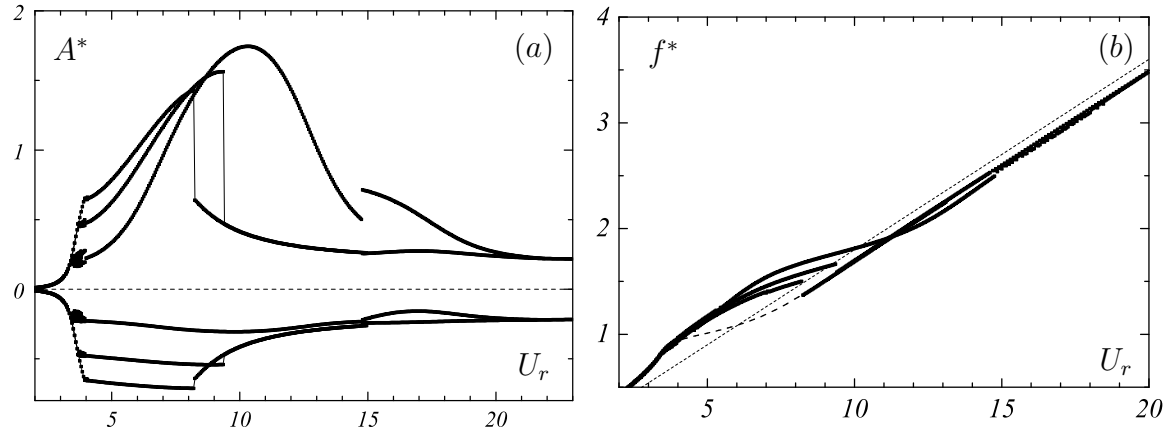

Figure 7.38: Bifurcation diagram of peak amplitudes and impact velocities for single-sided impacting motions obtained with the VDP model for $e = 65$, 0.47, 0.22.

The main frequency of the motion predicted by the model does not seem to depend on the offset value at the beginning of the impacting domain. However for $U_r > 6$, its increase with U_r depends on e, so that f increases with e decreasing for $6 < U_r < 7$.

This was not observed in the experiments.

Simulation of the VIV of the low-mass low-damping rigid cylinder studied experimentally in this project is now undertaken with two stops limiting the cylinder'oscillation.

7.3.2 VDP Oscillator with impact on symmetric stiff stops

In this case, the offset is successively set at the four different values used during the experimental tests, $e = 0.65$, 0.47 0.30 and 0.20.

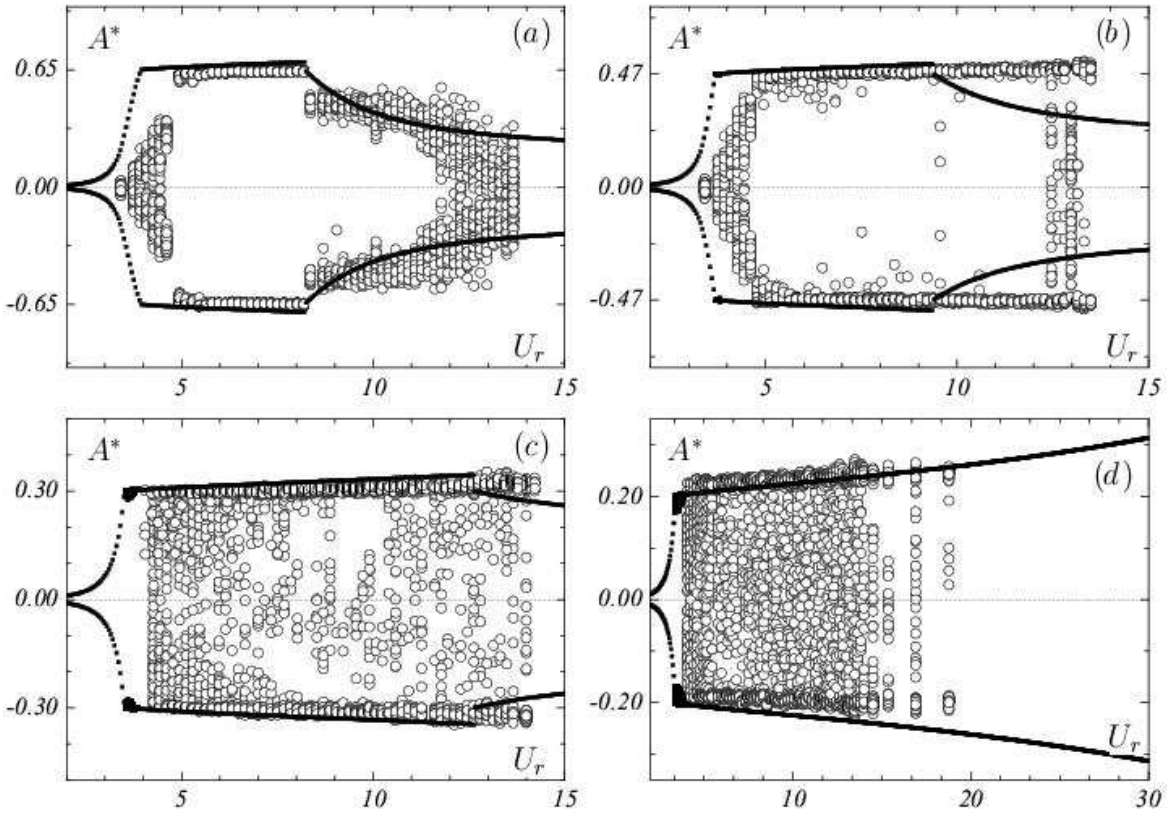

Figure 7.39: Bifurcation diagram of peak amplitudes for double-sided impacting motions. (a): $e = 0.65$; (b): $e = 0.47$; (c): $e = 0.30$; (d): $e = 0.20$; (—): VDP model; (∘): experimental data.

For $e = 0.65$ or 0.47, impacting domains extend over the same range of flow velocities as for the same offset values for the case of a single stop. For $e = 0.30$, impact occurs between $U_r = 3.70$ and 9.40, while for $e = 0.20$, it starts at $U_r = 3.40$ and occurs at a very large reduced velocity, larger than $U_r = 30$.

As illustrated by the bifurcation diagrams of peak amplitudes presented in figure 7.39, the VDP model predicts for any offset value investigated here the occurrence of a narrow chaotic window at the beginning of the impacting domain, and a stable 1-1-1 periodic cycle for larger flow velocities. The only changes appearing here when decreasing the offset is a slight increase of the width of the chaotic window at the beginning of the impacting domain, and obviously the increase of the width of the window of stability of the 1-1-1 cycle.

Dynamics of the route-to-chaos leading to this chaotic window are unclear; as illustrated by figure 7.40, it seems that the grazing bifurcation occurring at the start of impact leads directly to chaotic motions. Dynamics of the cylinder in this window are definitely chaotic as not even one single long-period periodic motion can be identified. Only some narrow windows of chaotic 1-1-1 motions can be identified around $U_r = 3.8$. It can also be noted that no asymmetric motions are observed in the model for double-sided impacting cases, as bifurcation diagrams of dynamic variables as peak amplitudes or impact

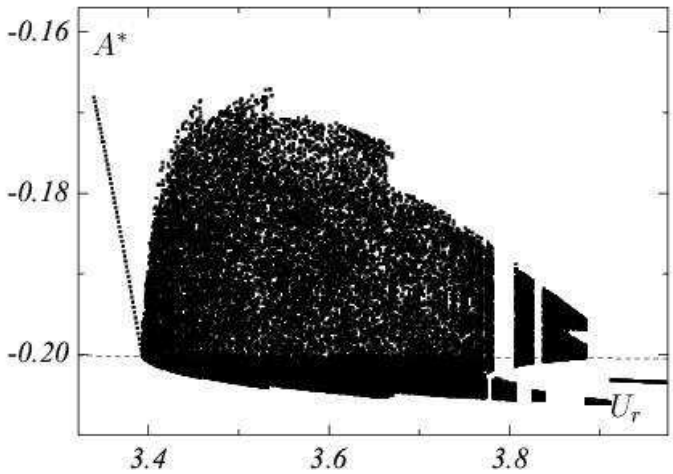

Figure 7.40: Chaotic window for double-sided impacting simulated with the VDP oscillator, here for $e = 0.20$.

velocities are exactly symmetric everywhere in the impacting domains.

The dynamics of the model fit the experimental response for the cases with $e = 0.65$ and 0.47, even if the impacting domain is wider than the experimental one in this latter case. However strong perturbations of the dynamics occurring nearly all over the impacting domain in the experimental tests for $e = 0.30$ and 0.20, responsible for the presence of many points between $-e$ and $+e$ in the respective bifurcation diagrams of peak amplitudes, are not predicted by the model.

As illustrated by figure 7.41(a), frequency distributions of the simulated 1-1-1 motions stable over most of the impacting domain with any offset value are made of a main peak and its first odd harmonics. The frequency of the main peak does not

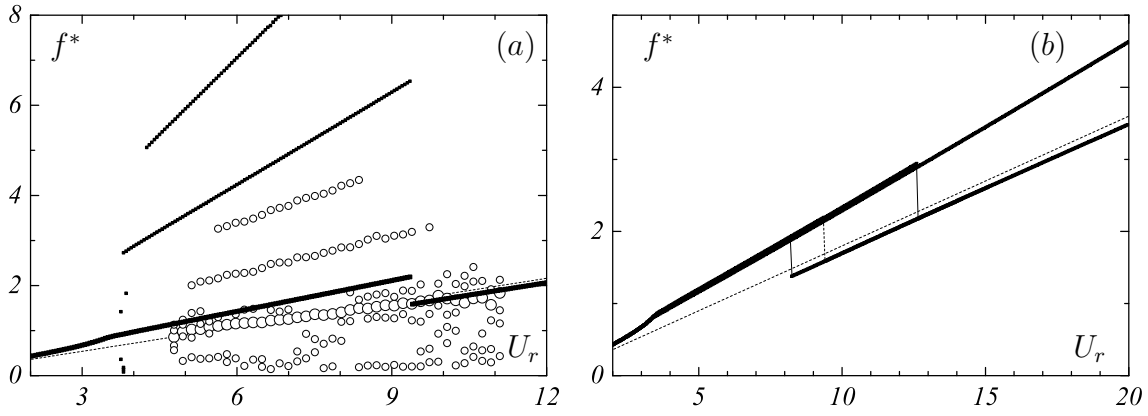

Figure 7.41: Frequency response for double-sided impacting motions. (a): Bifurcation diagram of peak frequencies for $e = 0.47$. (b): Predicted main peak frequency for $e = 0.65$, 0.47, 0.30 and 0.20.

seem to depend much on the offset value, as for all gap settings the main peak frequency, displayed in figure 7.41(b), exhibits the same increase with U_r. For every value of e, f increases linearly with U_r, and with a slope of about 0.23 over all the impacting domain, overestimating its experimental value. It jumps back to its value with linear restraints, close to f_{vs}, at the end of each impacting domain.

As shown by figure 7.42, impact velocities are predicted to increase, nearly linear with U_r increasing, for all gap values. Predicted maximum impact velocities are about to equal to their experimental values over most of the experimental impacting domain for $e = 0.65$. Decrease of the impact velocity for a fixed value of U_r when

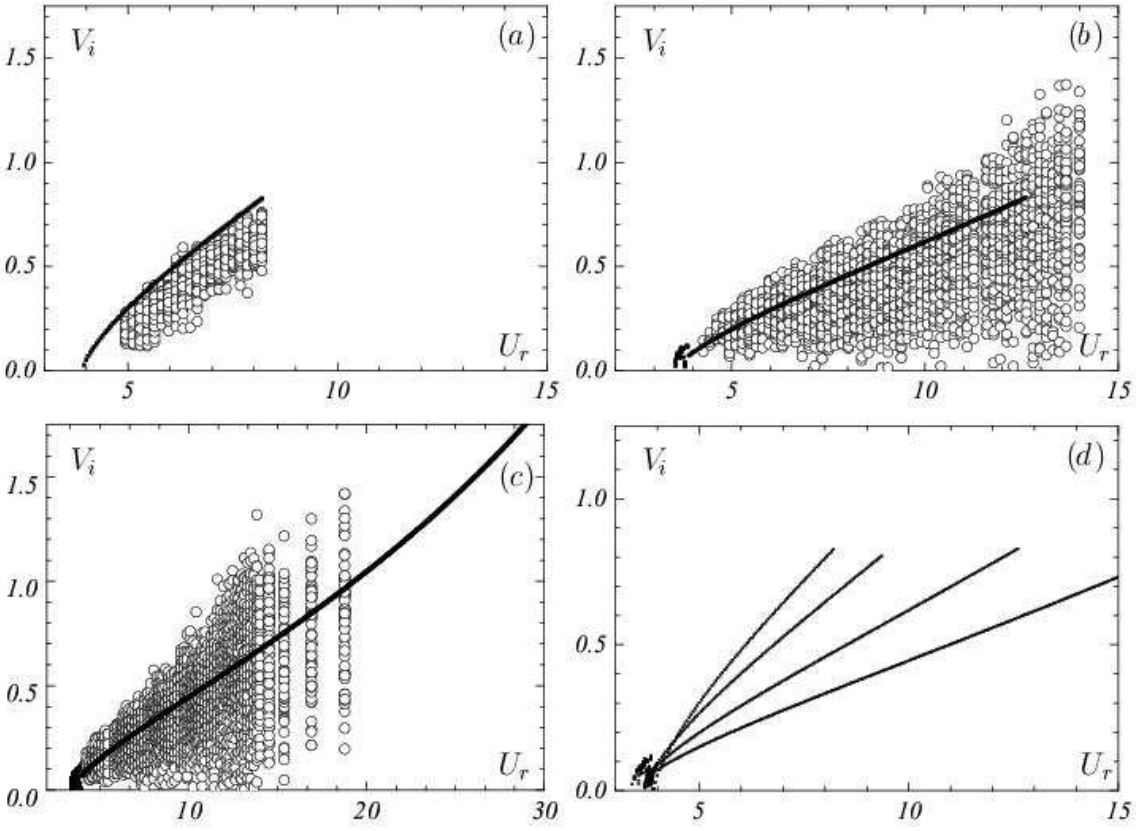

Figure 7.42: Bifurcation diagrams of impact velocities for double-sided impacting motions. (a): $e = 0.65$; (b): $e = 0.30$; (c): $e = 0.20$; (—): VDP model; (∘): experimental data. (d): Decrease of the reduced impact velocity with e decreasing.

decreasing e predicted by the model, illustrated by figure 7.42(d), takes place at a higher rate than in the experiments. This results in an underestimation of the maximum impact velocity increasing with e decreasing. Nevertheless, figures 7.42(a), (b) and (c) show that predicted impact velocities are in all cases a reasonable estimate of their experimental values.

7.3.3 Conclusions

The VDP oscillator exhibits features similar to those exhibited by a cylinder experiencing VIV and subject to non-linear structural restraints. The periodic impacting motions predicted over most of the impacting domain are similar to those observed in the experiments with large offsets. In the case of asymmetric amplitude limitation of the stop, the model provides good estimates of the maximum amplitude of oscillation of the cylinder, even for low offset values. The main frequency of the motion is overestimated in most cases, but the predicted impact velocities are good estimates of the experimental data over the impacting domain in every case investigated.

Chapter 8

Conclusions

In this thesis, an experimental and numerical investigation of the influence of non-smooth structural non-linearities of the support system of a low-mass low-damping rigid circular cylinder on its cross-flow vortex-induced vibrations has been conducted. Its objective was to develop a deeper understanding of the influence of strong structural non-linearities on the VIV of offshore structures, so that design of restraints can be improved in order to extend the life time of structures at sea. Our interest in VIV of a system with non-linear supports was also stimulated by the problem of predicting the response of a body with imperfectly fitting structural restraints.

8.1 Summary

In a first part of this project, an experimental investigation of the problem has been conducted. An experimental setup has been designed, built and tested initially in the case of linear structural restraints. The dynamic response of the cylinder and the

wake patterns observed show the occurrence of the different modes of excitation known to exist in cross-flow VIV of such low-$m^*\zeta$ cylinders restricted to move in the transverse direction. With linear structural restraints, this experimental setup shows a good agreement with similar experiments from the literature.

Stops, involving a non-smooth non-linearity of the system, were then introduced in the system to limit the amplitude of oscillation of the cylinder. As the experimental design allows variations of the stiffness ratio r_k and the offset e of the stop inserted, cases with impacts on symmetrically-placed soft stops were first investigated. With such restraints, the cylinder exhibits a response similar to that it exhibits with smooth hardening springs. The peak amplitude is not strongly affected but maximum amplitude occurs at higher reduced velocities with the strength of the non-linearity increased.

In increasing the stiffness of the stops, cases with impacts stiff stops, strongly limiting the motion of the cylinder can be achieved. The strong amplitude limitation of the motion has a major effect on the fluid-structure interaction, as dynamics of the cylinder's vibrations, and of its vortex wake, are changed when impact occurs. 2P vortex formation modes are not observed in either single-sided or double-sided impacting cases. In any conditions, flow visualisations show only one single vortex being shed after an impact, certainly because of the rapid change of direction of the cylinder due to impact, leading the shear structures developing behind the cylinder to meet. In every case with impacts investigated, the cylinder can exhibit periodic impacting motions in some ranges of flow velocity, but chaotic motions are also observed. At the beginning of each impacting domain, a narrow window of unpredictable impacting motions is observed, and it seems to be through a process of grazing bifurcations that periodic cycles become stable when increasing the flow velocity. In every case also, the dynamics of the cylinder become more complex with the flow velocity increasing, and with the offset e decreasing.

For all cases with impacts, investigation of the impact velocities and impact forces has also been conducted as these are of major importance in the design of offshore structures. In the cases of impacts on symmetrically-placed stiff stops, a linear increase of the average impact velocity is measured for any offset value, and this increase clearly depends on the offset e at which the rigid stops were placed. In the case of impacts on only one rigid stop, impact velocities seem to also be depending on the maximum amplitude between impacts. In both cases, the impact velocity decreases with the offset decreasing.

In a second part of this project, simple phenomenological models (the "Milan" wake oscillator model and a Van Der Pol (VDP) wake oscillator model) are shown to exhibit some features similar to those of the VIV of the low-mass low-damping cylinder studied in this project, in the case of limitation of the amplitude of the cylinder by stiff stops.

The Milan oscillator provides good predictions of the cylinder's dynamics for large offset values, and the succession of grazing bifurcations it exhibits at the beginning of the impacting domain is similar to the process observed in the experiments. However, the decrease of the amplitude of vibrations for single-sided impacting cases predicted all over the impacting domain when decreasing the offset is not observed in experimental data.

In the case of impacts on one stop, the maximum amplitude between impacts, as well as the impact velocities, predicted by the VDP oscillator are in good agreement with experimental data, over all the respective impacting domains and for any offset value investigated. Impact velocities in cases of double-sided impacting motions are also close to experimental values for every offset value. However, the main frequency of the motion is overestimated in all impacting cases. These results, even if not tested against variations of the stiffness of the stops or of the implementation time, reveal the strong ability of this VDP model to predict the VIV of structures with non-linear

compliance.

8.2 Recommendations for future work

In cases of asymmetric amplitude limitation, the cylinder is able to reach large amplitudes between impacts at large flow velocities when the offset value is small. It is however unclear how the vortex formation occurs in these strongly asymmetric cases. Further investigation of the fluid dynamics with other experimental techniques, such as DPIV, would be needed to clarify this point. Simulation of the problem with a DNS algorithm already validated for VIV of cylinders could also give a further insight on the influence of the amplitude limitation of the structure on the vortex formation process.

Bibliography

[1] V. Strouhal. Uber eine besondere art der tonerregung. *Ann. Physik. Chem*, 5(10):216–251, 1878.

[2] H. Bénard. Formation des centres de giration a l'arrière d'un obstacle en mouvement. *C.R. Acad. Sci. Paris*, 147:839–842, 1908.

[3] T. Von Kármán and H. Rubach. Uber den mechanismus des flüssigkeits und luftwiderstandes - on the resistance mechanisms of fluid and air. *Physikalische Zeitschrift*, 13:49–59, 1912.

[4] J.H. Gerrard. The mechanics of the formation region of vortices behind bluff bodies. *Journal of Fluid Mechanics*, 25:401–413, 1966.

[5] P.W. Bearman. Vortex shedding from oscillating bluff bodies. *Ann. Rev. Fluid. Mech.*, 16:195–222, 1984.

[6] G. Parkinson. Phenomena and modelling of flow-induced vibrations of bluff bodies. *Progress in Aerospace sciences*, 26:169–224, 1989.

[7] R.D. Blevins. *Flow-induced vibration*. Van Nostrand Reinhold, 1990.

[8] F.H. Abernathy and R.E. Kronauer. The formation of vortex streets. *Journal of Fluid Mechanics*, 13:1–20, 1962.

[9] M.L. Facchinetti. *Un modele phenomenologique des vibrations induites par detachement tourbillonnaire*. PhD thesis, Ecole Polytechnique, Palaiseau, 2003.

[10] N. Jauvtis and C.H.K. Williamson. Vortex-induced vibration of a cylinder with two degrees of freedom. *Journal of Fluid and Structures*, 17:1035–1042, 2003.

[11] N. Jauvtis and C.H.K. Williamson. The effect of two degrees of freedom on vortex-induced vibration at low mass and damping. *Journal of Fluid Mechanics*, 509:23–62, 2004.

[12] D. Jeon and M. Gharib. On circular cylinders undergoing two-degree-of-freedom forced motions. *Journal of Fluids and Structures*, 15:533–541, 2001.

[13] T. Sarpkaya. Hydrodynamic damping, flow-induced oscillations, and biharmonic response. *Journal of Offshore Mechanics and Arctic Engineering*, 117:232–238, 1995.

[14] C.C. Feng. *The measurement of vortex-induced effects in flow past stationary and oscillating circular and D-section cylinders*. PhD thesis, University of BritishColumbia, 1968.

[15] A. Khalak and C.H.K. Williamson. Fluid forces and dynamics of a hydroelastic structure with very low mass and damping. *Journal of Fluids and Structures*, 11:973–982, 1997.

[16] R. Govardhan and C.H.K. Williamson. Modes of vortex formation and frequency response of a freely vibrating cylinder. *Journal of Fluid Mechanics*, 420:85–130, 2000.

[17] T. Sarpkaya. A critical review of the intrinsic nature of vortex-induced vibrations. *Journal of Fluids and Structures*, 19:389–447, 2004.

[18] D. Brika and A. Lanneville. Vortex-induced vibrations of a long flexible circular cylinder. *Journal of Fluid Mechanics*, 250:481–508, 1993.

[19] C.H.K. Williamson and A. Roshko. Vortex formation in the wake of an oscillating cylinder. *Journal of Fluids and Structures*, 2:355–381, 1988.

[20] S. P. Singh and S. Mittal. Vortex-induced oscillations at low reynolds numbers : Hysteresis and vortex-shedding modes. *Journal of Fluids and Structures*, 20:1085–1104, 2005.

[21] D. Jeon and M. Gharib. On the relationship between the vortex formation process and cylinder wake vortex patterns. *Journal of Fluid Mechanics*, 519:161–181, 2004.

[22] M. Irani and L. Finn. Model testing for vortex-induced motions of spar platforms. *Procedings of OMAE04,* 23^{rd} *Int. Conference on Offshore Mechanics and Arctic engineering, Vancouver, Canada*, 2004.

[23] B. Stappenbelt and K. Thiagarajan. Vortex-induced vibration of catenary moored cylindrical structures. *Procedings of OMAE04,* 23^{rd} *Int. Conference on Offshore Mechanics and Arctic engineering, Vancouver, Canada*, 2004.

[24] B. Stappenbelt. *Vortex-induced vibration of moored cylindrical structures*. PhD thesis, University of Western Australia, 2006.

[25] F.S. Hover and M. S. Triantafyllou. The lock-in phenomena for cylinders with nonlinear compliance. *Conf. on Bluff Body Wakes and Vortex-Induced Vibrations, Washington D.C., USA*, 1998.

[26] M.K. Nygard, F.R. Botros, and H. Hannus. Evaluation of effect of contact between top tensioned risers in deep and ultra deep waters. *Proceedings of the International Offshore and Polar Engineering Conference*, 2:222 – 226, 2001.

[27] C. Bridge, H. Howells, N. Toy, G. Parke, and R. Woods. Full scale model tests of a steel catenary riser. *Proc. of the Second International Conference on Fluid Structure Interaction*, pages 107–116, 2003.

[28] L.A. Campos and C.A. Martins. Nonlinear dynamic response of a steel catenary riser at the touch-down point. *Proceedings of the Eleventh (2001) International Offshore and Polar Engineering Conference, Stavanger, Norway*, 2:234–238, 2001.

[29] J. A. Aranha, C. A. Martins, and C. P. Pesce. Analytical approximation for the dynamic bending moment at the touchdown point of a catenary riser. *International Journal of Offshore and Polar Engineering, Golden, Colorado*, 7(4):303–310, 1997.

[30] C. P. Pesce, J. A. Aranha, and C. A. Martins. Dynamic curvature in catenary risers at the touch down point region: An experimental study and the analytical boundary-layer solution. *International Journal of Offshore and Polar Engineering, Golden, Colorado*, 8(4):303–310, 1998.

[31] C. Bridge, H. Howells, N. Toy, G. Parke, and R. Woods. Steel catenary riser touchdown point vertical interaction models. *Offshore Technology Conference, Houston, Texas*, 2004.

[32] J. H. You. Numerical model for steel catenary riser on seafloor support. Master's thesis, Texas A&M University, College Station, Texas, 2005.

[33] M.S. Triantafyllou, A. Bliek, and H. Shin. Dynamic analysis as a tool for open-sea mooring system design. *SNAME Transactions*, 93:302–324, 1985.

[34] J. I. Gobat and M. A. Grosenbaugh. Dynamics in the touchdown region of catenary moorings. *Proceedings of the Eleventh (2001) International Offshore and Polar Engineering Conference, Stavanger, Norway*, 11(4):273–281, 2001.

[35] C. P. Pesce, C. A. Martins, and L. M. Y. Da Silveira. Riser-soil interaction: Local dynamics at tdp and a discussion on the eigenvalue and the viv problems. *Journal of Offshore Mechanics and Arctic Engineering*, 128(1):39–55, 2006.

[36] P.F. Verhulst. Notice sur la loi que la population pursuit dans son accroissement. *Correspondance mathématique et physique*, 10:113–121, 1838.

[37] J. Guckenheimer and P.J. Holmes. *Nonlinear oscillations, Dynamical systems and Bifurcations of vector fields*. Springer-Verlag, New York, 1983.

[38] F.C. Moon. *Chaotic Vibrations, an introduction for applied scientists and engineers*. Jhon Wiley and sons, New York, 1987.

[39] A. Cauchy. Mémoire sur un théorème fondamental dans le calcul intégral. *C. R. Acad. Sci. Paris*, 14:1020–1026, 1842.

[40] H. Poincaré. Sur le problème des trois corps et les équations de la dynamique. *Acta Mathematica*, 13:1–270, 1890.

[41] M.J. Feigenbaum. Quantitative universality for a class of nonlinear transformations. *Journal of Statictical Physics*, 19(1):25–52, 1978.

[42] J. Hadamard. Les surfaces courbures opposes et leurs lignes godsiques. *J. Math. Pures et Appl.*, 4:27–73, 1898.

[43] J.P. Meijaard. A mechanism for the onset of chaos in mechanical systems with motion-limiting stops. *Chaos, Solitons and Fractals*, 7(10):1649 – 1658, 1996.

[44] H. Whitney. Differentiable manifolds. *Annals of Mathematics*, 37:645–680, 1936.

[45] G.D. Birkhoff. Proof of the ergodic theorems. *Proc. Nat. Acad. Sci.*, pages 656–660, 1931.

[46] F. Takens. Detecting strange attractors in turbulence. *Lecture Notes in Mathematics*, pages 366–381, 1981.

[47] H. Kantz and T. Schreiber. *Nonlinear time series analysis*. Cambridge University Press, 1997.

[48] A.M. Fraser and H.L. Swinney. Independent coordinates for strange attractors from mutual information. *Physical Review A*, 33:1134–1140, 1986.

[49] T. Sauer, J.A. Yorke, and M. Casdagli. Embedology. *Journal of Statistical Physics*, 65(3-4):579–616, 1991.

[50] A. Wolf, J.B. Swift, and J.A. Vastano. Determining lyapunov exponent from a time series. *Physics*, 16D:285–317, 1984.

[51] M.T. Rosenstein, J. J. Collins, and C. J. De Luca. A practical method for calculating the largest lyapunov exponents from small data sets. *Physica D*, 65:117–134, 1993.

[52] J.P. Eckmann and D. Ruelle. Ergodic theory of chaos and strange attractors. *Reviews of Modern Physics*, 57(3):617 – 56, 1985.

[53] B. Blazejczyk-Okolewska, K. Czolczynski, and T. Kapitaniak. Classification principles of types of mechanical systems with impacts fundamental assumptions and rules. *European Journal of Mechanics - A/Solids*, 23(3):517–537, 2004.

[54] M. Di Bernardo, C.J. Budd, A.R. Champneys, and P. Kowalczyk. *Piecewise-smooth dynamical systems: Theory and Applications*. Springer, 2007.

[55] F. Peterka, K. Tadashi, and S. Iperac. Explanation of appearance and characteristics of intermittency chaos of the impact oscillator. *Chaos, Solitons & Fractals*, 19(5):1251–1259, 2004.

[56] M.B. Hindmarsh and D.J. Jefferies. On the motions of the offset impact oscillator. *J. Phys. A:*, 17:1791–1803, 1984.

[57] J.M.T. Thompson and R. Ghaffari. Chaos after period-doubling bifurcations in the resonance of an impact oscillator. *Physics Letters A*, 91A(1):5 – 8, 1982/08/16.

[58] S.W. Shaw and P. J. Holmes. A periodically forced piecewise linear oscillator. *Journal of Sound and Vibration*, 90(1):129 – 55, 1983.

[59] H. Lamba. Chaotic, regular and unbounded behaviour in the elastic impact oscillator. *Physica D*, 82:117–135, 1995.

[60] Budd C. and Dux F. Intermittency in impact oscillators close to resonance. *Nonlinearity*, 7:1191–1224, 1994.

[61] Budd C., Dux F., and Cliffe A. The effect of frequency and clearance variations on single-degree-of-freedom impact oscillators. *Journal of Sound and Vibration*, 184:475–502, 1995.

[62] A. B. Nordmark. Existence of periodic orbits in grazing bifurcations of impacting mechanical oscillators. *Nonlinearity*, 14:1517–1542, November 2001.

[63] F. Peterka and T. Kotera. Four ways from periodic to chaotic motion in the impact oscillator. *Machine Vib.*, 5:71–82, 1996.

[64] F. Peterka. Behaviour of impact oscillator with soft and preloaded stop. *Chaos, Solitons and Fractals*, 18:79–88, 2003.

[65] F. Peterka. Dynamics of mechanical systems with soft impacts. *Proceedings of IUTAM symposium on chaotic dynamics and control of systems and processes in mechanics, Rome, Italy*, 19(5):1251–1259, 2003.

[66] G.W. Luo and J.H. Xie. Stability of periodic motion, bifurcations and chaos of a two-degree-of-freedom vibratory system with symmertical rigid stops. *Journal of Sound and Vibration*, 273(3):543–568, 2004.

[67] G.W. Luo. Period-doubling bifurcations and routes to chaos of the vibratory systems contacting stops. *Physics letters. A*, 223(3-4):210–217, 2004.

[68] D.T Nguyen, S.T Noah, and C.F. Kettleborough. Impact behaviour of an oscillator with limiting stops - part 1: A parametric study. *Journal of Sound and Vibration*, 109(2):293–307, 1986.

[69] M.P. Païdoussis and G.X. Li. Cross-flow-induced chaotic vibrations of heat-exchanger tubes impacting on loose supports. *Journal of Sound and Vibration*, 152(2):305 – 326, 1992.

[70] N.W. Mureithi. *Nonlinear dynamics of a loosely-supported cylinder in cross-flow.* PhD thesis, Mc Gill University, Montreal, 1993.

[71] Y. Cai and S.S. Chen. Non-linear dynamics of loosely supported tubes in crossflow. *Journal of Sound and Vibration*, 168(3):449–468, 1993.

[72] Y. Cai and S.S. Chen. Chaotic vibrations of nonlinearly supported tubes in crossflow. *Transactions of the ASME. Journal of Pressure Vessel Technology*, 115(2):128–34, 1993.

[73] N. W. Mureithi, S. J. Price, and M. P. Païdoussis. The post-hopf-bifurcation response of a loosely supported cylinder in an array subjected to cross-flow - part i: Experimental results. *Journal of Fluids and Structures*, 8(8):833 – 852, 1994.

[74] N. W. Mureithi, S. J. Price, and M. P. Païdoussis. The post-hopf-bifurcation response of a loosely supported cylinder in an array subjected to cross-flow - part ii: Theoretical model and comparison with experiments. *Journal of Fluids and Structures*, 8(8):853–876, 1994.

[75] Y. Pomeau and P. Manneville. Intermittent transition to turbulence in dissipative dynamical systems. *Communications in Mathematical Physics*, 74(2):189 – 97, 1980.

[76] J.R. Chaplin. Hydrodynamic damping of a cylinder at $\beta \approx 10^6$. *Journal of Fluids and Structures*, 14:1101–1117, 2000.

[77] G.G. Stokes. On the effect of the internal friction of fluids on the motion of pendulums. *Transactions of the Cambridge Philosophical society*, 9:8–106, 1851.

[78] S. Bourdier and J.R. Chaplin. Vortex-induced vibrations of a rigid cylinder on nonlinear elastic supports. *Proceedings of the 6th international conference on FSI, AE & FIV+N, Vancouver*, 2006.

[79] A. Khalak and C.H.K. Williamson. Motions, forces and mode transitions in vortex-induced vibrations at low mass-damping parameter. *Journal of Fluids and Structures*, 13:813–851, 1999.

[80] A. Khalak and C.H.K. Williamson. Investigation of relative effects of mass and damping in vortex-induced vibration of a cylinder. *Journal of Wind engineering and Industrial Aerodynamics*, 71:341–350, 1997.

[81] G.W. Luo and J.H. Xie. Analysis of non synchronized sinusoidally driven dynamical system. *International Journal of Bifurcations and Chaos*, 10(7):1759–1772, 2000.

[82] H. Poincaré. L'espace et la méthode. *Revue de métaphysique et de morale*, pages 631–646, 1895.

[83] J.R. Chaplin, P.W. Bearman, E. Fontaine, K. Herfjord, M. Isherwood, C.M. Larsen, J.R. Meneghini, G. Moe, and M.S. Triantafyllou. Blind predictions of laboratory measurements of vortex-induced vibrations of a tension riser. *Proceedings of the 8th international conference on Flow-Induced Vibration FIV2004*, 2:285–290, 2004.

[84] R.E.D. Bishop and A.Y. Hassan. The lift and drag forces on a circular cylinder oscillating in a flowing fluid. *Proceedings, Royal Society, London*, 277, 1964.

[85] G.D. Birkhoff and E.H. Zarantello. Jets, wakes and cavities. *Academic Press, New York*, pages 291–292, 1957.

[86] R.T. Hartlen and I.G. Currie. Lift-oscillator model for vortex-induced vibration. *Journal of the Engineering Mechanics Divison*, 96(5):577–591, 1970.

[87] N. Minorsky. *Nonlinear oscillations*. Van Nostrand Company, Inc, 1962.

[88] M.L. Facchinetti and E. De Langre. Coupling of structure and wake oscillators in vortex-induced vibrations. *Journal of Fluids and Structures*, 19(2):123–140, 2004.

[89] M. Falco, F. Fossati, and F. Resta. On the vortex induced vibration on submarine cables: Design optimization of wrapped cables for controlling vibrations. *3rd Int. Symp. Cable Dynamics*, 1999.

[90] J.R. Morison, J.W. Johnson, M.P. O'Brien, and S.A. Schaff. The forces exerted by surface waves on piles. *Petroleum Transactions, American Institute of Mining engineers*, 189:145–154, 1950.